# The Double Renner Effect

a Dissertation submitted to the FB-C
of the Bergische Universität Wuppertal
and Ochanomizu University
in partial fulfillment of
the requirements for the degree of
Doctor of Natural Science

by
Tina Erica Odaka
from Tokyo

2003 Wuppertal

# Acknowledgement

It is my pleasure to thank Professor Per Jensen for his valuable guidance through each stage of my work, his tireless efforts towards providing me with a grant which allowed me to be able to work in Germany and complete my thesis, and his continuous passion for overcoming all the difficulties with the joint degree.

I express my sincere thanks to Prof. Tsuneo Hirano for his helpful discussions and his guidance during my work, and for suggesting the idea of a joint degree between the Bergische Universität Wuppertal and Ochanomizu University.

My warm thank also goes to Prof. Keiko Takano in her effort for organizing the exam in Ochanomizu University and her tremendous efforts for making the agreement with the Bergische Universität Wuppertal for me to have the joint degree.

My sincere thanks are due to Mr. Heinz-Peter Liebermann for his extensive work on calculating $HO_2$ $ab\ initio$ points. I would also like to express my sincere thanks to Mr. Peter Funke for his continuous help with all the technical problems related to the computer.

I would like to express my appreciation to Prof. Jonathan Tennyson for handing me the subroutines related to the stretching basis function and for the kind hospitality during my stay at his university.

I would also like to express my appreciation to Mr. Peter Langer and his colleague for me to use their computer resources and helpfull discussions. I would like to thank Prof. Masatoshi Ohishi and Dr. Lukas Pichl for their generosity in allowing me

to use their computational resocrces. Without those computer resources, it was not possible to accomplish the work for my thesis.

I would like to thank all the persons who made it possible for me to have the joint degree between the Bergische Universität Wuppertal and Ochanomizu Unjiversity. Especially, I would like to thank Mr. Masaaki Chikamoto, Prof. Nozomu Hamaya, Prof. Yukiko Hirano, Prof. Masuko Honda, Ms. Emi Igami, Prof. Ko Okumura, Prof. Isamu Matsumoto, Mr. Nobuyuki Ooyama, and Mr. Susumu Suzuki from Ochanomizu University and Prof. Hans-Josef Altenbach, Prof. Reint Eujen, Mr. Karl Andreas Golla, Ms. Marion Litz, Prof. Annegret Maack, Prof. Volker Ronge, and Ms. Annemarie Weber from the Bergische Universität Wuppertal.

I am very grateful to all my familly members for their financial and moral support throughout my work, especially I would like to thank Dr. Jean-Francois D'Eu for making corrections on my thesis.

My most sincere thanks are also due to all the faculty members and friends in Japan and Europe.

# Contents

**1 Introduction** **5**

**2 Theory** **9**

2.1 Hamiltonian . . . . . 9

2.1.1 Construction of the Jacobi Hamiltonian . . . . . 9

2.1.2 Total Hamiltonian . . . . . 17

2.2 The basis functions . . . . . 18

2.2.1 Rotation-spin basis functions . . . . . 19

2.2.2 Bending basis functions . . . . . 23

2.2.3 Electronic-rotation-spin basis functions . . . . . 29

2.2.4 Stretching basis functions . . . . . 31

2.2.5 Symmetry of the basis functions . . . . . 32

2.3 Construction of the matrix elements . . . . . 34

2.3.1 Matrix elements of $\hat{H}_e$ (HAMILV) . . . . . 38

2.3.2 Matrix elements of $\hat{H}_{PrR}$ (HBL1, HBL2) . . . . . 39

2.3.3 Matrix elements of $\hat{H}_b$ (HAMILB) . . . . . 39

2.3.4 Matrix elements of $\hat{H}_{ba}$ and $\hat{H}_{bb}$ (HAMILBA, HAMILBB) . . . . . 43

2.3.5 Matrix elements of $\hat{H}_{nk}$ (HAMILNK) . . . . . 44

2.3.6 Matrix elements of $\hat{H}_{dk}$(HAMILDK) . . . . . 45

2.3.7 Matrix elements from $\hat{H}_{SO}$ (HAMILSO) . . . . . 49

2.4 Diagonalization of the Hamiltonian . . . . . 50
2.4.1 $K$-block diagonalization . . . . . 50
2.4.2 $J$-block diagonalization . . . . . 53
2.5 What do we do with the eigenvalues and eigenfunctions? . . . . . 54
2.5.1 Assignment and notation for bent molecules . . . . . 54
2.5.2 Assignment and Notation for linear molecule . . . . . 59
2.5.3 Probability density functions . . . . . 60

**3 The program DR 63**
3.1 Basic definition of the system . . . . . 63
3.2 Construction of the stretching basis functions . . . . . 64
3.3 Starting the $K$ loop . . . . . 67
3.4 $J$-block diagonalization . . . . . 69

**4 The double Renner effect in ABC-type molecules 73**
4.1 What is MgNC? . . . . . 73
4.2 Applying DR to MgNC/MgCN . . . . . 76
4.2.1 Global potential energy surfaces . . . . . 76
4.2.2 Bending basis functions . . . . . 77
4.3 Results . . . . . 83
4.3.1 Computational details . . . . . 83
4.3.2 Vibronic energy levels . . . . . 87

**5 The double Renner effect in ABB-type molecules 119**
5.1 $HO_2$ . . . . . 119
5.2 Applying DR to $HO_2$ . . . . . 121
5.2.1 Global potential energy surfaces . . . . . 121
5.2.2 Bending basis functions . . . . . 123

5.3 Results . . . . . 123
5.3.1 Computational details . . . . . 123
5.3.2 Vibronic energy levels . . . . . 126

**6 Conclusion** **151**

**A A Theoretical Study of MgNC and MgCN in the $\widetilde{X}\ ^2\Sigma$ Electronic State** **169**

**B $Ab\ initio$ molecular orbital prediction of the Renner-Teller effect for the first excited state $^2\Pi$ of MgNC: Reinterpretation of the laser-induced fluorescence spectrum based on the predicted spectroscopic constants** **171**

**C An $ab\ initio$ study of the $\widetilde{A}\ ^2\Pi$ State and the $\widetilde{A}\ ^2\Pi \leftarrow \widetilde{X}\ ^2\Sigma$ Electronic Transition of MgNC** **173**

**D The Renner effect in triatomic molecule with appication to $\mathbf{CH_2^+}$ , MgNC and $\mathbf{NH_2}$** **175**

**E A Theoretical Study of $\widetilde{A}\ ^2\Pi$ MgCN** **177**

# Chapter 1

# Introduction

Within the Born-Oppenheimer approximation, the electronic energy of a molecule in a given electronic state can be determined by solving a Schrödinger equation obtained by fixing the nuclei in space. The most commonly used approach to this type of calculation is the so-called $ab\ initio$ method. As a result of the continuous development of computational methods and computational technology, $ab\ initio$ calculations produce increasingly more accurate potential energy surfaces for molecules at lower and lower cost. The rotation-vibration energies of the molecule are computed by solving the rotation-vibration Schrödinger equation. Such calculations are based on the potential energy surfaces determined in the $ab\ initio$ step. A molecule has infinitely many electronic states whose energies we at least, in principle, could obtain by $ab\ initio$ calculations. In the Born-Oppenheimer approximation, we obtain the rovibronic energies for one electronic state only. However, if two or more electronic states are close in energy, the Born-Oppenheimer approximations fails, and these states must be considered together when the rovibronic energies are obtained.

One case in which the Born-Oppenheimer approximation invariably fails is the Renner effect in a triatomic molecule. In 1934 Renner [1] realized that if, for a triatomic molecule, the electronic energy is doubly degenerate at linear geometries, it must nec-

essarily split into two separate components when the molecule bends. The two resulting electronic states are close in energy and the Born-Oppenheimer approximation fails for therein. 23 years after the paper by Renner, the first example of the Renner effect was observed by Dressler and Ramsay [2, 3] and it was $NH_2$. Renner suggested in his paper the possibility of two electronic states, both with linear equilibrium geometry to be degenerate at the linear configuration, but by chance, $NH_2$ was of a type that Renner did not consider. The two electronic surfaces which are degenerate at linear geometries of $NH_2$ have bent equilibrium geometry, the lower electronic state $\widetilde{X}^2B_1$, has a bent equilibrium geometry and the upper state $\widetilde{A}^2A_1$ has a linear equilibrium geometry. Pople and Longuet-Higgins gave a theoretical discussion of this case [4, 5]. The first example to be observed following Renner's ideas, i.e., two electronic states both with linear equilibrium geometry and degenerate at the linear configuration, was found in the ground electronic state of NCO [6].

We have carried on an extensive calculation for $\widetilde{X}\ ^2\Sigma$ MgNC and the isomer $\widetilde{X}\ ^2\Sigma$ MgCN. We constructed one Born-Oppenheimer potential energy surface using $ab\ initio$ method and calculated ro-vibrational energy levels with the program MORBID [7]. MORBID is a program calculating rovibrational energy levels by solving the rotation-vibration Schrödinger equation for one potential minimum on one Born-Oppenheimer surface. The electronic ground states $\widetilde{X}\ ^2\Sigma$ MgNC and $\widetilde{X}\ ^2\Sigma$ MgCN are well separated from the first electronic excited states $\widetilde{A}\ ^2\Pi$ MgNC and $\widetilde{A}\ ^2\Pi$ MgCN, thus we could calculate rotation-vibration energy levels for one Born-Oppenheimer surface, and we obtained result in good agreement with experimental result. Details are in Appendix A.

The first electronic excited state of MgNC, $\widetilde{A}\ ^2\Pi$ is a degenerate electronic state at lineality, and its equilibrium geometry is at the linear configuration. This state exhibits the Renner effect, and we have obtained two Born-Oppenheimer surfaces with $ab\ initio$ methods, and have calculated ro-vibronic energy levels using perturbation theory. The result are compared with the experiment results for the $\widetilde{A}\ ^2\Pi \leftarrow \widetilde{X}\ ^2\Sigma$ electronic

transition of MgNC obtained by R. R. Wright and T. A. Miller in 1999 [8]. In our study, we proposed different assignments from the one made by Wright and Miller. Details are in Appendix B.

To investigate the difference in assignment, we have extended our $ab\ initio$ potential energy surfaces and calculated Franck-Condon factors and effective rotational constants using the RENNER [9] program system. This work confirmed the reassignment of vibronic bands in the $\widetilde{A}\ ^2\Pi \leftarrow \widetilde{X}\ ^2\Sigma$ electronic transition as described in Appendix C. In this work, we investigated the wavefunctions of individual rovibronic levels by plotting probability density functions for the total wavefunction and for each Born-Oppenheimer electronic state. This provided further insight into the nature of the Renner interaction (Appendix D).

The isomer of $\widetilde{A}\ ^2\Pi$ MgNC, $\widetilde{A}\ ^2\Pi$ MgCN, is also a degenerate electronic state and exhibits the Renner effect. We determined $ab\ initio$ potential energy surface for $\widetilde{A}\ ^2\Pi$ MgCN, using the same $ab\ initio$ method employed to obtain the potential energy surfaces of $\widetilde{A}\ ^2\Pi$ MgNC. We then calculated rovibronic energy levels of $\widetilde{A}\ ^2\Pi$ MgCN using the RENNER program system. Transitions involving $\widetilde{A}\ ^2\Pi$ MgCN are not yet observed, and this is the first theoretical prediction of $\widetilde{A}\ ^2\Pi$ MgCN. The details are in Appendix E.

RENNER is a program calculating rovibrational energy levels by solving the rotation-vibration Schrödinger equation, in one potential minimum on each of the two Born-Oppenheimer potential surfaces. Here we extend this idea to a case when two different linear geometries (corresponding to doubly degenerate electronic state) are accessible in a molecule. In other words, if a linear geometry of a molecule, which exhibits Renner effect, is accessible from another linear geometry of the molecule, which also exhibits Renner effect, we name this phenomenon 'the double Renner effect.' In this thesis, we discuss the double Renner effect for a triatomic molecule.

For example, a double Renner effect will occur if the triatomic molecule ABC isomerizes between two linear minima ABC and BCA, and the electronic energy is doubly

degenerate at these minima. An example of this is afforded by the two isomers MgNC and MgCN in the $\widetilde{A}\ ^2\Pi$ electronic state. Also ABB-type molecules can exhibit the double Renner effect. In the $\widetilde{X}\ ^2A''$ and $\widetilde{A}\ ^2A'$ electronic states of $HO_2$, the proton orbits the OO moiety with two equivalent minima on each potential surface at bent geometries. At the two linear geometries $HO_2$ and OOH (which correspond to transition states on the potential energy surface) the two electronic states are degenerate as a $\Pi$ state. The two equivalent minima on each surface are separated by another transition state corresponding to a T-shaped geometry.

We have developed a program for calculating the rovibronic energies for a triatomic molecule in 'double-Renner'-degenerate electronic states. Our program can treat both ABC- and ABB-type molecules; the new program has been applied to $\widetilde{A}\ ^2\Pi$ MgNC/MgCN, and to $HO_2$ in the $\widetilde{X}\ ^2A''$ and $\widetilde{A}\ ^2A'$ states. We present detailed analyses of rotation-bending-electronic wavefunctions aimed at providing further insight into the nature of the double-Renner interaction.

The theory on double Renner effect is given in Chapter 2 and a description of on the program "DR" is in Chapter 3. The application to ABC-type molecules (here the $\widetilde{A}\ ^2\Pi$ MgNC/MgCN system) is in Chapter 4, and the application on ABB-type molecule ($\widetilde{X}\ ^2A''$ and $\widetilde{A}\ ^2A'$ $HO_2$ system) is the subject of Chapter 5.

# Chapter 2

# Theory

## 2.1 Hamiltonian

### 2.1.1 Construction of the Jacobi Hamiltonian

We use Jacobi coordinates to represent an atom (A) orbiting the other two atoms (B and C) (See Fig. 2.1). The Jacobi angle is called $\tau$, and the distances are called $r$ and $R$. $R$ represents the distance between the nuclei B and C, and $r$ is the distance from A to the B-C center of mass. We write the masses of the nuclei A, B and C as $m_A$, $m_B$ and $m_C$ respectively. $\mu_R$ and $\mu_r$ are the reduced masses corresponding to the $R$ and $r$ "bonds".

$$\mu_R = \frac{m_B m_C}{m_B + m_C} \tag{2.1}$$

$$\mu_r = \frac{m_A \times (m_B + m_C)}{m_A + m_B + m_C} \tag{2.2}$$

The molecular fixed coordinate system has its origin at the center of mass of the molecule. The $z$-axis of the molecule fixed coordinate system is set to be parallel to the BC-bond. The $y$-axis is perpendicular to the $z$-axis and pointing towards nucleus

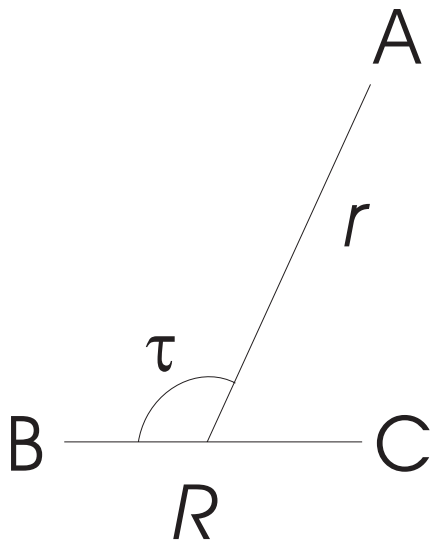


Figure 2.1: The Jacobi coordinate system. A, B and C represents the atoms in this coordinate system. $R$ and $r$ are the bond lengths. $\tau$ is the Jacobi angle.

A. The $x$-axis is perpendicular to both the $y$- and $z$-axis, and makes the xyz system right-handed.

From Wilson-Decius-Cross [10] , we know that

$$2T' = \sum_{i=1}^{3} m_i V_i^2, \tag{2.3}$$

with $T'$ for the total kinetic energy, and $V_i$ for the velocity of nucleus $i$ in the space fixed coordinate system. Here we write the vector pointing to atom $i$ from the origin of the molecule-fixed axis system as $\vec{r_i}$, the vector pointing to the origin of the molecular-fixed coordinate system from the origin of the space-fixed coordinate system as $\vec{R}_0$, the vector pointing to nucleus $i$ from the origin of the space-fixed coordinate system as $\vec{R}_i$, and we have

$$\vec{R}_i = \vec{R}_0 + \vec{r_i}. \tag{2.4}$$

$V_i$ can be written in the space fixed coordinate system and in the molecule-fixed coor-

dinate system as follows:

$$\vec{V_i} = \dot{\vec{R}}_0 + \vec{\omega} \times \vec{r_i} + \dot{\vec{v}}_i. \tag{2.5}$$

where $\vec{\omega}$ is the angular velocity in the space-fixed coordinate system, and $v_i$ is atom $i$'s velocity in the molecule-fixed coordinate system. With equation (2.5), we can separate the kinetic energy arising from the translation of the molecule-fixed coordinate system with respect to the space fixed coordinate system, by extracting out the kinetic energy term depending on $\vec{R}_0$ from (2.3).

$$2T' = \sum_{i=1}^{3} m_i(\vec{\omega} \times \vec{r_i})^2 + \sum_{i=1}^{3} m_i v_i^2 + 2\vec{\omega} \sum_{i=1}^{3} m_i \vec{r_i} \times \vec{v_i} \tag{2.6}$$

$$+\dot{\vec{R}}_0{}^2 \sum_{i=1}^{3} m_i + 2\dot{\vec{R}}_0 \sum_{i=1}^{3} m_i(\vec{\omega} \times \vec{r_i} + \vec{v_i}) \tag{2.7}$$

The last two terms, the first are related to the translation of molecular fixed coordinate system and the last is zero. Thus we neglect these term for constructing the Hamiltonian.

$$\begin{aligned} 2T_{CM} &= \dot{\vec{R}}_0{}^2 \sum_{i=1}^{3} m_i + 2\dot{\vec{R}}_0(\vec{\omega} \times \sum_{i=1}^{3} m_i \vec{r_i} + \sum_{i=1}^{3} m_i \vec{v_i}) \\ &= \dot{\vec{R}}_0{}^2 M \end{aligned} \tag{2.8}$$

$$M = m_A + m_B + m_C \tag{2.9}$$

Thus the internal kinetic energy $T$ is

$$2T = 2T' - 2T_{CM} = \sum_{i=1}^{3} m_i(\vec{\omega} \times \vec{r_i})^2 + \sum_{i=1}^{3} m_i v_i^2 + 2\vec{\omega} \sum_{i=1}^{3} m_i \vec{r_i} \times \vec{v_i}. \tag{2.10}$$

The vector $\vec{r_i}$ can be written in $R$, $r$, $\tau$ coordinate system as

$$\vec{r}_A = (0, r\sin\tau, r\cos\tau) - \vec{R}^* \tag{2.11}$$

$$\vec{r}_B = (0, 0, -\frac{m_C}{m_B + m_C} R) - \vec{R}^* \tag{2.12}$$

$$\vec{r}_C = (0, 0, \frac{m_B}{m_B + m_C} R) - \vec{R}^* \tag{2.13}$$

$$\vec{R}^* = \frac{m_A}{M}(0, r\sin\tau, r\cos\tau) \tag{2.14}$$

Thus the velocity in the molecule-fixed coordinate system is

$$\vec{v}_A = (0, \dot{r}\sin\tau + r\dot{\tau}\cos\tau, \dot{r}\cos\tau - r\dot{\tau}\sin\tau) - \dot{\vec{R}}^* \quad (2.15)$$

$$\vec{v}_B = (0, 0, -\frac{m_C}{m_B + m_C}\dot{R}) - \dot{\vec{R}}^* \quad (2.16)$$

$$\vec{v}_C = (0, 0, \frac{m_B}{m_B + m_C}\dot{R}) - \dot{\vec{R}}^* \quad (2.17)$$

$$\dot{\vec{R}}^* = \frac{m_A}{M}(0, \dot{r}\sin\tau + r\dot{\tau}\cos\tau, \dot{r}\cos\tau - r\dot{\tau}\sin\tau) \quad (2.18)$$

The kinetic energy $T$ is rewritten by inserting the expression for the $\vec{r}_i$ and $\vec{v}_i$

$$\begin{aligned} 2T &= (\mu_R R^2 + \mu_r r^2)\omega_x^2 + (\mu_R R^2 + \mu_r r^2\cos^2\tau)\omega_y^2 \\ &\quad + \mu_r r^2 \sin^2\tau\omega_z^2 - \mu_r r^2 \sin^2 2\tau\omega_y\omega_z \\ &\quad + \mu_R\dot{R}^2 + \mu_r\dot{r}^2 + \mu_r(r^2\dot{\tau}^2 - 2\omega_x\dot{\tau}r^2) \end{aligned} \quad (2.19)$$

Here we introduce the "I-tensor".

$$I_{xx} = \mu_R R^2 + \mu_r r^2 \quad (2.20)$$

$$I_{yy} = \mu_R R^2 + \mu_r r^2\cos^2\tau \quad (2.21)$$

$$I_{zz} = \mu_r r^2 \sin^2\tau \quad (2.22)$$

$$I_{yz} = -\frac{1}{2}\mu_r r^2 \sin^2 2\tau \quad (2.23)$$

$$I_{xy} = I_{xz} = 0 \quad (2.24)$$

With the I-tensor, we can rewrite the kinetic energy $T$ as follows.

$$2T = I_{xx}w_x^2 + I_{yy}w_y^2 + I_{zz}w_z^2 - 2I_{yz}w_y w_z + \mu_R\dot{R}^2 + \mu_r\dot{r}^2 + \mu_r(r^2\dot{\tau}^2 - 2w_x\dot{\tau}r^2) \quad (2.25)$$

To "clean up" the last term in equation (2.25), we introduce two additional elements of the I-tensor.

$$I_{x\tau} = -\mu_r r^2 \quad (2.26)$$

$$I_{\tau\tau} = \mu_r r^2 \quad (2.27)$$

Thus the final I-tensor $\mathbf{I}$ and angular velocity vector $\bar{w}$ will be written as

$$\mathbf{I} = \begin{Bmatrix} I_{yy} & Iyz & 0 & 0 \\ I_{yz} & Izz & 0 & 0 \\ 0 & 0 & I_{xx} & I_{x\tau} \\ 0 & 0 & I_{x\tau} & I_{\tau\tau} \end{Bmatrix} \tag{2.28}$$

$$\omega = \begin{Bmatrix} \omega_y \\ \omega_z \\ \omega_x \\ \omega_\tau = \dot{\tau} \end{Bmatrix}, \tag{2.29}$$

and the kinetic energy $T$ is

$$2T = \sum_{\alpha,\beta=x,y,z,\tau} I_{\alpha\beta}\omega_\alpha\omega_\beta + \mu_R\dot{R}^2 + \mu_r\dot{r}^2. \tag{2.30}$$

The classical total angular momentum for the system is

$$J_\alpha = \sum_{\beta=x,y,z,\tau} I_{\alpha\beta}\omega_\beta - \delta_{\alpha x}\mu_r\dot{r}^2\dot{\tau}\omega_x \tag{2.31}$$

with

$$J_\alpha = (\mathbf{I}\omega)_\alpha, \qquad \alpha = x, y, z, \tau \tag{2.32}$$

To change the classical kinetic energy term into a quantum mechanical Hamiltonian, we must express the classical kinetic energy in terms of the coordinates and their conjugate momenta, before using the quantum mechanical postulates. The momentum $P_i$, conjugate to the coordinate $q_i$ can be calculated as

$$P_i = \frac{\partial(T-V)}{\partial\dot{q}_i} = \frac{\partial T}{\partial\dot{q}_i} \tag{2.33}$$

since the potential energy $V$ does not depend on the $\dot{q}_i$. We calculate here the momenta $P_\tau$, $P_R$, $P_r$, conjugate to the $\tau$, $R$, $r$, coordinates respectively.

$$P_R = \frac{\partial T}{\partial\dot{R}} = \mu_R\dot{R} \tag{2.34}$$

$$P_r = \frac{\partial T}{\partial \dot{r}} = \mu_r \dot{r} \tag{2.35}$$

$$P_\tau = \frac{\partial T}{\partial \dot{\tau}} = \mu_r r^2 \dot{\tau} - \mu_r r^2 \omega_x = I_{\tau\tau}\dot{\tau} + I_{\tau x}\dot{\omega_x} \tag{2.36}$$

Thus

$$P_\tau = J_\tau = (Iw)_\tau \tag{2.37}$$

$$J_\alpha = \frac{\partial T}{\partial \omega_\alpha} \qquad \alpha = x, y, z, \tau \tag{2.38}$$

Since $\omega_\alpha$ is the angular velocity corresponding to the $\alpha$ axis, then $J_\alpha$ is the total angular momentum. Thus

$$\omega = \mathbf{I}^{-1}\mathbf{J} = \mu\mathbf{J} \tag{2.39}$$

The matrix $\mu$ is the inverse of $\mathbf{I}$.

$$\mu = \begin{Bmatrix} \mu_{yy} & \mu_{yz} & 0 & 0 \\ \mu_{yz} & \mu_{zz} & 0 & 0 \\ 0 & 0 & \mu_{xx} & \mu_{x\tau} \\ 0 & 0 & \mu_{x\tau} & \mu_{\tau\tau} \end{Bmatrix} \tag{2.40}$$

$$\mu_{yy} = \mu_{xx} = \mu_{x\tau} = \frac{1}{\mu_R R^2} \tag{2.41}$$

$$\mu_{zz} = \frac{1}{\mu_r r^2 \sin^2\tau} + \frac{\cot^2\tau}{\mu_R R^2} \tag{2.42}$$

$$\mu_{yz} = \frac{\cot\tau}{\mu_R R^2} \tag{2.43}$$

$$\mu_{\tau\tau} = \frac{1}{\mu_r r^2} + \frac{1}{\mu_R R^2} \tag{2.44}$$

Thus the kinetic operator $T$ will be

$$T = \frac{1}{2} \sum_{\alpha,\beta=x,y,z,\tau} \mu_{\alpha\beta} J_\alpha J_\beta + \frac{1}{2\mu_R} P_R^2 + \frac{1}{2\mu_r} P_r^2 \tag{2.45}$$

B. Podolsky [11] has shown that we can set up the classical Hamiltonian in terms of general coordinates $q_i$ and conjugate momenta $p_i$ and replace the $p_i$ by $-i\hbar\partial/\partial q_i$ to

obtain the Hamiltonian operator. This is called the "Podolsky trick". We have the kinetic operator $T$ in terms of the coordinates and their conjugate momenta. Here, we can use quantum mechanical postulates and obtain the quantum mechanical Hamiltonian. We need the determinant of the matrix $\mu$, $\mu$ to use the Podolsky trick.

$$\mu = Det(\mu) = Det(\mathbf{I}^{-1}) = (\mu_r^2 \mu_R^2 r^4 R^4 \sin^2\tau)^{-1} \tag{2.46}$$

With $\mu$ and $\bar{\mu}$, we can have derive the quantum mechanical Hamiltonian for the Jacobi coordinate system,

$$\begin{aligned}\hat{H} &= \frac{1}{2}\mu^{1/4} \sum_{\alpha,\beta=x,y,z,\tau} \hat{J}_\alpha \mu^{-1/2} \mu_{\alpha\beta} \hat{J}_\beta \mu^{1/4} \\ &+\frac{1}{2\mu_R}\mu^{1/4}\hat{P}_R\mu^{-1/2}\hat{P}_R\mu^{1/4} + \frac{1}{2\mu_r}\mu^{1/4}\hat{P}_r\mu^{-1/2}\hat{P}_r\mu^{1/4} + \hat{H}_e, \end{aligned} \tag{2.47}$$

where $\hat{H}_e$ is the electronic Hamiltonian. Now, $\hat{J}_\alpha$, $\hat{P}_R$ and $\hat{P}_r$ are quantum mechanical operators, and are given above as

$$\hat{J}_\alpha = -i\hbar\frac{\partial}{\partial\alpha} \tag{2.48}$$

$$\hat{P}_R = -i\hbar\frac{\partial}{\partial R} \tag{2.49}$$

$$\hat{P}_r = -i\hbar\frac{\partial}{\partial r} \tag{2.50}$$

Let us simplify the Hamiltonian $\hat{H}$. First, we know that $\mu$ and $\mu_{\alpha\beta}$ commute with $J_x$, $J_y$, $J_z$, and some of the terms in $\mu_{\alpha\beta}$ are zero. Thus,

$$\hat{H} = \frac{1}{2}\sum_{\alpha,\beta=x,y,z}\mu_{\alpha\beta}\hat{J}_\alpha\hat{J}_\beta \tag{2.51}$$

$$+\frac{1}{2}\mu^{1/4}\hat{J}_x\mu^{-1/2}\mu_{x\tau}\hat{J}_\tau\mu^{1/4} + \frac{1}{2}\mu^{1/4}\hat{J}_\tau\mu^{-1/2}\mu_{x\tau}\hat{J}_x\mu^{1/4} \tag{2.52}$$

$$+\frac{1}{2}\mu^{1/4}\hat{J}_\tau\mu^{-1/2}\mu_{\tau\tau}\hat{J}_\tau\mu^{1/4} \tag{2.53}$$

$$+\frac{1}{2\mu_R}\mu^{1/4}\hat{P}_R\mu^{-1/2}\hat{P}_R\mu^{1/4} + \frac{1}{2\mu_r}\mu^{1/4}\hat{P}_r\mu^{-1/2}\hat{P}_r\mu^{1/4} + \hat{H}_e. \tag{2.54}$$

The first term in $\hat{H}$ (Eq. (2.51)) can be re-written as

$$\frac{1}{2\mu_R R^2}\{\hat{J}_x^2 + \hat{J}_y^2 + \cot^2\tau\hat{J}_z^2 + \cot\tau(\hat{J}_y\hat{J}_z + \hat{J}_z\hat{J}_y)\} + \frac{1}{2\mu_r r^2\sin\tau}\hat{J}_z^2. \tag{2.55}$$

The second and third terms in $\hat{H}$ (Eq. (2.52)) can be re-written as

$$\begin{aligned}
&\frac{1}{2}(\mu^{-1/4}\mu_{x\tau}\hat{J}_x(\mu^{1/4}\hat{J}_\tau + [\hat{J}_\tau, \mu^{1/4}]) + \mu^{1/4}(\mu^{-1/4}\hat{J}_\tau + [\hat{J}_\tau, \mu^{-1/4}])\mu_{x\tau}\hat{J}_x) \\
&= \frac{1}{2}(\mu^{-1/4}\mu_{x\tau}\hat{J}_x(\mu^{1/4}\hat{J}_\tau + \frac{i\hbar\cot\tau\mu^{1/4}}{2}) + \mu^{1/4}(\mu^{-1/4}\hat{J}_\tau - \frac{i\hbar\cot\tau\mu^{-1/4}}{2})\mu_{x\tau}\hat{J}_x) \\
&= \frac{1}{2\mu_R R^2}(\hat{J}_x\hat{J}_\tau + \hat{J}_\tau\hat{J}_x). \qquad (2.56)
\end{aligned}$$

The fourth term in $\hat{H}$ (Eq. (2.53)) yields

$$\begin{aligned}
&\frac{1}{2}(\mu_{\tau\tau}\mu^{1/4}\hat{J}_\tau\mu^{-1/4}\hat{J}_\tau + \mu_{\tau\tau}\mu^{1/4}\hat{J}_\tau\mu^{-1/2}[\hat{J}_\tau, \mu^{1/4}]) \\
&= \frac{1}{2}(\mu_{\tau\tau}\hat{J}_\tau^2 + \mu_{\tau\tau}\mu^{1/4}[\hat{J}_\tau, \mu^{-1/4}]\hat{J}_\tau + \mu_{\tau\tau}\mu^{1/4}\hat{J}_\tau\mu^{-1/2}[\hat{J}_\tau, \mu^{1/4}]) \\
&= \frac{1}{2}(\mu_{\tau\tau}\hat{J}_\tau^2 + \mu_{\tau\tau}\mu^{1/4}(-\frac{i\hbar\cot\tau\mu^{-1/4}}{2}\hat{J}_\tau + \hat{J}_\tau\mu^{-1/4}\frac{i\hbar\cot\tau}{2})) \\
&= \frac{1}{2}(\mu_{\tau\tau}\hat{J}_\tau^2 + \frac{i\hbar}{2}\mu_{\tau\tau}\mu^{1/4}[\hat{J}_\tau, \cot\tau\mu^{-1/4}) \\
&= \left(\frac{1}{2\mu_r r^2} + \frac{1}{2\mu_R R^2}\right)\left\{\hat{J}_\tau^2 - \frac{\hbar^2}{8}\left(1 + \frac{1}{\sin^2\tau}\right)\right\}. \qquad (2.57)
\end{aligned}$$

The fifth term in $\hat{H}$ (Eq. (2.54)) is obtained as

$$\begin{aligned}
&\frac{\mu^{1/4}}{2\mu_R}\hat{P}_R\mu^{-1/2}(\mu^{1/4}\hat{P}_R + [\hat{P}_R, \mu^{1/4}]) \\
&= \frac{\mu^{1/4}}{2\mu_R}(\hat{P}_R\mu^{-1/4}\hat{P}_R + \hat{P}_R\mu^{-1/2}[\hat{P}_R, \mu^{1/4}]) \\
&= \frac{\mu^{1/4}}{2\mu_R}(\mu^{-1/4}\hat{P}_R^2 + [\hat{P}_R, \mu^{-1/4}]\hat{P}_R + \mu^{-1/2}[\hat{P}_R, \mu^{1/4}]\hat{P}_R + [\hat{P}_R, \mu^{-1/2}[\hat{P}_R, \mu^{1/4}]]) \\
&= \frac{\mu^{1/4}}{2\mu_R}(\mu^{-1/4}\hat{P}_R^2 + \frac{i\hbar\mu^{-1/4}}{R}\hat{P}_R - \frac{i\hbar\mu^{1/4}}{R}\mu^{-1/2}\hat{P}_R + [\hat{P}_R, -\frac{i\hbar\mu^{-1/4}}{R}]) \\
&= \frac{\hat{P}_R^2}{2\mu_R}. \qquad (2.58)
\end{aligned}$$

The sixth term in $\hat{H}$ (Eq. (2.54)) can be re-written analogously to equation (2.58). Thus from Eqs. (2.54)-(2.58) we can re-write $\hat{H}$ and we have the Jacobi quantum mechanical Hamiltonian.

$$\hat{H}_{Jacobi} = \frac{\hbar^2}{2\mu_R R^2}\{\hat{J}_x^2 + \hat{J}_y^2 + \cot^2\tau\hat{J}_z^2 + \hat{J}_\tau^2 + \hat{J}_x\hat{J}_\tau + \hat{J}_\tau\hat{J}_x + \cot\tau(\hat{J}_y\hat{J}_z + \hat{J}_z\hat{J}_y)\}$$

$$
\begin{aligned}
&+ \quad \frac{\hbar^2}{2\mu_r r^2}\left\{\frac{1}{\sin^2\tau}\hat{J}_z^2+\hat{J}_\tau^2\right\}-\frac{\hbar^2}{8}\left\{\frac{1}{\mu_R R^2}+\frac{1}{\mu_r r^2}\right\}\left\{1+\frac{1}{\sin^2\tau}\right\}\\
&+ \quad \frac{1}{2\mu_R}\hat{P}_R^2+\frac{1}{2\mu_r}\hat{P}_r^2+\hat{H}_e
\end{aligned}
\tag{2.59}
$$

### 2.1.2 Total Hamiltonian

The angular momentum operators, which are essential for describing our double Renner system are $\hat{L}$, $\hat{N}$, $\hat{S}$, and $\hat{J}$. $\hat{L}$ is the total electronic orbital angular momentum in the molecule, $\hat{N}$ is the rovibronic angular momentum in the molecule, and $\hat{S}$ is the total electron spin angular moemntum in the molecule. $\hat{J}$ is given by $\hat{J}=\hat{N}+\hat{S}$, the sum of rovibronic and electron spin angular momenta.

The Hamiltonian for Jacobi coordinate from last section will be re-written here, to include the Renner effect and spin orbit coupling. Thus $\hat{J}_x \rightarrow \hat{N}_x$ , $\hat{J}_y \rightarrow \hat{N}_y$ , $\hat{J}_z \rightarrow \hat{N}_z-\hat{L}_z$, and $\hat{J}_\tau \rightarrow \hat{N}_\tau$ so that

$$
\begin{aligned}
\hat{H}_{DR}= \quad & \frac{\hbar^2}{2\mu_R R^2}\{\hat{N}_x^2+\hat{N}_y^2+\cot^2\tau(\hat{N}_z-\hat{L}_z)^2+\hat{N}_\tau^2+\hat{N}_x\hat{N}_\tau+\hat{N}_\tau\hat{N}_x\\
&+ \quad \cot\tau(\hat{N}_y(\hat{N}_z-\hat{L}_z)+(\hat{N}_z-\hat{L}_z)\hat{N}_y)\}\\
&+ \quad \frac{\hbar^2}{2\mu_r r^2}\left\{\frac{1}{\sin^2\tau}(\hat{N}_z-\hat{L}_z)^2+\hat{N}_\tau^2\right\}-\frac{\hbar^2}{8}\left\{\frac{1}{\mu_R R^2}+\frac{1}{\mu_r r^2}\right\}\left\{1+\frac{1}{\sin^2\tau}\right\}\\
&+ \quad \frac{1}{2\mu_R}\hat{P}_R^2+\frac{1}{2\mu_r}\hat{P}_r^2+\hat{H}_e+\hat{H}_{SO}
\end{aligned}
\tag{2.60}
$$

$\hat{L}_z$ is the projection of the angular momentum operator $\hat{L}$ on to the $z$-axis. $\hat{N}_x$, $\hat{N}_y$, $\hat{N}_z$ are the projections of the angular momentum operators $\hat{N}$ on to $x$-, $y$-, and $z$-axes respectively.

## 2.2 The basis functions

In this section we describe how we define our basis functions. We choose the total basis function for the variational calculation as

$$\begin{aligned}\Psi_{\rm rve}^{J,M_J,S,\Gamma_{\rm rve}} &= \sum_{N=|J-S|}^{J+S}\sum_{K=0}^{N}\sum_{\Gamma_{\rm rve},N_r,N_R,\eta,v_2^\eta} c^{J,M_J,S,\Gamma_{\rm rve}}_{\eta,N,K,v_2^\eta,\Gamma_{\rm vib},N_r,N_R} \\ &\times |N_R,\Gamma_R\rangle|N_r,\Gamma_r\rangle|v_2^\eta,K,\Gamma_{v_2^\eta}\rangle|\eta;N,J,S,K,M_J,p\rangle. \qquad (2.61)\end{aligned}$$

Here, the basis function $|N_R,\Gamma_R\rangle$ describes the $R$ bond stretching motion with the vibrational symmetry $\Gamma_R$ in molecular symmetry (MS) group (See Chapter 2.2.5 together with Ref. [12]). and the principal quantum number $N_R$. The basis function $|N_r,\Gamma_r\rangle$ describes the $r$ bond stretching motion with the vibrational symmetry $\Gamma_r$ in MS group and the principal quantum number $N_r$. The basis function $|v_2^\eta,K,\Gamma_{v_2^\eta}\rangle$ describes the bending motion of the molecule along the Jacobi coordinate $\tau$, with $K$-type rotational angular momentum $K$ and the symmetry $\Gamma_{v_2^\eta}$ in the MS group. The function $|\eta;N,J,S,K,M_J,p\rangle$ describes the electronic motion, the effects of electron spin, and the rotation of the molecule. $N$, $J$, $M_J$, and $S$ are the quantum numbers which are associated with angular momentum operators. The spin quantum number $S$ is associated with the electronic spin operator $\hat{S}^2$. The total quantum number $J$ is associated with the total angular momentum operator $\hat{J}^2$. The rovibronic quantum number $N$ is associated with the rovibronic angular momentum operator $\hat{N}^2$. $M_J$ defines the projection of the total angular momentum $\hat{J}$ on to a space fixed axis.

$c^{J,M_J,S,\Gamma_{\rm rve}}_{\eta,N,K,v_2^\eta,N_r,N_R,\Gamma_{\rm vib}}$ are the expansion coefficients for the basis set. In the final diagonalization, the superscript of the coefficient $c^{J,M_J,S,\Gamma_{\rm rve}}_{\eta,N,K,v_2^\eta,N_r,N_R,\Gamma_{\rm vib}}$ which are $J$,$M_J$,$S$,$\Gamma_{\rm rve}$, make the final matrix in block-diagonalized form. Thus, these quantum numbers are called good quantum numbers, and we can use these quantum number for characterizing the rovibronic wavefunctions.

The $\Gamma_{\rm vib}$ express the symmetry of the vibrational basis functions in the MS group.

The $\Gamma_{\rm vib}$ is given as $\Gamma_{\rm vib} = \Gamma_R \otimes \Gamma_r \otimes \Gamma_{v_2^\eta}$. The $\Gamma_{\rm rve}$ express the total symmetry of the rovibronic basis functions in the MS group. The $\Gamma_{\rm rve}$ is given as $\Gamma_{\rm rve} = \Gamma_{\rm vib} \otimes \Gamma_{\rm ers}$. $\Gamma_{\rm ers}$ is the symmetry of the electronic-rotation-spin basis function $|\eta; N, J, S, K, M_J, p\rangle$ in the MS group. We discuss the detail of the MS symmetry group of ABB- and ABC-type molecule in Chapter 2.2.5. See Tables 2.1-2.6)

### 2.2.1 Rotation-spin basis functions

The electronic-rotation-spin basis function $|\eta; N, J, S, K, M_J, p\rangle$, is based on rotation-spin basis functions. Here we explain the rotation-spin basis functions $|N, J, S, K, M_J, p\rangle$. The rotation-spin basis function $|N, J, S, K, M_J, p\rangle$ is defined in terms of Hund's case (b) basis functions (See Refs. [12, 13]).

$$|N, J, S, K, M_J\rangle = \sum_{M=-N|}^{N} \sum_{M_S=-S}^{S} (-1)^{N-S+M_J\sqrt{2J+1}} \times \begin{pmatrix} N & S & J \\ M & M_S & -M_J \end{pmatrix} |S, M_S\rangle |N, k, M\rangle \tag{2.62}$$

The quantity in parentheses is a 3j-symbol (See Ref. [13]). $|S, M_S\rangle$ is an electronic spin function quantized along the space fixed axis. $|N, k, M\rangle$ is an eigenfunction for the rigid rotor. This function is a simultaneous eigenfunction for $\hat{N}^2$ (with eigenvalue $\hbar^2 N(N+1)$), $\hat{N}_z$ (with eigenvalue $\hbar k$)), $\hat{S}^2$ (with eigenvalue $\hbar^2 S(S+1)$), $\hat{J}^2$ (with eigenvalue $\hbar^2 J(J+1)$), and $\hat{J}_z$ (with eigenvalue $\hbar M_J$).

The Hund's case (b) basis function is a basis function for the case when the electron spin functions are quantized along space fixed axes. We treat here the case when the effects of the interactions of the electronic and nuclear spins are weak, (i.e. we are neglecting the electronic fine structure and nuclear hyperfine structure.)

We introduce the angular momentum ladder operators as follows.

$$\hat{N}_\pm = \hat{N}_x \pm i\hat{N}_y \tag{2.63}$$

We choose the phases of the basis functions $|N, k, M\rangle$ so that we have final matrix elements as real number. Thus the angular momentum ladder operators $\hat{N}_+$ and $\hat{N}_-$ are related to the rotational basis functions $|N, k, M\rangle$ as follows

$$\hat{N}_\pm|N, k, M_J\rangle = \pm i\hbar\sqrt{N(N+1) - k(k \mp 1)}|N, k \mp 1, M\rangle. \tag{2.64}$$

We can rewrite these relations as:

$$\hat{N}_x|N, J, S, K, M_J\rangle = \frac{\hat{N}_+ + \hat{N}_-}{2}|N, J, S, K, M_J\rangle \tag{2.65}$$

$$\hat{N}_y|N, J, S, K, M_J\rangle = \frac{\hat{N}_+ - \hat{N}_-}{2i}|N, J, S, K, M_J\rangle. \tag{2.66}$$

The rotation-spin basis function have to comply with the symmetry requirements. Thus the parity of the rovibronic states are very important. The parity of the rovibronic state is expressed using an integer $p$. The integer $p$ is equal to 0 or 1. With the symmetry operation, inversion operation $E^*$ it is defined as

$$E^*|\Psi_{\mathrm{rve}}^{J,M_J,S,\Gamma_{\mathrm{rve}}}\rangle = (-1)^p|\Psi_{\mathrm{rve}}^{J,M_J,S,\Gamma_{\mathrm{rve}}}\rangle. \tag{2.67}$$

(We discuss the detail of the relation of parity and the symmetry in Chapter 2.2.5. See Tables 2.1-2.6)

The rotation-spin basis functions which fulfill this symmetry operation are given by

$$\begin{aligned} &|N, J, S, K, M_J, p\rangle \\ &\begin{cases} = & \frac{1}{\sqrt{2}}\{|N, J, S, K, M_J\rangle + (-1)^{N+K+p}|N, J, S, -K, M_J\rangle\} \quad (K > 0) \\ = & |N, J, S, 0, M_J\rangle \qquad\qquad\qquad\qquad\qquad\qquad (K = 0). \end{cases} \end{aligned} \tag{2.68}$$

Here we use the Kronecker symbol $\delta_{0p}$. If $p = 0$ , then $\delta_{0p} = 1$: if $p = 1$ , then $\delta_{0p} = 0$. With this notation, we can show the effect of angular momentum operator $\hat{N}_z$ on the rotation-spin basis function.

If $K = 0$,

$$\hat{N}_z|N, J, S, 0, M_J, p\rangle = 0 \times \hbar|N, J, S, 0, M_J\rangle = 0. \tag{2.69}$$

and when $K > 0$,

$$\begin{aligned}
&\hat{N}_z|N, J, S, K, M_J, p\rangle \\
&= \hat{N}_z \frac{1}{\sqrt{2}}\{|N, J, S, K, M_J\rangle + (-1)^{N+K+p}|N, J, S, -K, M_J\rangle\} \\
&= \frac{1}{\sqrt{2}}\{K\hbar|N, J, S, K, M_J\rangle - K\hbar(-1)^{N+K+p}|N, J, S, -K, M_J\rangle\} \\
&= K\hbar \frac{1}{\sqrt{2}}\{|N, J, S, K, M_J\rangle + (-1)^{N+K+\delta_{0p}}|N, J, S, -K, M_J\rangle\} \\
&= K\hbar|N, J, S, K, M_J, \delta_{0p}\rangle. \qquad (2.70)
\end{aligned}$$

The effect of angular momentum operator $\hat{N}_\pm$ , $\hat{N}_x$ and $\hat{N}_y$ on the rotation-spin basis function is as follows.

If $K = 0$,

$$\hat{N}_\pm|N, J, S, 0, M_J, p\rangle = \pm i\hbar\sqrt{N(N+1)}|N, J, S, \mp 1, M_J\rangle. \qquad (2.71)$$

With equation (2.66),

$$\begin{aligned}
&\hat{N}_x|N, J, S, 0, M_J\rangle \\
&= i\hbar\sqrt{N(N+1)}\left\{\frac{1}{2}(|N, J, S, -1, M_J\rangle - |N, J, S, +1, M_J\rangle)\right\} \\
&= \frac{-i\hbar\sqrt{N(N+1)}}{\sqrt{2}}\left\{\frac{1}{\sqrt{2}}(|N, J, S, +1, M_J\rangle + (-1)^{N+1+p}|N, J, S, -1, M_J\rangle)\right\} \\
&= \frac{-i\hbar\sqrt{N(N+1)}}{\sqrt{2}}|N, J, S, 1, M_J, p\rangle \qquad ((-1)^{N+p} \equiv 1) \qquad (2.72) \\
&\hat{N}_y|N, J, S, 0, M_J\rangle \\
&= \hbar\sqrt{N(N+1)}\left\{\frac{1}{2}(|N, J, S, +1, M_J\rangle + |N, J, S, -1, M_J\rangle)\right\} \\
&= \frac{\hbar\sqrt{N(N+1)}}{\sqrt{2}}\left\{\frac{1}{\sqrt{2}}(|N, J, S, +1, M_J\rangle + (-1)^{N+1+p}|N, J, S, -1, M_J\rangle)\right\} \\
&= \frac{\hbar\sqrt{N(N+1)}}{\sqrt{2}}|N, J, S, 1, M_J, p\rangle \qquad ((-1)^{N+p} \equiv -1). \qquad (2.73)
\end{aligned}$$

When $K > 0$,

$$\hat{N}_\pm|N, J, S, K, M_J, p\rangle$$

$$
\begin{aligned}
&= \frac{1}{\sqrt{2}}\{\hat{N}_{\pm}|N,J,S,K,M_J\rangle + (-1)^{N+K+p}\hat{N}_{\pm}|N,J,S,-K,M_J\rangle\} \\
&= \frac{\pm i\hbar}{\sqrt{2}}\{\sqrt{N(N+1)-K(K\mp 1)}|N,J,S,K\mp 1,M_J\rangle \\
&\quad +(-1)^{N+K+p}\sqrt{N(N+1)-K(K\pm 1)}|N,J,S,-(K\pm 1),M_J\rangle\}.
\end{aligned}
\tag{2.74}
$$

Thus with equation (2.66),

$$
\begin{aligned}
&\hat{N}_x|N,J,S,K,M_J,p\rangle \\
&= \frac{i\hbar}{2\sqrt{2}}\Big[\sqrt{N(N+1)-K(K-1)} \\
&\quad \times\{|N,J,S,K-1,M_J\rangle + (-1)^{N+(K-1)+p}|N,J,S,-(K-1),M_J\rangle\} \\
&- \sqrt{N(N+1)-K(K+1)} \\
&\quad \times\{|N,J,S,K+1,M_J\rangle + (-1)^{N+(K+1)+p}|N,J,S,-(K+1),M_J\rangle\}\Big] \\
&\hat{N}_y|N,J,S,K,M_J,p\rangle \\
&= \frac{\hbar}{2\sqrt{2}}\Big[\sqrt{N(N+1)-K(K-1)} \\
&\quad \times\{|N,J,S,K-1,M_J\rangle + (-1)^{N+(K-1)+\delta_{0p}}|N,J,S,-(K-1),M_J\rangle\} \\
&+ \sqrt{N(N+1)-K(K+1)} \\
&\quad \times\{|N,J,S,K+1,M_J\rangle + (-1)^{N+(K+1)+\delta_{0p}}|N,J,S,-(K+1),M_J\rangle\}\Big].
\end{aligned}
$$

Depending on whether $K=1$ or $K>1$ , this can be written in a simplified form.

If $K>1$,

$$
\begin{aligned}
\hat{N}_x|N,J,S,K,M_J,p\rangle &= \frac{i\hbar}{2}\{\sqrt{N(N+1)-K(K-1)}|N,J,S,K-1,M_J,p\rangle \\
&\quad -\sqrt{N(N+1)-K(K+1)}|N,J,S,K+1,M_J,p\rangle\} \qquad (2.75) \\
\hat{N}_y|N,J,S,K,M_J,p\rangle &= \frac{\hbar}{2}\{\sqrt{N(N+1)-K(K-1)}|N,J,S,K-1,M_J,\delta_{0p}\rangle \\
&\quad +\sqrt{N(N+1)-K(K+1)}|N,J,S,K+1,M_J,\delta_{0p}\rangle\} \qquad (2.76)
\end{aligned}
$$

If $K = 1$

$$\begin{aligned}
\hat{N}_x|N,J,S,1,M_J,p\rangle &= \frac{i\hbar}{2}\{\frac{(-1)^{N+p}+1}{2}\sqrt{N(N+1)}|N,J,S,0,M_J\rangle \\
&\quad -\sqrt{N(N+1)-2}|N,J,S,2,M_J,p\rangle\} \qquad (2.77)\\
\hat{N}_y|N,J,S,1,M_J,p\rangle &= \frac{\hbar}{2}\{\frac{(-1)^{N+\delta_{0p}}+1}{2}\sqrt{N(N+1)}|N,J,S,0,M_J\rangle \\
&\quad +|N,J,S,2,M_J,\delta_{0p}\rangle\}. \qquad (2.78)
\end{aligned}$$

### 2.2.2 Bending basis functions

To construct bending basis functions, we pre-diagonalize the $\tau$-dependent part of the total Hamiltonian $\hat{H}_{DR}$. In other words, we simplify the Hamiltonian so that the Hamiltonian consists only of the bending-dependent part, then solve the Schrödinger equation to obtain the wavefunction. We will use these wavefunctions as bending basis functions.

Thus the potential energy function in this section is only required to depend on the bending angle. We let the bond lengths relax along the minimum energy path of isomerization. To make sure that the model Hamiltonian is Hermitian, we take the original Hamiltonian in Hermitian form for $\tau$ dependent part. The simplified Hamiltonian is,

$$\begin{aligned}
\hat{H}_{bend} = &\frac{\hbar^2}{2\mu_R R(\tau)^2}\frac{\cos^2\tau}{\sin^2\tau}(\hat{N}_z-\hat{L}_z)^2+\frac{\hbar^2}{2\mu_r r(\tau)^2}\frac{1}{\sin^2\tau}(\hat{N}_z-\hat{L}_z)^2 \\
+ &\hat{N}_\tau\left(\frac{\hbar^2}{2\mu_R R(\tau)^2}+\frac{\hbar^2}{2\mu_r r(\tau)^2}\right)\hat{N}_\tau \\
- &\frac{\hbar^2}{8}\left\{\frac{1}{\mu_R R(\tau)^2}+\frac{1}{\mu_r r(\tau)^2}\right\}\left\{1+\frac{1}{\sin^2\tau}\right\}+\hat{H}_e. \qquad (2.79)
\end{aligned}$$

Here we define

$$\begin{aligned}
\mu_{zz}(\tau) &= \frac{\hbar^2}{\sin^2\tau}\left(\frac{\cos^2\tau}{\mu_R R(\tau)^2}+\frac{1}{\mu_r r(\tau)^2}\right) \qquad (2.80)\\
\mu_{\tau\tau}(\tau) &= \hbar^2\left(\frac{1}{\mu_R R(\tau)^2}+\frac{1}{\mu_r r(\tau)^2}\right) \qquad (2.81)
\end{aligned}$$

$$g(\tau) \;=\; -\frac{1}{4}\left(1+\frac{1}{\sin^2\tau}\right), \tag{2.82}$$

and insertion of equations (2.80) - (2.82) to equation (2.79) shows that

$$\begin{aligned}\hat{H}_{bend} = &\;\frac{1}{2}\mu_{zz}(\tau)(\hat{N}_z-\hat{L}_z)^2+\frac{1}{2}\mu_{\tau\tau}(\tau)(\hat{N}_\tau^2+g(\tau))+\frac{1}{2}[\hat{N}_\tau,\mu_{\tau\tau}]\hat{N}_\tau+\hat{H}_e \\ = &\;\hat{H}_{ez}+\frac{1}{2}\mu_{\tau\tau}(\tau)(\hat{N}_\tau^2+g(\tau))+\frac{1}{2}[\hat{N}_\tau,\mu_{\tau\tau}(\tau)]\hat{N}_\tau, \end{aligned}\tag{2.83}$$

where

$$\hat{H}_{ez} \;=\; \hat{H}_e+\frac{1}{2}\mu_{zz}(\tau)(\hat{N}_z-\hat{L}_z)^2 \tag{2.84}$$

$$\;=\; \hat{H}_e+\frac{1}{2}\mu_{zz}(\tau)(\hat{N}_z^2+\hat{L}_z^2-2\hat{N}_z\hat{L}_z). \tag{2.85}$$

The Hamiltonian $\hat{H}_{ez}$ describes the electronic motion and the rotation around the molecule-fixed $z$-axis ($K$-type rotation) for a molecule at fixed bond angle $\tau$. This is the essential part of the Renner interaction, which mixes the rotational angular momentum, bending angular momentum and electronic angular momentum. Following the ideas of Barrow, Dixon, and Duxbury [14] we find the basis functions of the Hamiltonian $\hat{H}_{ez}$, which have the Renner interaction incorporated in it. We diagonalize a matrix $\hat{H}_{ez}$ in the electronic basis function $|\psi_e^{(-)}\rangle$ and $|\psi_e^{(+)}\rangle$. (We denote by $|\psi_e^{(-)}\rangle$ the lower potential energy surface electronic basis function and by $|\psi_e^{(+)}\rangle$ the upper potential energy surface electronic basis function.) The 2 $\times$ 2 matrix representation of $\hat{H}_{ez}$ is

$$\left\{\begin{array}{cc} V_0^{(-)}(\tau)+\frac{\hbar^2}{2}\mu_{zz}(\tau)(K^2+\Lambda^2) & \hbar^2\mu_{zz}(\tau)K\Lambda \\ \hbar^2\mu_{zz}(\tau)K\Lambda & V_0^{(+)}(\tau)+\frac{\hbar^2}{2}\mu_{zz}(\tau)(K^2+\Lambda^2)\end{array}\right\}. \tag{2.86}$$

We can write the eigenfunctions of this matrix as

$$\begin{aligned}|a;N,J,S,K,M_J,p\rangle \;=&\; \cos(\gamma_K(\tau))|\psi_e^{(-)}\rangle|N,J,S,K,M_J,p\rangle \\ &+\; \sin(\gamma_K(\tau))i|\psi_e^{(+)}\rangle|N,J,S,K,M_J,\delta_{0p}\rangle \\ |b;N,J,S,K,M_J,p\rangle \;=&\; \cos(\gamma_K(\tau))i|\psi_e^{(+)}\rangle|N,J,S,K,M_J,\delta_{0p}\rangle \\ &-\; \sin(\gamma_K(\tau))|\psi_e^{(-)}\rangle|N,J,S,K,M_J,p\rangle. \end{aligned}\tag{2.87}$$

$|\eta; N, J, S, K, M_J, p\rangle$ is the electronic-rotation-spin basis function ($\eta = a$ or $b$. See Chapter 2.2.3.).

The corresponding eigenvalues are

$$\begin{aligned} V_K^{\eta}(\tau) &= \frac{1}{2}\left(V_0^{(+)}(\tau) + V_0^{(-)}(\tau) + \right) + \frac{\hbar^2}{2}\mu_{zz}(\tau)(K^2 + \Lambda^2) \\ &\mp \frac{1}{2}\sqrt{\left(V_0^{(+)}(\tau) - V_0^{(-)}(\tau)\right)^2 + 4\hbar^4\mu_{zz}(\tau)^2K^2\Lambda^2}. \end{aligned} \tag{2.88}$$

From the definition of Eq. (2.88), Eq. (2.83) can be rewritten as

$$\begin{aligned} \hat{H}_{bend} = & V_K^{\eta}(\tau) + \frac{1}{2}\mu_{\tau\tau}(\tau)(\hat{N}_\tau^2 + g(\tau)) + \frac{1}{2}[\hat{N}_\tau, \mu_{\tau\tau}(\tau)]\hat{N}_\tau \\ = & V_K^{\eta}(\tau) + \frac{1}{2}\mu_{\tau\tau}(\tau)g(\tau) - \frac{\hbar^2}{2}\left(\mu_{\tau\tau}(\tau)\frac{\partial^2}{\partial\tau^2} + [\frac{\partial}{\partial\tau}, \mu_{\tau\tau}(\tau)]\frac{\partial}{\partial\tau}\right). \end{aligned} \tag{2.89}$$

We define the bending wavefunction $\Phi(\tau)$ as

$$\Phi(\tau) = \mu_{\tau\tau}(\tau)^{-\frac{1}{2}}\phi(\tau). \tag{2.90}$$

The Hamiltonian and basis function satisfy

$$\hat{H}_{bend}\Phi(\tau) = E\Phi(\tau) \tag{2.91}$$

and so

$$\begin{aligned} \left\{V_K^{\eta}(\tau) + \frac{1}{2}\mu_{\tau\tau}(\tau)g(\tau) - \frac{\hbar^2}{2}\left(\mu_{\tau\tau}(\tau)\frac{\partial^2}{\partial\tau^2} + [\frac{\partial}{\partial\tau}, \mu_{\tau\tau}(\tau)]\frac{\partial}{\partial\tau}\right)\right\} \\ \times\mu_{\tau\tau}(\tau)^{-\frac{1}{2}}\phi(\tau) = E\mu_{\tau\tau}(\tau)^{-\frac{1}{2}}\phi(\tau). \end{aligned} \tag{2.92}$$

Here,

$$\begin{aligned} & \left(\mu_{\tau\tau}(\tau)\frac{\partial^2}{\partial\tau^2} + [\frac{\partial}{\partial\tau}, \mu_{\tau\tau}(\tau)]\frac{\partial}{\partial\tau}\right)\mu_{\tau\tau}(\tau)^{-\frac{1}{2}}\phi(\tau) \\ = & \mu_{\tau\tau}(\tau)\frac{\partial^2}{\partial\tau^2}\left(\mu_{\tau\tau}(\tau)^{-\frac{1}{2}}\phi(\tau)\right) + \frac{\partial\mu_{\tau\tau}(\tau)}{\partial\tau}\frac{\partial}{\partial\tau}\left(\mu_{\tau\tau}(\tau)^{-\frac{1}{2}}\phi(\tau)\right) \\ = & \mu_{\tau\tau}(\tau)^{-\frac{1}{2}}\left\{\frac{\partial^2\phi(\tau)}{\partial\tau^2} - \frac{1}{2\mu_{\tau\tau}(\tau)}\frac{\partial^2\mu_{\tau\tau}(\tau)}{\partial\tau^2}\phi(\tau) + \left(\frac{1}{2\mu_{\tau\tau}(\tau)}\frac{\partial\mu_{\tau\tau}(\tau)}{\partial\tau}\right)^2\phi(\tau)\right\} \end{aligned} \tag{2.93}$$

With the equation (2.93), we can rewrite equation (2.92) as,

$$\frac{\partial^2}{\partial\tau^2}\phi(\tau) = \left\{\frac{2(V_K^\eta(\tau)-E)}{\hbar^2\mu_{\tau\tau}(\tau)} + \frac{1}{\hbar^2}g(\tau) + \frac{1}{2\mu_{\tau\tau}(\tau)}\frac{\partial^2\mu_{\tau\tau}(\tau)}{\partial\tau^2} - \left(\frac{1}{2\mu_{\tau\tau}(\tau)}\frac{\partial\mu_{\tau\tau}(\tau)}{\partial\tau}\right)^2\right\}\phi(\tau). \tag{2.94}$$

We use the Numerov-Cooley numerical integration method for solving Eq. (2.94) (See Ref. [15] and references therein), and obtain $E$ and $\phi(\tau)$ with this method. We determine numerical values of the bending wavefunction $\phi(\tau)$ at $N$ points for which

$$\tau_i = ih, \qquad i = 1, 2, ....., N \tag{2.95}$$

$$h = \frac{\pi}{(N+1)}, \tag{2.96}$$

where we know that $\psi(0) = 0$ and $\psi(\pi) = 0$; we let $\tau_i$ run from $h$ to $\pi - h$.

We define,

$$P_i = \phi(\tau_i) \tag{2.97}$$

$$I_i = \frac{2}{\hbar^2\mu_{\tau\tau}(\tau_i)} \tag{2.98}$$

$$U_i = \frac{1}{\hbar^2}g(\tau_i) + \frac{2V_K^\eta(\tau_i)}{\hbar^2\mu_{\tau\tau}(\tau_i)} + \frac{1}{2\mu_{\tau\tau}(\tau_i)}\frac{\partial^2\mu_{\tau\tau}(\tau_i)}{\partial\tau^2} - \left(\frac{1}{2\mu_{\tau\tau}(\tau_i)}\frac{\partial\mu_{\tau\tau}(\tau_i)}{\partial\tau}\right)^2 \tag{2.99}$$

$$Y_i = \left\{1 - \frac{h^2}{12}(U_i - I_iE)P_i\right\} \tag{2.100}$$

By neglecting sixth and higher order terms in $h$ (see details in Ref. [15]), the $Y_i$ follow the relation,

$$Y_{i+1} + Y_{i-1} - 2Y_i = h^2(U_i - I_iE)P_i \tag{2.101}$$

By assuming the values for $P_1$, $P_2$, and, $P_{N-1}$, $P_N$, with the relation between $Y_i$s in Eq. (2.101), we can obtain numerical wavefunctions with a guessed energy value $E_g$ by integrating outwards from $\tau = 0$ and inwards from $\tau = \pi$.

When $\tau \to 0$ and $\tau \to \pi$, the term $U_i$ diverges to infinity since the term $\sin^{-2}\tau$ in the equations (2.80) and (2.82) diverge to infinity

$$\lim_{\tau\to 0,\pi} T_i = \lim_{\tau\to 0,\pi} U_i = \frac{1}{\tau^2}\left((K \mp \Lambda)^2 - \frac{1}{4}\right). \tag{2.102}$$

With this, we can obtain values for $P_1$, $P_2$, and, $P_{N-1}$, $P_N$, (which we will need to solve the relations between $Y_i$s in Eq. (2.101),) by using a series solution around $\tau \to 0$ and $\tau \to \pi$.

We fit the first and last $M$ values of $T_i$ defined by

$$\begin{aligned} T_i = U_i - I_i E_g, \qquad i &= 1, 2, ...., M \\ i &= N - M + 1, N - M + 2, ...., N \end{aligned} \tag{2.103}$$

to the equation

$$t(\tau) = \frac{C_{-2}}{\tau^2} + \sum_{i=0}^{P} C_{2i} \tau^{2i} \tag{2.104}$$

$$C_{-2} = (K \mp \Lambda)^2 - \frac{1}{4} \tag{2.105}$$

with standard least squares fitting methods. We then solve the differential equation

$$\frac{\partial^2}{\partial \tau^2} \phi(\tau) = t(\tau) \phi(\tau) \tag{2.106}$$

for the first and the last $M$ points of $\phi(\tau_i)$. The first $M$ points of $\phi(\tau)$ are expressed as

$$\phi(\tau) = \tau^{\alpha} \sum_{i=0}^{Q} a_{2i} \tau^{2i}, \tag{2.107}$$

and last $M$ points of $\phi(\tau)$ are expressed as

$$\phi(\tau) = (\pi - \tau)^{\alpha} \sum_{i=0}^{Q} a_{2i} (\pi - \tau)^{2i}, \tag{2.108}$$

where,

$$\alpha = |K \mp \Lambda| + \frac{1}{2}. \tag{2.109}$$

With this fitted series, we obtain $P_i$ for $i = 1, 2, ...M$, and $i = N - M + 1, N - M + 2, ...N$. With equation (2.101), we can then calculate $P_i$ for $i = M + 1, M + 2, ..., N$, and $i = 1, 2, ..., N - M$ with guessed energy $E_g$. From these two numerical

wavefunctions calculated one at each end, we obtain an error function (See details in Ref. [15] and references therein). First, we normalize the wavefunction calculated from the two ends. Then we find for each of the two wavefunctions the point which has the biggest amplitude. We call these two points the meeting points. At the two meeting points, we calculate the energy correction terms $D(E_g)$ as follows.

We call the two wavefunctions $P_i^{(out)}$ and $P_i^{(in)}$, for outward and inward calculated wavefunctions, respectively. We have $P_c^{(out)}$ and $P_c^{(in)}$ at the meeting point $i = c$. We scale one of the two wavefunctions so that

$$P_c^{(in)} = P_c^{(out)} = P_c. \tag{2.110}$$

Also, we calculate scaled $Y_i$'s, $Y_c$, $Y_c^{(out)}$ and $Y_c^{(in)}$. If the guessed energy $E_g$ were an eigenvalue of the Schrödinger equation, the following equation

$$Y_{c+1}^{(in)} + Y_{c-1}^{(out)} - 2Y_c = h^2(U_c - I_c E_g)P_c \tag{2.111}$$

would be fulfilled. Thus we can define an error function for the guessed energy $E_g$ as,

$$F(E_g) = Y_{c+1}^{(in)} + Y_{c-1}^{(out)} - 2Y_c - h^2(U_c - I_c E_g)P_c \tag{2.112}$$

At each guessed energy $E_g$, we have $F(E_g)$ and we can correct the $E_g$ by the amount

$$D(E_g) = -\frac{F(E_g)}{\partial F(E_g)/\partial E_g} \tag{2.113}$$

and

$$D(E_g) = \frac{\{-(Y_{c+1}^{(in)} + Y_{c-1}^{(out)} - 2Y_c)/h^2 + (U_c - I_c E_g)P_c\}Y_c}{\sum_{i=1}^{N} I_i P_i^2}. \tag{2.114}$$

We calculate energy correction term $D(E_g)$ for each meeting point, and choose the smaller energy correction term $D(E_g)$ and correct the guessed energy $E_g$ by $D(E_g)$.

This iterative procedure continues until the $|D(E_g)|$ becomes smaller than the convergence threshold, and finally we obtain $E_g$ and $P_i(i = 1, 2, ....N)$ as an eigenvalue and eigenfunction of the Schrödinger equation. By counting the nodes of $P_i$, $(i =$

$1, 2, ....N)$ we know which vibrationally excited state we have formed. We multiply $\frac{1}{\sqrt{\mu_{\tau\tau}(\tau)}}$ with $P_i(i = 1, 2, ....N)$ from the definition in Eq. (2.90) and obtain the bending basis function $\Phi(\tau)$. We change the range of guessed energies $E_g$ until we have located all the required vibrational excitation states, and thus we obtain the bending basis set.

### 2.2.3 Electronic-rotation-spin basis functions

As mentioned in the last section, $|\psi_e^{(-)}\rangle$ denotes the lower potential energy surface electronic basis function and $|\psi_e^{(+)}\rangle$ denotes the upper potential energy surface electronic basis function. We choose the parity of these electronic basis function as $-$ for $|\psi_e^{(-)}\rangle$ and $+$ for $|\psi_e^{(+)}\rangle$.

The phase factor, and the $\tau$ dependence of electronic angular momentum matrix elements are defined as follows,

$$\langle\psi_e^{(-)}|\hat{L}_z^2|\psi_e^{(-)}\rangle = \hbar^2 f_{\Lambda_-^2}(\tau) \quad (2.115)$$

$$\langle\psi_e^{(+)}|\hat{L}_z^2|\psi_e^{(+)}\rangle = \hbar^2 f_{\Lambda_+^2}(\tau) \quad (2.116)$$

$$\langle\psi_e^{(-)}|\hat{L}_z|\psi_e^{(+)}\rangle = i\hbar f_{\Lambda_{-,+}}(\tau) \quad (2.117)$$

$$\langle\psi_e^{(+)}|\hat{L}_z|\psi_e^{(-)}\rangle = -i\hbar f_{\Lambda_{-,+}}(\tau) \quad (2.118)$$

The $\eta = a$ state is made up not only of the $|\psi_e^{(-)}\rangle$ state, but for $\tau$ values when there is little Renner effect, it consists almost only of $|\psi_e^{(-)}\rangle$ state. Similarly, the $\eta = b$ state is almost solely made up of $|\psi_e^{(+)}\rangle$ state if there is little Renner interaction.

Let us see what kind of matrix elements the electronic-rotation-spin basis functions produce. We denote the Hamiltonian relating to the electronic angular momentum as $\hat{H}_{el}$, and the Hamiltonian relating to rotational angular momentum as $\hat{H}_{rot}$. We define a simplified notation $c_{K_i}$, $s_{K_i}$ and $f_{\hat{H}_{rot}}(N, K_i, K_j, p_i, p_j)$ for the matrix elements that arise from the electronic-rotation-spin basis functions as follows

$$f_{\hat{H}_{rot}}(N_j, K_i, K_j, p_i, p_j) = \langle N_i, J, S, K_i, M_J, p_i|\hat{H}_{rot}|N_j, J, S, K_j, M_J, p_j\rangle \quad (2.119)$$

$$s_{K_i} = \sin(\gamma_{K_i}(\tau)) \tag{2.120}$$

$$c_{K_i} = \cos(\gamma_{K_i}(\tau)). \tag{2.121}$$

From Eq. (2.87),

$$\begin{aligned}
&\langle a; N_i, J, S, K_i, M_J, p_i|\hat{H}_{el}\hat{H}_{rot}|a; N_j, J, S, K_j, M_J, p_j\rangle \\
&\quad = \{c_{K_i}\langle\psi_e^{(-)}|\langle N_i, J, S, K_i, M_J, p_i| - s_{K_i} i\langle\psi_e^{(+)}|\langle N_i, J, S, K_i, M_J, \delta_{0p_i}|\} \\
&\quad\quad \hat{H}_{el}\hat{H}_{rot}\{c_{K_j}|\psi_e^{(-)}\rangle|N_j, J, S, K_j, M_J, p_j\rangle + s_{K_j} i|\psi_e^{(+)}\rangle|N_j, J, S, K_j, M_J, \delta_{0p_j}\rangle\} \\
&\quad = c_{K_i}c_{K_j}\langle\psi_e^{(-)}|\hat{H}_{el}|\psi_e^{(-)}\rangle f_{\hat{H}_{rot}}(N_j, K_i, K_j, p_i, p_j) \\
&\quad\quad + c_{K_i}s_{K_j} i\langle\psi_e^{(-)}|\hat{H}_{el}|\psi_e^{(+)}\rangle f_{\hat{H}_{rot}}(N_j, K_i, K_j, p_i\delta_{0p_j}) \\
&\quad\quad - s_{K_i}c_{K_j} i\langle\psi_e^{(+)}|\hat{H}_{el}|\psi_e^{(-)}\rangle f_{\hat{H}_{rot}}(N_j, K_i, K_j, \delta_{0p_i}, p_j) \\
&\quad\quad + s_{K_i}s_{K_j}\langle\psi_e^{(+)}|\hat{H}_{el}|\psi_e^{(+)}\rangle f_{\hat{H}_{rot}}(N_j, K_i, K_j, \delta_{0p_i}, \delta_{0p_j}) \\
&\langle a; N_i, J, S, K_i, M_J, p_i|\hat{H}_{el}\hat{H}_{rot}|b; N_j, J, S, K_j, M_J, p_j\rangle \\
&\quad = c_{K_i}c_{K_j} i\langle\psi_e^{(-)}|\hat{H}_{el}|\psi_e^{(+)}\rangle f_{\hat{H}_{rot}}(N_j, K_i, K_j, p_i\delta_{0p_j}) \\
&\quad\quad - c_{K_i}s_{K_j}\langle\psi_e^{(-)}|\hat{H}_{el}|\psi_e^{(-)}\rangle f_{\hat{H}_{rot}}(N_j, K_i, K_j, p_i, p_j) \\
&\quad\quad + s_{K_i}c_{K_j}\langle\psi_e^{(+)}|\hat{H}_{el}|\psi_e^{(+)}\rangle f_{\hat{H}_{rot}}(N_j, K_i, K_j, \delta_{0p_i}, \delta_{0p_j}) \\
&\quad\quad + s_{K_i}s_{K_j} i\langle\psi_e^{(+)}|\hat{H}_{el}|\psi_e^{(-)}\rangle f_{\hat{H}_{rot}}(N_j, K_i, K_j, \delta_{0p_i}, p_j) \\
&\langle b; N_i, J, S, K_i, M_J, p_i|\hat{H}_{el}\hat{H}_{rot}|a; N_j, J, S, K_j, M_J, p_j\rangle \\
&\quad = -c_{K_i}c_{K_j} i\langle\psi_e^{(+)}|\hat{H}_{el}|\psi_e^{(-)}\rangle f_{\hat{H}_{rot}}(N_j, K_i, K_j, \delta_{0p_i}, p_j) \\
&\quad\quad + c_{K_i}s_{K_j}\langle\psi_e^{(+)}|\hat{H}_{el}|\psi_e^{(+)}\rangle f_{\hat{H}_{rot}}(N_j, K_i, K_j, \delta_{0p_i}, \delta_{0p_j}) \\
&\quad\quad - s_{K_i}c_{K_j}\langle\psi_e^{(-)}|\hat{H}_{el}|\psi_e^{(-)}\rangle f_{\hat{H}_{rot}}(N_j, K_i, K_j, p_i, p_j) \\
&\quad\quad - s_{K_i}s_{K_j} i\langle\psi_e^{(-)}|\hat{H}_{el}|\psi_e^{(+)}\rangle f_{\hat{H}_{rot}}(N_j, K_i, K_j, p_i\delta_{0p_j}) \\
&\langle b; N_i, J, S, K_i, M_J, p_i|\hat{H}_{el}\hat{H}_{rot}|b; N_j, J, S, K_j, M_J, p_j\rangle \\
&\quad = c_{K_i}c_{K_j}\langle\psi_e^{(+)}|\hat{H}_{el}|\psi_e^{(+)}\rangle f_{\hat{H}_{rot}}(N_j, K_i, K_j, \delta_{0p_i}, \delta_{0p_j}) \\
&\quad\quad + c_{K_i}s_{K_j} i\langle\psi_e^{(+)}|\hat{H}_{el}|\psi_e^{(-)}\rangle f_{\hat{H}_{rot}}(N_j, K_i, K_j, \delta_{0p_i}, p_j) \\
&\quad\quad - s_{K_i}c_{K_j} i\langle\psi_e^{(-)}|\hat{H}_{el}|\psi_e^{(+)}\rangle f_{\hat{H}_{rot}}(N_j, K_i, K_j, p_i\delta_{0p_j})
\end{aligned}$$

$$+s_{K_i}s_{K_j}\langle\psi_e^{(-)}|\hat{H}_{el}|\psi_e^{(-)}\rangle f_{\hat{H}_{rot}}(N_j,K_i,K_j,p_i,p_j). \quad (2.122)$$

### 2.2.4 Stretching basis functions

We use Morse-like stretching function (Ref. [16]) to represent the stretching motion of the molecule. The eigenfunctions for a diatomic molecule with Morse potential function are well known. We will take the Morse-like stretching function as a basis-set for the $r$ and $R$ stretching coordinates. Details of Morse-like stretching functions can be found in reference [16], and we give a small summary below.

If we have a diatomic molecule with bond length $R$, equilibrium geometry $R_e$, reduced mass $\mu$, dissociation energy $D_e$, and fundamental vibration energy $\omega_e$, the Morse potential function $V(R)$ for this diatomic molecule is,

$$V(R) = D_e\{1-\exp[-\beta(R-R_e)]\}^2 - D_e. \quad (2.123)$$

The eigenfunctions of this diatomic molecule are known as Morse-oscillator functions. The form for the $n$-th vibrational excitation eigenfunction; the $n$-th Morse-oscillator function $\psi_n(y)$ is

$$\psi_n(y) = \sqrt{\beta}N_{n\alpha}\exp(-y/2)y^{\frac{b}{2}}L_n^{\alpha}(y) \quad (2.124)$$

$$y = A\exp[-\beta(R-R_e)]. \quad (2.125)$$

The parameter $A$, $b$, $\beta$ and the index $\alpha$ in equation (2.124) are defined as,

$$A = \frac{4D_e}{\omega_e} \quad (2.126)$$

$$\beta = \omega_e\sqrt{\frac{\mu}{2D_e}} \quad (2.127)$$

$$b = \alpha \quad (2.128)$$

$$\alpha = A-(2n-1). \quad (2.129)$$

The term $N_{n\alpha}$ is a normalization term. Since $N_{n\alpha}L_n^{\alpha}(y)$ is the normalized associated

Laguerre polynomial, we can easily apply Gauss-Laguerre integration for the numerical integration involving these functions.

Here, we deal with triatomic molecules. Unfortunately, the potential energy function is not a simple Morse potential. However, we can use the Morse stretching functions as a basis set for the variational problem. We need a complete orthonormal set of functions for the basis set. For this purpose, we choose $\alpha$ as constant integer value of $A$, $b$ as $(\alpha + 1)$ (See details, in section III. of [16])

We choose suitable values for the dissociation energy $D_e$ and the fundamental vibrational energy $\omega_e$ for each of the coordinates $R$ and $r$, and calculate constants $A$, $\beta$, $\alpha$ and $b$. With these constants, we obtain the normalization factor $N_{n\alpha}$. The matrix elements for the kinetic energy terms, $\frac{1}{2\mu_R}\hat{P}_R^2$ and $\frac{1}{2\mu_r}\hat{P}_r^2$ in the Hamiltonian can be calculated from analytical expressions in reference [16], equation (45). Hamiltonian matrix elements of $\frac{1}{r^2}$ and $\frac{1}{R^2}$, are obtained using Gauss-Laguerre integration.

### 2.2.5 Symmetry of the basis functions

As we can see from Eq. (2.87), the electronic-rotation-spin basis function $|\eta; N, J, S, K, M_J, p\rangle$ is based on the rotation-spin basis function (Eq. (2.68)). The symmetry of the electronic-rotation-spin basis function $\Gamma_{\rm ers}$ originates in the symmetry $\Gamma_{\rm rs}$ of the rotation-spin basis function. The symmetry of the rotation-spin basis function $\Gamma_{\rm rs}$ is defined from the parity of the rotation-spin basis function, $p$ (Eq. (2.67)).

Within the Double-Renner theory we can treat ABC- and ABB-type of triatomic molecule. ABC-type molecule belongs to the MS group $C_{\rm s}({\rm M})$ (See Table 2.1). The symmetry of the rotation-spin basis function $\Gamma_{\rm rs}$ in the MS group $C_{\rm s}({\rm M})$ are summarized in Table 2.2. The symmetry of electronic function $|\psi_e^{(-)}\rangle$ and $|\psi_e^{(+)}\rangle$ will always be $A'$ and $A"$, respectively or $A"$ and $A'$, respectively. Here we take $A'$ for $|\psi_e^{(-)}\rangle$ state and $A"$ for $|\psi_e^{(+)}\rangle$, and from Eq. (2.68), we can construct the relation between $\eta = a$ and $\eta = b$ function and the parity $p$ to the symmetry of electronic-rotation-spin basis function $\Gamma_{\rm ers}$.

Table 2.1: The character table of the MS group $C_{\rm s}({\rm M})$.

| $C_{\rm s}({\rm M})$ : | $E$ | $E^*$ | | |
|---|---|---|---|---|
| | 1 | 1 | | |
| $C_{\rm s}$ : | $E$ | $\sigma_{yz}$ | | |
| $A'$ : | 1 | 1 | : | $\hat{N}_x$, $\hat{L}_x$ |
| $A$" : | 1 | -1 | : | $\hat{N}_y$,$\hat{N}_z$,$\hat{L}_y$,$\hat{L}_z$ |

$E$ is the identity operator. When $E^*$ operator, the inversion operation, is applied to a molecule, it inverts the spatial coordinates of all the nuclei and electrons through the molecular center of mass.

Table 2.2: The symmetry $\Gamma_{\rm rs}$ of the rotation-spin basis function in the MS group $C_{\rm s}({\rm M})$.

| | $K=0$ | $K\neq 0$ |
|---|---|---|
| $p=0$ | $A'(N$ even) | $A'$ |
| $p=1$ | $A$"$(N$ odd) | $A$" |

If $K=0$, we have $\sin(\gamma)=0$ and $\cos(\gamma)=1$ and so for $N$ even, we only use the $\eta=a$ function in the total basis functions for $\Gamma_{\rm ers}=A'$. These relations are summarized in Table 2.3. All the bending and stretching basis functions in ABC-type molecule are totally symmetric. Thus the total symmetry of the basis function depends on the symmetry of the electronic-rotation-spin basis function, $\Gamma_{\rm rve}=\Gamma_{\rm ers}$, and the relation summarized in Table 2.3 produces $\Gamma_{\rm rve}$.

An ABB-type molecule belongs to the MS group $C_{2{\rm v}}({\rm M})$ (See Table 2.4). The symmetry of the rotation-spin basis function $\Gamma_{\rm rs}$ in the MS group $C_{2{\rm v}}({\rm M})$ are summarized in Table 2.5. In an ABB-type molecule, the symmetry of electronic functions $|\psi_e^{(-)}\rangle$ and $|\psi_e^{(+)}\rangle$ will be $A_1\oplus B_1$, $B_1\oplus A_1$, $A_2\oplus B_2$ or $B_2\oplus A_2$. Here we take $A_1$ for $|\psi_e^{(-)}\rangle$ state and $B_1$ for $|\psi_e^{(+)}\rangle$, and from Eq. (2.68), we construct the relation between $\eta=a$ and $\eta=b$ function and the parity $p$ to the symmetry of electronic-rotation-spin basis function

Table 2.3: The relation of the $K$, $N$ quantum numbers and $\eta$ states to the symmetry $\Gamma_{\rm ers}$ of the electronic-rotation-spin basis function and the symmetry $\Gamma_{\rm rve}$ of the total basis function in the MS group $C_{\rm s}$(M).

| $\Gamma_{\rm ers} = \Gamma_{\rm rve}$ | $K = 0$ | | $K \neq 0$ |
|---|---|---|---|
| | $N$ even | $N$ odd | |
| $A'$ | $\eta = a$, $p = 0$ | $\eta = b$, $p = 0$ | $p = 0$ |
| $A$" | $\eta = b$, $p = 1$ | $\eta = a$, $p = 1$ | $p = 1$ |

$\Gamma_{\rm ers}$. If $K = 0$, we have $\sin(\gamma) = 0$ and $\cos(\gamma) = 1$ so for case $N$ even, we only use $\eta = a$ functions in the total basis function for $\Gamma_{\rm ers} = A_1$. These relations are summarized in Table 2.6. The stretching basis functions along the $r$ and $R$ coordinates are totally symmetric in the MS group $C_{2\rm v}(\rm M)$ while the bending basis functions are not. The operation $(12)$ exchange the atom 1 and 2. The atoms 1 and 2 are here the atoms B. Thus the operation $(12)$ on the $\tau$ coordinate changes it as

$$(12)\tau = \pi - \tau. \tag{2.130}$$

Some bending basis functions change their sign with the (12) symmetry operation. Those bending basis functions which do not change sign with the (12) operation have $A_1$ symmetry, and those which change the sign with the (12) operation have $B_2$ symmetry. Thus the total symmetry of the basis function becomes $\Gamma_{\rm rve} = \Gamma_{v_2^\eta} \otimes \Gamma_{\rm ers}$ . The relations between the $K$, $N$ quantum numbers and the $\Gamma_{v_2^\eta}$, the parity $p$ and the $\eta = a$, $\eta = b$ functions are summarized in Table 2.7.

## 2.3 Construction of the matrix elements

To obtain the rovibronic energy levels of the molecule, we need to solve the eigenvalue problem, from the well known physical principle, the Schrödinger equation.

$$\hat{H}\Psi = E\Psi \tag{2.131}$$

Table 2.4: The character table of the MS group $C_{2v}$(M). Atom B corresponds to atom 1 and 2.

| $C_{2v}$(M) : | $E$ | (12) | $E^*$ | $(12)^*$ | | |
|---|---|---|---|---|---|---|
| | 1 | 1 | 1 | 1 | | |
| $C_{2v}$ : | $E$ | $C_{2y}$ | $\sigma_{yz}$ | $\sigma_{xy}$ | | |
| $A_1$ : | 1 | 1 | 1 | 1 | : | |
| $A_2$ : | 1 | 1 | -1 | -1 | : | $\hat{N}_y$, $\hat{L}_y$ |
| $B_1$ : | 1 | -1 | -1 | 1 | : | $\hat{N}_z$, $\hat{L}_z$ |
| $B_2$ : | 1 | -1 | 1 | -1 | : | $\hat{N}_x$, $\hat{L}_x$ |

$E$ is the identity operator. Here atom 1 and 2 is the B atom in the molecule ABB (12) operator exchanges atom 1 and 2. When $E^*$ operator, the inversion operation, is applied to a molecule, it inverts the spatial coordinates of all the nuclei and electrons through the molecular center of mass. $(12)^*$ operator is the combination of (12) and $E^*$ operator.

Table 2.5: The symmetry $\Gamma_{rs}$ of the rotation-spin basis function in the MS group $C_{2v}$(M).

| | $K = 0$ | $K$ even | $K$ odd |
|---|---|---|---|
| $p = 0$ | $A_1$($N$ even) | $A_1$ | $B_2$ |
| $p = 1$ | $B_1$($N$ odd) | $B_1$ | $A_2$ |

Table 2.6: The relation of the $K$, $N$ quantum numbers and $\eta$ states to the symmetry $\Gamma_{\rm ers}$ of the electronic-rotation-spin basis function in the MS group $C_{2\rm v}$(M).

| $\Gamma_{\rm ers}$ | $K=0$ | | $K=$ even | $K=$ odd |
|---|---|---|---|---|
| | $N$ even | $N$ odd | | |
| $A_1$ | $\eta=a$, $p=0$ | $\eta=b$, $p=0$ | $p=0$ | |
| $A_2$ | | | | $p=1$ |
| $B_1$ | $\eta=b$, $p=1$ | $\eta=a$, $p=1$ | $p=1$ | |
| $B_2$ | | | | $p=0$ |

Table 2.7: The relation of the $K$, $N$ quantum numbers and $\eta$ states to the symmetry $\Gamma_{\rm rve}$ in the total basis function of the MS group $C_{2\rm v}$(M).

| $\Gamma_{\rm rve}$ | $K=0$ | | $K=$ even | $K=$ odd |
|---|---|---|---|---|
| | $N$ even | $N$ odd | | |
| $A_1$ | $\eta=a$ | $\eta=b$ | $\Gamma_{\rm vib}=A_1$ | $\Gamma_{\rm vib}=B_2$ |
| | $\Gamma_{\rm vib}=A_1$, $p=0$ | | $p=0$ | |
| $A_2$ | $\eta=b$ | $\eta=a$ | $\Gamma_{\rm vib}=B_2$ | $\Gamma_{\rm vib}=A_1$ |
| | $\Gamma_{\rm vib}=B_2$, $p=1$ | | $p=1$ | |
| $B_1$ | $\eta=b$ | $\eta=a$ | $\Gamma_{\rm vib}=A_1$ | $\Gamma_{\rm vib}=B_2$ |
| | $\Gamma_{\rm vib}=A_1$, $p=1$ | | $p=1$ | |
| $B_2$ | $\eta=a$ | $\eta=b$ | $\Gamma_{\rm vib}=B_2$ | $\Gamma_{\rm vib}=A_1$ |
| | $\Gamma_{\rm vib}=B_2$, $p=0$ | | $p=0$ | |

With integration of total wavefunction Eq. (2.61) working on the Hamiltonian expressed in Eq. (2.60),

$$\begin{aligned}\langle\Psi_{\rm rve}^{J,M_J,S,\Gamma_{\rm rve}}|\hat{H}_{DR}|\Psi_{\rm rve}^{J,M_J,S,\Gamma_{\rm rve}}\rangle &= \langle\Psi_{\rm rve}^{J,M_J,S,\Gamma_{\rm rve}}|E|\Psi_{\rm rve}^{J,M_J,S,\Gamma_{\rm rve}}\rangle \\ &= E\langle\Psi_{\rm rve}^{J,M_J,S,\Gamma_{\rm rve}}|\Psi_{\rm rve}^{J,M_J,S,\Gamma_{\rm rve}}\rangle, \end{aligned} \tag{2.132}$$

we will obtain the Hamiltonian matrix $\mathbf{H}$

$$\mathbf{H}^{\mathbf{J},\mathbf{M_J},\mathbf{S},\mathbf{\Gamma}_{\rm rve}} = \langle\Psi_{\rm rve}^{J,M_J,S,\Gamma_{\rm rve}}|\hat{H}_{DR}|\Psi_{\rm rve}^{J,M_J,S,\Gamma_{\rm rve}}\rangle. \tag{2.133}$$

The quantum numbers $J, M_J, S, \Gamma_{\rm rve}$, are the "good quantum numbers", which label the eigenvalues of the Hamiltonian. The matrix representations of the Hamiltonian is block diagonal in these quantum numbers. Therefore we can diagonalize separate matrix blocks for each value of the good quantum numbers. We write elements of the Hamiltonian matrix for each good quantum number value as

$$\begin{aligned} H_{ij}^{J,M_J,S,\Gamma_{\rm rve}} &= \langle N_{R_i}|\langle N_{r_i}|\langle v_{2_i}^{\eta_i}, K_i, \Gamma_{v_{2_i}}^{\eta_i}|\langle\eta_i; N_i, J, S, K_i, M_J, p_i| \\ &\quad \hat{H}_{DR}|N_{R_j}\rangle|N_{r_j}\rangle|v_{2_j}^{\eta_j}, K, \Gamma_{v_{2_j}}^{\eta_j}\rangle|\eta_j; N_j, J, S, K_j, M_J, p_j\rangle. \end{aligned} \tag{2.134}$$

Subscripts $i$ and $j$ denote the "not good" quantum numbers (these quantum numbers will not make the Hamiltonian matrix block diagonal) of the vibrational or angular momentum quantum numbers.

By using the relation $\hat{N}^2 = \hat{N}_x^2 + \hat{N}_y^2 + \hat{N}_z^2$, we can rewrite Eq. (2.60) as,

$$\hat{H} = \hat{H}_e + \hat{H}_{PrR} + \hat{H}_b + \hat{H}_{ba} + \hat{H}_{bb} + \hat{H}_{nk} + \hat{H}_{dk} + \hat{H}_{SO}, \tag{2.135}$$

$$\hat{H}_{PrR} = \frac{1}{2\mu_r}\hat{P}_r^2 + \frac{1}{2\mu_R}\hat{P}_R^2 \tag{2.136}$$

$$\hat{H}_b = \left\{\frac{\hbar^2}{2\mu_R R^2} + \frac{\hbar^2}{2\mu_r r^2}\right\}\left\{\hat{N}_\tau^2 - \frac{1}{4}\left(1 + \frac{1}{\sin^2(\tau)}\right)\right\} \tag{2.137}$$

$$\hat{H}_{ba} = \left\{\frac{\hbar^2}{2\mu_R R^2}\cot^2(\tau)\right\}(\hat{N}_z^2 + \hat{L}_z^2 - 2\hat{N}_z\hat{L}_z) \tag{2.138}$$

$$\hat{H}_{bb} = \left\{\frac{\hbar^2}{2\mu_r r^2}\frac{1}{\sin^2(\tau)}\right\}(\hat{N}_z^2 + \hat{L}_z^2 - 2\hat{N}_z\hat{L}_z) \quad (2.139)$$

$$\hat{H}_{nk} = \frac{\hbar^2}{2\mu_R R^2}(\hat{N}^2 - \hat{N}_z^2) \quad (2.140)$$

$$\hat{H}_{dk} = \frac{\hbar^2}{2\mu_R R^2}\left\{\hat{N}_x\hat{N}_\tau + \hat{N}_\tau\hat{N}_x + \frac{\hat{N}_y\hat{N}_z + \hat{N}_z\hat{N}_y - (\hat{N}_y\hat{L}_z + \hat{L}_z\hat{N}_y)}{\tan(\tau)}\right\} \quad (2.141)$$

Starting with the next section, we will show how to combine the parts of the Hamiltonian (eqs. (2.137)-(2.189)) to construct the total Hamiltonian matrix $\mathbf{H}^{\mathbf{J},\mathbf{M_J},\mathbf{S},\mathbf{\Gamma}_{\rm rve}}$.

### 2.3.1 Matrix elements of $\hat{H}_e$ (HAMILV)

This term is obtained by three-dimensional integration over products of basis function pairs and the potential energy function. The potential energies are calculated by $ab\ initio$ methods, and fitted to an analytical function. The integration over the $r$ and $R$ coordinates are made using Gauss-Laguerre quadrature, and the integration over the $\tau$ coordinate is made with Gauss-Legendre quadrature.

As described in Chapter 2.2.2, we have numerical bending basis functions $\Psi(\tau_i)$ on a regular grid. The number of integration points in the bending basis set are extremely many, thus we choose to use the Gauss-Legendre integration method for computing the integrals involving the potential energy function. Since Gauss-Legendre integration requires a non-regular grid of integration points, we have re-constructed the numerical bending basis functions in the interval required by Gauss-Legendre integration. Values for the numerical bending basis function around $0$ and $\pi$ are obtained from Eq. (2.107) and 2.108. Intermediate points are calculated by interpolation of a great number of equally spaced numerical values of the bending basis functions in question.

We denote the lower potential energy function by $V(r,R,\tau)^{(-)}$ and upper potential energy function as $V(r,R,\tau)^{(-)}$. We have by definition

$$\langle\psi_e^{(-)}|\hat{H}_e|\psi_e^{(-)}\rangle = V(r,R,\tau)^{(-)} \quad (2.142)$$

$$\langle\psi_e^{(-)}|\hat{H}_e|\psi_e^{(+)}\rangle = V(r,R,\tau)^{(+)} \quad (2.143)$$

$$\langle\psi_e^{(-)}|\hat{H}_e|\psi_e^{(+)}\rangle \;=\; \langle\psi_e^{(+)}|\hat{H}_e|\psi_e^{(-)}\rangle = 0, \tag{2.144}$$

and with Eq. (2.122), the Hamiltonian matrix of $\hat{H}_e$ can be written as

$$\begin{aligned}
&\langle N_{R_i}|\langle N_{r_i}|\langle v_{2_i}^{\eta_i}, K_i, \Gamma_{v_{2_i}}^{\eta_i}|\langle \eta_i; N_i, J, S, K_i, M_J, p_i| \\
&\qquad \hat{H}_e|N_{R_j}\rangle|N_{r_j}\rangle|v_{2_j}^{\eta_j}, K, \Gamma_{v_{2_j}}^{\eta_j}\rangle|\eta_j; N_j, J, S, K_j, M_J, p_j\rangle \\
&= \delta_{N_iN_j}\delta_{K_iK_j}\langle N_{R_i}|\langle N_{r_i}|\int \Psi^{\eta_i}_{v_{2_i},K_i,\Gamma^{\eta_i}_{v_{2_i}}}(\tau)X_{\eta_i\eta_j}\Psi^{\eta_j}_{v_{2_j},K_j,\Gamma^{\eta_j}_{v_{2_j}}}(\tau)d\tau|N_{R_j}\rangle|N_{r_j}\rangle.
\end{aligned} \tag{2.145}$$

Here, we write the bending basis function as $|v_{2_j}^{\eta_j}, K, \Gamma_{v_{2_j}}^{\eta_j}\rangle = \Psi^{\eta_j}_{v_{2_j},K_j,\Gamma^{\eta_j}_{v_{2_j}}}(\tau)$.

The term $X_{\eta_i\eta_j}$ in the equation (2.145) is obtained as follows; when $\eta_i = \eta_j$

$$X_{aa} \;=\; c_{K_j}^2 V(r,R,\tau)^{(-)} + s_{K_j}^2 V(r,R,\tau)^{(+)} \tag{2.146}$$

$$X_{bb} \;=\; c_{K_j}^2 V(r,R,\tau)^{(+)} + s_{K_j}^2 V(r,R,\tau)^{(-)}, \tag{2.147}$$

but when $\eta_i \neq \eta_j$

$$X_{ab} = X_{ba} = c_{K_j}s_{K_j}\left(V(r,R,\tau)^{(+)} - V(r,R,\tau)^{(-)}\right). \tag{2.148}$$

### 2.3.2 Matrix elements of $\hat{H}_{PrR}$ (HBL1, HBL2)

The matrix elements for $\hat{H}_{PrR}$ are very simple to derive.

$$\begin{aligned}
&\langle N_{R_i}|\langle N_{r_i}|\langle v_{2_i}^{\eta_i}, K_i, \Gamma_{v_{2_i}}^{\eta_i}|\langle \eta_i; N_i, J, S, K_i, M_J, p_i| \\
&\qquad \left(\frac{1}{2\mu_r}\hat{P}_r^2 + \frac{1}{2\mu_R}\hat{P}_R^2\right)|N_{R_j}\rangle|N_{r_j}\rangle|v_{2_j}^{\eta_j}, K, \Gamma_{v_{2_j}}^{\eta_j}\rangle|\eta_j; N_j, J, S, K_j, M_J, p_j\rangle \\
&= \delta_{N_iN_j}\delta_{K_iK_j}\delta_{\eta_i\eta_j}\delta_{v_{2_i}^{\eta_i}v_{2_j}^{\eta_j}}\left(\delta_{N_{R_i}N_{R_j}}\langle N_{r_i}|\frac{\hat{P}_r^2}{2\mu_r}|N_{r_j}\rangle + \langle N_{R_i}|\frac{\hat{P}_R^2}{2\mu_R}|N_{R_j}\rangle\delta_{N_{r_i}N_{r_j}}\right)
\end{aligned} \tag{2.149}$$

### 2.3.3 Matrix elements of $\hat{H}_b$ (HAMILB)

The matrix elements for $\hat{H}_b$ are

$$\langle N_{R_i}|\langle N_{r_i}|\langle v_{2_i}^{\eta_i}, K_i, \Gamma_{v_{2_i}}^{\eta_i}|\langle \eta_i; N_i, J, S, K_i, M_J, p_i|$$

$$
\begin{aligned}
& \left\{\frac{\hbar^2}{2\mu_R R^2}+\frac{\hbar^2}{2\mu_r r^2}\right\}\left\{\hat{N}_\tau^2-\frac{1}{4}\left(1+\frac{1}{\sin^2(\tau)}\right)\right\} \\
& |N_{R_j}\rangle|N_{r_j}\rangle|v_{2_j}^{\eta_j},K,\Gamma_{v_{2_j}}^{\eta_j}\rangle|\eta_j;N_j,J,S,K_j,M_J,p_j\rangle \\
= & \left(\langle N_{R_i}|\frac{\hbar^2}{2\mu_R R^2}|N_{R_j}\rangle\langle N_{r_i}|N_{r_j}\rangle+\langle N_{R_i}|N_{R_j}\rangle\langle N_{r_i}|\frac{\hbar^2}{2\mu_r r^2}|N_{r_j}\rangle\right) \\
& \langle v_{2_i}^{\eta_i},K_i,\Gamma_{v_{2_i}}^{\eta_i}|\langle\eta_i;N_i,J,S,K_i,M_J,p_i|\left\{\hat{N}_\tau^2-\frac{1}{4}\left(1+\frac{1}{\sin^2(\tau)}\right)\right\} \\
& |v_{2_j}^{\eta_j},K,\Gamma_{v_{2_j}}^{\eta_j}\rangle|\eta_j;N_j,J,S,K_j,M_J,p_j\rangle \qquad (2.150)
\end{aligned}
$$

Here, $\hat{N}_\tau^2=-\hbar^2\frac{\partial^2}{\partial\tau^2}$. We rearrange the part of the Hamiltonian matrix involving $-\frac{\partial^2}{\partial\tau^2}$ .[1]

$$
\begin{aligned}
& \langle v_{2_i}^{\eta_i},K_i,\Gamma_{v_{2_i}}^{\eta_i}|\langle\eta_i;N_i,J,S,K_i,M_J,p_i|-\frac{\partial^2}{\partial\tau^2}|v_{2_j}^{\eta_j},K,\Gamma_{v_{2_j}}^{\eta_j}\rangle|\eta_j;N_j,J,S,K_j,M_J,p_j\rangle \\
= & \left(\langle\frac{\partial}{\partial\tau}\left(v_{2_i}^{\eta_i},K_i,\Gamma_{v_{2_i}}^{\eta_i}\right)|\langle\eta_i;N_i,J,S,K_i,M_J,p_i|\right. \\
& \qquad \left.+\langle v_{2_i}^{\eta_i},K_i,\Gamma_{v_{2_i}}^{\eta_i}|\langle\frac{\partial}{\partial\tau}\left(\eta_i;N_i,J,S,K_i,M_J,p_i\right)|\right) \\
\times & \left(|\frac{\partial}{\partial\tau}\left(v_{2_j}^{\eta_j},K,\Gamma_{v_{2_j}}^{\eta_j}\right)\rangle|\left(\eta_j;N_j,J,S,K_j,M_J,p_j\right)\rangle\right. \\
& \qquad \left.+|v_{2_j}^{\eta_j},K,\Gamma_{v_{2_j}}^{\eta_j}\rangle|\frac{\partial}{\partial\tau}\left(\eta_j;N_j,J,S,K_j,M_J,p_j\right)\rangle\right) \\
= & \delta_{\eta_i\eta_j}\delta_{N_iN_j}\delta_{K_iK_j}\delta_{p_ip_j}\int X_{\eta_i\eta_j}d\tau \qquad (2.151)
\end{aligned}
$$

The derivatives of $|\eta;N,J,S,K,M_J,p\rangle$ with respect to $\tau$ are

$$
\begin{aligned}
|\frac{\partial}{\partial\tau}\left(a;N,J,S,K,M_J,p\right)\rangle &= -\sin(\gamma_K(\tau))\frac{\partial\gamma_K(\tau)}{\partial\tau}|\psi_e^{(-)}\rangle|N,J,S,K,M_J,p\rangle \\
&+ \cos(\gamma_K(\tau))i\frac{\partial\gamma_K(\tau)}{\partial\tau}|\psi_e^{(+)}\rangle|N,J,S,K,M_J,\delta_{0p}\rangle \\
&= |b;N,J,S,K,M_J,p\rangle\frac{\partial\gamma_K(\tau)}{\partial\tau} \\
|\frac{\partial}{\partial\tau}\left(b;N,J,S,K,M_J,p\right)\rangle &= -\sin(\gamma_K(\tau))i\frac{\partial\gamma_K(\tau)}{\partial\tau}|\psi_e^{(+)}\rangle|N,J,S,K,M_J,\delta_{0p}\rangle \\
&- \cos(\gamma_K(\tau))\frac{\partial\gamma_K(\tau)}{\partial\tau}|\psi_e^{(-)}\rangle|N,J,S,K,M_J,p\rangle
\end{aligned}
$$

[1]Since, $\frac{\partial}{\partial\tau}(\psi_a\psi_b)=\frac{\partial\psi_a}{\partial\tau}\psi_b+\psi_a\frac{\partial\psi_b}{\partial\tau}$ . So, $\int\psi_a\frac{\partial\psi_b}{\partial\tau}d\tau=\int\frac{\partial}{\partial\tau}(\psi_a\psi_b)d\tau-\int\frac{\partial\psi_a}{\partial\tau}\psi_b d\tau=-\int\frac{\partial\psi_a}{\partial\tau}\psi_b d\tau$. Thus, $\int(\psi_a\frac{\partial^2}{\partial\tau^2}\psi_b)d\tau=\int(\psi_a\frac{\partial}{\partial\tau}\frac{\partial}{\partial\tau}\psi_b)d\tau=\int-(\frac{\partial\psi_a}{\partial\tau}\frac{\partial\psi_b}{\partial\tau})d\tau$

$$= \quad -|a; N, J, S, K, M_J, p\rangle \frac{\partial \gamma_K(\tau)}{\partial \tau}. \tag{2.152}$$

Rewriting the bending basis function as $|v_{2_j}^{\eta_j}, K_j, \Gamma_{v_{2_j}}^{\eta_j}\rangle = \Psi^{\eta_j}_{v_{2_j}, K_j, \Gamma^{\eta_j}_{v_{2_j}}}(\tau)$, the term $X_{\eta_i \eta_j}$ in Eq. (2.151) can be written as follows: when $\eta_i = \eta_j$,

$$X_{aa} = X_{bb} = \frac{\partial \Psi^{\eta_i}_{v_{2_i}, K_i, \Gamma^{\eta_i}_{v_{2_i}}}(\tau)}{\partial \tau} \frac{\partial \Psi^{\eta_i}_{v_{2_j}, K_i, \Gamma^{\eta_i}_{v_{2_j}}}(\tau)}{\partial \tau} + \Psi^{\eta_i}_{v_{2_i}, K_i, \Gamma^{\eta_i}_{v_{2_i}}}(\tau) \Psi^{\eta_i}_{v_{2_j}, K_i, \Gamma^{\eta_i}_{v_{2_j}}}(\tau) \left( \frac{\partial \gamma_{K_i}(\tau)}{\partial \tau} \right)^2,$$

whereas when $\eta_i \neq \eta_j$

$$\begin{aligned} X_{ab} = & \left( \Psi^{a}_{v_{2_i}, K_i, \Gamma^{a}_{v_{2_i}}}(\tau) \frac{\partial \Psi^{b}_{v_{2_j}, K_i, \Gamma^{b}_{v_{2_j}}}(\tau)}{\partial \tau} - \frac{\partial \Psi^{a}_{v_{2_i}, K_i, \Gamma^{a}_{v_{2_i}}}(\tau)}{\partial \tau} \Psi^{b}_{v_{2_j}, K_i, \Gamma^{b}_{v_{2_j}}}(\tau) \right) \frac{\partial \gamma_{K_i}(\tau)}{\partial \tau} \\ X_{ba} = & \left( \Psi^{a}_{v_{2_j}, K_i, \Gamma^{a}_{v_{2_j}}}(\tau) \frac{\partial \Psi^{b}_{v_{2_i}, K_i, \Gamma^{b}_{v_{2_i}}}(\tau)}{\partial \tau} - \frac{\partial \Psi^{a}_{v_{2_j}, K_i, \Gamma^{a}_{v_{2_j}}}(\tau)}{\partial \tau} \Psi^{b}_{v_{2_i}, K_i, \Gamma^{b}_{v_{2_i}}}(\tau) \right) \frac{\partial \gamma_{K_i}(\tau)}{\partial \tau}. \end{aligned} \tag{2.153}$$

Thus Eq. (2.150) can be written as,

$$= \delta_{N_i N_j} \delta_{K_i K_j} \left( \langle N_{R_i} | \frac{\hbar^2}{2\mu_R R^2} | N_{R_j} \rangle \delta_{N_{r_i} N_{r_j}} + \delta_{N_{R_i} N_{R_j}} \langle N_{r_i} | \frac{\hbar^2}{2\mu_r r^2} | N_{r_j} \rangle \right) \times \int X_{\eta_i \eta_j} d\tau. \tag{2.154}$$

The quantity $X_{\eta_i \eta_j}$ in equation (2.154) is as follows; when $\eta_i = \eta_j$

$$\begin{aligned} X_{aa} \quad = \quad & X_{bb} = \hbar^2 \frac{\partial \Psi^{\eta_i}_{v_{2_i}, K_i, \Gamma^{\eta_i}_{v_{2_i}}}(\tau)}{\partial \tau} \frac{\partial \Psi^{\eta_i}_{v_{2_j}, K_i, \Gamma^{\eta_i}_{v_{2_j}}}(\tau)}{\partial \tau} \\ + \quad & \left\{ \hbar^2 \left( \frac{\partial \gamma_{K_i}(\tau)}{\partial \tau} \right)^2 - \frac{1}{4} \left( 1 + \frac{1}{\sin^2 \tau} \right) \right\} \Psi^{\eta_i}_{v_{2_i}, K_i, \Gamma^{\eta_i}_{v_{2_i}}}(\tau) \Psi^{\eta_i}_{v_{2_j}, K_i, \Gamma^{\eta_i}_{v_{2_j}}}(\tau) \end{aligned} \tag{2.155}$$

and when $\eta_i \neq \eta_j$,

$$X_{ab} = \left( \Psi^{a}_{v_{2_i},K_i,\Gamma^{a}_{v_{2_i}}}(\tau) \frac{\partial \Psi^{b}_{v_{2_j},K_i,\Gamma^{b}_{v_{2_j}}}(\tau)}{\partial \tau} - \frac{\partial \Psi^{a}_{v_{2_i},K_i,\Gamma^{a}_{v_{2_i}}}(\tau)}{\partial \tau} \Psi^{b}_{v_{2_j},K_i,\Gamma^{b}_{v_{2_j}}}(\tau) \right) \times \hbar^2 \frac{\partial \gamma_{K_i}(\tau)}{\partial \tau} \tag{2.156}$$

$$X_{ba} = \left( \Psi^{a}_{v_{2_j},K_i,\Gamma^{a}_{v_{2_j}}}(\tau) \frac{\partial \Psi^{b}_{v_{2_i},K_i,\Gamma^{b}_{v_{2_i}}}(\tau)}{\partial \tau} - \frac{\partial \Psi^{a}_{v_{2_j},K_i,\Gamma^{a}_{v_{2_j}}}(\tau)}{\partial \tau} \Psi^{b}_{v_{2_i},K_i,\Gamma^{b}_{v_{2_i}}}(\tau) \right) \times \hbar^2 \frac{\partial \gamma_{K_i}(\tau)}{\partial \tau}. \tag{2.157}$$

The first term, and the term $\sin \tau^{-2}$ in second term of equation (2.155) can easily produce numerical errors; these each terms quickly go to infinity when $\tau \to 0$ and $\tau \to \pi$. The terms $X_{aa}$ and $X_{bb}$ will not go to infinity since infinite values cancel, but they are proved to produce numerical errors. The basis function $\Psi^{\eta}_{v_2,K,\Gamma^{\eta}_{v_2}}(\tau)$ in the term $X_{aa}$ and $X_{bb}$ is the normalized eigenfunction of the Hamiltonian $\hat{H}_{bend}$ in equation (2.91). Where we write the bending vibrational energy obtained in the pre-diagonalisation step as $E^{\eta,K}_{v_2}$ and write the basis function in a simplified way as $\Psi^{\eta}_{v_2,K,\Gamma^{\eta}_{v_2}}(\tau) = \Phi^{\eta,K}_{v_2}(\tau)$, we have following equation from equations (2.89) and (2.91).

$$\begin{aligned} &\Phi^{\eta,K}_{v_{2_i}}(\tau) \Bigg\{ V^{\eta}_{K}(\tau) + \frac{1}{2}\mu_{\tau\tau}(\tau) g(\tau) \\ &- \frac{\hbar^2}{2} \left( \mu_{\tau\tau}(\tau) \frac{\partial^2}{\partial \tau^2} + [\frac{\partial}{\partial \tau}, \mu_{\tau\tau}(\tau)] \frac{\partial}{\partial \tau} \right) \Bigg\} \Phi^{\eta,K}_{v_{2_j}}(\tau) = E^{\eta,K}_{v_{2_j}} \Phi^{\eta,K}_{v_{2_i}}(\tau) \Phi^{\eta,K}_{v_{2_j}}(\tau) \end{aligned}$$

$$\begin{aligned} &\int \left\{ \hbar^2 \frac{\partial \Phi^{\eta,K}_{v_{2_i}}(\tau)}{\partial \tau} \frac{\partial \Phi^{\eta,K}_{v_{2_j}}(\tau)}{\partial \tau} - \frac{1}{4} \left( 1 + \frac{1}{\sin^2 \tau} \right) \Phi^{\eta,K}_{v_{2_i}}(\tau) \Phi^{\eta,K}_{v_{2_j}}(\tau) \right\} d\tau \\ &= \int \frac{-2\Phi^{\eta,K}_{v_{2_i}}(\tau)}{\mu_{\tau\tau}(\tau)} \left\{ \frac{\partial \mu_{\tau\tau}(\tau)}{\partial \tau} \frac{\partial \Phi^{\eta,K}_{v_{2_j}}(\tau)}{\partial \tau} + \left( V^{\eta}_{K}(\tau) - E^{\eta,K}_{v_{2_j}} \right) \Phi^{\eta,K}_{v_{2_j}}(\tau) \right\} d\tau \end{aligned} \tag{2.158}$$

Thus we use the relation in equation (2.158) for calculating the terms $X_{aa}$ and $X_{bb}$ in equation (2.154).

### 2.3.4 Matrix elements of $\hat{H}_{ba}$ and $\hat{H}_{bb}$ (HAMILBA, HAMILBB)

For the part of Hamiltonian matrix elements arising from $\hat{H}_{ba}$ and $\hat{H}_{bb}$, we first derive how the electronic-rotation-spin basis function is affected by the angular momentum operators in $\hat{H}_{ba}$ and $\hat{H}_{bb}$.

From equation (2.70) we know

$$\begin{aligned}\langle N_i, J, S, K_i, M_J, p_i|\hat{N}_z^2|N_i, J, S, K_i, M_J, p_j\rangle &= \delta_{N_iN_j}\delta_{K_iK_j}\delta_{p_ip_j}K_i^2\hbar^2 \\ \langle N_i, J, S, K_i, M_J, p_i|\hat{N}_z|N_i, J, S, K_i, M_J, p_j\rangle &= \delta_{N_iN_j}\delta_{K_iK_j}(1-\delta_{p_ip_j})K_i\hbar \end{aligned} \quad (2.159)$$

and from equations (2.118) and (2.87) we can obtain that

$$\langle \eta_i; N_i, J, S, K_i, M_J, p_i|\hat{N}_z^2|\eta_j; N_j, J, S, K_j, M_J, p_j\rangle = \delta_{\eta_i\eta_j}\delta_{N_iN_j}\delta_{K_iK_j}\delta_{p_ip_j}K_i^2\hbar^2 \quad (2.160)$$

$$\langle \eta_i; N_i, J, S, K_i, M_J, p_i|\hat{L}_z^2|\eta_j; N_j, J, S, K_j, M_J, p_j\rangle = \delta_{\eta_i\eta_j}\delta_{N_iN_j}\delta_{K_iK_j}\delta_{p_ip_j}\hbar^2 \times X_{\eta_i\eta_j}$$

$$\begin{cases} X_{aa} &= c_{K_i}^2 f_{\Lambda_-^2}(\tau) + s_{K_i}^2 f_{\Lambda_+^2}(\tau) \\ X_{ab} &= X_{ba} = c_{K_i}s_{K_i}\left(f_{\Lambda_+^2}(\tau) - f_{\Lambda_-^2}(\tau)\right) \\ X_{bb} &= c_{K_i}^2 f_{\Lambda_+^2}(\tau) + s_{K_i}^2 f_{\Lambda_-^2}(\tau) \end{cases} \quad (2.161)$$

$$\begin{aligned}&\langle \eta_i; N_i, J, S, K_i, M_J, p_i|\hat{N}_z\hat{L}_z|\eta_j; N_j, J, S, K_j, M_J, p_j\rangle \\ &\qquad = \delta_{N_iN_j}\delta_{K_iK_j}\delta_{p_ip_j}\hbar^2 K_i f_{\Lambda_{-,+}}(\tau) \quad \times \quad X_{\eta_i\eta_j} \\ &\qquad \begin{cases} X_{aa} &= -X_{bb} &= -2s_{K_i}c_{K_i} \\ X_{ab} &= X_{ba} &= s_{K_i}^2 - c_{K_i}^2. \end{cases}\end{aligned} \quad (2.162)$$

Thus the Hamiltonian matrix elements of $\hat{H}_{ba}$ (Eq. (2.138)) are

$$\begin{aligned}&\langle N_{R_i}|\langle N_{r_i}|\langle v_{2_i}^{\eta_i}, K_i, \Gamma_{v_{2_i}}^{\eta_i}|\langle \eta_i; N_i, J, S, K_i, M_J, p_i| \\ &\qquad \hat{H}_{ba}|N_{R_j}\rangle|N_{r_j}\rangle|v_{2_j}^{\eta_j}, K_j, \Gamma_{v_{2_j}}^{\eta_j}\rangle|\eta_j; N_j, J, S, K_j, M_J, p_j\rangle \\ &= \delta_{N_iN_j}\delta_{K_iK_j}\delta_{N_{r_i}N_{r_j}}\langle N_{R_i}|\frac{\hbar^2}{2\mu_R R^2}|N_{R_j}\rangle \\ &\qquad \times\hbar^2\int \Psi^{\eta_i}_{v_{2_i},K_i,\Gamma_{v_{2_i}}^{\eta_i}}(\tau)\Psi^{\eta_j}_{v_{2_j},K_i,\Gamma_{v_{2_j}}^{\eta_j}}(\tau)X_{\eta_i\eta_j}\frac{\cos^2(\tau)}{\sin^2(\tau)}d\tau. \end{aligned} \quad (2.163)$$

Further, the Hamiltonian matrix elements of $\hat{H}_{bb}$ (Eq. (2.139)) are

$$\begin{aligned}
&\langle N_{R_i}|\langle N_{r_i}|\langle v_{2_i}^{\eta_i}, K_i, \Gamma_{v_{2_i}}^{\eta_i}|\langle \eta_i; N_i, J, S, K_i, M_J, p_i| \\
&\qquad \hat{H}_{bb}|N_{R_j}\rangle|N_{r_j}\rangle|v_{2_j}^{\eta_j}, K_j, \Gamma_{v_{2_j}}^{\eta_j}\rangle|\eta_j; N_j, J, S, K_j, M_J, p_j\rangle \\
&= \delta_{N_iN_j}\delta_{K_iK_j}\delta_{N_{R_i}N_{R_j}}\langle N_{r_i}|\frac{\hbar^2}{2\mu_r r^2}|N_{r_j}\rangle \\
&\qquad \times\hbar^2\int \Psi^{\eta_i}_{v_{2_i},K_i,\Gamma^{\eta_i}_{v_{2_i}}}(\tau)\Psi^{\eta_j}_{v_{2_j},K_i,\Gamma^{\eta_j}_{v_{2_j}}}(\tau)\frac{X_{\eta_i\eta_j}}{\sin^2(\tau)}d\tau. \qquad (2.164)
\end{aligned}$$

The term $X_{\eta_i\eta_j}$ in equations (2.163) and (2.164) is given as

$$\begin{aligned}
X_{aa} &= K_i^2 + c_{K_i}^2 f_{\Lambda_-^2}(\tau) + s_{K_i}^2 f_{\Lambda_+^2}(\tau) + 4s_{K_i}c_{K_i}K_i f_{\Lambda_{-,+}}(\tau) \qquad (2.165)\\
X_{bb} &= K_i^2 + c_{K_i}^2 f_{\Lambda_+^2}(\tau) + s_{K_i}^2 f_{\Lambda_-^2}(\tau) - 4s_{K_i}c_{K_i}K_i f_{\Lambda_{-,+}}(\tau) \qquad (2.166)\\
X_{ab} &= X_{ba} = 2K_i(c_{K_i}^2 - s_{K_i}^2)f_{\Lambda_{-,+}}(\tau). + c_{K_i}s_{K_i}\left(f_{\Lambda_+^2}(\tau) - f_{\Lambda_-^2}(\tau)\right). \qquad (2.167)
\end{aligned}$$

### 2.3.5 Matrix elements of $\hat{H}_{nk}$ (HAMILNK)

This is the Hamiltonian matrix contribution involving the rotational angular momentum. The matrix elements are non-zero only when $\Delta K = 0$ and $\Delta N = 0$. When we diagonalize the Hamiltonian matrix, we first diagonalize the elements which have $\Delta K = 0$ and $\Delta N = 0$, and we call this $K$-block diagonalization. (See details in Chapter 2.4) Therefor we do not include $\hat{H}_{nk}$ term in the $K$-block diagonalization. The term will be added when we do the final diagonalization ($J$-block diagonalization, see also in Chapter 2.4). The Hamiltonian matrix elements from Eq. (2.140) are

$$\begin{aligned}
&\langle N_{R_i}|\langle N_{r_i}|\langle v_{2_i}^{\eta_i}, K_i, \Gamma_{v_{2_i}}^{\eta_i}|\langle \eta_i; N_i, J, S, K_i, M_J, p_i| \\
&\qquad \hat{H}_{nk}|N_{R_j}\rangle|N_{r_j}\rangle|v_{2_j}^{\eta_j}, K_j, \Gamma_{v_{2_j}}^{\eta_j}\rangle|\eta_j; N_j, J, S, K_j, M_J, p_j\rangle \\
&= \delta_{N_iN_j}\delta_{K_iK_j}\delta_{\eta_i\eta_j}\delta_{N_{r_i}N_{r_j}}\delta_{v_{2_i}^{\eta_i}v_{2_j}^{\eta_j}}\hbar^2\{N_i(N_i+1) - K_i^2\}\langle N_{R_i}|\frac{\hbar^2}{2\mu_R R^2}|N_{R_j}\rangle. \qquad (2.168)
\end{aligned}$$

### 2.3.6 Matrix elements of $\hat{H}_{dk}$(HAMILDK)

This term produces nonvanishing matrix elements only when $\Delta K = 1$ and $\Delta N = 0$. Thus we do not include it for the $K$-block diagonalization. It will be added when we do the final diagonalization ($J$-block diagonalization).

The operators $\hat{N}_\tau$ and $\hat{N}_x$ commute and so do $\hat{L}_z$ and $\hat{N}_y$. Thus we can write the Hamiltonian matrix elements from equation (2.141) as

$$\begin{aligned}
&\langle N_{R_i}|\langle N_{r_i}|\langle v_{2_i}^{\eta_i}, K_i, \Gamma_{v_{2_i}}^{\eta_i}|\langle \eta_i; N_i, J, S, K_i, M_J, p_i| \\
&\qquad \hat{H}_{dk}|N_{R_j}\rangle|N_{r_j}\rangle|v_{2_j}^{\eta_j}, K_j, \Gamma_{v_{2_j}}^{\eta_j}\rangle|\eta_j; N_j, J, S, K_j, M_J, p_j\rangle \\
&= \delta_{N_{r_i}N_{r_j}}\langle N_{R_i}|\frac{\hbar^2}{2\mu_R R^2}|N_{R_j}\rangle\langle v_{2_i}^{\eta_i}, K_i, \Gamma_{v_{2_i}}^{\eta_i}|\langle \eta_i; N_i, J, S, K_i, M_J, p_i| \\
&\qquad \left\{2\hat{N}_x\hat{N}_\tau + \left(\hat{N}_y\hat{N}_z + \hat{N}_z\hat{N}_y - 2\hat{N}_y\hat{L}_z\right)\frac{\cos(\tau)}{\sin(\tau)}\right\} \\
&\qquad |v_{2_j}^{\eta_j}, K_j, \Gamma_{v_{2_j}}^{\eta_j}\rangle|\eta_j; N_j, J, S, K_j, M_J, p_j\rangle. \qquad (2.169)
\end{aligned}$$

Here,

$$\begin{aligned}
&\langle v_{2_i}^{\eta_i}, K_i, \Gamma_{v_{2_i}}^{\eta_i}|\langle \eta_i; N_i, J, S, K_i, M_J, p_i|\hat{N}_x\hat{N}_\tau|v_{2_j}^{\eta_j}, K_j, \Gamma_{v_{2_j}}^{\eta_j}\rangle|\eta_j; N_j, J, S, K_j, M_J, p_j\rangle \\
&= -i\hbar\langle v_{2_i}^{\eta_i}, K_i, \Gamma_{v_{2_i}}^{\eta_i}|\langle \eta_i; N_i, J, S, K_i, M_J, p_i|\hat{N}_x \\
&\qquad \times\Big(|\frac{\partial}{\partial\tau}\left(v_{2_j}^{\eta_j}, K, \Gamma_{v_{2_j}}^{\eta_j}\right)\rangle|\eta_j; N_j, J, S, K_j, M_J, p_j\rangle \\
&\qquad\qquad +|v_{2_j}^{\eta_j}, K, \Gamma_{v_{2_j}}^{\eta_j}\rangle|\frac{\partial}{\partial\tau}\left(\eta_j; N_j, J, S, K_j, M_J, p_j\right)\rangle\Big). \qquad (2.170)
\end{aligned}$$

Thus,

$$\begin{aligned}
&\langle v_{2_i}^{\eta_i}, K_i, \Gamma_{v_{2_i}}^{\eta_i}|\langle \eta_i; N_i, J, S, K_i, M_J, p_i|\Big\{2\hat{N}_x\hat{N}_\tau + \frac{\hat{N}_y\hat{N}_z + \hat{N}_z\hat{N}_y - 2\hat{N}_y\hat{L}_z}{\tan(\tau)}\Big\} \\
&\qquad |v_{2_j}^{\eta_j}, K_j, \Gamma_{v_{2_j}}^{\eta_j}\rangle|\eta_j; N_j, J, S, K_j, M_J, p_j\rangle \\
&= \langle v_{2_i}^{\eta_i}, K_i, \Gamma_{v_{2_i}}^{\eta_i}|\Big(-2i\hbar\langle \eta_i; N_i, J, S, K_i, M_J, p_i|\hat{N}_x|\frac{\partial}{\partial\tau}\left(\eta_j; N_j, J, S, K_j, M_J, p_j\right)\rangle \\
&+ \langle \eta_i; N_i, J, S, K_i, M_J, p_i|\frac{\hat{N}_y\hat{N}_z + \hat{N}_z\hat{N}_y - 2\hat{N}_y\hat{L}_z}{\tan(\tau)}|\eta_j; N_j, J, S, K_j, M_J, p_j\rangle\Big)|v_{2_j}^{\eta_j}, K, \Gamma_{v_{2_j}}^{\eta_j}\rangle
\end{aligned}$$

$$- \quad 2i\hbar\langle v_{2_i}^{\eta_i}, K_i, \Gamma_{v_{2_i}}^{\eta_i}|\langle\eta_i; N_i, J, S, K_i, M_J, p_i|\hat{N}_x|\eta_j; N_j, J, S, K_j, M_J, p_j\rangle|\frac{\partial}{\partial\tau}\left(v_{2_j}^{\eta_j}, K, \Gamma_{v_{2_j}}^{\eta_j}\right)\rangle. \tag{2.171}$$

With Eq. (2.122), we obtain

$$\begin{aligned}
&\langle a; N_i, J, S, K_i, M_J, p_i|\hat{L}_z\hat{N}_y|a; N_j, J, S, K_j, M_J, p_j\rangle \\
&\quad = \quad \hbar f_{\Lambda_{-,+}}\{-c_{K_i}s_{K_j}f_{\hat{N}_y}(N_j, K_i, K_j, p_i, \delta_{0p_j}) - s_{K_i}c_{K_j}f_{\hat{N}_y}(N_j, K_i, K_j, \delta_{0p_i}, p_j)\} \\
&\langle a; N_i, J, S, K_i, M_J, p_i|\hat{L}_z\hat{N}_y|b; N_j, J, S, K_j, M_J, p_j\rangle \\
&\quad = \quad \hbar f_{\Lambda_{-,+}}\{-c_{K_i}c_{K_j}f_{\hat{N}_y}(N_j, K_i, K_j, p_i, \delta_{0p_j}) + s_{K_i}s_{K_j}f_{\hat{N}_y}(N_j, K_i, K_j, \delta_{0p_i}, p_j)\} \\
&\langle b; N_i, J, S, K_i, M_J, p_i|\hat{L}_z\hat{N}_y|a; N_j, J, S, K_j, M_J, p_j\rangle \\
&\quad = \quad \hbar f_{\Lambda_{-,+}}\{-c_{K_i}c_{K_j}f_{\hat{N}_y}(N_j, K_i, K_j, \delta_{0p_i}, p_j) + s_{K_i}s_{K_j}f_{\hat{N}_y}(N_j, K_i, K_j, p_i, \delta_{0p_j})\} \\
&\langle b; N_i, J, S, K_i, M_J, p_i|\hat{L}_z\hat{N}_y|b; N_j, J, S, K_j, M_J, p_j\rangle \\
&\quad = \quad \hbar f_{\Lambda_{-,+}}\{c_{K_i}s_{K_j}f_{\hat{N}_y}(N_j, K_i, K_j, \delta_{0p_i}, p_j) + s_{K_i}c_{K_j}f_{\hat{N}_y}(N_j, K_i, K_j, p_i, \delta_{0p_j})\}.
\end{aligned} \tag{2.172}$$

Similarly, we obtain the matrix elements for $\hat{N}_x$, $\hat{N}_y\hat{N}_z$, and $\hat{N}_z\hat{N}_y$ as

$$\begin{aligned}
&\langle a; N_i, J, S, K_i, M_J, p_i|\hat{H}_{rot}|a; N_j, J, S, K_j, M_J, p_j\rangle \\
&\quad = \quad c_{K_i}c_{K_j}f_{\hat{H}_{rot}}(N_j, K_i, K_j, p_i, p_j) + s_{K_i}s_{K_j}f_{\hat{H}_{rot}}(N_j, K_i, K_j, \delta_{0p_i}, \delta_{0p_j}) \\
&\langle a; N_i, J, S, K_i, M_J, p_i|\hat{H}_{rot}|b; N_j, J, S, K_j, M_J, p_j\rangle \\
&\quad = \quad -c_{K_i}s_{K_j}f_{\hat{H}_{rot}}(N_j, K_i, K_j, p_i, p_j) + s_{K_i}c_{K_j}f_{\hat{H}_{rot}}(N_j, K_i, K_j, \delta_{0p_i}, \delta_{0p_j}) \\
&\langle b; N_i, J, S, K_i, M_J, p_i|\hat{H}_{rot}|a; N_j, J, S, K_j, M_J, p_j\rangle \\
&\quad = \quad c_{K_i}s_{K_j}f_{\hat{H}_{rot}}(N_j, K_i, K_j, \delta_{0p_i}, \delta_{0p_j}) - s_{K_i}c_{K_j}f_{\hat{H}_{rot}}(N_j, K_i, K_j, p_i, p_j) \\
&\langle b; N_i, J, S, K_i, M_J, p_i|\hat{H}_{rot}|b; N_j, J, S, K_j, M_J, p_j\rangle \\
&\quad = \quad c_{K_i}c_{K_j}f_{\hat{H}_{rot}}(N_j, K_i, K_j, \delta_{0p_i}, \delta_{0p_j}) + s_{K_i}s_{K_j}f_{\hat{H}_{rot}}(N_j, K_i, K_j, p_i, p_j).
\end{aligned} \tag{2.173}$$

From Eqs. (2.171) - (2.173) , Eq. (2.169) can be rewritten as

$$
\begin{aligned}
&= \delta_{N_i N_j}\delta_{N_{r_i} N_{r_j}} \langle N_{R_i}|\frac{\hbar^2}{2\mu_R R^2}|N_{R_j}\rangle \\
&\times \int \Bigg( \Psi^{\eta_i}_{v_{2_i},K_i,\Gamma^{\eta_i}_{v_{2_i}}}(\tau)\Psi^{\eta_j}_{v_{2_j},K_j,\Gamma^{\eta_j}_{v_{2_j}}}(\tau) \times X_{\eta_i\eta_j} \\
&+ \frac{2\hbar}{i}\Psi^{\eta_i}_{v_{2_i},K_i,\Gamma^{\eta_i}_{v_{2_i}}}(\tau)\frac{\partial \Psi^{\eta_j}_{v_{2_j},K_j,\Gamma^{\eta_j}_{v_{2_j}}}(\tau)}{\partial\tau} \times Y_{\eta_i\eta_j}\Bigg) d\tau,
\end{aligned} \tag{2.174}
$$

where, $X_{\eta_i\eta_j}$ in Eq. (2.174) is given as follows; when $\eta_i = \eta_j = a$,

$$
\begin{aligned}
X_{aa} &= \frac{1}{\tan\tau}\Big\{ c_{K_i}c_{K_j} f_{\hat{N}_y\hat{N}_z+\hat{N}_z\hat{N}_y}(N_j,K_i,K_j,p_i,p_j) \\
&+ s_{K_i}s_{K_j} f_{\hat{N}_y\hat{N}_z+\hat{N}_z\hat{N}_y}(N_j,K_i,K_j,\delta_{0p_i},\delta_{0p_j}) \\
&+ 2\hbar f_{\Lambda-+}\Big( c_{K_i}s_{K_j} f_{\hat{N}_y}(N_j,K_i,K_j,p_i,\delta_{0p_j}) + s_{K_i}c_{K_j} f_{\hat{N}_y}(N_j,K_i,K_j,\delta_{0p_i},p_j)\Big)\Big\} \\
&+ \frac{2\hbar}{i}\frac{\partial\gamma_{K_j}(\tau)}{\partial\tau}\Big( - c_{K_i}s_{K_j} f_{\hat{N}_x}(N_j,K_i,K_j,p_i,p_j) + s_{K_i}c_{K_j} f_{\hat{N}_x}(N_j,K_i,K_j,\delta_{0p_i},\delta_{0p_j})\Big)
\end{aligned} \tag{2.175}
$$

when $\eta_i = \eta_j = b$,

$$
\begin{aligned}
X_{bb} &= \frac{1}{\tan\tau}\Big\{ c_{K_i}c_{K_j} f_{\hat{N}_y\hat{N}_z+\hat{N}_z\hat{N}_y}(N_j,K_i,K_j,\delta_{0p_i},\delta_{0p_j}) \\
&+ s_{K_i}s_{K_j} f_{\hat{N}_y\hat{N}_z+\hat{N}_z\hat{N}_y}(N_j,K_i,K_j,p_i,p_j) \\
&- 2\hbar f_{\Lambda-+}\Big( c_{K_i}s_{K_j} f_{\hat{N}_y}(N_j,K_i,K_j,\delta_{0p_i},p_j) + s_{K_i}c_{K_j} f_{\hat{N}_y}(N_j,K_i,K_j,p_i,\delta_{0p_j})\Big)\Big\} \\
&+ \frac{2\hbar}{i}\frac{\partial\gamma_{K_j}(\tau)}{\partial\tau}\Big( - c_{K_i}s_{K_j} f_{\hat{N}_x}(N_j,K_i,K_j,\delta_{0p_i},\delta_{0p_j}) + s_{K_i}c_{K_j} f_{\hat{N}_x}(N_j,K_i,K_j,p_i,p_j)\Big)
\end{aligned} \tag{2.176}
$$

when $\eta_i = a$, $\eta_j = b$,

$$
\begin{aligned}
X_{ab} &= \frac{1}{\tan\tau}\Big\{ - c_{K_i}s_{K_j} f_{\hat{N}_y\hat{N}_z+\hat{N}_z\hat{N}_y}(N_j,K_i,K_j,p_i,p_) \\
&+ s_{K_i}c_{K_j} f_{\hat{N}_y\hat{N}_z+\hat{N}_z\hat{N}_y}(N_j,K_i,K_j,\delta_{0p_i},\delta_{0p_j}) \\
&+ 2\hbar f_{\Lambda-+}\Big( c_{K_i}c_{K_j} f_{\hat{N}_y}(N_j,K_i,K_j,p_i,\delta_{0p_j}) - s_{K_i}s_{K_j} f_{\hat{N}_y}(N_j,K_i,K_j,\delta_{0p_i},p_j)\Big)\Big\} \\
&- \frac{2\hbar}{i}\frac{\partial\gamma_{K_j}(\tau)}{\partial\tau}\Big( c_{K_i}c_{K_j} f_{\hat{N}_x}(N_j,K_i,K_j,p_i,p_j) + s_{K_i}s_{K_j} f_{\hat{N}_x}(N_j,K_i,K_j,\delta_{0p_i},\delta_{0p_j})\Big)
\end{aligned}
$$

$$(2.177)$$

and when $\eta_i = b$, $\eta_j = a$,

$$\begin{aligned} X_{ba} &= \frac{1}{\tan\tau}\Big\{c_{K_i}s_{K_j}f_{\hat{N}_y\hat{N}_z+\hat{N}_z\hat{N}_y}(N_j,K_i,K_j,\delta_{0p_i},\delta_{0p_j}) \\ &- s_{K_i}c_{K_j}f_{\hat{N}_y\hat{N}_z+\hat{N}_z\hat{N}_y}(N_j,K_i,K_j,p_i,p_) \\ &+ 2\hbar f_{\Lambda-+}\Big(c_{K_i}c_{K_j}f_{\hat{N}_y}(N_j,K_i,K_j,\delta_{0p_i},p_j) - s_{K_i}s_{K_j}f_{\hat{N}_y}(N_j,K_i,K_j,p_i,\delta_{0p_j})\Big)\Big\} \\ &+ \frac{2\hbar}{i}\frac{\partial\gamma_{K_j}(\tau)}{\partial\tau}\Big(c_{K_i}c_{K_j}f_{\hat{N}_x}(N_j,K_i,K_j,\delta_{0p_i},\delta_{0p_j}) + s_{K_i}s_{K_j}f_{\hat{N}_x}(N_j,K_i,K_j,p_i,p_j)\Big) \end{aligned} \quad (2.178)$$

The term $Y_{\eta_i\eta_j}$ in Eq. (2.174) are as follows; when $\eta_i = \eta_j$

$$Y_{aa} = c_{K_i}c_{K_j}f_{\hat{N}_x}(N_j,K_i,K_j,p_i,p_j) + s_{K_i}s_{K_j}f_{\hat{N}_x}(N_j,K_i,K_j,\delta_{0p_i},\delta_{0p_j}) \quad (2.179)$$

$$Y_{bb} = c_{K_i}c_{K_j}f_{\hat{N}_x}(N_j,K_i,K_j,\delta_{0p_i},\delta_{0p_j}) + s_{K_i}s_{K_j}f_{\hat{N}_x}(N_j,K_i,K_j,p_i,p_j), \quad (2.180)$$

and when $\eta_i \neq \eta_j$,

$$Y_{ab} = -c_{K_i}s_{K_j}f_{\hat{N}_x}(N_j,K_i,K_j,p_i,p_j) + s_{K_i}c_{K_j}f_{\hat{N}_x}(N_j,K_i,K_j,\delta_{0p_i},\delta_{0p_j}) \quad (2.181)$$

$$Y_{ba} = c_{K_i}s_{K_j}f_{\hat{N}_x}(N_j,K_i,K_j,\delta_{0p_i},\delta_{0p_j}) - s_{K_i}c_{K_j}f_{\hat{N}_x}(N_j,K_i,K_j,p_i,p_j). \quad (2.182)$$

The function $f_{\hat{H}_{rot}}(N_j,K_i,K_j,p_i,p_j)$ has the following values. When $K_j = 0$, if $K_i = 1$ and $(-1)^{N+p_i} = 1$ then the function $f_{\hat{N}_x}(N_j,K_i,K_j,p_i,p_j)$ will have a non-zero value of

$$f_{\hat{N}_x}(N_j,1,0,p_i,p_j) = -i\hbar\frac{\sqrt{N_j(N_j+1)}}{\sqrt{2}}. \quad (2.183)$$

When $K_j = 1$, $K_i = 0$ and $(-1)^{N+p_j} = -1$, or $K_j = 1$ and $K_i = 2$ or $K_j \geq 2$ and $K_i = K_j \pm 1$ then $f_{\hat{N}_x}(N_j,K_i,K_j,p_i,p_j)$ will have a non-zero value of

$$f_{\hat{N}_x}(N_j,K_i,K_j,p_i,p_j) = (K_j - K_i)\frac{i\hbar}{2}\delta_{p_ip_j}\sqrt{N_j(N_j+1) - K_j(K_j\pm 1)}. \quad (2.184)$$

When $K_j = 0$, $K_i = 1$ and $(-1)^{N+p_i} = -1$ then the function $f_{\hat{N}_y}(N_j,K_i,K_j,p_i,p_j)$ can have a non-zero value of

$$f_{\hat{N}_y}(N_j,1,0,p_i,p_j) = \hbar\frac{\sqrt{N_j(N_j+1)}}{\sqrt{2}}. \quad (2.185)$$

When $K_j = 1$, $K_i = 0$ and $(-1)^{N+p_j} = -1$, or $K_j = 1$ and $K_i = 2$ or $K_j \geq 2$ and $K_i = K_j \pm 1$ then $f_{\hat{N}_y}(N_j, K_i, K_j, p_i, p_j)$ has a non-zero value of

$$f_{\hat{N}_y}(N_j, K_i, K_j, p_i, p_j) = \frac{\hbar}{2}(1 - \delta_{p_i p_j})\sqrt{N_j(N_j+1) - K_j(K_j \pm 1)}. \tag{2.186}$$

When $K_j = 0$, $K_i = 1$ and $(-1)^{N+p_i} = 1$ then the function $f_{\hat{N}_y\hat{N}_z+\hat{N}_z\hat{N}_y}(N_j, K_i, K_j, p_i, p_j)$ can have a non-zero value of

$$f_{\hat{N}_y\hat{N}_z+\hat{N}_z\hat{N}_y}(N_j, 1, 0, p_i, p_j) = \hbar^2 \frac{\sqrt{N_j(N_j+1)}}{\sqrt{2}}. \tag{2.187}$$

When $K_j \geq 1$ and $K_i \geq 1$, $K_i = K_j \pm 1$ then $f_{\hat{N}_y\hat{N}_z+\hat{N}_z\hat{N}_y}(N_j, K_i, K_j, p_i, p_j)$ will have a non-zero value of

$$f_{\hat{N}_y\hat{N}_z+\hat{N}_z\hat{N}_y}(N_j, K_i, K_j, p_i, p_j) = \frac{\hbar^2}{2}\delta_{p_i p_j}\sqrt{N_j(N_j+1) - K_j(K_j \pm 1)}(2K_j \pm 1). \tag{2.188}$$

### 2.3.7 Matrix elements from $\hat{H}_{SO}$ (HAMILSO)

This term yields non-vanishing Hamiltonian matrix elements only when $\Delta K = 0$ and $\Delta N = 0, 1$. Thus, we we do not include this term in the $K$-block diagonalization.

For the Hamiltonian $\hat{H}_{SO}$, we use the expressions given by Hallin and Merer (Ref. [17]). The Hamiltonian matrix elements of $\hat{H}_{SO}$ are

$$\begin{aligned}
&\langle N_{R_i}|\langle N_{r_i}|\langle v_{2_i}^{\eta_i}, K_i, \Gamma_{v_{2_i}}^{\eta_i}|\langle \eta_i; N_i, J, S, K_i, M_J, p_i| \\
&\qquad \hat{H}_{SO}|N_{R_j}\rangle|N_{r_j}\rangle|v_{2_j}^{\eta_j}, K_j, \Gamma_{v_{2_j}}^{\eta_j}\rangle|\eta_j; N_j, J, S, K_j, M_J, p_j\rangle \\
&= \delta_{K_i K_j}\delta_{p_i p_j}\delta_{N_{R_i} N_{R_j}}\delta_{N_{r_i} N_{r_j}}\delta_{v_{2_i}^{\eta_i} v_{2_j}^{\eta_j}}\hbar c f(J, S, N_i, N_j, K_j) \\
&\qquad \times \int \Psi^{\eta_i}_{v_{2_i}, K_i, \Gamma_{v_{2_i}}^{\eta_i}}(\tau)\Psi^{\eta_j}_{v_{2_j}, K_j, \Gamma_{v_{2_j}}^{\eta_j}}(\tau) A_{SO}(\tau) f_{\Lambda-,+} \times X_{\eta_i\eta_j} d\tau.
\end{aligned} \tag{2.189}$$

Where

$$\begin{aligned}
f(J, S, N_i, N_j, K_j) &= (-1)^{N_i+N_j+S+J-K}\sqrt{(2S+1)S(S+1)(2N_i+1)(2N_j+1)} \\
&\quad \times \begin{pmatrix} N_i & 1 & N_j \\ -K_j & 0 & K_j \end{pmatrix} \begin{Bmatrix} N_i & S & J \\ S & N_j & 1 \end{Bmatrix}.
\end{aligned} \tag{2.190}$$

The quantity in the parentheses is a 3j-symbol (Ref. [13]) and the quantity in curly braces is a 6j-symbol (Ref. [13]). The function $A_{SO}(\tau)$ represents the spin-orbit interaction constant calculated with $ab\ initio$ theory.

The term $X_{\eta_i\eta_j}$ in the equation (2.189) is given as follows; when $\eta_i = \eta_j$

$$X_{aa} = -X_{bb} = -2\sin(\tau)\cos(\tau) = -\sin 2\tau \tag{2.191}$$

whereas $\eta_i \neq \eta_j$

$$X_{ab} = X_{ba} = -\cos^2(\tau) + \sin^2(\tau) = -\cos 2\tau \tag{2.192}$$

## 2.4 Diagonalization of the Hamiltonian

From equations (2.132) and (2.61), we know that by diagonalizing Hamiltonian matrix $\mathbf{H}^{\mathbf{J},\mathbf{M_J},\mathbf{S},\mathbf{\Gamma}_{\mathrm{rve}}}$ in equation (2.133), we obtain the energy levels $E$ with the associated eigenvector coefficients $c^{J,M_J,S,\Gamma_{\mathrm{rve}}}_{\eta,N,K,v_2^{\eta,\Gamma_{\mathrm{vib}}},N_r,N_R}$ defining the wavefunction as a linear combination of basis functions. We diagonalize the total Hamiltonian matrix in two steps. The first step is called $K$-block diagonalization, and the second step is called $J$-block diagonalization.

### 2.4.1 $K$-block diagonalization

For the $K$-block diagonalization we include the Hamiltonian matrix elements which have non-zero values when $\Delta K = 0$ and $\Delta N = 0$. The term from $\hat{H_{nk}}$ has non-zero elements when $\Delta K = 0$ and $\Delta N = 0$, but we do not include this term in the $K$-block diagonalization since it changes its value with the quantum number $N$. Thus for the $K$-block diagonalization, we collect the terms from $\hat{H}_e$, $\hat{H}_{PrR}$, $\hat{H}_b$, $\hat{H}_{ba}$ and $\hat{H}_{bb}$, then diagonalize the resulting matrix block using the LAPACK library [18].

$$\mathbf{H}^{\mathbf{K},\mathbf{\Gamma}_{\mathrm{vib}},\eta}_{\mathbf{ij}} = \langle N_{R_i}|\langle N_{r_i}|\langle v_{2_i}^{\eta_i}, K_i, \Gamma_{\mathrm{vib}}|\langle \eta_i; N, J, S, K, M_J, p|$$

$$\left\{\hat{H}_e + \hat{H}_{PrR} + \hat{H}_b + \hat{H}_{ba} + \hat{H}_{bb}\right\} |N_{R_j}\rangle |N_{r_j}\rangle |v_{2_j}^{\eta_j}, K, \Gamma_{\rm vib}\rangle |\eta_j; N, J, S, K, M_J, p\rangle \tag{2.193}$$

For each $K$ quantum number with $\Gamma_{\rm vib}$, we prepare 1, 2 or 4 set of eigenvalues and eigenfunctions depending on $K = 0$ or $K \neq 0$, and ABC- or ABB-type molecule.

In case of an ABC-type molecule, as we can see from Table 2.3, when $K = 0$, we need the $K$-block just with $\eta = a$ or $\eta = b$ states depending on whether the $N$ quantum number is even or odd. Thus we need to prepare the $K$-block for each $\eta = a$ and $\eta = b$ state separately when $K = 0$, but when $K \neq 0$ we do not need to separate this block into two sub-blocks.

In case of an ABB-type molecule, as we can see from Table 2.7, when $K \neq 0$, we need to separate the $K$-block into $\Gamma_{\rm vib} = A_1$ states and $\Gamma_{\rm vib} = B_2$ states. Further, when $K = 0$, we need to separate the $K$-block into $\Gamma_{\rm vib} = A_1$ states with $\eta = a$ states, $\Gamma_{\rm vib} = A_1$ states with $\eta = b$ states, $\Gamma_{\rm vib} = B_2$ states with $\eta = a$ states, and $\Gamma_{\rm vib} = B_2$ states with $\eta = b$ states.

The dimension $nmax$ of each $K$-block $\mathbf{H_{ij}^{K,\Gamma_{vib},\eta}}$ depends not only on whether $K = 0$ or $K \neq 0$ in the case of ABC- or ABB-type molecules, but also on the chosen size of the bending and stretching basis sets. We denote the number of basis functions for $r$-, $R$-, stretching basis set as $nmaxr$, $nmaxR$ , respectively; the bending basis set for $\eta = a$ and $\eta = b$ has the $nmaxba$ and $nmaxbb$ functions, respectively.

In case of an ABC-type molecule, when $K \neq 0$, $nmax$ is calculated as

$$nmax_{(K\neq 0)} = nmaxr \times nmaxR \times (nmaxba + nmaxbb)\,. \tag{2.194}$$

When $K = 0$, with $\eta = a$ state we have

$$nmax_{(K=0,\eta=a)} = nmaxr \times nmaxR \times nmaxba. \tag{2.195}$$

When $K = 0$, with $\eta = b$ state:

$$nmax_{(K=0,\eta=b)} = nmaxr \times nmaxR \times nmaxbb. \tag{2.196}$$

The numbers of $A_1$ and $B_2$ state bending basis functions in each $\eta$ state, $nmaxb\eta A_1$ and $nmaxb\eta B_2$, respectively, are given by the following relation

$$nmaxb\eta A_1 = nmaxb\eta B_2 + n \quad (n = 0 or 1) \tag{2.197}$$

For an ABB-type molecule, we have different expressions for $nmax$ depending on $K$, $\Gamma_{\rm vib}$ and $\eta$. For $K \neq 0$ and $\Gamma_{\rm vib} = A_1$ we obtain

$$nmax_{(K\neq 0,\Gamma_{\rm vib}=A_1)} = nmaxr \times nmaxR \times (nmaxbaA_1 + nmaxbbA_1)\,. \tag{2.198}$$

$K \neq 0$ and $\Gamma_{\rm vib} = B_2$

$$nmax_{(K\neq 0,\Gamma_{\rm vib}=B_2)} = nmaxr \times nmaxR \times (nmaxbaB_2 + nmaxbbB_2)\,. \tag{2.199}$$

$K = 0$, $\eta = a$ and $\Gamma_{\rm vib} = A_1$

$$nmax_{(K=0,\eta=a,\Gamma_{\rm vib}=A_1)} = nmaxr \times nmaxR \times nmaxbaA_1. \tag{2.200}$$

$K = 0$, with $\eta = a$ and $\Gamma_{\rm vib} = B_2$

$$nmax_{(K=0,\eta=a,\Gamma_{\rm vib}=B_2)} = nmaxr \times nmaxR \times nmaxbaB_2. \tag{2.201}$$

$K = 0$, with $\eta = b$ and $\Gamma_{\rm vib} = A_1$

$$nmax_{(K=0,\eta=b,\Gamma_{\rm vib}=A_1)} = nmaxr \times nmaxR \times nmaxbbA_1. \tag{2.202}$$

$K = 0$, with $\eta = b$ and $\Gamma_{\rm vib} = B_2$

$$nmax_{(K=0,\eta=b,\Gamma_{\rm vib}=B_2)} = nmaxr \times nmaxR \times nmaxbbB_2. \tag{2.203}$$

We set a contraction energy limit before the $J$-block diagonalization. We select those wavefunctions from the $K$-block diagonalization whose energies are lower than the contraction energy limit. The number of eigenvalues selected for each $K$ and $\Gamma_{\rm vib}$ state is called $nmaxk(K, \Gamma_{\rm vib}, \eta)$; We save the corresponding eigenvectors as a matrix $\mathbf{C}^{\mathbf{K},\mathbf{\Gamma}_{\rm vib},\eta}$. The dimension of the matrix $\mathbf{C}^{\mathbf{K},\mathbf{\Gamma}_{\rm vib},\eta}$ is $nmax \times nmaxk(K, \Gamma_{\rm vib}, \eta)$

### 2.4.2 $J$-block diagonalization

Now we move on to the $J$-block diagonalization. We collect the terms for the $J$-block diagonalization in the Hamiltonian matrix $\mathbf{H}^{\mathbf{J},\mathbf{M_J},\mathbf{S},\mathbf{\Gamma}_{\rm rve}}$. For the terms with $\Delta K = 0$ and $\Delta N = 0$ we just need to add the Hamiltonian matrix elements from $\hat{H}_{SO}$ and $\hat{H}_{nk}$ to the $K$-block Hamiltonian matrix $\mathbf{H}^{\mathbf{K},\mathbf{\Gamma}{\rm vib},\eta}$ which we have already prepared. We have terms with $\Delta K = 0$ and $\Delta N = 1$; these terms only come from the Hamiltonian operator $\hat{H}_{SO}$. We have terms with $\Delta K = 1$ and $\Delta N = 0$; these terms originate in the Hamiltonian operator $\hat{H}_{dk}$ only.

For each $K_iN_i$ and $K_jN_j$ block in $\mathbf{H}^{\mathbf{J},\mathbf{M_J},\mathbf{S},\mathbf{\Gamma}_{\rm rve}}$, we multiply by the matrix $\mathbf{C}^{\mathbf{K},\mathbf{\Gamma}_{\rm vib},\eta}$ to have the contracted final Hamiltonian matrix $\mathbf{Hc}^{\mathbf{J},\mathbf{M_J},\mathbf{S},\mathbf{\Gamma}_{\rm rve}}$ as

$$\mathbf{Hc}^{\mathbf{J},\mathbf{M_J},\mathbf{S},\mathbf{\Gamma}_{\rm rve}}_{\mathbf{K_iN_i},\mathbf{K_jN_j}} = (\mathbf{C}^{\mathbf{K_i},\mathbf{\Gamma}_{\mathbf{vib_i}},\eta_{\mathbf{i}}})^{-1}\mathbf{H}^{\mathbf{J},\mathbf{M_J},\mathbf{S},\mathbf{\Gamma}_{\rm rve}}_{\mathbf{K_iN_i},\mathbf{K_jN_j}}\mathbf{C}^{\mathbf{K_j},\mathbf{\Gamma}_{\mathbf{vib_j}},\eta_{\mathbf{j}}}. \tag{2.204}$$

The dimension of the contracted final Hamiltonian matrix block $\mathbf{Hc}^{\mathbf{J},\mathbf{M_J},\mathbf{S},\mathbf{\Gamma}_{\rm rve}}_{\mathbf{K_iN_i},\mathbf{K_jN_j}}$ is $nmaxk(K_i,\Gamma_{vib_i},\eta_i) \times nmaxk(K_j,\Gamma_{vib_j},\eta_j)$ thus we can reduce the memory use in the $J$-block diagonalization.

We diagonalize the contracted $J$-block Hamiltonian matrix $\mathbf{Hc}^{\mathbf{J},\mathbf{M_J},\mathbf{S},\mathbf{\Gamma}_{\rm rve}}$ with LAPACK routines [18]. The calculated eigenvalues correspond to the energy levels $E$ of the total Hamiltonian, and the calculated eigencoefficients for an energy level $E_i$ correspond to the $i$th column of the coefficient matrix $\mathbf{C}^{\mathbf{J},\mathbf{M_J},\mathbf{S},\mathbf{\Gamma}_{\rm rve}}_{\mathbf{i}}$. The relation between $\mathbf{C}^{\mathbf{K},\mathbf{\Gamma}_{\rm vib},\eta}$ and $\mathbf{C}^{\mathbf{J},\mathbf{M_J},\mathbf{S},\mathbf{\Gamma}_{\rm rve}}_{\mathbf{i}}$ with the coefficients for the total basis set (Eq. (2.61)) on $i$ th energy level is as follows:

$$\begin{aligned}
\Psi_i^{J,M_J,S,\Gamma_{\rm rve}} &= \sum_{N=|J-S|}^{J+S}\sum_{K=0}^{N}\sum_{\Gamma_{\rm rve},N_r,N_R,\eta,v_2^\eta} C^{J,M_J,S,\Gamma_{\rm rve}}_{\eta,N,K,v_2^{\eta,\Gamma_{\rm vib}},N_r,N_R} \\
&\quad \times|N_R,\Gamma_R\rangle|N_r,\Gamma_r\rangle|v_2^\eta,K,\Gamma_{v_2^\eta}\rangle\eta;N,J,S,K,M_J,p\rangle \\
&= \sum_{N}\sum_{K=0}^{N}\sum_{\Gamma_{\rm vib},\eta} C^{J,M_J,S,\Gamma{\rm rve}}_{i,g}\sum_{q} C^{K,\Gamma_{\rm vib},\eta}_{g,q} \\
&\quad \times|N_R,\Gamma_R\rangle|N_r,\Gamma_r\rangle|v_2^\eta,K,\Gamma_{v_2^\eta}\rangle|\eta;N,J,S,K,M_J,p\rangle
\end{aligned} \tag{2.205}$$

$$c^{J,M_J,S,\Gamma_{\rm rve}}_{\eta,N,K,v_2^{\eta,\Gamma_{\rm vib}},N_r,N_R} = \sum_{K=0}^{N}\sum_{\Gamma_{\rm vib},\eta}\sum_{q} C^{J,M_J,S,\Gamma{\rm rve}}_{i,g} C^{K,\Gamma_{\rm vib},\eta}_{g,q} \tag{2.206}$$

Here $q$ represent the labels for $K$-block matrix $\eta, v_2^{\eta,\Gamma_{\rm vib}}, N_r$ and $N_R$. $g$ represent the labels of the $g$th energy from the $K$-block matrix and comprises the lavels of $K, \Gamma_{\rm vib}, \eta$ and $N$.

## 2.5 What do we do with the eigenvalues and eigenfunctions?

In spectroscopy, we assign quantum numbers to each vibronic energy level. We can annotate a vibronic energy level with stretching and bending quantum numbers. From these quantum numbers, we have some idea of the "origin" of the energy levels. The resulting eigenvalues, which are the resulting energy levels, each has a corresponding eigenfunction. To annotate an energy level, we find the biggest coefficient $c^{J,M_J,S,\Gamma_{\rm rve}}_{\eta,N,K,v_2^{\eta,\Gamma_{\rm vib}},N_r,N_R}$ of equation (2.61). The $v_2^{\eta}, N_r, N_R, \Gamma_{\rm vib}$ derived from this coefficient will relate to the notation for the vibration quantum numbers. With $N$ and $K$, we can label rotational quantum numbers. The way we have different quantum numbers for linear molecules and bent molecules. We will explain the notation for the bent molecule and then we detail that for the linear molecule.

The wavefunction can be used not only for annotating energy levels but to get further insight into the nature of the double-Renner interaction. We compute probability density functions for visualizing the wavefunctions and this will be explained in the last part of this section.

### 2.5.1 Assignment and notation for bent molecules

The notation for stretching and bending vibrational quantum numbers is very straightforward in this case. $N_r$ corresponds to the principal $r$ bond stretching motion quantum number, $N_R$ corresponds to the principal $R$ bond stretching motion quantum number,

$\Gamma_{\rm vib}$ corresponds to the symmetry of the bending basis functions, and $v_2^\eta$ is the quantum number for bending motion. $\eta$ shows the dominant electronic state for the energy level. When the molecule is in the high energy region, or when the molecule has other energy levels fairly close (resonance) it always becomes difficult to define a set of quantum numbers for an energy state. The energy state has significant contribution from two or more basis states. If one energy state has ca. 90% (or more) contribution from one dominant coefficient, we can easily define the quantum number.

The quantum numbers for rotational state are not as straightforward as for the vibrational state. The quantum number $K$ corresponds to the rotational quantum number $K_a$. However, in the case of a bent molecule we also need $K_c$. We have to consider the asymmetric-top labels of rotational states.

We take as example an ABB-type bent molecule here. We say our ABB-type molecule has the moments of inertia in the order $I_{zz} \leq I_{yy} \leq I_{xx}$. The $a$-, $b$-, and $c$-axes of asymmetric molecule are defined so that $I_{aa} \leq I_{bb} \leq I_{cc}$. In case of a symmetric top molecule a molecule with $(I_{aa} <) I_{bb} = I_{cc}$ is called a prolate type molecule and a molecule with $I_{aa} = I_{bb} (< I_{cc})$ is called an oblate type molecule. We define that a prolate type molecule has a $I^r$ basis and an oblate type molecule has a $III^r$ basis. To assign rotational quantum number in an asymmetric top molecule, we first need to think of two extreme cases, which are the oblate and the prolate type molecule's rotational quantum numbers. When the ABB-type molecule has $I^r$ basis, the $x$-, $y$-, $z$- axes will correlate as $xyz = bca$ when it has $III^r$ basis, the $x$-, $y$-, $z$- axes will correlate as $xyz = abc$.

We now derive the equivalent rotations (See section 12.1 of Ref. [12]) for the operations in $C_{2\rm v}(\rm M)$, the molecular symmetry group of the molecule ABB (See Table 2.4). When we carry of the operation $(12)$, this corresponds to a 180° rotation of the molecule-fixed axes about the $b$ axis (See Fig. 2.2). We call this rotation $R_b^\pi$. The identity operation $E$ changes nothing; we call the corresponding rotation $R_0$. Table 2.8

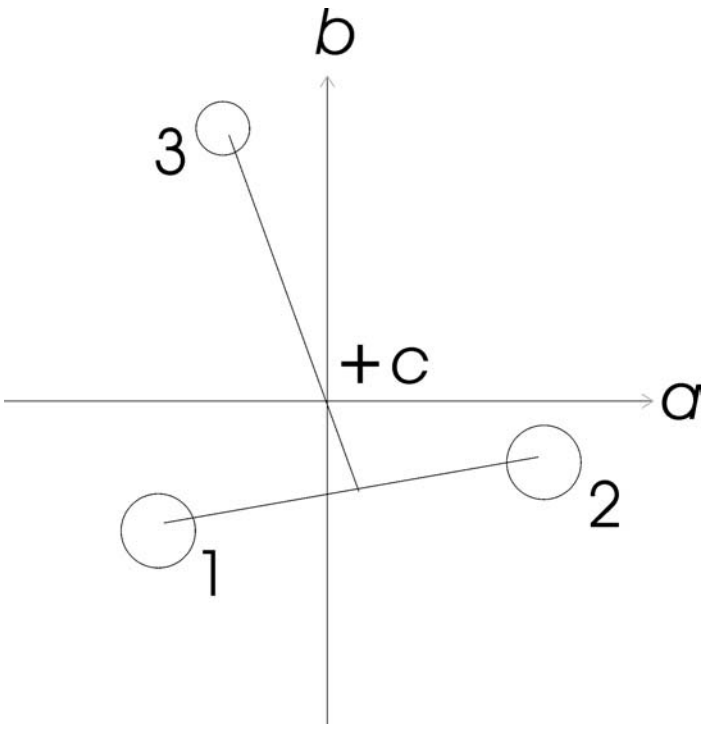


Figure 2.2: The ABB molecule with molecular fixed coordinate system. Nuclei 1 and 2 correspond to nucleus B of the ABB molecule, and nucleus 3 corresponds to the nucleus A. The $a$ axes points from nucleus 1 to nucleus 2. The $b$ axes points from nucleus 1 and 2 to nucleus 3. The $c$ axis points out of the plane of paper, so that it makes a right handed coordinate system.

summarizes all the identifications of $C_{2v}(\mathrm{M})$ symmetry elements with respect to the axes $a$, $b$ and $c$ in Fig. 2.2. As mentioned before, a prolate molecule has $I^r$ basis, where the $xyz$ axes correspond to the $bca$ axes of an ABB-type molecule. An oblate molecule has a $III^r$ basis, where the $xyz$ axes correspond to the $abc$ axes of an ABB-type molecule. Thus we can define the identification of the $C_{2v}(\mathrm{M})$ symmetry elements in terms of the axes $x$, $y$ and $z$ of the prolate and oblate molecules. These relations are also summarized in Table 2.8.

We know that the rotational wavefunctions of the molecule ABB in a $I^r$ basis are linear combinations of symmetric top rotational wavefunctions $|N, K_a, M\rangle$, and in a

Table 2.8: The identification of the symmetry elements of MS group $C_{2v}(M)$.

| $C_{2v}(M)$ : | $E$ | $(12)$ | $E^*$ | $(12)^*$ | |
|---|---|---|---|---|---|
| $a$-, $b$-, $c$ axis of molecule ABB : | $R_0$ | $R_b^\pi$ | $R_c^\pi$ | $R_a^\pi$ | |
| Corresponding $x$-, $y$-, $z$ axis of prolate molecule in molecule ABB : | $R_0$ | $R_x^\pi$ | $R_y^\pi$ | $R_z^\pi$ | $I^r$ basis |
| Corresponding $x$-, $y$-, $z$- axis of oblate molecule in molecule ABB : | $R_0$ | $R_y^\pi$ | $R_z^\pi$ | $R_x^\pi$ | $III^r$ basis |

$III^r$ basis they are linear combinations of symmetric top rotational wavefunctions $|N, K_c, M\rangle$. The effect of the operation $R_\alpha^\pi$ on a rotational wavefunction $|N, K, M\rangle$ is well known.[2] We can calculate the representation generated by the function $|N, K_a, M\rangle$ for each $K_a$ and the result is summarized in Table 2.9. From Table 2.9, we know that the symmetry of a rotational function is $A_1$ when $K_a$ and $K_c$ are both even, it will be $A_2$ when $K_a$ and $K_c$ are both odd, it will be $B_1$ when $K_a$ is even and $K_c$ is odd, and it will be $B_2$ when $K_a$ is odd and $K_c$ is even. (This is summarized in Table 2.10. )

We know that $K_a + K_c = N$ or $N + 1$. Thus if one knows the symmetry label of a rotational function, with quantum number $N$ and $K = K_a$, one can assign the quantum number $K_c$ using the relation between $K_a$ and $K_c$ and the symmetry labelling ( Table 2.10).

The symmetry label of the energy level is $\Gamma_{\text{rve}}$. $\Gamma_{\text{rve}}$ has a contribution from the electronic state symmetry, the symmetry of vibrational function, and the symmetry of the rotational function. We have included the contribution from the electronic symmetry, and the symmetry of vibrational function to the relation summarized in Table 2.10, and constructed Table 2.11. With Table 2.11, one can assign $K_c$ from $N$, $K_a$ and the symmetry of electronic state $\Gamma_e$, $\Gamma_{\text{vib}}$ and $\Gamma_{\text{rve}}$.

[2]See Ref. [12], Section 12.2. These relations are summarized with explanation in equations (12-36) to (12-47)

Table 2.9: Representation of the $C_{2v}$(M) group for a molecule ABB generated by the basis functions $|N, K_a, M\rangle$ and $|N, K_c, M\rangle$ .

| $K_a$ | | $\Gamma_{rot}$ | $K_c$ | | $\Gamma_{rot}$ |
|---|---|---|---|---|---|
| 0 | $N$ even | $A_1$ | 0 | $N$ even | $A_1$ |
| 0 | $N$ odd | $B_1$ | 0 | $N$ odd | $B_2$ |
| odd | | $A_2 + B_2$ | odd | | $A_2 + B_1$ |
| even | | $A_1 + B_1$ | even | | $A_1 + B_2$ |

Table 2.10: Symmetry species of rotational functions of a molecule ABB.

| $K_aK_c$ | $\Gamma_{rot}$ | $K_aK_c$ | $\Gamma_{rot}$ |
|---|---|---|---|
| ee | $A_1$ | oo | $A_2$ |
| eo | $B_1$ | oe | $B_2$ |

"ee" corresponds to $K_aK_c$ being both even, and "oo" corresponds to $K_aK_c$ being both odd. "eo" corresponds to $K_a$ even and $K_c$ odd. "oe" corresponds to $K_c$ even and $K_a$ odd.

Table 2.11: Symmetry species of $\Gamma_{\rm rve}$ of a molecule ABB, with $\Gamma_e$ and $\Gamma_{\rm vib}$.

| | $\Gamma_e$ | $A_1$ | $A_1$ | $B_1$ | $B_1$ |
|---|---|---|---|---|---|
| | $\Gamma_{\rm vib}$ | $A_1$ | $B_2$ | $A_1$ | $B_2$ |
| $\Gamma_{\rm rve}$ | | $K_aK_c$ | $K_aK_c$ | $K_aK_c$ | $K_aK_c$ |
| $A_1$ | | ee | oe | eo | oo |
| $A_2$ | | oo | eo | oe | ee |
| $B_1$ | | eo | oo | ee | oe |
| $B_2$ | | oe | ee | oo | eo |

"ee" corresponds to $K_aK_c$ being both even, and "oo" corresponds to $K_aK_c$ being both odd. "eo" corresponds to $K_a$ even and $K_c$ odd. "oe" corresponds to $K_c$ even and $K_a$ odd.

### 2.5.2 Assignment and Notation for linear molecule

The notation for stretching vibrations and rotational quantum numbers is very straightforward in this case. $N_r$ corresponds to the $r$ stretching and quantum number, $N_R$ to the $R$ stretching quantum number and the quantum number $N$ is the rotational quantum number.

In a linear molecule, we have the angular momentum quantum number for bending vibration $l$. The quantum number $l = K$. $v_2^\eta$ is the quantum number for bending motion, but this is in "bent" molecule notation (see also Eq. (13-177) of Ref. [12]). The definition of the linear molecule's bending quantum number $v_2^{\mathrm{lin},\eta}$ has to take into account the angular momentum quantum number for bending vibration $l$, and it is defined as

$$v_2^{\mathrm{lin,eta}} = 2v_2^\eta + |K \mp \Lambda|. \tag{2.207}$$

We have the $\Lambda$ term since we have Renner effect. The minus sign corresponds to the lower electronic surface and the plus sign corresponds to the upper electronic surface. The linear molecule's each vibronic energy levels are labeled by labels $\Sigma$, $\Pi$, $\Delta$, ... each corresponding to the $K$ quantum value 0, 1, 2, .... The projection of the electron spin onto the molecule-fixed $a$ axis is defined as quantum number $P = |K + \Sigma|$, where $\Sigma = \pm 1/2$. Thus each vibronic state will have notations as $\Sigma_P$, $\Pi_P$,$\Delta_P$ ... There are some states which have same notation as for example $\Sigma_{1/2}$ with same vibrational quantum number set. Here, a state with lower energy is called a $\mu$ state, and a state with higher energy is called a $\kappa$ state [19]. An example is the states $(v_1, v_2^{\mathrm{lin}}, v_3)$ with $v_2^{\mathrm{lin}}$ odd. Each of these states has two sub-states of $\Sigma_P$ vibronic symmetry. The lower sub-state of the $\Sigma_P$ vibronic symmetry is called $\mu\Sigma_P$ state and the upper sub-state of the $\Sigma_P$ vibronic symmetry is called the $\kappa\Sigma_P$ state. Similarly, a state with an even value of $v_2^{\mathrm{lin}} > 0$ has two sub-states of $\Pi_P$ vibronic symmetry. The lower sub-state is called $\mu\Pi_P$ and the upper sub-state is called $\kappa\Pi_P$.

For a molecule in a doublet state, each vibronic state can have very small splitting.

We have the $e$ and $f$ labels for this splitting and it is defined so that an $e$ state has the parity $+(-1)^{J-1/2}$ and an $f$ state has the parity $-(-1)^{J-1/2}$ [12, 20].

### 2.5.3 Probability density functions

It is very interesting to visualize the wavefunction in order to "understand" the molecule by means of quantum mechanics. We can plot rotation-bending-electronic wavefunction squares in two dimensional view or three dimensional view, by integrating out some coordinates in the wavefunction squares.

The normalized probability density function $f(\tau)$ is defined so that the differential probability $dp$ of finding the molecule with the bending coordinate in the infinitesimal interval between $\tau$ and $\tau$ + $d\rho$ is given by

$$dp = f(\tau)\, d\tau, \tag{2.208}$$

where the volume element used for normalizing the function in equation (2.61) is choosen so that

$$f(\tau) \;=\; \int_0^\infty dr \int_0^\infty dR \int_{\mathrm{rot,e,es}} dV \times |\Psi_{\mathrm{rve}}^{J,M_J,S,\Gamma_{\mathrm{rve}}}|^2, \tag{2.209}$$

where $dV$ is the volume element associated with integration over the coordinates describing rotation, electronic orbital motion, and electron spin. With equation (2.61) the equation (2.209) can be written as follows.

$$\begin{aligned} f(\tau) \;=\; & \sum_{N=|J-S|}^{J+S} \sum_{K=0}^{N} \sum_{N_r,N_R,\eta} \sum_{\Gamma_{\mathrm{vib}},v_2^\eta} \int_0^\infty dr \int_0^\infty dR \int_{\mathrm{rot,e,es}} dV \;\; c^{J,M_J,S,\Gamma_{\mathrm{rve}}}_{\eta,N,K,v_2^{\eta,\Gamma_{\mathrm{vib}}},N_r,N_R} \\ & \times \{|N_R,\Gamma_R\rangle |N_r,\Gamma_r\rangle |v_2^\eta,K,\Gamma_{v_2^\eta}\rangle |\eta;N,J,S,K,M_J,p\rangle\}^2 \\ = \; & \sum_{N=|J-S|}^{J+S} \sum_{K=0}^{N} \sum_{N_r,N_R,} \sum_{v_{2_i}^{\eta,\Gamma_{\mathrm{vib}}}} \sum_{v_{2_j}^{\eta,\Gamma_{\mathrm{vib}}}} \\ & c^{J,M_J,S,\Gamma_{\mathrm{rve}}}_{\eta,N,K,v_{2_i}^{\eta,\Gamma_{\mathrm{vib}}},N_r,N_R} \;\; c^{J,M_J,S,\Gamma_{\mathrm{rve}}}_{\eta,N,K,v_{2_j}^{\eta,\Gamma_{\mathrm{vib}}},N_r,N_R} \times \phi_{v_{2_i}^{\eta,\Gamma_{\mathrm{vib}}}}(\tau) \;\; \phi_{v_{2_j}^{\eta,\Gamma_{\mathrm{vib}}}}(\tau) \end{aligned} \tag{2.210}$$

The two-dimensional probability density function is defined analogously.

$$\begin{aligned} f(r,\tau) &= \int_0^\infty dR \int_{\mathrm{rot,e,es}} dV \times |\Psi_{\mathrm{rve}}^{J,M_J,S,\Gamma_{\mathrm{rve}}}|^2, \\ &= \sum_{N=|J-S|}^{J+S} \sum_{K=0}^{N} \sum_{N_R,} \sum_{N_{r_i}} \sum_{N_{r_j}} \sum_{v_{2_i}^{\eta,\Gamma_{\mathrm{vib}}}} \sum_{v_{2_j}^{\eta,\Gamma_{\mathrm{vib}}}} \\ &\quad c_{\eta,N,K,v_{2_i}^{\eta,\Gamma_{\mathrm{vib}}},N_{r_i},N_R}^{J,M_J,S,\Gamma_{\mathrm{rve}}} \quad c_{\eta,N,K,v_{2_j}^{\eta,\Gamma_{\mathrm{vib}}},N_{r_j},N_R}^{J,M_J,S,\Gamma_{\mathrm{rve}}} \\ &\quad \times \phi_{N_{r_i}}(r) \;\; \phi_{N_{r_j}}(r) \;\; \phi_{v_{2_i}^{\eta,\Gamma_{\mathrm{vib}}}}(\tau) \;\; \phi_{v_{2_j}^{\eta,\Gamma_{\mathrm{vib}}}}(\tau) \end{aligned} \tag{2.211}$$

To provide further insight into the nature of the double-Renner interaction, we have also calculated partial probability density functions. We project the total wavefunction $\Psi_{\mathrm{rve}}^{J,M_J,S,\Gamma_{\mathrm{rve}}}$ onto each electronic surfaces.

$$f_\sigma(\tau) = \int_0^\infty dr \int_0^\infty dR \int_{\mathrm{rot}} dV' \times \left| \left\langle \psi_e^{(\sigma)} | \Psi_{\mathrm{rve}}^{J,M_J,S,\Gamma_{\mathrm{rve}}} \right\rangle_{\mathrm{e}} \right|^2, \tag{2.212}$$

where $\sigma = -$ or $+$ and $dV'$ is the volume element associated with integration over the coordinates describing rotation end electronic spin. The subscript 'e' on the integrand matrix element signifies that in this matrix element, integration is over the electronic coordinates (describing electronic orbital motion) only. $f_\sigma(\tau)\, d\tau$, $\sigma = -$ or $+$, is the differential probability of finding the molecule in the Born-Oppenheimer electronic state $\psi_e^{(\sigma)}$ with its bending coordinate between $\tau$ and $\tau$ + $d\tau$. $f_-(\tau)$ and $f_+(\tau)$ can measure the extent of the mixing of the two electronic states $\psi_e^{(-)}$ and $\psi_e^{(+)}$ in the wavefunction $\Psi_{\mathrm{rve}}^{J,M_J,S,\Gamma_{\mathrm{rve}}}$ at a given value of $\tau$, and we have

$$f(\tau) = f_-(\tau) + f_+(\tau). \tag{2.213}$$

The over-all probability of finding the molecule with wavefunction $\Psi_{\mathrm{rve}}^{J,M_J,S,\Gamma_{\mathrm{rve}}}$ in the Born-Oppenheimer electronic state $\psi_e^{(\sigma)}$, $\sigma = -$ or $+$, is

$$P_\sigma = \int_0^\pi f_\sigma(\tau)\, d\tau \tag{2.214}$$

with $P_- + P_+ = 1$.

With equations (2.61), (2.87), (2.120) and (2.121), equation (2.212) can be rewritten as follows.

$$
\begin{aligned}
f_-(\tau) \;=\; & \sum_{N=|J-S|}^{J+S} \sum_{K=0}^{N} \sum_{N_r,N_R} \sum_{\eta_i} \sum_{\eta_j} \sum_{v_{2_i}^{\eta_i,\Gamma_{\rm vib}}} \sum_{v_{2_j}^{\eta_j,\Gamma_{\rm vib}}} c^{J,M_J,S,\Gamma_{\rm rve}}_{\eta,N,K,v_{2_i}^{\eta_i,\Gamma_{\rm vib}},N_r,N_R} c^{J,M_J,S,\Gamma_{\rm rve}}_{\eta,N,K,v_{2_j}^{\eta_j,\Gamma_{\rm vib}},N_r,N_R} \\
& \times\{C_K^2 \phi_{v_{2_i}^{\eta=a,\Gamma_{\rm vib}}}(\tau)\phi_{v_{2_j}^{\eta=a,\Gamma_{\rm vib}}}(\tau) + C_K S_K(\phi_{v_{2_i}^{\eta=a,\Gamma_{\rm vib}}}(\tau)\phi_{v_{2_j}^{\eta=b,\Gamma_{\rm vib}}}(\tau) \\
& + \phi_{v_{2_i}^{\eta=b,\Gamma_{\rm vib}}}(\tau)\phi_{v_{2_j}^{\eta=a,\Gamma_{\rm vib}}}(\tau)) + S_K^2 \phi_{v_{2_i}^{\eta=b,\Gamma_{\rm vib}}}(\tau)\phi_{v_{2_j}^{\eta=b,\Gamma_{\rm vib}}}(\tau)\} \qquad (2.215)
\end{aligned}
$$

$$
\begin{aligned}
f_+(\tau) \;=\; & \sum_{N=|J-S|}^{J+S} \sum_{K=0}^{N} \sum_{N_r,N_R} \sum_{\eta_i} \sum_{\eta_j} \sum_{v_{2_i}^{\eta_i,\Gamma_{\rm vib}}} \sum_{v_{2_j}^{\eta_j,\Gamma_{\rm vib}}} c^{J,M_J,S,\Gamma_{\rm rve}}_{\eta,N,K,v_{2_i}^{\eta_i,\Gamma_{\rm vib}},N_r,N_R} c^{J,M_J,S,\Gamma_{\rm rve}}_{\eta,N,K,v_{2_j}^{\eta_j,\Gamma_{\rm vib}},N_r,N_R} \\
& \times\{S_K^2 \phi_{v_{2_i}^{\eta=a,\Gamma_{\rm vib}}}(\tau)\phi_{v_{2_j}^{\eta=a,\Gamma_{\rm vib}}}(\tau) - C_K S_K(\phi_{v_{2_i}^{\eta=a,\Gamma_{\rm vib}}}(\tau)\phi_{v_{2_j}^{\eta=b,\Gamma_{\rm vib}}}(\tau) \\
& + \phi_{v_{2_i}^{\eta=b,\Gamma_{\rm vib}}}(\tau)\phi_{v_{2_j}^{\eta=a,\Gamma_{\rm vib}}}(\tau)) + C_K^2 \phi_{v_{2_i}^{\eta=b,\Gamma_{\rm vib}}}(\tau)\phi_{v_{2_j}^{\eta=b,\Gamma_{\rm vib}}}(\tau)\} \qquad (2.216)
\end{aligned}
$$

# Chapter 3

# The program DR

In this chapter we discuss the program DR. The program DR is written in Fortran 90. The program first constructs basis set functions according to the parameters given in the input file. Then it calculates the Hamiltonian matrix elements for each $K$-block matrix and constructs the $K$-block matrix. The $K$-block matrices are diagonalized using LAPACK routines [18], and after diagonalizing a sufficient number of the $K$-blocks, it constructs the $J$-block matrix. The $J$-block matrix is also diagonalized using LAPACK routines [18]. The eigenvalues obtained from the $J$-block matrix diagonalization will be the solution of the Schrödinger equation for the Double Renner system.

## 3.1 Basic definition of the system

The input requires following definitions for the system.

- **MASSES**: The atomic massis for atoms B, C and A of the system in atomic mass units.
- **LAMBDA**: The electronic angular momentum of the system. If the system has $\Pi$ electronic state at linear geometry, it is 1. $\Delta$ corresponds to $\lambda = 2$, etc.

- **MULTI**: The spin multiplicity minus one. If doublet, it is 1.
- **XSO**: The spin-orbit interaction constant.
- **ZNORENNER**: Performs calculation with Renner effect or without Renner effect. "T" (True) for the calculation with Renner effect, "F" (False) for the calculation without Renner effect, with one Born-Oppenheimer surface.
- **ZABB**: Defines if the molecule is ABC-type or ABB-type. "T" for ABB-type molecule, "F" for ABC-type molecule.
- **MAXJ**: The number of $K$-blocks to be produced. This also defines the number of $J$-blocks we can calculate from the $K$-blocks. If MULTI is odd, the $J$-block starts from $J = 1/2$ and ends at $J = MAXJ - S/2$, and if MULTI is even, the $J$-block starts from $J = 0$ and ends at $J = MAXJ - S$.

## 3.2 Construction of the stretching basis functions

The input for constructing stretching basis function requires following parameters.

- **RE1**: The equilibrium distance for the BC moiety, in Bohr.
- **DISS1**: The dissociation energy for the BC moiety, in Hartree.
- **WE1**: The harmonic frequency for the BC moiety, in Hartree.
- **RE2**: The equilibrium distance from the atom A to the BC moiety, in Bohr.
- **DISS2**: The dissociation energy from the atom A to the BC moiety, in Hartree.
- **WE2**: The harmonic frequency from the atom A to the BC moiety, in Hartree.
- **NPNT1**: The number of integration points for the BC moiety.
- **NMAX1**: The maximum quantum number for the basis set for the BC moiety.

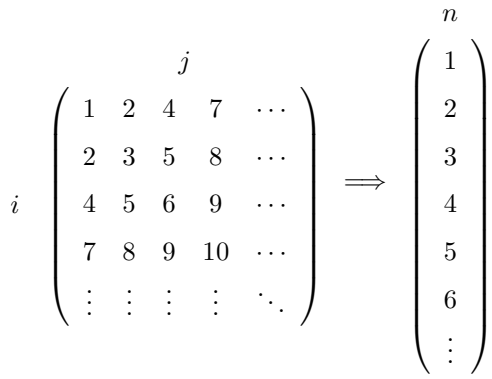


Figure 3.1: A symmetry matrix element $(i, j)$ are saved in n th vector element.

- $\mathbf{NPNT2}$: The number of integration points for the distance from the atom A to the BC moiety.
- $\mathbf{NMAX2}$: The maximum quantum number for the basis set for the A-(BC) stretching.

The stretching basis functions are constructed using these parameters, with the method described in Chapter 2.2. Kinetic energy elements $\langle N_{R_i}|\frac{\hat{P}_R^2}{2\mu_R}|N_{R_j}\rangle$ and $\langle N_{r_i}|\frac{\hat{P}_r^2}{2\mu_r}|N_{r_j}\rangle$ are stored in vector $\mathbf{HBL1}$ and $\mathbf{HBL2}$ respectively. Elements $\langle N_{R_i}|\frac{1}{R^2}|N_{R_j}\rangle$ and $\langle N_{r_i}|\frac{1}{r^2}|N_{r_j}\rangle$ are sorted in the vectors $\mathbf{R1M2}$ and $\mathbf{R2M2}$ respectively. We store these elements not in a matrix but in a vector. These matrices are symmetric; thus by saving these matrix elements in a vector saves memory space for computation. A matrix element $(i, j)$ is saved in a vector element as shown in Fig. 3.1.

Stretching basis functions and terms $\mathbf{HBL1}$, $\mathbf{HBL2}$, $\mathbf{R1M2}$, and $\mathbf{R2M2}$ are calculated using routines supplied by Prof. Jonathan Tennyson [16].

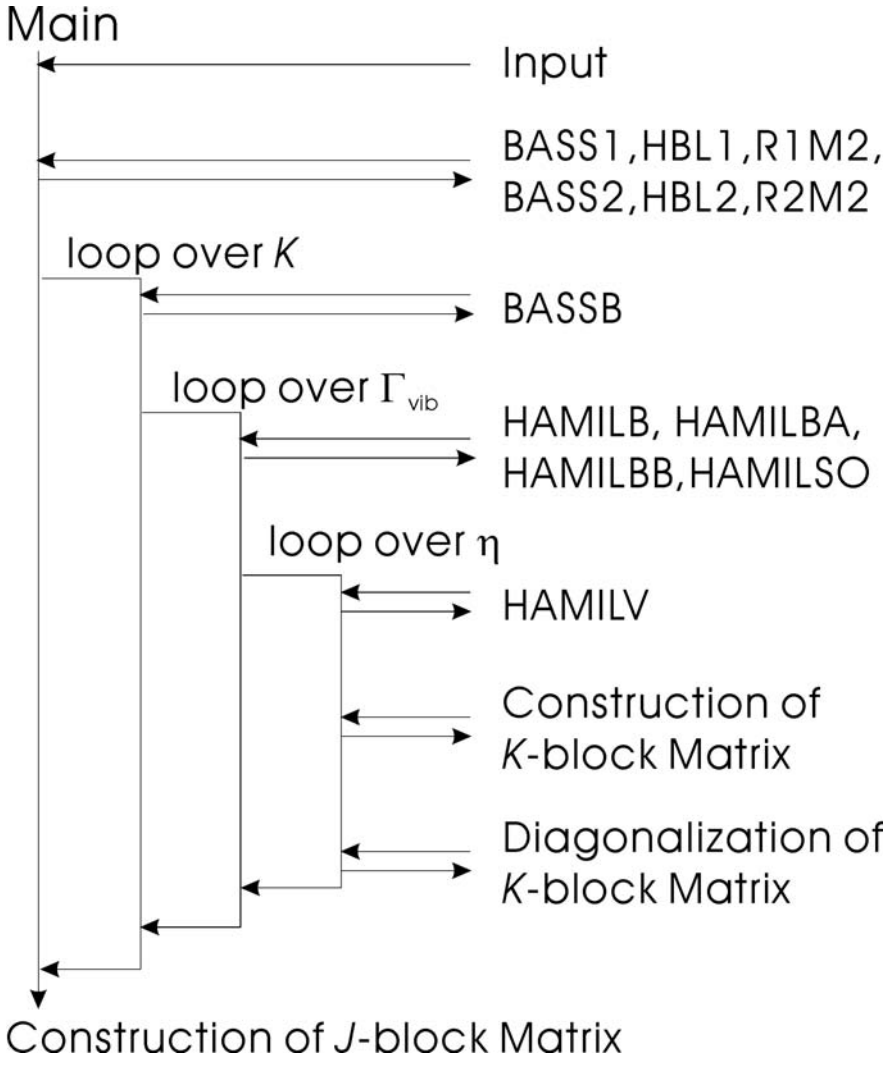


Figure 3.2: A schematic drawing for the program DR with $K$-block Hamiltonian matrix construction and $K$-block diagonalization. **BASS1**, **BASS2** and **BASSB** contain the stretching basis function for $R$ and $r$ coordinate and the bending basis function respectively. **HBL1**, **HBL2**, **R1M2**, **R2M2**, **HAMILB**, **HAMILBA**, **HAMILBB**, **HAMILSO** and **HAMILV** are the Hamiltonian matrix elements. See details in the text.

## 3.3 Starting the $K$ loop

We have different bending basis functions for each $K$ block. For each $K$ block, we first construct these basis functions. The input for constructing bending basis functions for the $\eta = a$ and $\eta = b$ states requires the following parameters.

- $\mathbf{MAXBA}$: The maximum quantum number value for the $\eta = a$ bending basis set.
- $\mathbf{MAXBB}$: The maximum quantum number value for the $\eta = b$ bending basis set.
- $\mathbf{NSTINT}$: The number of integration points for Numerov-Cooley integration.
- $\mathbf{NSERIN}$: Defines the number of points $M$, used to fit in equation (2.103).
- $\mathbf{NSERP}$ : Defines the variable $P$ in equation (2.104).
- $\mathbf{NSERQ}$ : Defines the variable $Q$ in equations (2.107) and (2.108).
- $\mathbf{VMIN}$: The starting energy for searching for the Numerov-Cooley wavefunction.
- $\mathbf{VMAX}$: The maximum energy for searching for the Numerov-Cooley wavefunction.

The Numerov-Cooley bending basis functions are constructed using the method described in Chapter 2.2.2, then turned into Laguerre integration bending basis functions. The parameters required for this change of formations are:

- $\mathbf{NPNTB}$: The number of integration point for Laguerre integration of the bending basis functions.
- $\mathbf{NSPB}$: The number of points produced by Numerov-Cooley integration to reproduce a integration point for Laguerre integration.

The subroutine for constructing bending basis functions is called ”drbend”.

Then, the program DR starts by constructing Hamiltonian matrix elements required by the $K$-block Hamiltonian matrix. The $K$-block matrix is constructed for each $\Gamma_{\rm vib}$

state. (When $K = 0$ we have to distinguish $\eta = a$ and $\eta = b$ states, thus the program constructs each $\eta$ state for each $\Gamma_{\rm vib}$.) As shown in Fig. 3.2, the program starts to loop over $\Gamma_{\rm vib}$ after constructing bending basis functions. For ABC-type molecules, the program loops only once for $\Gamma_{\rm vib}$.

Now the program constructs bending basis function-related matrix elements of $\hat{H}_b$, $\hat{H}_{ba}$, $\hat{H}_{bb}$ and $\hat{H}_{SO}$ in the subroutine "hamilbend". These matrix elements are stored in the vectors $\mathbf{HAMILB}$, $\mathbf{HAMILBA}$, $\mathbf{HAMILBB}$, and $\mathbf{HAMILSO}$, respectively. $\mathbf{HAMILB}$ corresponds to the term $\int X_{\eta_i\eta_j} d\tau$ in equation (2.154). $\mathbf{HAMILBA}$ corresponds to the term $\hbar^2 \int \Psi^{\eta_i}_{v_{2_i},K_i,\Gamma^{\eta_i}_{v_{2_i}}}(\tau)\Psi^{\eta_j}_{v_{2_j},K_i,\Gamma^{\eta_j}_{v_{2_j}}}(\tau) X_{\eta_i\eta_j}\frac{\cos^2(\tau)}{\sin^2(\tau)}d\tau$ in equation (2.163)) and $\mathbf{HAMILBB}$ corresponds to the term $\hbar^2 \int \Psi^{\eta_i}_{v_{2_i},K_i,\Gamma^{\eta_i}_{v_{2_i}}}(\tau)\Psi^{\eta_j}_{v_{2_j},K_i,\Gamma^{\eta_j}_{v_{2_j}}}(\tau)\frac{X_{\eta_i\eta_j}}{\sin^2(\tau)}d\tau$ in equation (2.164). $\mathbf{HAMILSO}$ corresponds to the term

$\int \Psi^{\eta_i}_{v_{2_i},K_i,\Gamma^{\eta_i}_{v_{2_i}}}(\tau)\Psi^{\eta_j}_{v_{2_j},K_j,\Gamma^{\eta_j}_{v_{2_j}}}(\tau) A_{SO}(\tau) f_{\Lambda-,+} \times X_{\eta_i\eta_j} d\tau$ in equation (2.189). These four terms are calculated with Numerov-Cooley bending basis functions. The terms are constructed twice for each $K$-block, if we have an ABB-type molecule, but with an ABC-type molecule they are constructed once for each $K$-block. $\mathbf{HAMILSO}$ will be saved on hard disk at this point, since it will not be included in the $K$-block diagonalization, but it is needed in the $J$-block diagonalization.

As shown in Fig. 3.2, the program starts to loop over $\eta$ after the construction of Hamiltonian matrix elements $\mathbf{HAMILB}$, $\mathbf{HAMILBA}$, $\mathbf{HAMILBB}$, and $\mathbf{HAMILSO}$. Then the program constructs Hamiltonian matrix element $\mathbf{HAMILV}$. The program collects each Hamiltonian matrix which is constructed up to now (except $\mathbf{HAMILSO}$) and constructs the $K$-block Hamiltonian matrix.

The input data needed for performing $K$-block diagonalization is

- $\mathbf{CONTMAX}$: The threshold limit for contraction of a $K$-block. The eigenvalues which are bigger than the zero point energy in the $K$-block plus CONTMAX, will not be used in $J$-block diagonalization.

The program diagonalizes the $K$-block Hamiltonian matrix using LAPACK routines. Since we have an $nmax(K,\eta,\Gamma_{\rm vib}) \times nmax(K,\eta,\Gamma_{\rm vib})$ (See Eqs. (2.194)-(2.203)) $K$-block Hamiltonian matrix, we obtain $nmax(K,\eta,\Gamma_{\rm vib})$ eigenvalues, and eigenfunctions but we only save up to the limit defined from the input $\mathbf{CONTMAX}$ to the hard disk. Then the program calculates another $K$-block Hamiltonian matrix untill the program finish making the required number of $K$-blocks.

## 3.4 $J$-block diagonalization

$J$-blocks are constructed as shown in Fig. 3.3. The quantum number $J$ defines the quantum number $N$ in the $J$-block Hamiltonian matrix. The quantum number $N$ is defined as $N = |J-S|,...|J+S|$. The quantum number $K$ is defined from $N$, as $K = 0,1,...N$. As shown in Fig. 3.4, the program loops over each $J$ quantum number. For each $J$ state we have the good quantum number $\Gamma_{\rm rve}$. Thus the program also loops over each $\Gamma_{\rm rve}$ state.

As detailed in Chapter 2.2.5, we have to be careful which basis functions we use for constructing final matrix so that it has the correct symmetry $\Gamma_{\rm rve}$. Thus for each $K$-block in the $J$-block for specific $\Gamma_{\rm rve}$ state, we have to choose the symmetry of the bending basis function $\Gamma_{\rm vib}$, the electronic state $\eta$ and the parity of the sytem $p$ according to Table 2.3 for ABC-type molecules and Table 2.6 for ABB-type molecules.

As shown in Fig. 3.3, the $J$-block consists of many $K$-blocks. The $K$-block Hamiltonian matrix with $\Delta K = 0$ and $\Delta N = 0$ is called $\mathbf{HAMILDIAG}$, the $K$-block Hamiltonian matrix with $\Delta K = 1$ and $\Delta N = 0$ is called $\mathbf{HAMILDK}$, and the $K$-block Hamiltonian matrix with $\Delta K = 0$ and $\Delta N = 1$ is called $\mathbf{HAMILDN}$. Each has shorthand notation $\mathbf{DIAG}$, $\mathbf{DK}$ and $\mathbf{DN}$, respectively in Fig. 3.3. Apart from $\mathbf{HAMILDIAG}$, $\mathbf{HAMILDK}$ and $\mathbf{HAMILDN}$, all the other $K$-block Hamiltonian matrix elements in the $J$-block Hamiltonian matrix are zero.

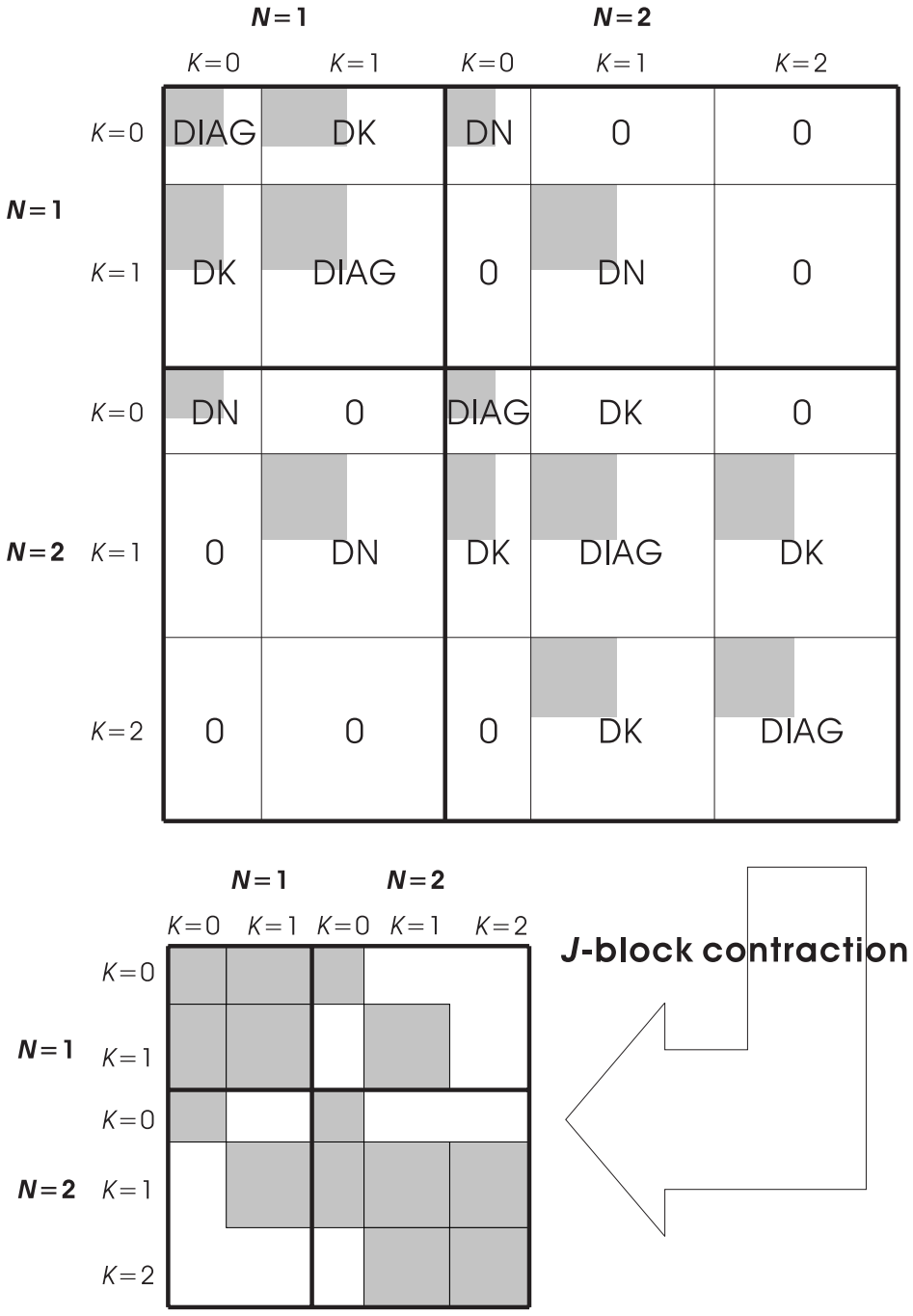


Figure 3.3: A schematic diagram showing how the program DR constructs the $J$-block Hamiltonian matrix from the contracted $K$-block Hamiltonian matrix. **HAMILDIAG**, **HAMILDK** and **HAMILDN** have the shorthand notations **DIAG**, **DK** and **DN**, respectively. See details in the text.

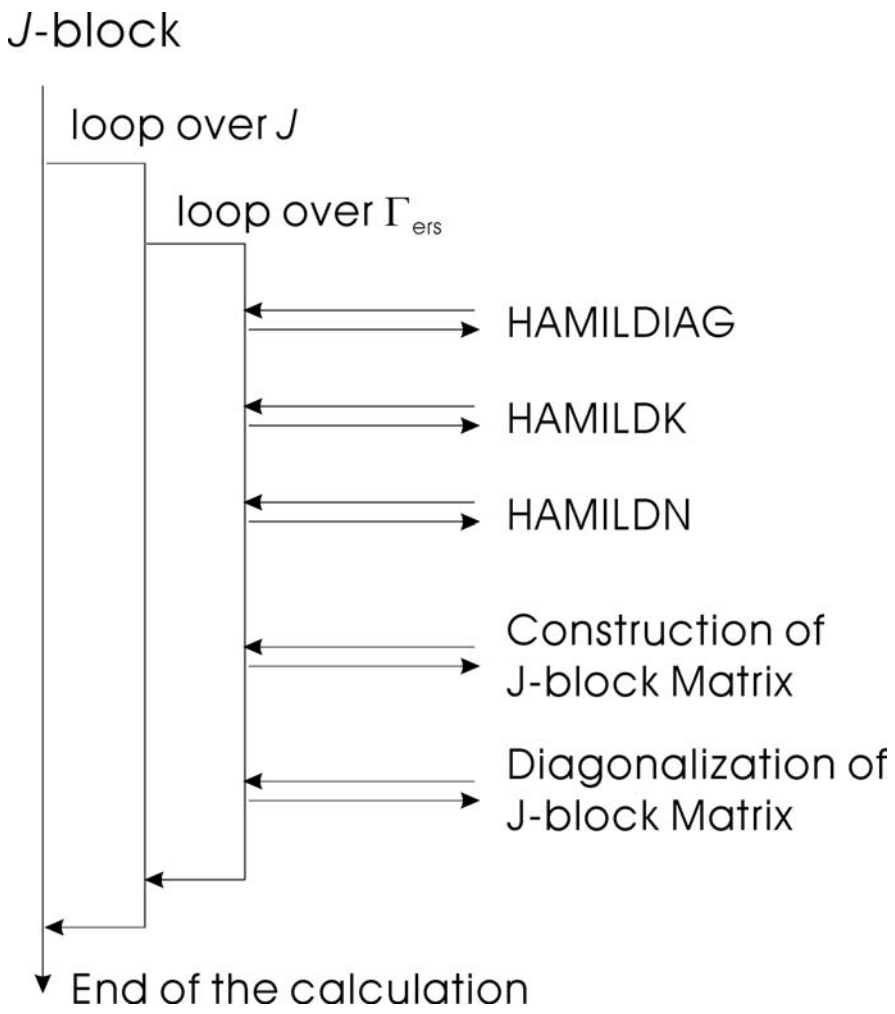


Figure 3.4: A schematic representation of the program DR with $J$-block Hamiltonian matrix construction and $J$-block diagonalization. **HAMILDIAG**, **HAMILDK** and **HAMILDN** are the Hamiltonian matrix elements. See details in the text.

The program first constructs the Hamiltonian matrix $\mathbf{HAMILDIAG}$(See Fig. 3.4). It consist of $K$-blocks saved at the $K$-block diagonalization, $\mathbf{HAMILSO}$, the vector saved in the $K$-loop and terms from matrix elements of $\hat{H}_{nk}$ (see Chapter 2.3.5). Then the program contracts the Hamiltonian matrix $\mathbf{HAMILDIAG}$, as described in Chapter 2.4.2 (See equation (2.204)).

Then the program constructs the Hamiltonian matrix $\mathbf{HAMILDK}$. (See Fig. 3.4) It consist of matrix elements of $\hat{H}_{dk}$ (see Chapter 2.3.6). The program also contracts the Hamiltonian matrix $\mathbf{HAMILDK}$, as described in Chapter 2.4.2.

Finally the program constructs the Hamiltonian matrix $\mathbf{HAMILDN}$. (See Fig. 3.4) It consists of $\mathbf{HAMILSO}$, the vector saved in the $K$-loop. The program also contracts the Hamiltonian matrix $\mathbf{HAMILDK}$, as described in Chapter 2.4.2.

The program collects all of these contracted Hamiltonian matrices $\mathbf{HAMILDIAG}$, $\mathbf{HAMILDK}$ and $\mathbf{HAMILDN}$. As shown in the bottom of the Fig. 3.3, with each contraction of each $K$-block, the final $J$-block Hamiltonian matrix becomes much smaller and easier to diagonalize. The program diagonalizes the final $J$-block Hamiltonian matrix with LAPACK routines, and we obtain the eigenvalues and eigenfunctions for the double Renner system.

# Chapter 4

# The double Renner effect in ABC-type molecules

Now we move on to the application to ABC-type molecules. As an example of an ABC-type molecule, we take the first electronic excited state of MgNC and MgCN ($\widetilde{A}\ ^2\Pi$) system.

## 4.1 What is MgNC?

Unlike the HCN and $H_2O$ molecules, MgNC must sound very exotic for a person who is not familiar with this molecule. In 1986 Guélin $et\ al.$ [21] found, in radio-astronomical observations, six transitions originating in the circumstellar envelope of the late-type carbon star IRC+10216. On this first occasion when humans observed the molecule, nobody thought about the possibility that these lines originate in MgNC, although there had been a first theoretical calculation of the MgNC structure in 1985 by Bauschlicher $et\ al$ [22]. These authors studied a series of metal cyanides. They reported theoretical calculations of the ground $^2A'$ state surface of MCN (M=Be, Mg, Ca and Ba) and determined the lowest energy structures and dissociation energies.

For seven years the six lines observed by Guélin $et\ al.$ remained unassigned. They were later identified as the rotational spectrum of the MgNC radical [23, 24], thus MgNC became the first Mg containing molecule to be observed in interstellar space.

The identification was made in collaboration between laboratory experiment by Kawaguchi $et\ al.$ and computational theoretical chemistry by Hirano $et\ al.$. These authors tried to imagine all possible molecules that could be responsible for the six lines, and made theoretical calculations to determine the energy regions where these molecule have transitions, so that they could be more easily found in rotational spectroscopic experiments. The identification has stimulated great interest in MgNC.

In 1994, Ishii $et\ al.$ calculated the potential energy surface for the ground electronic state $\widetilde{X}\ ^2\Sigma^+$ of MgNC by the single and double excitation configuration interaction (SDCI) $ab\ initio$ molecular orbital (MO) method, using a triple-zeta valence plus two 3d-type polarization functions (TZ2P) basis set. From this potential energy surface, Ishii $et\ al.$ obtained the standard spectroscopic parameters, and the rotational constant $B_0$ of the vibrational ground state, by perturbation methods [24, 25]. Other reported theoretical calculations on $\widetilde{X}\ ^2\Sigma^+$ MgNC are Barrientos and Largo [26] with MP2(full) / 6-31G* calculations in 1995, QCISD (full) / 6-311G** calculations by Petrie [27] in 1996, UMP2 (full) / 6-311+G(3df) calculations and CISD (full) / 6-311G(2d) calculations by Guélin $et\ al.$ [28] in 1995, RCCSD(T) (valence) / cc-pVQZ calculations by Woon [29] in 1996 and B3LYP / 6-311+G(3df) calculations by Kieninger $et\ al.$ [30] in 1998.

The rotationally resolved spectroscopic data presently available for $\widetilde{X}\ ^2\Sigma^+$ MgNC comprise the rotational spectrum by Anderson and Ziurys [31] in 1994, Kagi $et\ al.$ [32] in 1996, and Kagi and Kawaguchi in 2000 [33].

The isomer of $\widetilde{X}\ ^2\Sigma^+$ MgNC, $\widetilde{X}\ ^2\Sigma^+$ MgCN, has been identified as an interstellar molecule by Ziurys $et\ al.$ [34] in 1995. Only the rotational spectrum in the vibrational ground state was observed by Anderson $et\ al.$ [35]. Theoretical investigations on

MgCN were carried out with MP2 (full) / 6-311G** calculations by Gardner $et\ al.$ [36] in 1993, MP2 (full) / 6-31G* calculations by Barrientos and Largo [26] in 1995 and by Petrie [27] in 1996, RCCSD(T) (core-valence) / cc-pCVTZ calculations by Woon [29] in 1996 and B3LYP / 6-311+G(3df) calculations by Kieninger $et\ al.$ [30] in 1998.

Further more we have reported potential energy surfaces calculated by the Averaged Coupled-Pair Functional (ACPF) method with TZ3P+f (Mg), TZ2P+f(N,C) basis sets including core-valence correlation due to the Mg 2s and 2p electrons. The $ab\ initio$ results are used for determining the standard spectroscopic constants of $\widetilde{X}\ ^2\Sigma^+$ MgNC and MgCN. Furthermore, we have reported variational calculations of the rotation-vibration energies, and simulated spectra of the lowest rotation-vibration bands (Appendix A). The calculated $ab\ initio$ points were later used to make a global potential energy surface for $\widetilde{X}\ ^2\Sigma^+$ MgNC /MgCN, and we carried out rotation-vibration calculations taking into account of the isomerization between MgNC and MgCN [37].

The interest on $\widetilde{X}\ ^2\Sigma^+$ MgNC and $\widetilde{X}\ ^2\Sigma^+$ MgCN stimulated interest in its electronic excited state. Wright and Miller observed Laser Induced Fluorescence (LIF) spectrum of $\widetilde{A}\ ^2\Pi \leftarrow \widetilde{X}\ ^2\Sigma^+$ MgNC [8]. Fukushima and Ishiwata [38] observed some vibrationally excited states of $\widetilde{A}\ ^2\Pi$ MgNC in the transition spectrum of $\widetilde{A}\ ^2\Pi \leftarrow \widetilde{X}\ ^2\Sigma^+$ MgNC. Steimle and Bousquet [39] observed dipole moments of $\widetilde{A}\ ^2\Pi$ MgNC.

We reported theoretical predictions of rovibronic energies for the first excited electronic state of MgNC using internally contracted multi-reference singles and doubles configuration interaction (MR-SDCI) [40, 41, 42] level with Davidson's correction [43] for quadruple excitations (denoted as +Q). The basis set employed for Mg is TZ3P+f (see Appendix B) and for N and C, aug-cc-pVQZ [44, 45]; the method of calculation is denoted as MR-SDCI(+Q)/[TZ3P+f (Mg), aug-cc-pVQZ (C and N)]. We calculated vibronic energy levels using the specroscopic constants obtained from the $ab\ initio$ calculations and made a reassignment in the LIF spectrum reported by Wright and Miller [8]. Taketsugu and Carter calculated vibronic energy levels by variational method us-

ing the potential energy surface reported in Appendix B, and confirmed our assignment [46].

We have calculated ro-vibronic energy levels of $\widetilde{A}\ ^2\Pi$ , together with transition wavenumbers and relative intensities for the $\widetilde{A}\ ^2\Pi \leftarrow \widetilde{X}\ ^2\Sigma^+$ electronic transition. The calculations are carried out with the program system RENNER [9]. The potential energy surface are constructed from the $ab\ initio$ potential energy data described in Appendix B supplemented by $ab\ initio$ points calculated at larger bending displacements from linearity (see Appendix C and D). The result also confirmed the assignment in Appendix A. The theoretical prediction on its isomer $\widetilde{A}\ ^2\Pi$ MgCN was carried out using the same $ab\ initio$ method described in Appendix E together with the program system RENNER [9].

As we have carried out the series of studies on MgNC and it's isomer MgCN (Appendix A-E and Ref. [37]) we understood that $\widetilde{X}\ ^2\Sigma$ MgNC/MgCN and $\widetilde{A}\ ^2\Pi$ MgNC/MgCN both have very low isomerization barrier. The observed $\widetilde{A}\ ^2\Pi$ MgNC has bigger vertical excitation energy than $\widetilde{A}\ ^2\Pi$ MgCN, and the possibility of isomerization in the Renner state is also high. This led us to the idea of the double Renner system.

## 4.2 Applying DR to MgNC/MgCN

### 4.2.1 Global potential energy surfaces

We constructed global potential energy surfaces by grafting an intermediate Mg-(NC) surface onto local MgNC and MgCN surfaces. As described in detail in Appendix C and E, we computed high accuracy potential energy surfaces around the MgNC and MgCN local minima. Thus to have global potential energy surfaces, we used the same $ab\ initio$ method as in Appendix B, MR-SDCI(+Q)/[TZ3P+f (Mg), aug-cc-pVQZ (C and N)] and computed further 176 points, which consist of 92 points for the lower surface ($1^2A$" electronic state) and 84 points for the upper surface ($2^2A'$ electronic state). For the $\tau$

coordinate, we computed points at $\tau = 60°$, $80°$, $90°$, $100°$ and $120°$ (MgCN has lower potential energy minimum than MgNC. We take MgNC as $\tau = 0°$ and MgCN as $\tau = 180°$ here). For the $r$ coordinate, the NC bond, we computed points at the distances 1.8, 2.0, 2.2, 2.4 and 2.6 Bohr and for the $R$ coordinate, the distance between NC moiety and Mg, we have computed points at the distances 3.0, 3.3, 3.5, 4.0, 4.3, 4.5 and 5.0 Bohr. We have fitted these $ab\ initio$ points to the function

$$y_r = 1 - \exp\{-a_r^{\tau,\sigma}(r - r_e^{\tau,\sigma})\} \quad (4.1)$$

$$y_R = 1 - \exp\{-a_R^{\tau,\sigma}(R - R_e^{\tau,\sigma})\} \quad (4.2)$$

$$E(r,R)^{\tau,\sigma} = \sum_{i,j} F_{i,j}^{\tau,\sigma}(y_r)^i(y_R)^j \quad (4.3)$$

at each $\tau$ grid for the lower ($\sigma = -$) and upper ($\sigma = +$) surface. The parameters are summarized in Tables 4.1 - 4.5. The averaged standard deviation for the lower and upper electronic surfaces are 34.2 cm$^{-1}$ and 65.7 cm$^{-1}$ respectively.

The potential energies at the geometries with $\tau \leq 40$ are computed using the MgNC local potential (See Appendix C). The potential energies at the geometries with $\tau \geq 140$ are computed using the MgCN local potential (See Appendix E). The potential energies $E(r,R,\tau)^\sigma$ at the geometries ($r$,$R$,$\tau$) with $40° < \tau < 140°$ are computed using an interpolation method; We have computed the potential energies $E(r,R,\tau_{grid})^\sigma$ at $\tau_{grid} = 0°$, $20°$, $40°$, $60°$, $80°$, $90°$, $100°$, $120°$, $140°$, $160°$ and $180°$ using the potential energy surfaces from Eq. (4.3) and the local potential energy surfaces of Appendix C and E. Then we have interpolated the potential energies between the $\tau$ values.

### 4.2.2 Bending basis functions

To obtain bending basis functions, we first tried the minimum energy path for the isomerization in the Jacobi angle $\tau$ as potential energy functions. We calculated the minimum energy paths from the global potential energy surfaces described in the previous

Table 4.1: Potential energy parameters for equation (4.3), with $\tau = 60°$.

| | $\tau = 60°$ | |
|---|---|---|
| | $\sigma = -$ | $\sigma = +$ |
| $V^{\sigma,\tau}$/Hartree | $-292.4444125(1622)^a$ | $-292.4446590(3098)$ |
| $r_{e^{\sigma,\tau}}$/Bohr | 2.2301(7) | 2.2181(13) |
| $R_{e^{\sigma,\tau}}$/Bohr | 3.9868(11) | 3.8585(18) |
| $\alpha_r^{\sigma,\tau}$/Bohr$^{-1}$ | $2.00^b$ | 2.00 |
| $\alpha_R^{\sigma,\tau}$/Bohr$^{-1}$ | 1.00 | 1.80 |
| $F_{20}^{\sigma,\tau}$/cm$^{-1}$ | 27532.4(248.3) | 27556.4(377.0) |
| $F_{02}^{\sigma,\tau}$/cm$^{-1}$ | 12044.2(384.4) | 3457.6(384.5) |
| $F_{11}^{\sigma,\tau}$/cm$^{-1}$ | $-3194.5(120.0)$ | $-12227.5(709.0)$ |
| $F_{30}^{\sigma,\tau}$/cm$^{-1}$ | 5647.3(148.5) | 5668.6(243.7) |
| $F_{03}^{\sigma,\tau}$/cm$^{-1}$ | | $-779.6(118.3)$ |
| $F_{21}^{\sigma,\tau}$/cm$^{-1}$ | $-1822.4(453.0)$ | $-205.5(117.8)$ |
| $F_{12}^{\sigma,\tau}$/cm$^{-1}$ | 690.0(164.8) | |
| $F_{40}^{\sigma,\tau}$/cm$^{-1}$ | | |
| $F_{04}^{\sigma,\tau}$/cm$^{-1}$ | 13590.1(876.3) | 5070.1(412.3) |
| $F_{31}^{\sigma,\tau}$/cm$^{-1}$ | $-691.2(288.9)$ | |
| $F_{13}^{\sigma,\tau}$/cm$^{-1}$ | | 16176.3(875.7) |
| $F_{22}^{\sigma,\tau}$/cm$^{-1}$ | | |
| $dev^c$/cm$^{-1}$ | 49.9 | 77.1 |
| $np^d$ | 15 | 15 |

[a]Quantities in parentheses are standard errors in units of the last digit given. [b]Parameters for which no standard error is given were held fixed in the least squares fit. [c]Standard deviations for each fit are given in the line *dev*. [d]The number of points used in each fit are given in the line *np*.

Table 4.2: Potential energy parameters for equation (4.3), with $\tau = 80°$.

| | $\tau = 80°$ | |
|---|---|---|
| | $\sigma = -$ | $\sigma = +$ |
| $V^{\sigma,\tau}$/Hartree | $-292.4451679(1434)^a$ | $-292.4516470(1196)$ |
| $r_{e^{\sigma,\tau}}$/Bohr | 2.2372(9) | 2.2690(12) |
| $R_{e^{\sigma,\tau}}$/Bohr | 3.8345(24) | 3.7595(20) |
| $\alpha_r^{\sigma,\tau}$/Bohr$^{-1}$ | $2.00^b$ | 2.00 |
| $\alpha_R^{\sigma,\tau}$/Bohr$^{-1}$ | 1.00 | 1.80 |
| $F_{20}^{\sigma,\tau}$/cm$^{-1}$ | 28597.1(120.5) | 25074.3(215.0) |
| $F_{02}^{\sigma,\tau}$/cm$^{-1}$ | 12763.0(260.5) | 6435.5(48.2) |
| $F_{11}^{\sigma,\tau}$/cm$^{-1}$ | $-695.2(52.7)$ | 1907.8(79.0) |
| $F_{30}^{\sigma,\tau}$/cm$^{-1}$ | 12664.6(396.1) | 11094.3(661.5) |
| $F_{03}^{\sigma,\tau}$/cm$^{-1}$ | 5737.9(149.0) | 3343.9(37.6) |
| $F_{21}^{\sigma,\tau}$/cm$^{-1}$ | 115.9(46.9) | 2230.7(232.3) |
| $F_{12}^{\sigma,\tau}$/cm$^{-1}$ | $-502.0(91.7)$ | |
| $F_{40}^{\sigma,\tau}$/cm$^{-1}$ | 4029.4(253.5) | 3399.8(318.1) |
| $F_{04}^{\sigma,\tau}$/cm$^{-1}$ | 5115.0(448.6) | 550.0 |
| $F_{31}^{\sigma,\tau}$/cm$^{-1}$ | | 771.8(121.0) |
| $F_{13}^{\sigma,\tau}$/cm$^{-1}$ | | |
| $F_{22}^{\sigma,\tau}$/cm$^{-1}$ | | |
| $dev^c$/cm$^{-1}$ | 43.7 | 43.9 |
| $np^d$ | 21 | 17 |

[a]Quantities in parentheses are standard errors in units of the last digit given. [b]Parameters for which no standard error is given were held fixed in the least squares fit. [c]Standard deviations for each fit are given in the line *dev*. [d]The number of points used in each fit are given in the line *np*.

Table 4.3: Potential energy parameters for equation (4.3), with $\tau = 90°$.

| | $\tau = 90°$ | |
|---|---|---|
| | $\sigma = -$ | $\sigma = +$ |
| $V^{\sigma,\tau}$/Hartree | $-292.4451201(1326)^a$ | $-292.4554197(4224)$ |
| $r_{e^{\sigma,\tau}}$/Bohr | 2.2340(10) | 2.2739(9) |
| $R_{e^{\sigma,\tau}}$/Bohr | 3.8272(34) | 3.6985(30) |
| $\alpha_r^{\sigma,\tau}$/Bohr$^{-1}$ | $2.00^b$ | 2.00 |
| $\alpha_R^{\sigma,\tau}$/Bohr$^{-1}$ | 1.00 | 1.80 |
| $F_{20}^{\sigma,\tau}$/cm$^{-1}$ | 28563.2(127.0) | 25512.4(313.8) |
| $F_{02}^{\sigma,\tau}$/cm$^{-1}$ | 12301.8(209.2) | 10952.3(580.7) |
| $F_{11}^{\sigma,\tau}$/cm$^{-1}$ | $-269.2(109.5)$ | 2618.2(111.1) |
| $F_{30}^{\sigma,\tau}$/cm$^{-1}$ | 11559.1(607.9) | 13379.3(678.4) |
| $F_{03}^{\sigma,\tau}$/cm$^{-1}$ | 7353.3(367.5) | $-1198.6(570.8)$ |
| $F_{21}^{\sigma,\tau}$/cm$^{-1}$ | 53.0(81.4) | 2809.3(306.0) |
| $F_{12}^{\sigma,\tau}$/cm$^{-1}$ | | |
| $F_{40}^{\sigma,\tau}$/cm$^{-1}$ | 3401.0(373.8) | 4464.3(296.1) |
| $F_{04}^{\sigma,\tau}$/cm$^{-1}$ | 3000.0 | |
| $F_{31}^{\sigma,\tau}$/cm$^{-1}$ | | 961.3(155.1) |
| $F_{13}^{\sigma,\tau}$/cm$^{-1}$ | $-853.2(249.0)$ | |
| $F_{22}^{\sigma,\tau}$/cm$^{-1}$ | | |
| $dev^c$/cm$^{-1}$ | 33.8 | 32.4 |
| $np^d$ | 16 | 14 |

[a]Quantities in parentheses are standard errors in units of the last digit given. [b]Parameters for which no standard error is given were held fixed in the least squares fit. [c]Standard deviations for each fit are given in the line *dev*. [d]The number of points used in each fit are given in the line *np*.

Table 4.4: Potential energy parameters for equation (4.3), with $\tau = 100°$.

| | $\tau = 100°$ | |
|---|---|---|
| | $\sigma = -$ | $\sigma = +$ |
| $V^{\sigma,\tau}$/Hartree | $-292.4458897(3268)^a$ | $-292.4462359(4242)$ |
| $r_{e^{\sigma,\tau}}$/Bohr | 2.2324(6) | 2.2534(20) |
| $R_{e^{\sigma,\tau}}$/Bohr | 3.8182(168) | 3.8597(108) |
| $\alpha_r^{\sigma,\tau}$/Bohr$^{-1}$ | $2.00^b$ | 2.00 |
| $\alpha_R^{\sigma,\tau}$/Bohr$^{-1}$ | 1.00 | 1.80 |
| $F_{20}^{\sigma,\tau}$/cm$^{-1}$ | 29341.1(90.7) | 25565.6(336.5) |
| $F_{02}^{\sigma,\tau}$/cm$^{-1}$ | 13213.3(932.7) | 4059.1(167.5) |
| $F_{11}^{\sigma,\tau}$/cm$^{-1}$ | $-316.1(90.9)$ | |
| $F_{30}^{\sigma,\tau}$/cm$^{-1}$ | 14347.9(221.4) | 10459.1(802.9) |
| $F_{03}^{\sigma,\tau}$/cm$^{-1}$ | $-7953.9(4729.5)$ | 3640.6(158.9) |
| $F_{21}^{\sigma,\tau}$/cm$^{-1}$ | | 1666.6(540.0) |
| $F_{12}^{\sigma,\tau}$/cm$^{-1}$ | $-1300.3(220.3)$ | |
| $F_{40}^{\sigma,\tau}$/cm$^{-1}$ | 5007.0(149.4) | 3205.3(440.1) |
| $F_{04}^{\sigma,\tau}$/cm$^{-1}$ | 19352.1(4507.0) | 2000.0 |
| $F_{31}^{\sigma,\tau}$/cm$^{-1}$ | $-122.2(50.8)$ | 642.8(321.2) |
| $F_{13}^{\sigma,\tau}$/cm$^{-1}$ | | 2333.0(235.5) |
| $F_{22}^{\sigma,\tau}$/cm$^{-1}$ | $-769.7(181.4)$ | $-222.7(165.7)$ |
| $dev^c$/cm$^{-1}$ | 29.5 | 93.9 |
| $np^d$ | 22 | 20 |

[a]Quantities in parentheses are standard errors in units of the last digit given. [b]Parameters for which no standard error is given were held fixed in the least squares fit. [c]Standard deviations for each fit are given in the line *dev*. [d]The number of points used in each fit are given in the line *np*.

Table 4.5: Potential energy parameters for equation (4.3), with $\tau = 120°$.

| | $\tau = 120°$ | |
|---|---|---|
| | $\sigma = -$ | $\sigma = +$ |
| $V^{\sigma,\tau}$/Hartree | $-292.4453866(454)^a$ | $-292.4408203(2129)$ |
| $r_{e^{\sigma,\tau}}$/Bohr | 2.2237(4) | 2.2253(14) |
| $R_{e^{\sigma,\tau}}$/Bohr | 4.2315(9) | 4.2515(29) |
| $\alpha_r^{\sigma,\tau}$/Bohr$^{-1}$ | $2.00^b$ | 2.00 |
| $\alpha_R^{\sigma,\tau}$/Bohr$^{-1}$ | 1.00 | 1.80 |
| $F_{20}^{\sigma,\tau}$/cm$^{-1}$ | 29826.3(59.1) | 29729.7(239.8) |
| $F_{02}^{\sigma,\tau}$/cm$^{-1}$ | 13930.1(32.3) | 5613.8(84.4) |
| $F_{11}^{\sigma,\tau}$/cm$^{-1}$ | $-1804.1(35.2)$ | $-826.0(38.0)$ |
| $F_{30}^{\sigma,\tau}$/cm$^{-1}$ | 14022.1(136.6) | 13856.3(602.7) |
| $F_{03}^{\sigma,\tau}$/cm$^{-1}$ | 4163.9(42.0) | 2862.7(30.4) |
| $F_{21}^{\sigma,\tau}$/cm$^{-1}$ | | |
| $F_{12}^{\sigma,\tau}$/cm$^{-1}$ | 52.4(50.9) | |
| $F_{40}^{\sigma,\tau}$/cm$^{-1}$ | 4883.5(98.8) | 4740.3(431.4) |
| $F_{04}^{\sigma,\tau}$/cm$^{-1}$ | 4000.0 | 500.0 |
| $F_{31}^{\sigma,\tau}$/cm$^{-1}$ | 229.9(22.6) | |
| $F_{13}^{\sigma,\tau}$/cm$^{-1}$ | | |
| $F_{22}^{\sigma,\tau}$/cm$^{-1}$ | $-205.8(45.6)$ | 45.3(13.6) |
| $dev^c$/cm$^{-1}$ | 16.2 | 71.3 |
| $np^d$ | 18 | 18 |

[a]Quantities in parentheses are standard errors in units of the last digit given. [b]Parameters for which no standard error is given were held fixed in the least squares fit. [c]Standard deviations for each fit are given in the line *dev*. [d]The number of points used in each fit are given in the line *np*.

section, and fit them to $\cos\tau$ series,

$$V^{\sigma}(\tau) = \sum_i G^i_{V,\sigma} \cos^i \tau \tag{4.4}$$

$$R^{\sigma}(\tau) = \sum_i G^i_{R,\sigma} \cos^i \tau \tag{4.5}$$

$$r^{\sigma}(\tau) = \sum_i G^i_{r,\sigma} \cos^i \tau. \tag{4.6}$$

$V^{\pm}(\tau)$ are the potential energies along the minimum energy paths, $R^{\pm}(\tau)$ and $r^{\pm}(\tau)$ are $R$ and $r$ bond length changes along the minimum energy paths. The fitted potential energy surface is shown in Fig. 4.1. As seen in the figure, the ${}^2A'$ potential energy surface has a local minimum around $\tau = 90^{\circ}$. We have tried to produce the bending basis function along this potential energy surface, but some computers we used had some numerical problem with the deep local minimum in the middle.

Thus to make life easy, we re-produced the potential energy surface used to generate the bending basis functions without the huge change in the middle. The parameters used for re-producing the bending basis functions are summarized in Table 4.6. The plotted potential energy surface is given in Fig. 4.2. To compensate for the fact that we do not have exact bending basis functions for the minimum energy paths, we employed more bending basis functions in the $K$-block diagonalization.

## 4.3 Results

### 4.3.1 Computational details

We calculated ro-vibronic energy levels of the $\widetilde{A}^2\Pi$ MgCN - $\widetilde{A}^2\Pi$ MgNC system using the program DR described in the previous chapter. For the $\eta = a$ and $\eta = b$ bending basis set we employed 19 and 25 bending basis functions, respectively. These wavefunctions are calculated from the minimum energy path parameters in Table 4.6. We have 5999 integration points for Numerov-Cooley integration, and 80 integration points

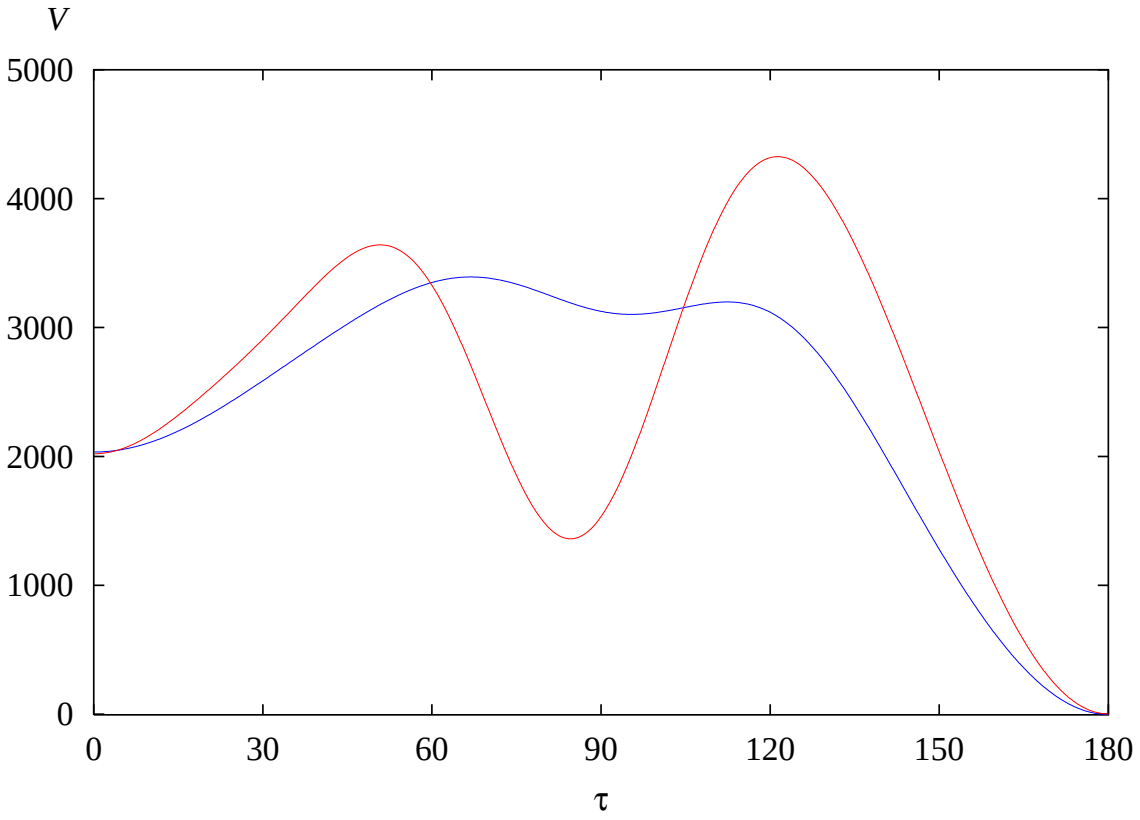


Figure 4.1: The minimum energy path of $\widetilde{A}^2\Pi$ MgNC/MgCN produced from the potential energy function expanded in Eq. (4.3) together with the parameters in Tables 4.1 - 4.5. $\tau$ is given in degrees and the potential $V$ is given in $cm^{-1}$. The blue curve shows the lower potential energy surface and the red curve shows the upper potential energy surface.

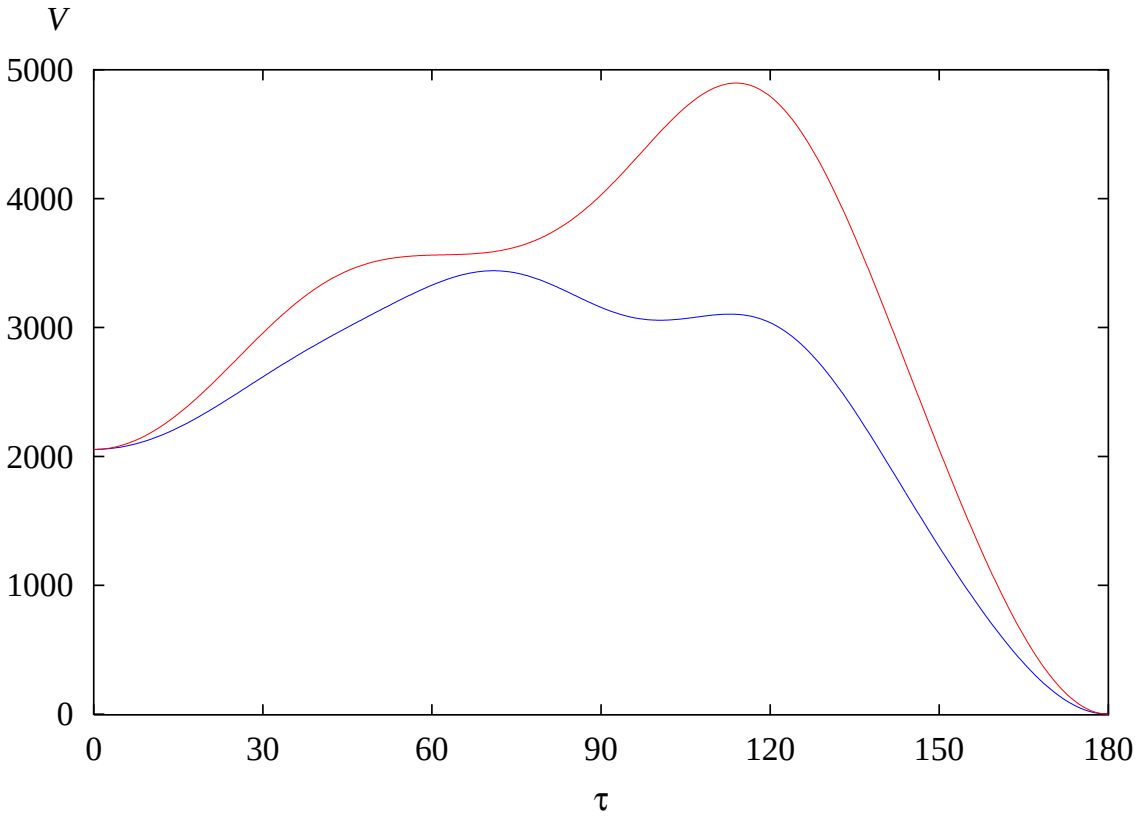


Figure 4.2: The potential energy path used to produce bending basis functions for the $\widetilde{A}^2\Pi$ MgNC/MgCN. The expressions for the functions are given in Eq. (4.4) and the parameter values are given in Table 4.6. $\tau$ is given in degrees and the potential $V$ is given in $\mathrm{cm}^{-1}$. The blue curve shows the lower potential energy surface and the red curve shows the upper potential energy surface.

Table 4.6: Minimum energy paths parameters in equation (4.6) for lower($\sigma = -$) and upper ($\sigma = +$) electronic surface

| $i$ | $G^i_{V,-}$ [a] | $(G^i_{V,+} - G^i_{V,-})$[a] | $G^i_{R,-}$/ Bohr | $G^i_{R,+}$/ Bohr | $G^i_{r,-}$/ Bohr | $G^i_{r,+}$/ Bohr |
|---|---|---|---|---|---|---|
| 0 | 0.014382040 | 0.003974870 | 3.805197247 | 3.635205540 | 2.232506969 | 2.233315838 |
| 1 | 0.004730499 | -0.015630810 | -0.194491648 | 0.157470176 | 0.021490055 | 0.033174605 |
| 2 | 0.008743513 | 0.003666078 | 1.525880468 | 1.933010986 | 0.001541810 | 0.018581112 |
| 3 | -0.029462306 | 0.048816400 | -0.002494302 | -1.070477811 | -0.005630305 | -0.035469597 |
| 4 | -0.041755341 | -0.004108562 | -0.790221104 | -0.966563912 | -0.025363354 | -0.072895254 |
| 5 | 0.082067071 | -0.067072613 | 0.027323684 | 1.014526537 | -0.009019280 | 0.014664757 |
| 6 | 0.038792009 | -0.007597047 | 0.250214660 | 0.187550205 | 0.012326126 | 0.042222786 |
| 7 | -0.082156929 | 0.046754812 | -0.017027922 | -0.286786385 | 0.005065069 | -0.000396938 |
| 8 | -0.015481356 | 0.004064917 | | | | |
| 9 | 0.029502288 | -0.012868103 | | | | |

[a] $G^i_{V,+}-$ and $G^i_{V,-}$ are given in Hartree.

for Gauss-Laguerre integration.

For the stretching basis functions, we employed 6 and 16 functions for $R$ and $r$ coordinates, respectively. The parameters used for constructing stretching basis functions are as follows. The equilibrium distance RE1 and RE2 used for this calculation are 2.2077984 and 4.5669501 Bohr, respectively. The dissociation energy parameter DISS1 and DISS2 are 2.9 and 0.5 Hartree, respectively. The harmonic frequency parameter WE1 and WE2 are 0.0105 and 0.0025 Hartree, respectively. The number of integration points for the $R$ and $r$ coordinates are 15 and 30, respectively.

The spin orbit interaction constant values at the equilibrium geometry for $\widetilde{A}^2$MgNC and $\widetilde{A}^2$MgCN state are 34.85 and 39.11 cm$^{-1}$, respectively (See Appendix B, C and E). Thus we have used the spin-orbit interaction function $f_{\rm SO}(\tau)$ calculated from the spin-orbit coupling constant for MgNC (34.85 cm$^{-1}$) and MgCN (39.11 cm$^{-1}$).

$$f_{\rm SO}(\tau) = 34.85 + \frac{(39.11 - 34.85)}{\pi} \times (\tau) \tag{4.7}$$

The threshold limit energy constant for $K$-block contraction, CONTMAX is taken to be 5000 cm$^{-1}$.

### 4.3.2 Vibronic energy levels

Calculated eigenvalues are summarized in Tables 4.7 - 4.13. For Tables 4.7 - 4.13 and 4.15, the over-all probability $P_-$ and $P_+$ are shown for each eigenvalue. The over-all probability $P_-$ and $P_+$ can be related to the $\mu$ and $\kappa$ notation. Normally, a state with dominant contribution from the lower electronic state ($P_- > P_+$) is the $\mu$ state, and a state with dominant contribution from the upper electronic state ($P_+ > P_-$) is the $\kappa$ state. Some probability density functions corresponding to these eigenvalues are shown in Figs. 4.3 - 4.21. The over-all probability ($P_-$ and $P_+$) and the probability density functions are calculated from the coefficient matrix elements $\mathbf{C}_{\mathbf{i,g}}^{\mathbf{J,M_J,S,\Gamma}_{\mathrm{rve}}}$ (See (2.206)) bigger than 0.05.

Fig. 4.3 shows a wavefunction localized around $\tau = 180°$. This is the $\widetilde{A}^2\Pi$ MgCN zero point vibration state. Vibronic energy levels of $\widetilde{A}^2\Pi$ MgCN (0 cm$^{-1}$ to 2912 cm$^{-1}$ region) calculated with the program DR are compared with the result from Appendix E in Tables 4.7 and 4.9 - 4.12. As seen in those tables the energies, calculated with the program DR are in good agreement with the energies calculated with program RENNER [9] and in perturbation method. The energies differ by up to 30 cm$^{-1}$. In most of the cases the program DR calculates lower energies than RENNER does. This is because although we have used the part of potential we include the isomerization of $\widetilde{A}^2\Pi$ MgCN/MgNC in DR, thus the energies are calculated from a shallower potential energy surface than used in the previous studies.

The spin orbit splitting calculated with DR and RENNER for $\widetilde{A}^2\Pi$ MgCN $(0,0,0)$ and $(1,0,0)$ state are 38.25 and 38.8 cm$^{-1}$, 38.18 and 38.6 cm$^{-1}$, respectively. The spin orbit splitting for $\widetilde{A}^2\Pi$ MgCN $(0,0,0)$ and $(1,0,0)$ state are in very good agreement. But the spin orbit splitting calculated with RENNER and DR for $\widetilde{A}^2\Pi$ MgCN $(0,0,1)$ and

Table 4.7: Vibronic term values (in $cm^{-1}$) of MgNC. Energy levels with $P = J = 1/2, 3/2$ are listed here. When an energy have $e$ and $f$ pairs, the lower component and the splitting are given.

| State $(\nu_1, \nu_2, \nu_3)$ | | notation | | $\Gamma_{\rm rve}$ | No.[a] | $P^b_-$ | $P^b_+$ | $\Delta^c_{ef}$ | DR[d] | RENNER[e] | PT[f] |
|---|---|---|---|---|---|---|---|---|---|---|---|
| MgCN, Fig. 4.3 | $(0,0,0)$ | $\Pi_{1/2}$ | $f$ | $A$" | 1 | 59.7 | 40.3 | 0.01 | 0.00 | 0.0 | 0.0 |
| MgCN | $(0,0,0)$ | $\Pi_{3/2}$ | $f$ | $A'$ | 2 | 60.0 | 40.0 | 0.00 | 38.25 | 38.8 | 39.1 |
| MgCN | $(0,1,0)$ | $\mu\Sigma_{1/2}$ | $f$ | $A$" | 2 | 97.5 | 2.5 | 0.34 | 195.92 | 218.6 | 194.7 |
| MgCN | $(0,1,0)$ | $\Delta_{3/2}$ | $f$ | $A'$ | 4 | 64.6 | 35.3 | 0.00 | 234.45 | 253.1 | 237.6 |
| MgCN | $(0,1,0)$ | $\kappa\Sigma_{1/2}$ | $e$ | $A'$ | 3 | 2.5 | 97.4 | 0.34 | 315.79 | 338.1 | 319.6 |
| MgCN | $(0,2,0)$ | $\mu\Pi_{1/2}$ | $f$ | $A$" | 4 | 65.2 | 34.8 | 0.00 | 398.47 | 407.9 | 387.3 |
| MgCN | $(0,2,0)$ | $\mu\Pi_{3/2}$ | $f$ | $A'$ | 7 | 66.3 | 33.5 | 0.00 | 404.20 | 416.6 | 394.2 |
| MgCN | $(0,0,1)$ | $\Pi_{1/2}$ | $f$ | $A$" | 5 | 51.5 | 48.4 | 0.01 | 520.83 | 523.8 | 548.2 |
| MgCN | $(0,0,1)$ | $\Pi_{3/2}$ | $f$ | $A'$ | 9 | 51.3 | 48.4 | 0.00 | 543.64 | 559.1 | 587.3 |
| MgCN | $(0,2,0)$ | $\kappa\Pi_{1/2}$ | $f$ | $A$" | 6 | 48.1 | 51.8 | 0.00 | 577.10 | 586.0 | 569.0 |
| MgCN | $(0,3,0)$ | $\mu\Sigma_{1/2}$ | $f$ | $A$" | 7 | 97.5 | 2.4 | 0.37 | 585.66 | 602.5 | 547.0 |
| MgCN | $(0,2,0)$ | $\kappa\Pi_{3/2}$ | $e$ | $A$" | 11 | 50.3 | 49.5 | 0.04 | 586.45 | 580.9 | 562.1 |
| MgCN | $(0,3,0)$ | $\mu\Delta_{3/2}$ | $f$ | $A'$ | 13 | 68.9 | 30.9 | 0.00 | 608.52 | 624.1 | 583.7 |
| MgCN | $(0,1,1)$ | $\mu\Sigma_{1/2}$ | $f$ | $A$" | 8 | 96.8 | 3.1 | 0.34 | 730.19 | 761.8 | 770.8 |
| MgCN | $(0,1,1)$ | $\Delta_{3/2}$ | $f$ | $A'$ | 15 | 54.1 | 45.7 | 0.00 | 757.14 | 782.5 | 813.7 |
| MgCN | $(0,4,0)$ | $\mu\Pi_{1/2}$ | $f$ | $A$" | 9 | 72.8 | 26.8 | 0.03 | 774.68 | 785.0 | 705.8 |
| MgCN | $(0,4,0)$ | $\mu\Pi_{3/2}$ | $f$ | $A'$ | 17 | 75.6 | 24.1 | 0.00 | 779.17 | 789.7 | 709.9 |
| MgCN | $(0,3,0)$ | $\kappa\Sigma_{1/2}$ | $e$ | $A'$ | 10 | 3.7 | 96.2 | 0.38 | 791.51 | 809.8 | 787.4 |
| MgCN | $(0,3,0)$ | $\kappa\Delta_{3/2}$ | $f$ | $A'$ | 19 | 44.5 | 54.9 | 0.00 | 828.75 | 851.3 | 812.7 |
| MgCN | $(0,1,1)$ | $\kappa\Sigma_{1/2}$ | $e$ | $A'$ | 11 | 1.7 | 98.2 | 0.35 | 870.42 | 902.6 | 895.7 |
| MgCN | $(0,2,1)$ | $\mu\Pi_{1/2}$ | $e$ | $A'$ | 12 | 66.9 | 32.8 | 0.01 | 941.95 | | |
| MgCN | $(0,2,1)$ | $\mu\Pi_{3/2}$ | $f$ | $A'$ | 22 | 66.3 | 33.1 | 0.00 | 946.81 | | |
| MgCN | $(0,5,0)$ | $\mu\Sigma_{1/2}$ | $f$ | $A$" | 13 | 99.4 | 0.5 | 0.37 | 953.80 | | |
| MgCN | $(0,5,0)$ | $\mu\Delta_{3/2}$ | $f$ | $A'$ | 24 | 76.8 | 22.8 | 0.00 | 970.80 | | |
| MgCN | $(0,4,0)$ | $\kappa\Pi_{3/2}$ | $e$ | $A$" | 25 | 30.9 | 68.7 | 0.01 | 1026.77 | 1040.7 | 1000.5 |
| MgCN | $(0,4,0)$ | $\kappa\Pi_{1/2}$ | $f$ | $A$" | 14 | 30.5 | 69.3 | 0.02 | 1033.09 | 1040.2 | 1004.6 |
| MgCN | | $\kappa\Pi_{1/2}$ | $f$ | $A$" | 15 | 49.9 | 50.0 | 0.01 | 1092.67 | | |
| MgCN | | $\mu\Pi_{3/2}$ | $f$ | $A'$ | 28 | 50.3 | 49.2 | 0.00 | 1114.30 | | |
| MgCN | | $\mu\Pi_{1/2}$ | $f$ | $A$" | 16 | 74.0 | 25.8 | 0.00 | 1133.74 | | |
| MgCN | | $\mu\Sigma_{1/2}$ | $f$ | $A$" | 17 | 94.6 | 5.1 | 0.29 | 1136.30 | | |
| MgCN | | $\mu\Pi_{3/2}$ | $f$ | $A'$ | 31 | 75.7 | 23.9 | 0.01 | 1137.42 | | |
| MgCN | | $\mu\Pi_{1/2}$ | $f$ | $A$" | 18 | 53.9 | 45.9 | 0.09 | 1142.51 | | |
| MgCN | | $\mu\Pi_{3/2}$ | $f$ | $A'$ | 33 | 54.2 | 44.9 | 0.00 | 1154.22 | | |
| MgCN | | $\mu\Delta_{3/2}$ | $f$ | $A'$ | 34 | 64.5 | 34.8 | 0.00 | 1158.07 | | |
| MgCN | | $\kappa\Sigma_{1/2}$ | $e$ | $A'$ | 19 | 2.4 | 97.3 | 0.38 | 1258.39 | | |
| MgCN | | $\kappa\Delta_{3/2}$ | $f$ | $A'$ | 36 | 29.3 | 70.1 | 0.00 | 1269.24 | | |
| MgCN | | $\mu\Sigma_{1/2}$ | $f$ | $A$" | 20 | 97.4 | 2.4 | 0.34 | 1289.44 | | |
| MgCN | | $\mu\Sigma_{1/2}$ | $f$ | $A$" | 21 | 97.6 | 2.1 | 0.38 | 1306.22 | | |
| MgCN | | $\mu\Delta_{3/2}$ | $f$ | $A'$ | 39 | 74.1 | 25.3 | 0.00 | 1318.93 | | |
| MgCN | | $\mu\Delta_{3/2}$ | $f$ | $A'$ | 40 | 59.8 | 39.9 | 0.00 | 1322.56 | | |

[a] The numbering of the energies found in each $P = 1/2, 3/2$, $\Gamma_{\rm ers}$ state. [b] The over-all probability given in %. See Chapter 2.5.3. [c] The energy difference between the $e$ and $f$ states, give in $cm^{-1}$. See Chapter 2.5.2 for $e$ and $f$ notations. [d] Energy calculated with the program DR. [e] See Appendix E. Energy calculated with the program RENNER, using part of the potential energy surface used in this work. [f] Ref. See Appendix E. Energy calculated in perturbation method, using part of the potential energy surface used in this work.

Table 4.8: Vibronic term values (in $cm^{-1}$) of MgNC. Energy levels with $P = J = 1/2, 3/2$ are listed here. When an energy have $e$ and $f$ pairs, the lower component and the splitting are given.

| State | notation | | $\Gamma_{\rm rve}$ | No.[a] | $P^b_-$ | $P^b_+$ | $\Delta^c_{ef}$ | DR[d] |
|---|---|---|---|---|---|---|---|---|
| MgCN | $\mu\Pi_{1/2}$ | $f$ | $A$" | 22 | 74.2 | 25.5 | 0.02 | 1331.17 |
| MgCN | $\mu\Pi_{3/2}$ | $f$ | $A'$ | 42 | 75.7 | 23.8 | 0.00 | 1335.23 |
| MgCN | $\kappa\Sigma_{1/2}$ | $e$ | $A'$ | 23 | 2.1 | 97.7 | 0.40 | 1367.58 |
| MgCN | $\kappa\Delta_{3/2}$ | $f$ | $A'$ | 44 | 41.7 | 57.7 | 0.00 | 1398.59 |
| MgCN | $\kappa\Sigma_{1/2}$ | $e$ | $A'$ | 24 | 1.5 | 98.4 | 0.38 | 1439.78 |
| MgCN | $\mu\Pi_{3/2}$ | $f$ | $A'$ | 46 | 67.6 | 31.8 | 0.00 | 1468.61 |
| MgCN | $\mu\Pi_{1/2}$ | $f$ | $A$" | 25 | 62.5 | 37.3 | 0.01 | 1475.32 |
| MgCN | $\kappa\Pi_{1/2}$ | $f$ | $A$" | 26 | 42.9 | 56.8 | 0.02 | 1493.02 |
| MgCN | $\kappa\Pi_{3/2}$ | $f$ | $A'$ | 49 | 42.4 | 56.9 | 0.01 | 1498.48 |
| MgCN | $\mu\Pi_{1/2}$ | $e$ | $A'$ | 27 | 66.7 | 32.8 | 0.01 | 1508.48 |
| MgCN | $\mu\Pi_{3/2}$ | $e$ | $A$" | 50 | 67.2 | 31.8 | 0.02 | 1508.95 |
| MgCN | $\mu\Pi_{3/2}$ | $f$ | $A'$ | 51 | 65.8 | 33.4 | 0.00 | 1510.24 |
| MgCN | $\mu\Sigma_{1/2}$ | $f$ | $A$" | 28 | 99.4 | 0.5 | 0.38 | 1514.72 |
| MgCN | $\mu\Delta_{3/2}$ | $f$ | $A'$ | 53 | 76.2 | 23.1 | 0.00 | 1530.15 |
| MgCN | $\kappa\Pi_{3/2}$ | $f$ | $A'$ | 54 | 29.6 | 69.5 | 0.00 | 1607.96 |
| MgCN | $\kappa\Pi_{1/2}$ | $f$ | $A$" | 29 | 28.8 | 70.7 | 0.01 | 1612.64 |
| MgCN | $\mu\Sigma_{1/2}$ | $f$ | $A$" | 30 | 98.8 | 1.0 | 0.44 | 1637.42 |
| MgCN | $\mu\Delta_{3/2}$ | $f$ | $A'$ | 57 | 75.1 | 24.2 | 0.00 | 1650.45 |
| MgCN | $\mu\Pi_{1/2}$ | $f$ | $A$" | 31 | 67.3 | 32.4 | 0.02 | 1696.81 |
| MgCN | $\mu\Pi_{3/2}$ | $f$ | $A'$ | 58 | 69.1 | 29.8 | 0.02 | 1697.30 |
| MgCN | $\mu\Pi_{3/2}$ | $f$ | $A'$ | 59 | 71.2 | 27.9 | 0.00 | 1698.32 |
| MgCN | $\kappa\Pi_{1/2}$ | $e$ | $A'$ | 32 | 48.8 | 50.9 | 0.01 | 1707.27 |
| MgCN | $\kappa\Pi_{3/2}$ | $f$ | $A'$ | 61 | 40.9 | 58.3 | 0.01 | 1709.19 |
| MgCN | $\kappa\Sigma_{1/2}$ | $e$ | $A'$ | 33 | 13.9 | 85.6 | 0.29 | 1711.81 |
| MgCN | $\mu\Sigma_{1/2}$ | $f$ | $A$" | 34 | 75.8 | 23.7 | 0.20 | 1715.58 |
| MgCN | $\kappa\Delta_{3/2}$ | $e$ | $A$" | 64 | 35.0 | 64.2 | 0.01 | 1722.11 |
| MgCN | $\mu\Delta_{3/2}$ | $f$ | $A'$ | 65 | 63.7 | 35.5 | 0.00 | 1729.23 |
| MgCN | $\mu\Pi_{1/2}$ | $f$ | $A$" | 35 | 64.9 | 35.0 | 0.01 | 1780.72 |
| MgCN | $\mu\Pi_{1/2}$ | $f$ | $A$" | 36 | 81.4 | 18.2 | 0.01 | 1805.24 |
| MgCN | $\mu\Pi_{3/2}$ | $e$ | $A$" | 67 | 81.2 | 18.2 | 0.01 | 1805.55 |
| MgCN | $\mu\Pi_{3/2}$ | $f$ | $A'$ | 69 | 67.1 | 32.5 | 0.00 | 1818.02 |
| MgCN | $\kappa\Sigma_{1/2}$ | $e$ | $A'$ | 37 | 7.1 | 92.7 | 0.46 | 1847.04 |
| MgCN | $\kappa\Delta_{3/2}$ | $e$ | $A$" | 71 | 29.6 | 69.8 | 0.09 | 1848.70 |
| MgCN | $\mu\Sigma_{1/2}$ | $f$ | $A$" | 38 | 92.4 | 7.4 | 0.35 | 1869.86 |
| MgCN | $\mu\Delta_{3/2}$ | $f$ | $A'$ | 73 | 77.8 | 21.5 | 0.00 | 1884.00 |
| MgCN | $\mu\Pi_{1/2}$ | $f$ | $A$" | 39 | 74.6 | 25.1 | 0.01 | 1918.45 |
| MgCN | $\mu\Pi_{3/2}$ | $f$ | $A'$ | 75 | 75.7 | 23.6 | 0.01 | 1921.71 |
| MgCN | $\mu\Sigma_{1/2}$ | $f$ | $A$" | 40 | 98.3 | 1.5 | 0.36 | 1930.34 |
| MgCN | $\kappa\Pi_{3/2}$ | $f$ | $A'$ | 77 | 21.8 | 77.6 | 0.01 | 1937.50 |
| MgCN | $\kappa\Pi_{1/2}$ | $f$ | $A$" | 41 | 20.6 | 78.9 | 0.00 | 1939.33 |

See footnote for Table 4.7

Table 4.9: Vibronic term values (in $cm^{-1}$) of MgNC. Energy levels with $P = J = 1/2, 3/2$ are listed here. When an energy have $e$ and $f$ pairs, the lower component and the splitting are given.

| State $(\nu_1, \nu_2, \nu_3)$ | | notation | | $\Gamma_{rve}$ | No.[a] | $P^b_-$ | $P^b_+$ | $\Delta^c_{ef}$ | DR[d] | RENNER[e] | PT[f] |
|---|---|---|---|---|---|---|---|---|---|---|---|
| MgCN | | $\kappa\Delta_{3/2}$ | $f$ | $A'$ | 79 | 37.1 | 62.3 | 0.00 | 1953.87 | | |
| MgCN | | $\mu\Sigma_{1/2}$ | $f$ | $A"$ | 42 | 99.1 | 0.7 | 0.51 | 1963.44 | | |
| MgCN | | $\kappa\Sigma_{1/2}$ | $e$ | $A'$ | 43 | 1.0 | 98.7 | 0.48 | 1973.05 | | |
| MgCN | | $\mu\Delta_{3/2}$ | $e$ | $A"$ | 82 | 82.0 | 17.0 | 0.02 | 1975.51 | | |
| MgNC, Fig. 4.4 | $(0,0,0)$ | $\Pi_{1/2}$ | $f$ | $A"$ | 44 | 60.4 | 39.6 | 0.00 | 1983.99 | | |
| MgCN | | $\mu\Delta_{3/2}$ | $f$ | $A'$ | 84 | 62.0 | 37.4 | 0.00 | 1988.04 | | |
| MgNC | $(0,0,0)$ | $\Pi_{3/2}$ | $e$ | $A"$ | 85 | 60.9 | 39.0 | 0.01 | 2018.20 | | |
| MgCN | | $\mu\Pi_{3/2}$ | $e$ | $A"$ | 86 | 77.6 | 21.7 | 0.05 | 2040.37 | | |
| MgCN | | $\mu\Pi_{1/2}$ | $f$ | $A"$ | 45 | 77.4 | 22.4 | 0.06 | 2041.25 | | |
| MgCN | | $\kappa\Sigma_{1/2}$ | $e$ | $A'$ | 46 | 1.7 | 98.1 | 0.35 | 2078.06 | | |
| MgCN | | $\kappa\Pi_{1/2}$ | $e$ | $A'$ | 47 | 29.3 | 70.5 | 0.01 | 2088.52 | | |
| MgCN | | $\kappa\Pi_{3/2}$ | $f$ | $A'$ | 89 | 28.8 | 70.4 | 0.04 | 2088.74 | | |
| MgCN | | $\mu\Sigma_{1/2}$ | $f$ | $A"$ | 48 | 99.3 | 0.5 | 0.41 | 2111.39 | | |
| MgNC | $(0,1,0)$ | $\mu\Sigma_{1/2}$ | $f$ | $A"$ | 49 | 96.5 | 3.4 | 0.34 | 2112.80 | | |
| MgCN | | $\mu\Delta_{3/2}$ | $f$ | $A'$ | 93 | 76.6 | 22.8 | 0.01 | 2123.11 | | |
| MgCN | | $\mu\Pi_{1/2}$ | $f$ | $A"$ | 50 | 74.1 | 25.6 | 0.04 | 2124.33 | | |
| MgCN | | $\mu\Pi_{3/2}$ | $f$ | $A'$ | 95 | 75.1 | 24.0 | 0.02 | 2126.18 | | |
| MgCN | $(1,0,0)$ | $\Pi_{1/2}$ | $f$ | $A"$ | 51 | 59.7 | 40.2 | 0.01 | 2126.37 | 2137.0 | 2134.6 |
| MgCN | | $\mu\Pi_{1/2}$ | $f$ | $A"$ | 52 | 77.9 | 21.8 | 0.04 | 2133.45 | | |
| MgCN | | $\mu\Pi_{3/2}$ | $f$ | $A'$ | 98 | 79.6 | 19.4 | 0.00 | 2135.50 | | |
| MgNC | $(0,1,0)$ | $\Delta_{3/2}$ | $f$ | $A'$ | 99 | 66.0 | 33.8 | 0.00 | 2140.84 | | |
| MgCN | | $\kappa\Sigma_{3/2}$ | $e$ | $A'$ | 53 | 1.5 | 98.2 | 0.67 | 2148.04 | | |
| MgCN | | $\kappa\Delta_{3/2}$ | $f$ | $A'$ | 101 | 21.6 | 77.6 | 0.00 | 2159.98 | | |
| MgCN | $(1,0,0)$ | $\Pi_{3/2}$ | $f$ | $A'$ | 102 | 60.0 | 40.0 | 0.00 | 2164.55 | 2175.6 | 2173.7 |
| MgNC | $(0,1,0)$ | $\kappa\Sigma_{1/2}$ | $e$ | $A'$ | 54 | 3.6 | 96.4 | 0.36 | 2204.62 | | |
| MgCN | | $\mu\Sigma_{1/2}$ | $f$ | $A"$ | 55 | 98.9 | 0.8 | 0.61 | 2207.10 | | |
| MgCN | | $\mu\Delta_{3/2}$ | $f$ | $A'$ | 105 | 75.8 | 23.2 | 0.01 | 2218.41 | | |
| MgCN | | $\kappa\Pi_{3/2}$ | $e$ | $A"$ | 106 | 25.6 | 73.4 | 0.02 | 2223.66 | | |
| MgCN | | $\kappa\Pi_{1/2}$ | $e$ | $A'$ | 56 | 25.2 | 74.5 | 0.01 | 2228.44 | | |
| MgNC | $(0,2,0)$ | $\mu\Pi_{1/2}$ | $f$ | $A"$ | 57 | 68.2 | 31.8 | 0.10 | 2247.78 | | |
| MgNC | $(0,2,0)$ | $\mu\Pi_{3/2}$ | $f$ | $A'$ | 109 | 69.9 | 30.0 | 0.04 | 2251.88 | | |
| MgCN | | $\mu\Sigma_{1/2}$ | $f$ | $A"$ | 58 | 97.7 | 1.9 | 0.68 | 2287.15 | | |
| MgCN | | $\mu\Delta_{3/2}$ | $f$ | $A'$ | 111 | 73.5 | 25.4 | 0.09 | 2299.95 | | |
| MgCN | | $\mu\Pi_{1/2}$ | $f$ | $A"$ | 59 | 77.9 | 21.6 | 0.05 | 2300.31 | | |
| MgCN | | $\mu\Pi_{3/2}$ | $f$ | $A'$ | 113 | 78.4 | 20.0 | 0.03 | 2305.33 | | |
| MgCN | | $\kappa\Sigma_{1/2}$ | $e$ | $A'$ | 60 | 3.1 | 96.4 | 0.55 | 2312.14 | | |
| MgCN | $(1,1,0)$ | $\mu\Sigma_{1/2}$ | $f$ | $A"$ | 61 | 97.5 | 2.4 | 0.34 | 2318.26 | 2348.5 | 2326.9 |
| MgCN | | $\kappa\Delta_{3/2}$ | $e$ | $A"$ | 115 | 37.3 | 61.9 | 0.01 | 2318.52 | | |
| MgCN | | $\kappa\Pi_{3/2}$ | $f$ | $A'$ | 117 | 35.6 | 63.3 | 0.00 | 2319.82 | | |
| MgCN | | $\kappa\Pi_{1/2}$ | $f$ | $A"$ | 62 | 39.8 | 59.9 | 0.06 | 2320.93 | | |

See footnote for Table 4.7

Table 4.10: Vibronic term values (in $cm^{-1}$) of MgNC. Energy levels with $P = J = 1/2, 3/2$ are listed here. When an energy have $e$ and $f$ pairs, the lower component and the splitting are given.

| State ($\nu_1, \nu_2, \nu_3$) | | notation | | $\Gamma_{rve}$ | No.[a] | $P^b_-$ | $P^b_+$ | $\Delta^c_{ef}$ | DR[d] | RENNER[e] | PT[f] |
|---|---|---|---|---|---|---|---|---|---|---|---|
| MgCN | | $\mu\Sigma_{1/2}$ | $f$ | $A$" | 63 | 92.2 | 7.5 | 0.37 | 2327.76 | | |
| MgCN | | $\mu\Delta_{3/2}$ | $f$ | $A'$ | 120 | 69.8 | 29.3 | 0.00 | 2337.68 | | |
| MgCN | (1, 1, 0) | $\Delta_{3/2}$ | $f$ | $A'$ | 121 | 64.4 | 35.4 | 0.00 | 2357.93 | 2383.9 | 2369.8 |
| MgNC | (0, 3, 0) | $\mu\Sigma_{3/2}$ | $f$ | $A$" | 64 | 95.9 | 4.0 | 0.28 | 2365.37 | | |
| MgCN | | $\kappa\Pi_{3/2}$ | $f$ | $A'$ | 123 | 23.0 | 76.3 | 0.01 | 2366.43 | | |
| MgNC | (0, 2, 0) | $\kappa\Pi_{3/2}$ | $f$ | $A'$ | 124 | 36.8 | 63.0 | 0.02 | 2369.54 | | |
| MgCN | | $\kappa\Pi_{1/2}$ | $e$ | $A'$ | 65 | 29.0 | 70.4 | 0.07 | 2371.75 | | |
| MgNC | (0, 2, 0) | $\kappa\Pi_{1/2}$ | $e$ | $A'$ | 66 | 39.5 | 60.5 | 0.15 | 2375.31 | | |
| MgCN | | $\mu\Pi_{1/2}$ | $f$ | $A$" | 67 | 72.6 | 27.0 | 0.19 | 2380.47 | | |
| MgNC | (0, 3, 0) | $\mu\Delta_{3/2}$ | $f$ | $A'$ | 128 | 70.6 | 29.0 | 0.02 | 2383.71 | | |
| MgCN | | $\mu\Pi_{3/2}$ | $f$ | $A'$ | 129 | 78.3 | 20.7 | 0.06 | 2385.53 | | |
| MgCN | (1, 1, 0) | $\kappa\Sigma_{1/2}$ | $e$ | $A'$ | 68 | 2.4 | 97.6 | 0.34 | 2441.19 | 2470.6 | 2451.8 |
| MgCN | | $\mu\Pi_{1/2}$ | $f$ | $A$" | 69 | 85.4 | 14.3 | 0.30 | 2455.86 | | |
| MgCN | | $\mu\Pi_{3/2}$ | $e$ | $A$" | 131 | 85.7 | 13.7 | 1.11 | 2457.05 | | |
| MgCN | | $\kappa\Delta_{3/2}$ | $f$ | $A'$ | 133 | 28.6 | 70.5 | 0.01 | 2462.44 | | |
| MgCN | | $\kappa\Sigma_{1/2}$ | $e$ | $A'$ | 70 | 17.4 | 82.1 | 0.40 | 2465.98 | | |
| BENT, Fig. 4.5 | (0, 0, 0) | $\kappa\Pi_{1/2}$ | | $A$" | 71 | 0.0 | 100.0 | | 2469.19 | | |
| MgCN | | $\mu\Sigma_{1/2}$ | $f$ | $A$" | 73 | 80.0 | 19.6 | 0.39 | 2483.50 | | |
| MgNC | (0, 4, 0) | $\mu\Pi_{1/2}$ | $f$ | $A$" | 74 | 77.4 | 22.5 | 0.38 | 2487.86 | | |
| MgNC | (0, 4, 0) | $\mu\Pi_{3/2}$ | $f$ | $A'$ | 141 | 79.4 | 20.3 | 0.10 | 2492.43 | | |
| MgCN | | $\mu\Delta_{3/2}$ | $f$ | $A'$ | 142 | 75.2 | 24.2 | 0.01 | 2494.28 | | |
| MgCN | | $\mu\Pi_{1/2}$ | $f$ | $A$" | 75 | 65.2 | 34.6 | 0.00 | 2518.43 | | |
| MgNC | | $\mu\Pi_{3/2}$ | $f$ | $A'$ | 144 | 66.4 | 33.3 | 0.00 | 2524.19 | | |
| MgCN | | $\mu\Pi_{1/2}$ | $f$ | $A$" | 76 | 76.4 | 23.3 | 0.05 | 2530.13 | | |
| MgNC | (0, 3, 0) | $\kappa\Sigma_{1/2}$ | $e$ | $A'$ | 77 | 1.9 | 98.0 | 0.62 | 2532.71 | | |
| MgNC | (0, 3, 0) | $\mu\Pi_{3/2}$ | $f$ | $A'$ | 146 | 77.1 | 22.1 | 0.03 | 2533.53 | | |
| MgNC | | $\kappa\Delta_{3/2}$ | $e$ | $A$" | 148 | 29.9 | 69.7 | 0.02 | 2537.20 | | |
| MgCN | | $\kappa\Pi_{3/2}$ | $f$ | $A'$ | 149 | 20.6 | 78.5 | 0.00 | 2542.36 | | |
| MgCN | | $\mu\Pi_{1/2}$ | $f$ | $A$" | 78 | 50.3 | 48.9 | 0.29 | 2543.23 | | |
| MgCN | | $\mu\Sigma_{1/2}$ | $f$ | $A$" | 79 | 65.0 | 34.5 | 0.61 | 2546.11 | | |
| MgCN | | $\mu\Delta_{3/2}$ | $e$ | $A$" | 152 | 60.5 | 38.2 | 0.06 | 2557.20 | | |
| MgCN | | $\kappa\Delta_{3/2}$ | $e$ | $A$" | 153 | 45.4 | 53.7 | 0.02 | 2564.33 | | |
| MgCN | | $\kappa\Sigma_{1/2}$ | $e$ | $A'$ | 80 | 4.1 | 95.4 | 0.74 | 2567.66 | | |
| MgNC | (0, 0, 1) | $\Pi_{1/2}$ | $f$ | $A$" | 81 | 60.1 | 39.8 | 0.00 | 2571.69 | | |
| MgCN | | $\kappa\Delta_{3/2}$ | $f$ | $A'$ | 156 | 28.2 | 71.1 | 0.01 | 2583.01 | | |
| MgCN | | $\kappa\Sigma_{1/2}$ | $e$ | $A'$ | 82 | 0.8 | 99.0 | 0.50 | 2583.15 | | |
| MgNC | (0, 5, 0) | $\mu\Sigma_{1/2}$ | $f$ | $A$" | 83 | 98.8 | 1.1 | 0.52 | 2595.79 | | |
| MgNC | (0, 0, 1) | $\Pi_{3/2}$ | $f$ | $A'$ | 159 | 60.6 | 39.3 | 0.00 | 2605.87 | | |
| MgNC | (0, 5, 0) | $\mu\Delta_{3/2}$ | $f$ | $A'$ | 160 | 80.5 | 19.1 | 0.07 | 2610.50 | | |
| MgCN | | $\mu\Sigma_{3/2}$ | $f$ | $A$" | 84 | 98.7 | 1.0 | 3.45 | 2614.48 | | |

See footnote for Table 4.7

Table 4.11: Vibronic term values (in $cm^{-1}$) of MgNC. Energy levels with $P = J = 1/2, 3/2$ are listed here. When an energy have $e$ and $f$ pairs, the lower component and the splitting are given.

| State $(\nu_1, \nu_2, \nu_3)$ | | notation | | $\Gamma_{\rm rve}$ | No.[a] | $P^b_-$ | $P^b_+$ | $\Delta^c_{ef}$ | DR[d] | RENNER[e] | PT[f] |
|---|---|---|---|---|---|---|---|---|---|---|---|
| MgCN | | $\mu\Delta_{3/2}$ | $f$ | $A'$ | 162 | 83.3 | 16.1 | 2.72 | 2629.45 | | |
| MgCN | $(1,0,1)$ | $\Pi_{1/2}$ | $f$ | $A"$ | 85 | 58.8 | 41.0 | 0.01 | 2636.56 | 2659.8 | 2681.8 |
| MgCN | | $\mu\Pi_{1/2}$ | $f$ | $A"$ | 86 | 63.2 | 36.5 | 0.01 | 2638.35 | | |
| MgCN | | $\mu\Pi_{3/2}$ | $e$ | $A"$ | 165 | 70.9 | 28.1 | 0.08 | 2658.32 | | |
| MgCN | | $\mu\Pi_{1/2}$ | $f$ | $A"$ | 87 | 74.0 | 25.7 | 0.25 | 2661.15 | | |
| MgCN | $(1,0,1)$ | $\Pi_{3/2}$ | $f$ | $A'$ | 167 | 55.6 | 44.0 | 0.01 | 2662.97 | 2693.8 | 2720.9 |
| MgCN | | $\mu\Pi_{3/2}$ | $f$ | $A'$ | 168 | 70.6 | 28.7 | 0.01 | 2671.82 | | |
| MgNC | $(0,4,0)$ | $\kappa\Pi_{3/2}$ | $f$ | $A'$ | 169 | 24.2 | 75.4 | 0.11 | 2688.34 | | |
| MgCN | | $\mu\Sigma_{1/2}$ | $f$ | $A"$ | 88 | 99.2 | 0.6 | 0.47 | 2691.32 | | |
| MgNC | $(0,4,0)$ | $\kappa\Pi_{1/2}$ | $e$ | $A'$ | 89 | 25.8 | 74.1 | 0.27 | 2694.11 | | |
| MgCN | | $\mu\Pi_{1/2}$ | $f$ | $A"$ | 90 | 54.1 | 45.8 | 0.02 | 2699.58 | | |
| MgCN | | $\mu\Sigma_{1/2}$ | $f$ | $A"$ | 91 | 90.3 | 9.6 | 0.35 | 2703.79 | | |
| MgNC | $(0,1,1)$ | $\mu\Sigma_{1/2}$ | $f$ | $A"$ | 92 | 96.5 | 3.4 | 0.35 | 2704.90 | | |
| MgCN | | $\kappa\Pi_{3/2}$ | $f$ | $A'$ | 175 | 46.2 | 53.6 | 0.01 | 2706.68 | | |
| MgCN | | $\kappa\Pi_{1/2}$ | $f$ | $A"$ | 93 | 32.1 | 67.0 | 0.23 | 2709.95 | | |
| MgCN | | $\kappa\Pi_{3/2}$ | $f$ | $A'$ | 177 | 35.9 | 62.7 | 0.03 | 2713.60 | | |
| MgNC | $(0,6,0)$ | $\mu\Pi_{1/2}$ | $f$ | $A"$ | 94 | 78.4 | 21.4 | 0.34 | 2715.79 | | |
| MgCN | | $\mu\Pi_{3/2}$ | $e$ | $A"$ | 179 | 78.7 | 19.5 | 0.82 | 2719.93 | | |
| MgCN | | $\mu\Pi_{1/2}$ | $e$ | $A'$ | 95 | 78.5 | 20.7 | 1.14 | 2720.72 | | |
| MgCN | | $\mu\Pi_{3/2}$ | $f$ | $A'$ | 180 | 71.8 | 26.3 | 0.33 | 2721.31 | | |
| MgNC | $(0,6,0)$ | $\mu\Pi_{3/2}$ | $f$ | $A'$ | 181 | 80.5 | 18.8 | 0.44 | 2721.91 | | |
| MgCN | | $\mu\Delta_{3/2}$ | $e$ | $A"$ | 182 | 77.5 | 21.2 | 0.05 | 2725.19 | | |
| MgCN | | $\mu\Delta_{3/2}$ | $f$ | $A'$ | 183 | 69.6 | 29.9 | 0.00 | 2726.73 | | |
| MgNC | $(0,1,1)$ | $\Delta_{3/2}$ | $f$ | $A'$ | 184 | 65.3 | 34.4 | 0.00 | 2733.29 | | |
| BENT, Fig. 4.6 | $(0,1,0)$ | $\kappa\Pi_{1/2}$ | | $A"$ | 96 | 0.0 | 99.9 | | 2743.74 | | |
| MgCN | | $\kappa\Sigma_{1/2}$ | $e$ | $A'$ | 98 | 0.9 | 98.7 | 0.78 | 2753.30 | | |
| MgCN | | $\mu\Sigma_{1/2}$ | $f$ | $A"$ | 99 | 97.6 | 2.1 | 0.55 | 2755.65 | | |
| MgCN | | $\kappa\Delta_{3/2}$ | $f$ | $A'$ | 191 | 20.5 | 78.2 | 0.04 | 2762.68 | | |
| MgCN | | $\kappa\Pi_{3/2}$ | $e$ | $A"$ | 192 | 35.0 | 64.2 | 0.63 | 2778.25 | | |
| MgCN | | $\kappa\Pi_{1/2}$ | $f$ | $A"$ | 100 | 32.9 | 66.7 | 0.75 | 2786.17 | | |
| MgCN | | $\mu\Delta_{3/2}$ | $f$ | $A'$ | 193 | 70.8 | 28.1 | 0.01 | 2786.84 | | |
| MgCN | | $\mu\Pi_{1/2}$ | $f$ | $A"$ | 101 | 65.4 | 34.0 | 2.47 | 2794.92 | | |
| MgNC | $(0,1,1)$ | $\kappa\Sigma_{1/2}$ | $e$ | $A'$ | 101 | 3.6 | 96.3 | 0.34 | 2796.22 | | |
| MgCN | | $\mu\Pi_{3/2}$ | $e$ | $A"$ | 196 | 66.6 | 32.7 | 5.23 | 2799.63 | | |
| MgNC | $(0,7,0)$ | $\mu\Sigma_{1/2}$ | $f$ | $A"$ | 103 | 77.8 | 22.0 | 1.93 | 2820.05 | | |
| MgCN(+MgNC), Fig. 4.7 | | $\mu\Sigma_{1/2}$ | $f$ | $A"$ | 104 | 91.7 | 7.7 | 1.00 | 2834.59 | | |
| MgNC | | $\kappa\Delta_{3/2}$ | $e$ | $A"$ | 199 | 35.4 | 63.7 | 0.84 | 2835.60 | | |
| MgNC(+MgCN), Fig. 4.8 | | $\mu\Sigma_{1/2}$ | $e$ | $A'$ | 104 | 50.1 | 49.2 | 0.48 | 2835.71 | | |
| MgCN | | $\kappa\Pi_{3/2}$ | $e$ | $A"$ | 200 | 39.3 | 59.1 | 0.64 | 2837.37 | | |
| MgNC | | $\kappa\Delta_{3/2}$ | $f$ | $A'$ | 201 | 34.2 | 65.0 | 1.72 | 2837.67 | | |

See footnote for Table 4.7

Table 4.12: Vibronic term values (in $cm^{-1}$) of MgNC. Energy levels with $P = J = 1/2, 3/2$ are listed here. When an energy have $e$ and $f$ pairs, the lower component and the splitting are given.

| State $(\nu_1, \nu_2, \nu_3)$ | | notation | | $\Gamma_{\rm rve}$ | No.[a] | $P^b_-$ | $P^b_+$ | $\Delta^c_{ef}$ | DR[d] | RENNER[e] | PT[f] |
|---|---|---|---|---|---|---|---|---|---|---|---|
| MgCN | $(1,1,1)$ | $\mu\Sigma_{1/2}$ | $f$ | $A$" | 106 | 97.1 | 2.8 | 0.35 | 2841.79 | 2891.0 | 2902.0 |
| MgCN | | $\kappa\Pi_{1/2}$ | $e$ | $A'$ | 106 | 28.6 | 71.0 | 0.03 | 2841.91 | | |
| MgCN(+MgNC) | | $\mu\Delta_{3/2}$ | $f$ | $A'$ | 205 | 65.1 | 33.6 | 0.62 | 2844.41 | | |
| MgNC | $(0,2,1)$ | $\mu\Pi_{1/2}$ | $f$ | $A$" | 108 | 67.3 | 32.5 | 0.13 | 2844.59 | | |
| MgNC(+MgCN) | | $\mu\Delta_{3/2}$ | $f$ | $A'$ | 207 | 68.6 | 30.0 | 0.30 | 2845.44 | | |
| MgNC | | $\mu\Pi_{3/2}$ | $f$ | $A'$ | 208 | 69.1 | 30.6 | 0.06 | 2848.86 | | |
| MgCN | | $\mu\Pi_{1/2}$ | $f$ | $A$" | 109 | 74.9 | 24.8 | 0.10 | 2854.70 | | |
| MgCN | | $\mu\Pi_{3/2}$ | $f$ | $A'$ | 210 | 76.1 | 22.7 | 0.05 | 2861.49 | | |
| MgCN | $(1,1,1)$ | $\mu\Delta_{3/2}$ | $f$ | $A'$ | 211 | 56.7 | 43.0 | 0.00 | 2871.16 | 2912.7 | 2944.9 |
| MgCN | | $\mu\Sigma_{1/2}$ | $f$ | $A$" | 110 | 98.8 | 0.8 | 1.53 | 2873.62 | | |
| MgCN | | $\mu\Delta_{3/2}$ | $f$ | $A'$ | 213 | 81.0 | 17.9 | 0.70 | 2885.70 | | |
| MgCN | | $\mu\Pi_{1/2}$ | $f$ | $A$" | 111 | 73.3 | 26.4 | 0.02 | 2891.15 | | |
| MgCN | | $\mu\Pi_{3/2}$ | $f$ | $A'$ | 215 | 75.4 | 24.2 | 0.00 | 2895.64 | | |
| MgCN | | $\kappa\Sigma_{1/2}$ | $e$ | $A'$ | 112 | 1.8 | 98.0 | 0.39 | 2898.80 | | |
| MgCN | $(1,1,1)$ | $\kappa\Sigma_{1/2}$ | $e$ | $A'$ | 113 | 3.0 | 96.9 | 0.38 | 2911.54 | 3033.5 | 3026.9 |
| MgCN | | $\kappa\Sigma_{1/2}$ | $e$ | $A'$ | 114 | 0.9 | 98.7 | 0.67 | 2936.90 | | |
| MgCN | | $\kappa\Delta_{3/2}$ | $e$ | $A$" | 219 | 27.5 | 71.3 | 0.24 | 2939.22 | | |
| MgCN | | $\kappa\Delta_{3/2}$ | $f$ | $A'$ | 220 | 42.6 | 56.7 | 0.00 | 2949.74 | | |
| MgCN | | $\mu\Pi_{1/2}$ | $f$ | $A$" | 115 | 76.0 | 23.6 | 0.12 | 2953.39 | | |
| MgCN | | $\mu\Pi_{3/2}$ | $f$ | $A'$ | 222 | 76.0 | 22.5 | 0.16 | 2956.09 | | |
| MgNC | | $\kappa\Pi_{3/2}$ | $e$ | $A$" | 223 | 37.5 | 61.7 | 0.13 | 2957.06 | | |
| MgCN | | $\mu\Sigma_{1/2}$ | $f$ | $A$" | 116 | 93.9 | 5.6 | 3.32 | 2961.49 | | |
| MgNC | | $\mu\Sigma_{1/2}$ | $f$ | $A$" | 117 | 78.5 | 21.4 | 0.34 | 2964.74 | | |
| MgNC | | $\mu\Pi_{3/2}$ | $e$ | $A$" | 225 | 51.4 | 48.1 | 0.34 | 2966.69 | | |
| MgNC | | $\mu\Pi_{1/2}$ | $f$ | $A$" | 118 | 51.2 | 48.6 | 0.20 | 2968.16 | | |
| MgNC | | $\mu\Pi_{1/2}$ | $f$ | $A$" | 119 | 56.4 | 43.5 | 1.10 | 2969.96 | | |
| MgCN | | $\mu\Delta_{3/2}$ | $f$ | $A'$ | 228 | 55.9 | 42.5 | 1.35 | 2971.59 | | |
| MgCN | | $\kappa\Pi_{3/2}$ | $e$ | $A$" | 230 | 18.5 | 79.9 | 0.21 | 2975.74 | | |
| MgCN | | $\kappa\Sigma_{1/2}$ | $e$ | $A'$ | 120 | 6.9 | 92.5 | 0.29 | 2977.35 | | |
| MgCN | | $\kappa\Pi_{3/2}$ | $e$ | $A$" | 231 | 13.0 | 85.6 | 0.63 | 2978.71 | | |
| MgCN | | $\kappa\Pi_{1/2}$ | $f$ | $A$" | 121 | 15.2 | 84.2 | 0.74 | 2979.91 | | |
| MgNC | | $\mu\Delta_{3/2}$ | $e$ | $A$" | 232 | 70.3 | 29.0 | 0.01 | 2984.70 | | |
| MgNC | | $\kappa\Pi_{1/2}$ | $f$ | $A$" | 122 | 42.5 | 57.1 | 0.06 | 2987.41 | | |
| MgCN | | $\kappa\Sigma_{1/2}$ | $e$ | $A'$ | 123 | 1.5 | 98.4 | 0.37 | 2988.13 | | |
| MgNC | | $\kappa\Pi_{3/2}$ | $f$ | $A'$ | 236 | 45.0 | 54.3 | 0.75 | 2994.74 | | |
| MgCN | | $\kappa\Delta_{3/2}$ | $f$ | $A'$ | 237 | 46.3 | 52.3 | 0.37 | 3000.12 | | |
| BENT, Fig. 4.9 | $(0,2,0)$ | $\kappa\Pi_{1/2}$ | | $A$" | 124 | 0.0 | 99.9 | | 3011.69 | | |
| MgCN | | $\mu\Pi_{1/2}$ | $e$ | $A'$ | 125 | 87.6 | 11.5 | 0.03 | 3014.74 | | |
| MgCN | | $\mu\Pi_{3/2}$ | $f$ | $A'$ | 240 | 86.0 | 12.2 | 0.24 | 3015.49 | | |
| MgCN | | $\mu\Pi_{3/2}$ | $e$ | $A$" | 241 | 85.4 | 12.6 | 0.05 | 3017.10 | | |

See footnote for Table 4.7

Table 4.13: Vibronic term values (in $cm^{-1}$) of MgNC. Energy levels with $P = J = 1/2, 3/2$ are listed here. When an energy have $e$ and $f$ pairs, the lower component and the splitting are given.

| State ($\nu_1, \nu_2, \nu_3$) | | notation | | $\Gamma_{rve}$ | No.[a] | $P^b_-$ | $P^b_+$ | $\Delta^c_{ef}$ | DR[d] |
|---|---|---|---|---|---|---|---|---|---|
| MgCN | | $\mu\Sigma_{1/2}$ | $f$ | $A$" | 126 | 99.3 | 0.6 | 1.41 | 3017.59 |
| MgCN | | $\mu\Pi_{1/2}$ | $f$ | $A$" | 128 | 84.3 | 15.5 | 1.61 | 3030.45 |
| MgCN | | $\mu\Pi_{3/2}$ | $e$ | $A$" | 245 | 83.2 | 15.8 | 1.59 | 3030.98 |
| MgCN | | $\mu\Delta_{3/2}$ | $f$ | $A'$ | 245 | 75.3 | 23.3 | 0.37 | 3031.50 |
| MgCN | | $\mu\Pi_{3/2}$ | $f$ | $A'$ | 247 | 80.4 | 17.8 | 5.95 | 3034.07 |
| MgCN | | $\mu\Pi_{1/2}$ | $e$ | $A'$ | 129 | 66.9 | 32.8 | 0.01 | 3052.01 |
| MgCN | | $\mu\Pi_{3/2}$ | $f$ | $A'$ | 249 | 66.4 | 33.1 | 0.00 | 3056.40 |
| MgCN | | $\mu\Sigma_{1/2}$ | $f$ | $A$" | 130 | 99.4 | 0.5 | 0.38 | 3069.40 |
| MgCN | | $\kappa\Delta_{3/2}$ | $f$ | $A'$ | 251 | 28.0 | 70.6 | 0.02 | 3086.12 |
| MgCN | | $\mu\Delta_{3/2}$ | $f$ | $A'$ | 252 | 72.9 | 26.5 | 0.00 | 3086.51 |
| MgCN | | $\kappa\Pi_{3/2}$ | $f$ | $A'$ | 253 | 24.8 | 74.1 | 0.01 | 3088.28 |
| MgNC | | $\kappa\Sigma_{1/2}$ | $f$ | $A$" | 131 | 47.0 | 52.6 | 1.73 | 3088.57 |
| MgCN | | $\kappa\Pi_{1/2}$ | $e$ | $A'$ | 132 | 24.5 | 75.2 | 0.02 | 3091.09 |
| MgCN | | $\kappa\Sigma_{1/2}$ | $e$ | $A'$ | 133 | 2.6 | 97.0 | 0.63 | 3092.58 |
| MgNC | | $\mu\Pi_{1/2}$ | $f$ | $A$" | 134 | 76.6 | 22.9 | 0.69 | 3095.51 |
| MgNC | | $\kappa\Delta_{3/2}$ | $e$ | $A$" | 258 | 39.9 | 59.7 | 1.59 | 3098.21 |
| MgNC | | $\mu\Sigma_{1/2}$ | $f$ | $A$" | 135 | 56.8 | 42.9 | 4.29 | 3100.46 |
| MgNC | | $\mu\Pi_{3/2}$ | $f$ | $A'$ | 259 | 77.8 | 21.4 | 0.34 | 3100.74 |
| | | | | | | | | | |
| BENT, Fig. 4.10 | $(0, 3, 0)$ | $\kappa\Pi_{1/2}$ | | $A$" | 154 | 0.0 | 90.8 | | 3259.33 |
| BENT+(MgCN), Fig. 4.11 | | $\mu\Sigma_{1/2}$ | | $A$" | 158 | 96.9 | 0.0 | | 3294.02 |
| BENT+(MgCN, MgNC), Fig. 4.12 | $(0, 0, 0)$ | $\mu\Pi_{1/2}$ | | $A$" | 161 | 97.0 | 0.7 | | 3317.86 |
| BENT+(MgCN), Fig. 4.13 | | $\mu\Sigma_{1/2}$ | | $A$" | 162 | 99.2 | 0.0 | | 3325.06 |
| MgCN+(Delocalized), Fig. 4.14 | | $\mu\Sigma_{1/2}$ | | $A$" | 168 | 95.0 | 0.0 | | 3369.54 |
| MgNC+(Delocalized), Fig. 4.15 | | $\mu\Sigma_{1/2}$ | | $A$" | 171 | 98.3 | 0.0 | | 3382.86 |
| MgCN+(Delocalized), Fig. 4.16 | | $\mu\Pi_{1/2}$ | | $A$" | 178 | 89.4 | 7.0 | | 3424.07 |
| MgNC+(Delocalized), Fig. 4.17 | | $\mu\Sigma_{1/2}$ | | $A$" | 180 | 52.4 | 39.7 | | 3435.41 |
| MgNC+(Delocalized), Fig. 4.18 | | $\mu\Sigma_{1/2}$ | | $A$" | 182 | 46.4 | 46.0 | | 3441.50 |
| MgNC+(Delocalized), Fig. 4.19 | | $\mu\Sigma_{1/2}$ | | $A$" | 185 | 97.8 | 0.0 | | 3493.14 |
| Delocalized, Fig. 4.20 | | $\kappa\Pi_{1/2}$ | | $A$" | 186 | 37.4 | 56.2 | | 3512.87 |
| Delocalized, Fig. 4.21 | | $\mu\Sigma_{1/2}$ | | $A$" | 187 | 75.5 | 20.3 | | 3514.34 |

See footnote for Table 4.7

(a)

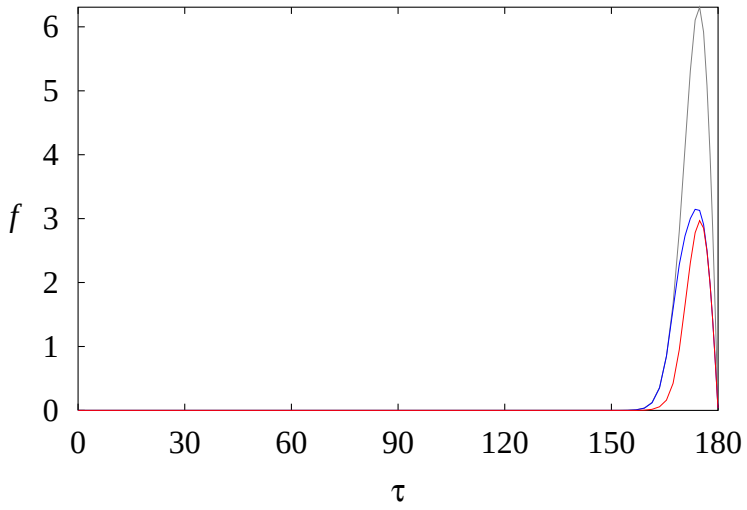


(b)

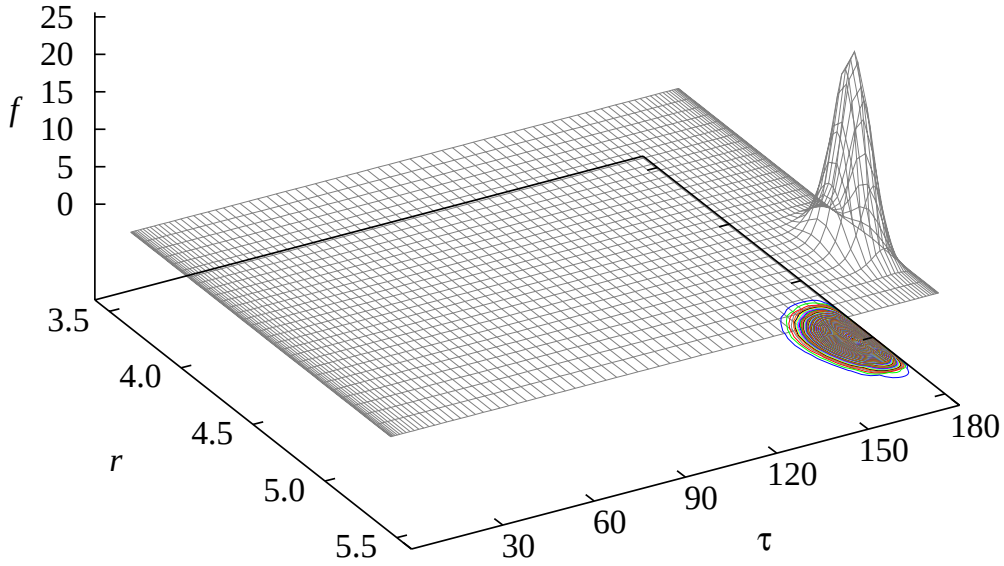


Figure 4.3: Probability density functions (See 2.5.3) for the $\widetilde{A}^2\Pi$ MgCN $(0,0,0)$ state.

Here, the $\tau$ and $r$ coordinates are given in degrees and Bohr, respectively. Figure (a) shows one-dimensional probability density functions. The blue curve is $f_-(\tau)$ (the lower electronic surface's probability density function), the red curve is $f_+(\tau)$ (the upper electronic surface's probability density function) and the black curve is $f(\tau)$ (the total probability density function). The gray surface in Figure (b) shows the two-dimensional probability density function $f(r,\tau)$. Coloured lines are the contour plot of the two-dimensional probability density function $f(r,\tau)$. Contours are plotted for 0.1 separations.

(a)

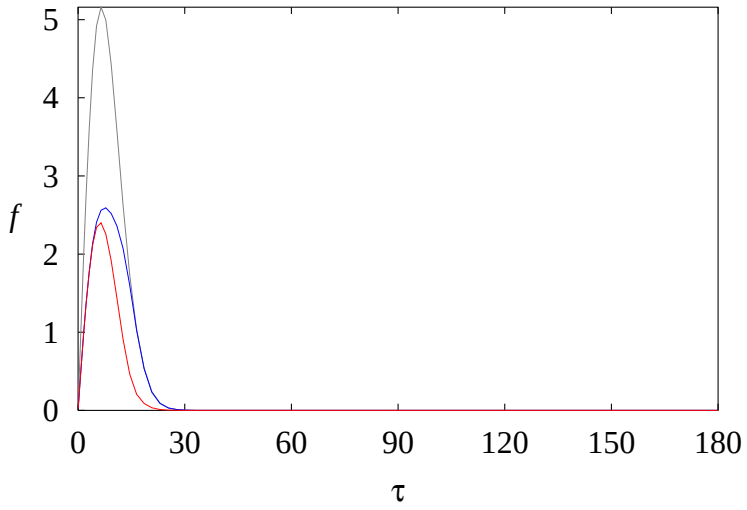


(b)

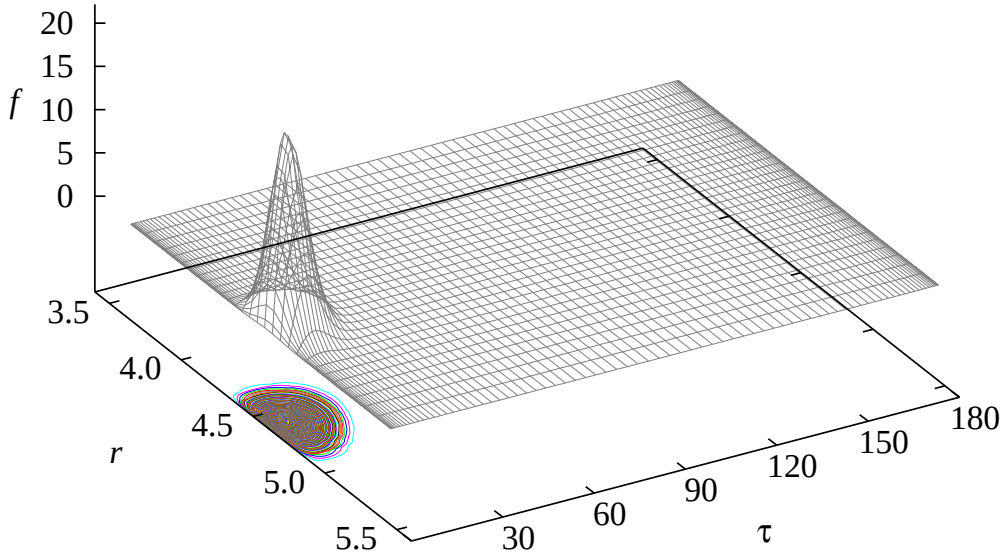


Figure 4.4: Probability density functions (See 2.5.3) for the $\widetilde{A}^2\Pi$MgNC $(0,0,0)$ state.

Here, the $\tau$ and $r$ coordinates are given in degrees and Bohr, respectively. Figure (a) shows one-dimensional probability density functions. The blue curve is $f_-(\tau)$ (the lower electronic surface's probability density function), the red curve is $f_+(\tau)$ (the upper electronic surface's probability density function) and the black curve is $f(\tau)$ (the total probability density function). The gray surface in Figure (b) shows the two-dimensional probability density function $f(r,\tau)$. Coloured lines are the contour plot of the two-dimensional probability density function $f(r,\tau)$. Contours are plotted for 0.1 separations.

(a)

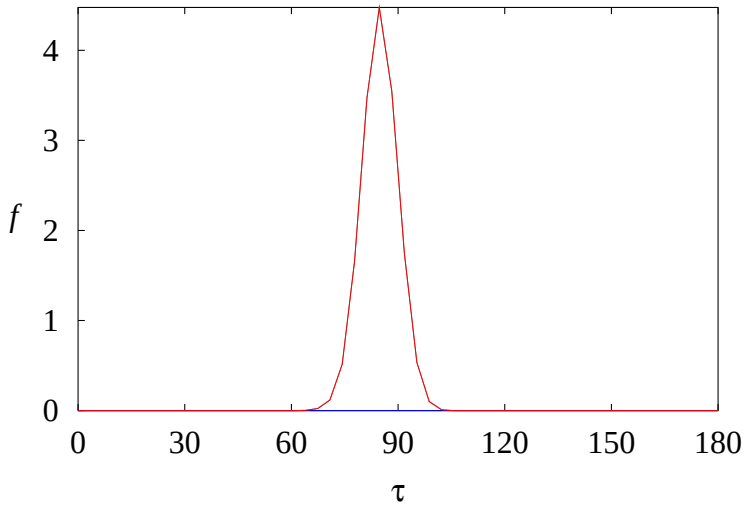


(b)

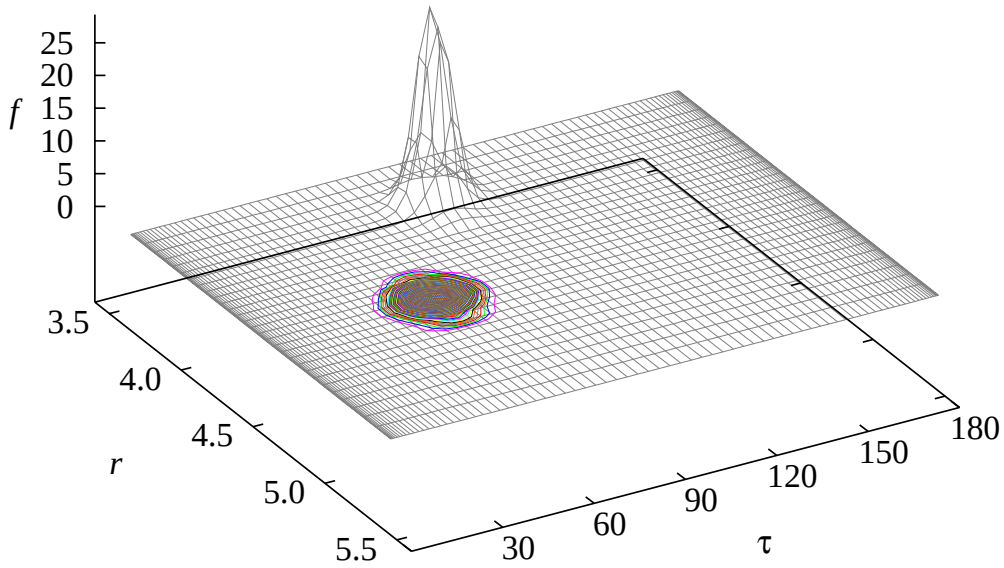


Figure 4.5: Probability density functions (See 2.5.3) for the bent $2^2A'$MgNC $(0, 0, 0)$ state.

Here, the $\tau$ and $r$ coordinates are given in degrees and Bohr, respectively. Figure (a) shows one-dimensional probability density functions. The blue curve is $f_-(\tau)$ (the lower electronic surface's probability density function), the red curve is $f_+(\tau)$ (the upper electronic surface's probability density function) and the black curve is $f(\tau)$ (the total probability density function). The gray surface in Figure (b) shows the two-dimensional probability density function $f(r, \tau)$. Coloured lines are the contour plot of the two-dimensional probability density function $f(r, \tau)$. Contours are plotted for 0.1 separations.

(a)

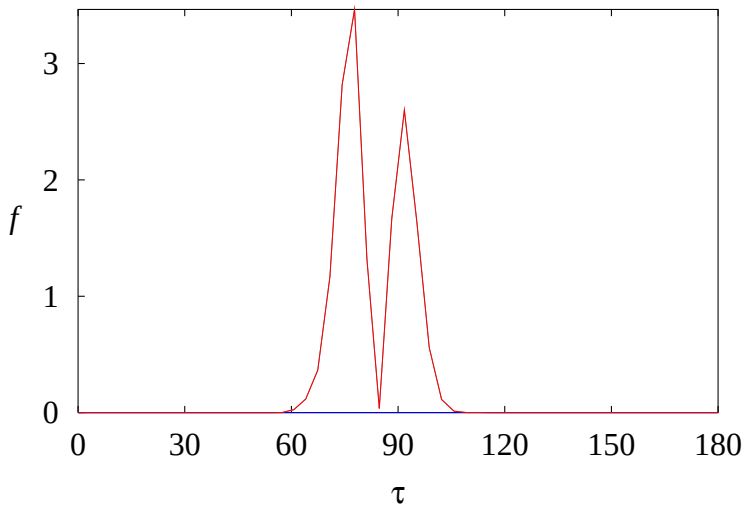


(b)

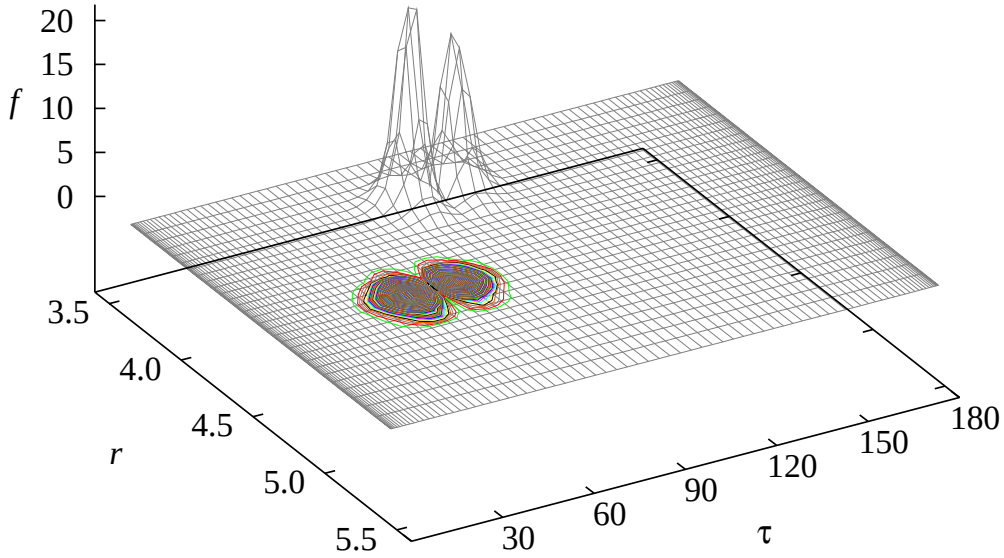


Figure 4.6: Probability density functions (See 2.5.3) for the bent $2^2A'$MgNC $(0, 1, 0)$ state.

Here, the $\tau$ and $r$ coordinates are given in degrees and Bohr, respectively. Figure (a) shows one-dimensional probability density functions. The blue curve is $f_-(\tau)$ (the lower electronic surface's probability density function), the red curve is $f_+(\tau)$ (the upper electronic surface's probability density function) and the black curve is $f(\tau)$ (the total probability density function). The gray surface in Figure (b) shows the two-dimensional probability density function $f(r, \tau)$. Coloured lines are the contour plot of the two-dimensional probability density function $f(r, \tau)$. Contours are plotted for 0.1 separations.

(a)

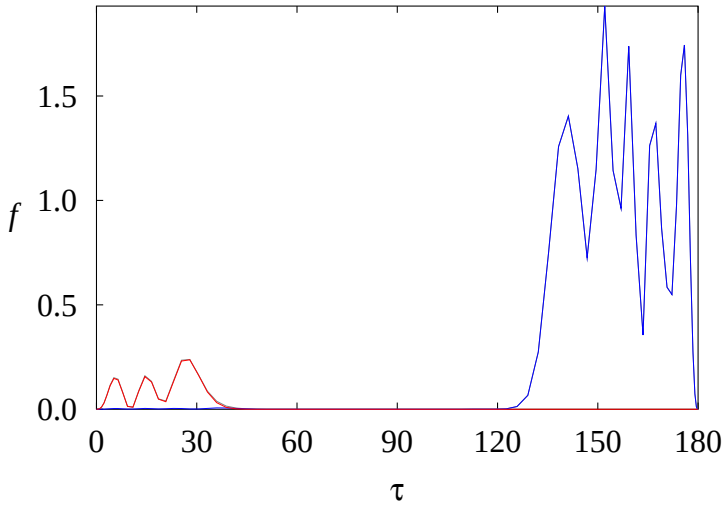


(b)

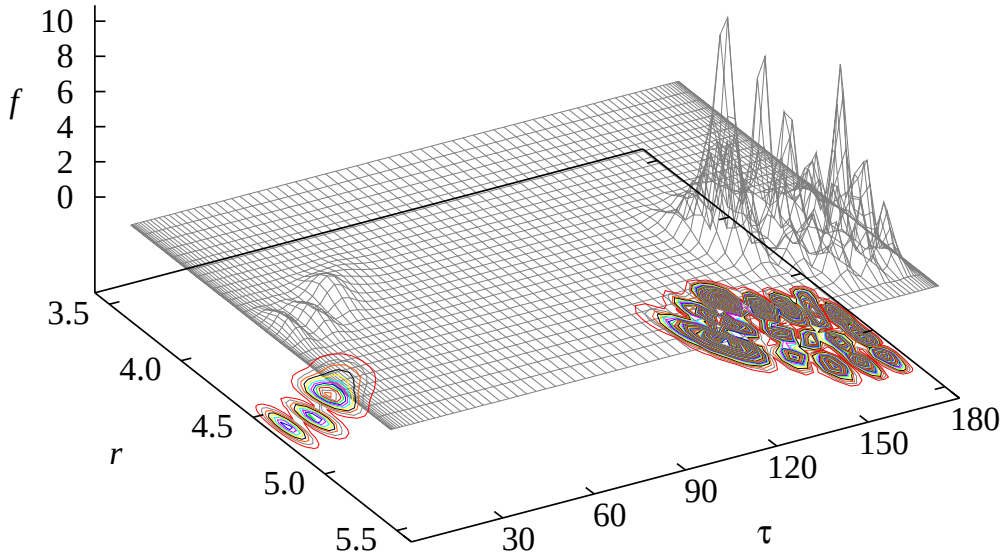


Figure 4.7: Probability density functions (See 2.5.3) for the $J = 1/2$, $\Gamma_{\text{ers}} = A$" 104th state.

Here, the $\tau$ and $r$ coordinates are given in degrees and Bohr, respectively. Figure (a) shows one-dimensional probability density functions. The blue curve is $f_-(\tau)$ (the lower electronic surface's probability density function), the red curve is $f_+(\tau)$ (the upper electronic surface's probability density function) and the black curve is $f(\tau)$ (the total probability density function). The gray surface in Figure (b) shows the two-dimensional probability density function $f(r, \tau)$. Coloured lines are the contour plot of the two-dimensional probability density function $f(r, \tau)$. Contours are plotted for 0.1 separations.

(a)

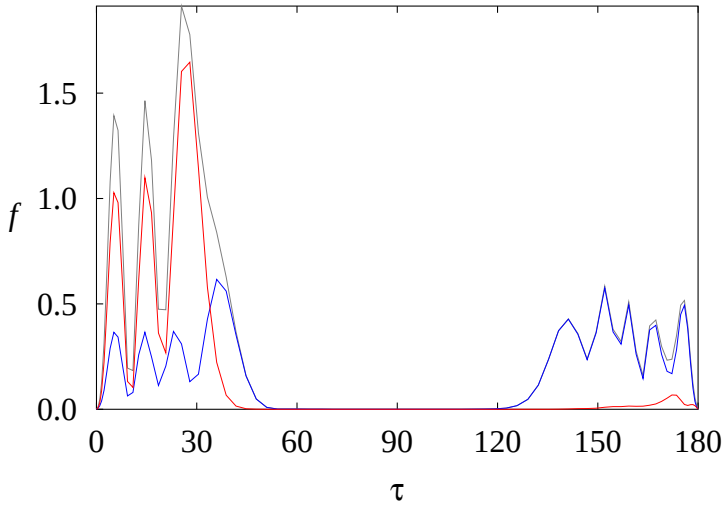


(b)

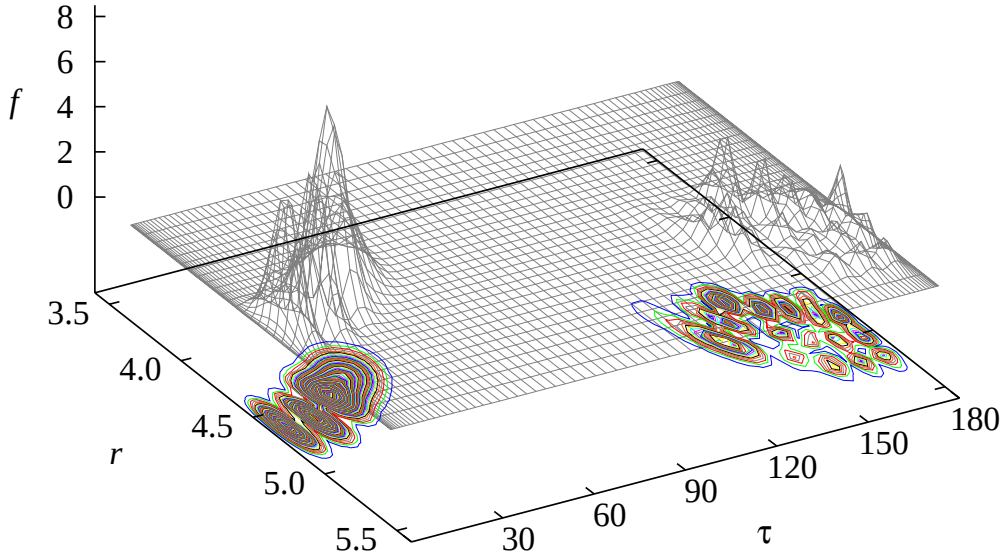


Figure 4.8: Probability density functions (See 2.5.3) for the $J = 1/2$, $\Gamma_{\text{ers}} = A'$ 104th state.

Here, the $\tau$ and $r$ coordinates are given in degrees and Bohr, respectively. Figure (a) shows one-dimensional probability density functions. The blue curve is $f_-(\tau)$ (the lower electronic surface's probability density function), the red curve is $f_+(\tau)$ (the upper electronic surface's probability density function) and the black curve is $f(\tau)$ (the total probability density function). The gray surface in Figure (b) shows the two-dimensional probability density function $f(r, \tau)$. Coloured lines are the contour plot of the two-dimensional probability density function $f(r, \tau)$. Contours are plotted for 0.1 separations.

(a)

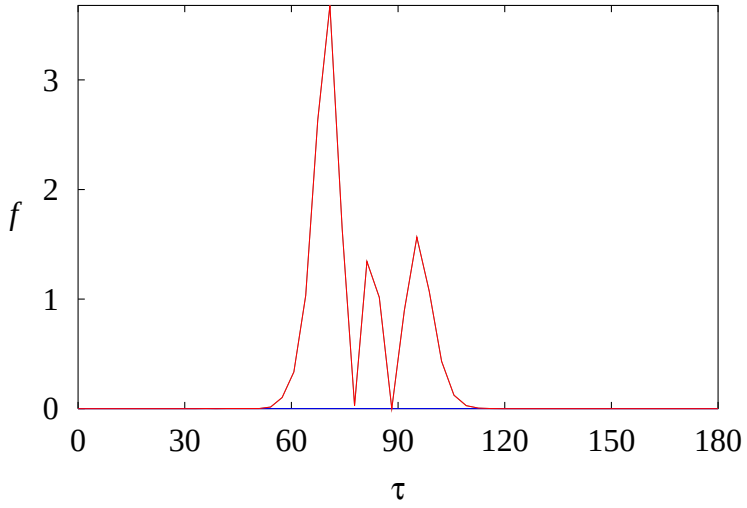


(b)

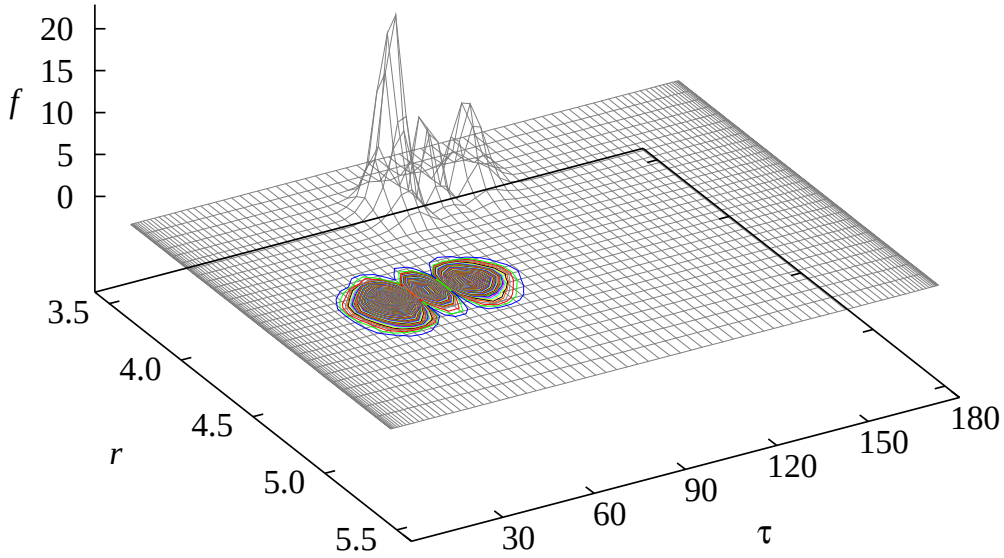


Figure 4.9: Probability density functions (See 2.5.3) for the bent $2^2A'$MgNC $(0, 2, 0)$ state.

Here, the $\tau$ and $r$ coordinates are given in degrees and Bohr, respectively. Figure (a) shows one-dimensional probability density functions. The blue curve is $f_-(\tau)$ (the lower electronic surface's probability density function), the red curve is $f_+(\tau)$ (the upper electronic surface's probability density function) and the black curve is $f(\tau)$ (the total probability density function). The gray surface in Figure (b) shows the two-dimensional probability density function $f(r, \tau)$. Coloured lines are the contour plot of the two-dimensional probability density function $f(r, \tau)$. Contours are plotted for 0.1 separations.

(a)

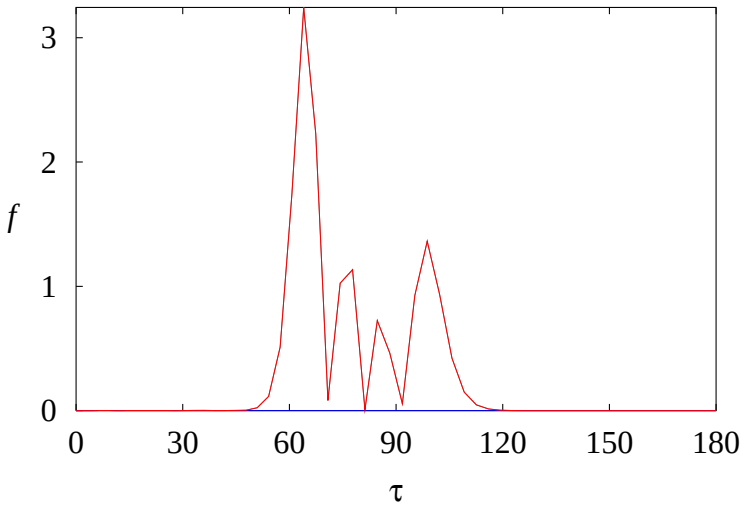


(b)

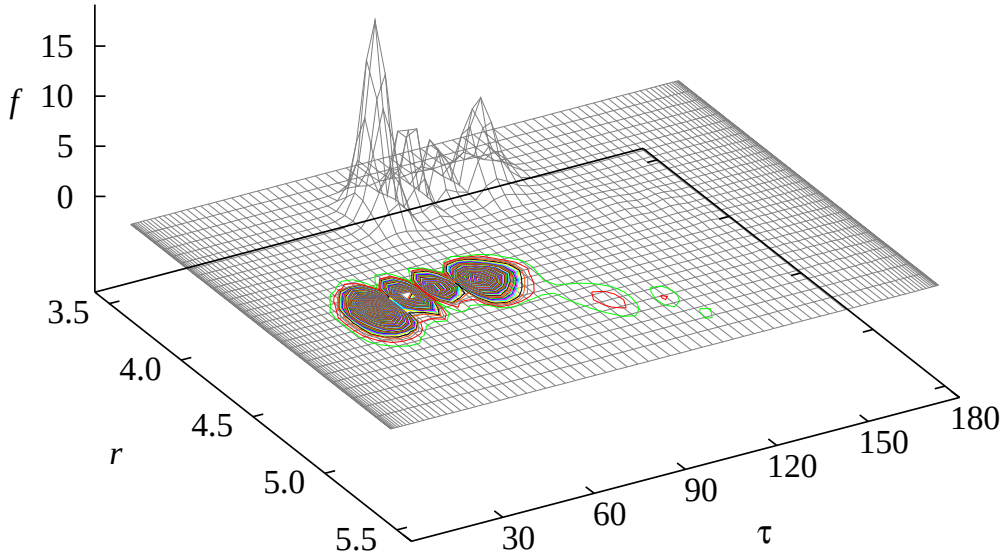


Figure 4.10: Probability density functions (See 2.5.3) for the bent $2^2A'$MgNC $(0, 3, 0)$ state.

Here, the $\tau$ and $r$ coordinates are given in degrees and Bohr, respectively. Figure (a) shows one-dimensional probability density functions. The blue curve is $f_-(\tau)$ (the lower electronic surface's probability density function), the red curve is $f_+(\tau)$ (the upper electronic surface's probability density function) and the black curve is $f(\tau)$ (the total probability density function). The gray surface in Figure (b) shows the two-dimensional probability density function $f(r, \tau)$. Coloured lines are the contour plot of the two-dimensional probability density function $f(r, \tau)$. Contours are plotted for 0.1 separations.

(a)

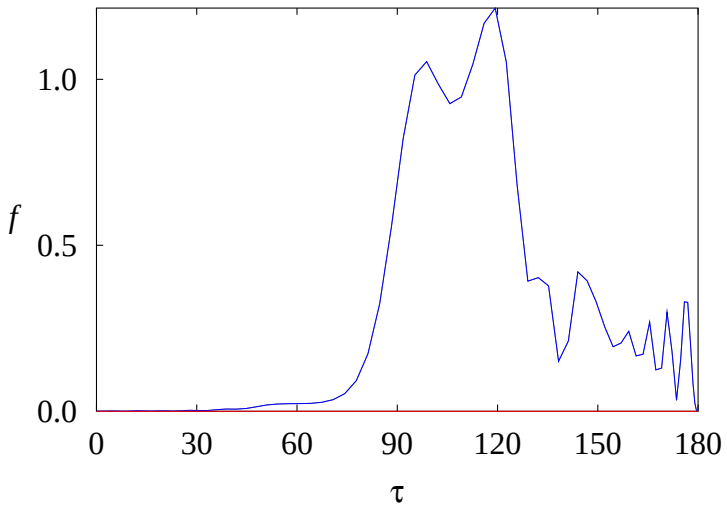


(b)

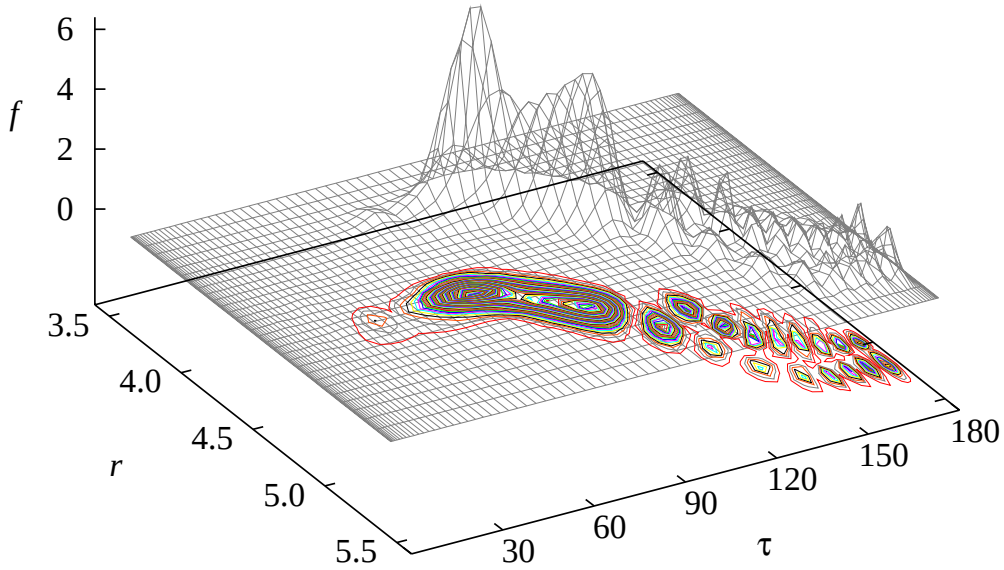


Figure 4.11: Probability density functions (See 2.5.3) for the $J = 1/2$, $\Gamma_{\text{ers}} = A$" 158th state.

Here, the $\tau$ and $r$ coordinates are given in degrees and Bohr, respectively. Figure (a) shows one-dimensional probability density functions. The blue curve is $f_-(\tau)$ (the lower electronic surface's probability density function), the red curve is $f_+(\tau)$ (the upper electronic surface's probability density function) and the black curve is $f(\tau)$ (the total probability density function). The gray surface in Figure (b) shows the two-dimensional probability density function $f(r, \tau)$. Coloured lines are the contour plot of the two-dimensional probability density function $f(r, \tau)$. Contours are plotted for 0.1 separations.

$(1,0,1)$ state are 35.3 and 22.81 cm$^{-1}$, 34.0 and 26.41cm$^{-1}$, respectively. The spin orbit splitting for $\widetilde{A}^2\Pi$ MgCN $(0,0,1)$ and $(1,0,1)$ state are not in good agreement. This is because in the DR calculation, the calculated $\widetilde{A}^2\Pi$ MgCN $(0,0,1)$ $J=3/2$ and $(1,0,1)$ $J=3/2$ states have a Fermi interaction with a nearby $J=3/2$ state.

From 1092 cm$^{-1}$, the wavefunction localized on $\widetilde{A}^2\Pi$ MgCN side starts to have too high bending excitation and becomes complicated to analyze, thus we do not always give the assignment (See Tables 4.7 - 4.13).

Fig. 4.4 shows a wavefunction localised around $\tau = 0^{\circ}$. This is the $\widetilde{A}^2\Pi$ MgNC zero point vibration state. MgNC zero point vibration state is at 1984 cm$^{-1}$ higher energy than the MgCN vibrational ground state (See Table 4.9).

We have summarized the vibronic energy levels of $\widetilde{A}^2$ MgNC calculated with DR together with experimental result by Wright and Miller [8] and Fukushima and Ishiwata [38] in Table 4.14. As shown in in the table, the spin orbit splitting for the $(0,0,0)$ and $(0,0,1)$ state agrees with experiment. Our calculated energies with the program DR differ less than 10 cm$^{-1}$ to the observed values from Wright and Miller [8]. The experimental result by Fukushima $et\ al$ presented at HRMS2003 [47] does not agree very well with our theoretical calculation on the $\mu$ states. For $\kappa$ states, it agrees better than for the $\mu$ states.

Our calculated value for $(0,1,0)\mu\Sigma$ state does not agree well with the calculated value with RENNER but agrees with other theoretical calculations.

For states with bending quantum number higher than four, the calculated result with the program DR is more than 10 cm$^{-1}$ higher than the energy calculated result the program RVIB3; these states have more contribution from bent geometry and these $ab\ initio$ points are not included for the potential energy surface used with the program RVIB3.

In Table 4.11, $\widetilde{A}^2\Pi$ we have MgNC and $\widetilde{A}^2\Pi$ MgCN localized vibrations, and at 2469 cm$^{-1}$, we see the $(0,0,0)$ state of "bent" $2^2A'$ MgNC. The wavefunction for this state is

shown in Fig. 4.5, and one can clearly see that the wavefunction is localized around $\tau = 90^{\circ}$. As shown in Fig. 4.5 (a), the wavefunction has its dominant contribution from the upper potential energy surface. As seen in Fig. 4.1 the upper electronic surface $2^2A'$ state has a local minimum around $\tau = 90^{\circ}$, and this state originates in this lake in the potential energy surface. At 275 cm$^{-1}$ above this state, we see the next bent state $2^2A'$ MgNC $(0, 1, 0)$ (See Fig. 4.6), and 268 cm$^{-1}$ further above this state, we see the next bent state $2^2A'$ MgNC $(0, 2, 0)$ (See Fig. 4.9). The $2^2A'$ MgNC $(0, 3, 0)$ state is shown in Fig. 4.10 and is 248 cm$^{-1}$ above the $2^2A'$ MgNC $(0, 2, 0)$ state.

The $2^2A'$ MgNC $(0, 0, 0)$, $(0, 1, 0)$ and $(0, 2, 0)$ state has 12 rotational levels with $J = 1/2$, $3/2$ and $\Gamma_{\rm ers} = A'$, $A$"; these are summarized in Table 4.15. For each vibronic state, the $J = 1/2$ state consists of $N = 0$ and $N = 1$ states. The $N = 0$ state has one $K = 0$ substate and the $N = 1$ state has one $K = 0$ and two $K = 1$ substates. Thus the $J = 1/2$ state has four substates. Each vibronic state with $J = 3/2$ consists of $N = 1$ and $N = 2$ states. The $N = 1$ state has one $K = 0$ and two $K = 1$ substates. The $N = 1$ state has one $K = 0$, two $K = 1$ and two $K = 2$ substates. Thus the $J = 3/2$ state has eight substates. This explains why each vibronic state has 12 rotational levels. Since the equilibrium geometry of the molecule is bent, the $z$-axis (B-C bond as shown in 2.1) is no longer the molecular axis corresponding to the quantum number $K$. Thus the quantum number $K$ in Table 4.15 is no longer a useful quantum number.

We see the first tunneling wavefunction at 2835 cm$^{-1}$ as shown in Fig. 4.7. It is mostly localized at $\widetilde{A}^2\Pi$ MgCN and has small amplitude at $\widetilde{A}^2\Pi$ MgNC. At 1 cm$^{-1}$ above this state, we see another tunneling wavefunction mostly localized around $\widetilde{A}^2\Pi$ MgNC and with small amplitude at $\widetilde{A}^2\Pi$ MgCN. (See Fig. 4.8)

At 3294 cm$^{-1}$ we see a MgCN to bent localized state, as shown in Fig. 4.11. This state originates in the lower electronic state $1^2A$". As seen in the Fig. 4.1 the lower electronic surface $1^1A$" state has a very shallow local minimum around $\tau = 90^{\circ}$, and this state originates to this shallow shoulder on the potential energy surface towards

MgCN local minima. The states shown in Fig. 4.12 (3318 cm$^{-1}$) and in Fig. 4.13 (3325 cm$^{-1}$) also originate in the shallow shoulder on the lower electronic surface (The $1^2A"$ state).

Above 3370 cm$^{-1}$ we see delocalized states. Figure 4.14 (3370 cm$^{-1}$) has some amplitude at MgNC to bent geometry with large amplitude around MgCN. This state originates in the lower electronic state $1^2A"$. The next delocalized state is shown in Fig. 4.15. This state lies at 3383 cm$^{-1}$; it has large amplitude around MgNC, and some amplitude around MgCN. These two states originate in the lower electronic surface ($1^2A"$ state).

As shown in Fig. 4.16 (3424 cm$^{-1}$), we see another delocalized state which has some amplitude at MgNC and more amplitude on the MgCN side. This state originates in the lower electronic state at bent geometries, but in both the linear geometries MgNC and MgCN, it originates in both the $1^2A"$ and the $2^2A'$ electronic states. At 3435 cm$^{-1}$ (Fig. 4.17), at 3441 cm$^{-1}$ (Fig. 4.18) and at 3493 cm$^{-1}$ (Fig. 4.19) we have a delocalized state with more amplitude on the MgNC side. All of these three states have some amplitude on the MgCN side. The states shown in Fig. 4.17 and Fig. 4.18 have amplitude for bent geometries and this part originates in the lower electronic surface. The wavefunction around the MgNC linear geometry originates in both electronic surfaces. The state shown in Fig. 4.19 does not have large amplitude in bent geometries. This state originates in $1^2A"$, the lower electronic state.

At 3513 cm$^{-1}$ (Fig. 4.20) and at 3514 cm$^{-1}$ (Fig. 4.21) we have states well mixed from both electronic surfaces. The state shown in Fig. 4.20 has large amplitude at bent geometries but the state shown in Fig. 4.21 is delocalized.

As reported in our recent study of $\widetilde{X}^2\Sigma^+$ MgNC/MgCN [37], we can examine the possibility of isomerization from $\widetilde{X}^2\Sigma^+$ MgNC to $\widetilde{X}^2\Sigma^+$ MgCN through these delocalized $\widetilde{A}^2\Pi$ MgNC/MgCN state by calculating the transition intensity.

(a)

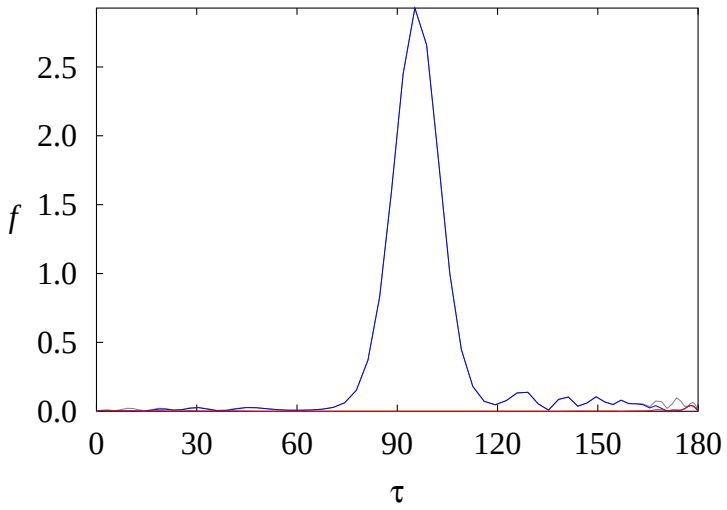


(b)

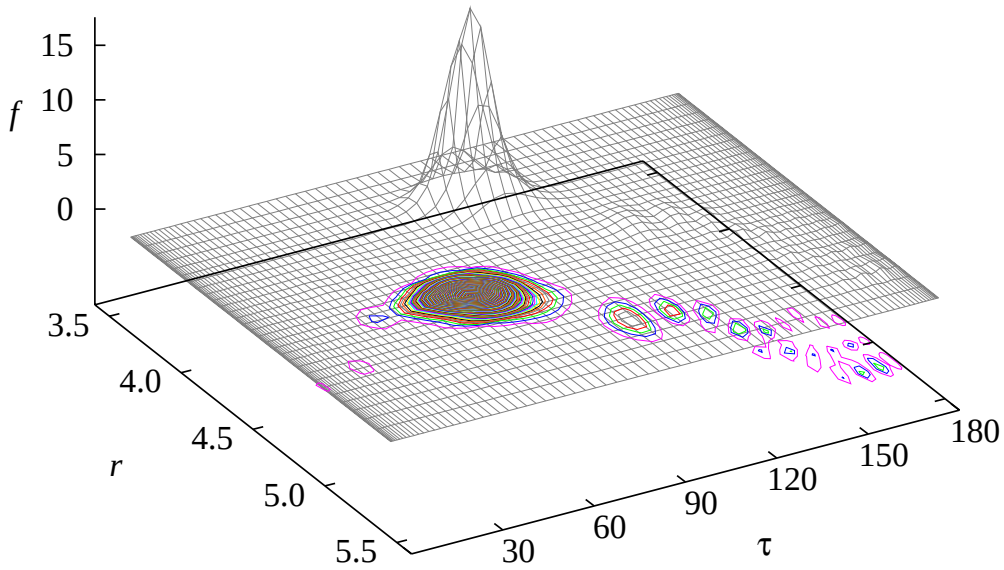


Figure 4.12: Probability density functions (See 2.5.3) for the $J = 1/2$, $\Gamma_{\text{ers}} = A$" 161st state.

Here, the $\tau$ and $r$ coordinates are given in degrees and Bohr, respectively. Figure (a) shows one-dimensional probability density functions. The blue curve is $f_{-}(\tau)$ (the lower electronic surface's probability density function), the red curve is $f_{+}(\tau)$ (the upper electronic surface's probability density function) and the black curve is $f(\tau)$ (the total probability density function). The gray surface in Figure (b) shows the two-dimensional probability density function $f(r, \tau)$. Coloured lines are the contour plot of the two-dimensional probability density function $f(r, \tau)$. Contours are plotted for 0.1 separations.

(a)

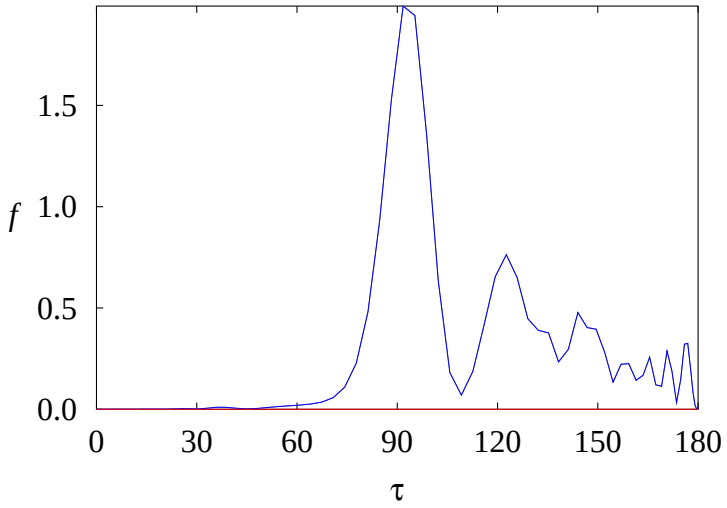


(b)

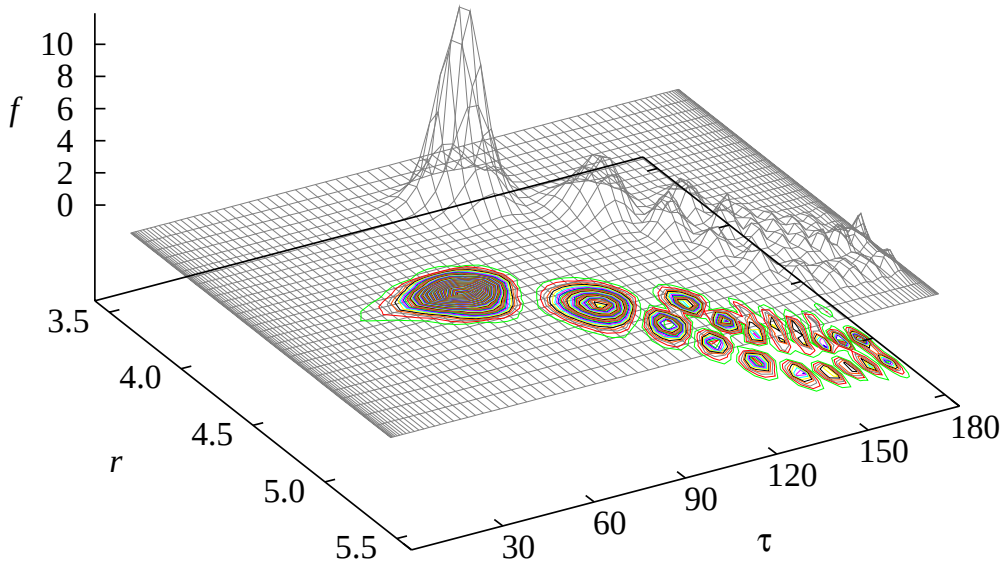


Figure 4.13: Probability density functions (See 2.5.3) for the $J = 1/2$, $\Gamma_{\text{ers}} = A$" 162nd state.

Here, the $\tau$ and $r$ coordinates are given in degrees and Bohr, respectively. Figure (a) shows one-dimensional probability density functions. The blue curve is $f_-(\tau)$ (the lower electronic surface's probability density function), the red curve is $f_+(\tau)$ (the upper electronic surface's probability density function) and the black curve is $f(\tau)$ (the total probability density function). The gray surface in Figure (b) shows the two-dimensional probability density function $f(r, \tau)$. Coloured lines are the contour plot of the two-dimensional probability density function $f(r, \tau)$. Contours are plotted for 0.1 separations.

(a)

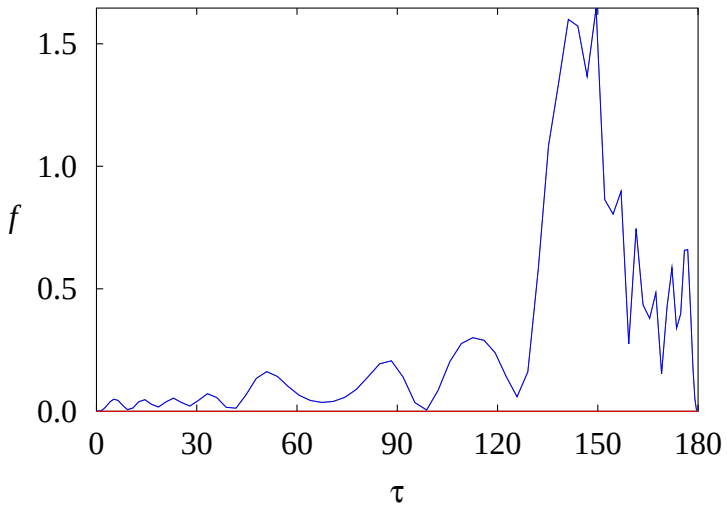


(b)

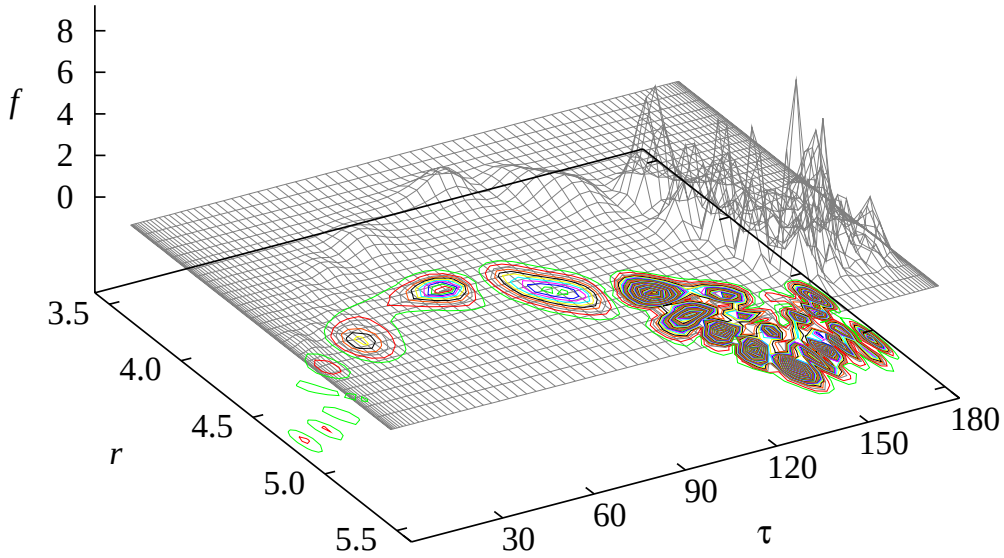


Figure 4.14: Probability density functions (See 2.5.3) for the $J = 1/2$, $\Gamma_{\text{ers}} = A$" 168th state.

Here, the $\tau$ and $r$ coordinates are given in degrees and Bohr, respectively. Figure (a) shows one-dimensional probability density functions. The blue curve is $f_-(\tau)$ (the lower electronic surface's probability density function), the red curve is $f_+(\tau)$ (the upper electronic surface's probability density function) and the black curve is $f(\tau)$ (the total probability density function). The gray surface in Figure (b) shows the two-dimensional probability density function $f(r, \tau)$. Coloured lines are the contour plot of the two-dimensional probability density function $f(r, \tau)$. Contours are plotted for 0.1 separations.

(a)

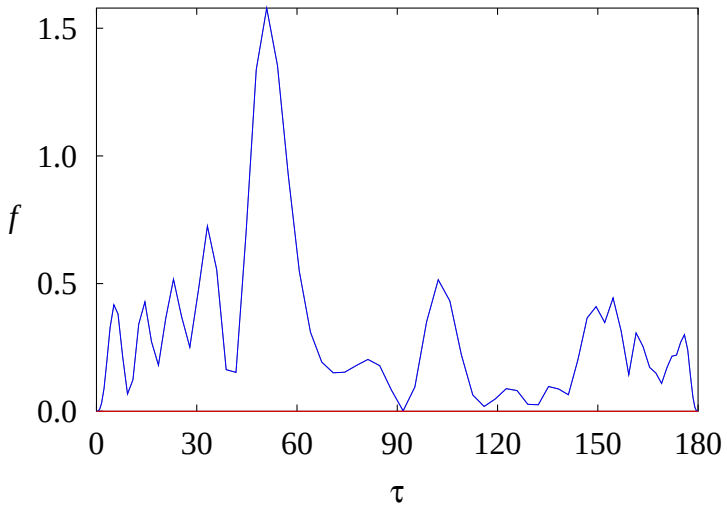


(b)

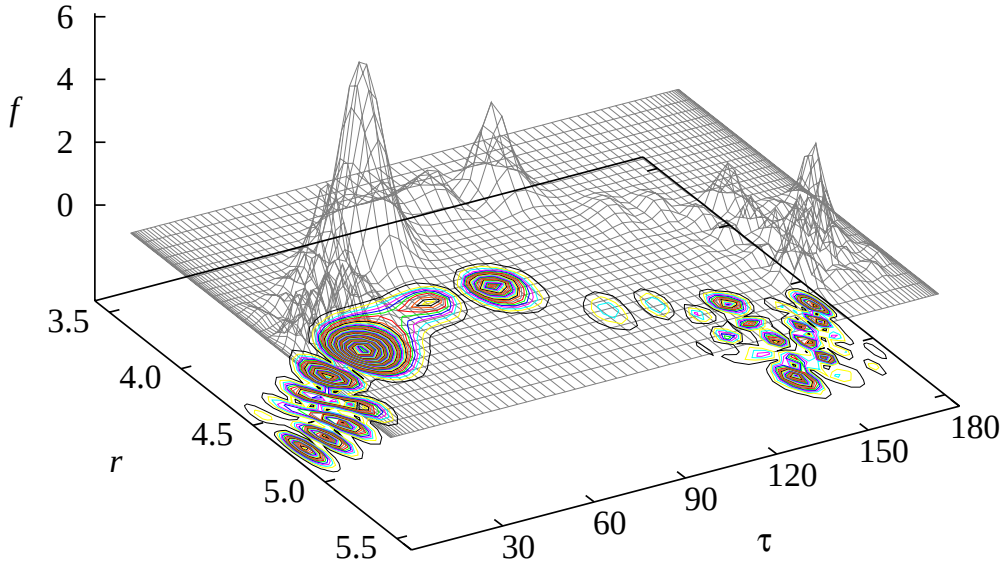


Figure 4.15: Probability density functions (See 2.5.3) for the $J = 1/2$, $\Gamma_{\text{ers}} = A$" 171th state.

Here, the $\tau$ and $r$ coordinates are given in degrees and Bohr, respectively. Figure (a) shows one-dimensional probability density functions. The blue curve is $f_-(\tau)$ (the lower electronic surface's probability density function), the red curve is $f_+(\tau)$ (the upper electronic surface's probability density function) and the black curve is $f(\tau)$ (the total probability density function). The gray surface in Figure (b) shows the two-dimensional probability density function $f(r, \tau)$. Coloured lines are the contour plot of the two-dimensional probability density function $f(r, \tau)$. Contours are plotted for 0.1 separations.

(a)

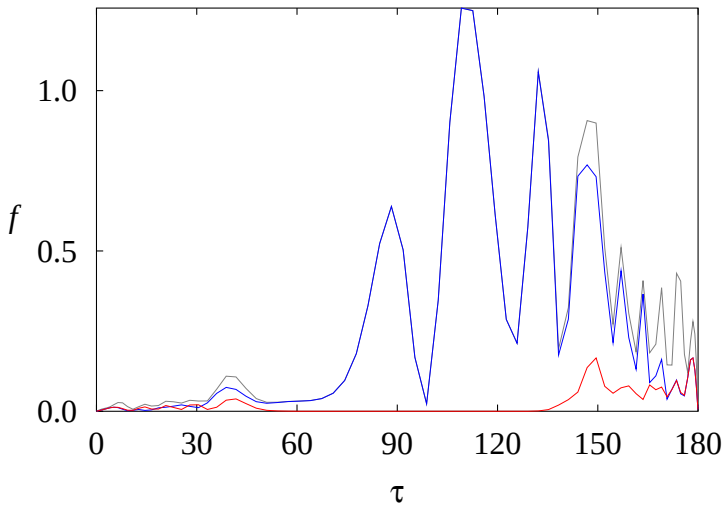


(b)

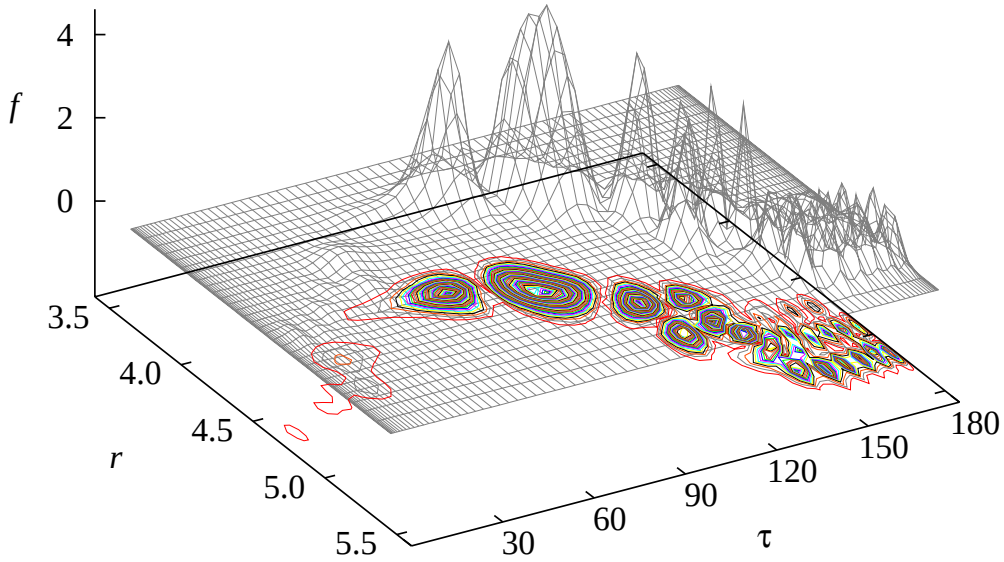


Figure 4.16: Probability density functions (See 2.5.3) for the $J = 1/2$, $\Gamma_{\text{ers}} = A$" 178th state.

Here, the $\tau$ and $r$ coordinates are given in degrees and Bohr, respectively. Figure (a) shows one-dimensional probability density functions. The blue curve is $f_-(\tau)$ (the lower electronic surface's probability density function), the red curve is $f_+(\tau)$ (the upper electronic surface's probability density function) and the black curve is $f(\tau)$ (the total probability density function). The gray surface in Figure (b) shows the two-dimensional probability density function $f(r, \tau)$. Coloured lines are the contour plot of the two-dimensional probability density function $f(r, \tau)$. Contours are plotted for 0.1 separations.

(a)

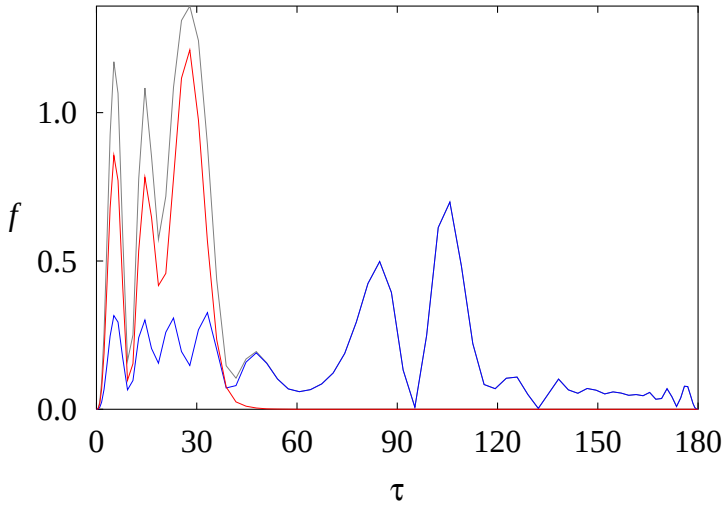


(b)

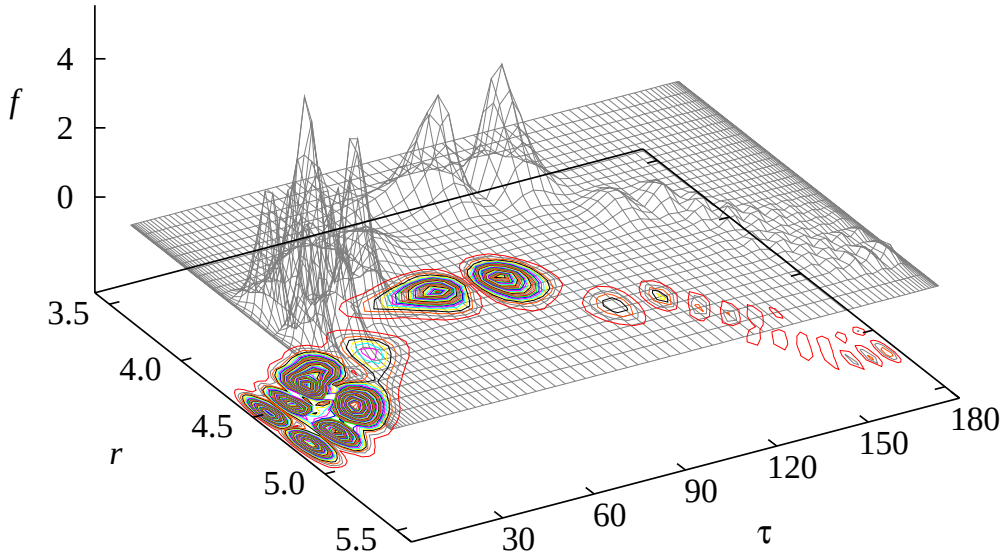


Figure 4.17: Probability density functions (See 2.5.3) for the $J = 1/2$, $\Gamma_{\text{ers}} = A$" 180th state.

Here, the $\tau$ and $r$ coordinates are given in degrees and Bohr, respectively. Figure (a) shows one-dimensional probability density functions. The blue curve is $f_-(\tau)$ (the lower electronic surface's probability density function), the red curve is $f_+(\tau)$ (the upper electronic surface's probability density function) and the black curve is $f(\tau)$ (the total probability density function). The gray surface in Figure (b) shows the two-dimensional probability density function $f(r, \tau)$. Coloured lines are the contour plot of the two-dimensional probability density function $f(r, \tau)$. Contours are plotted for 0.1 separations.

(a)

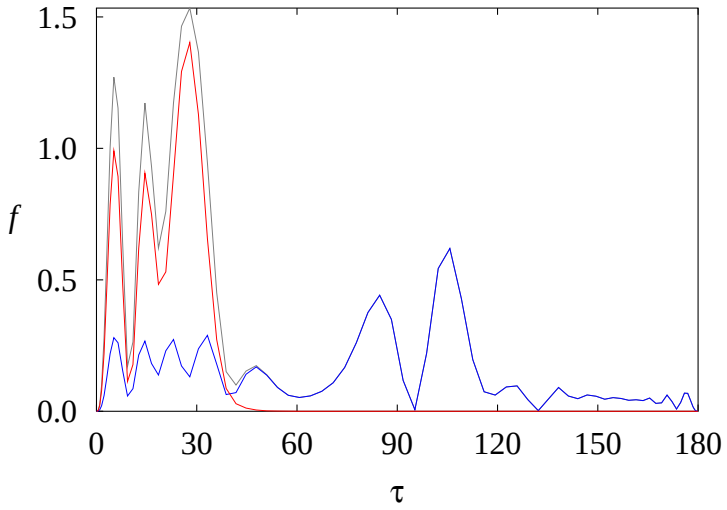


(b)

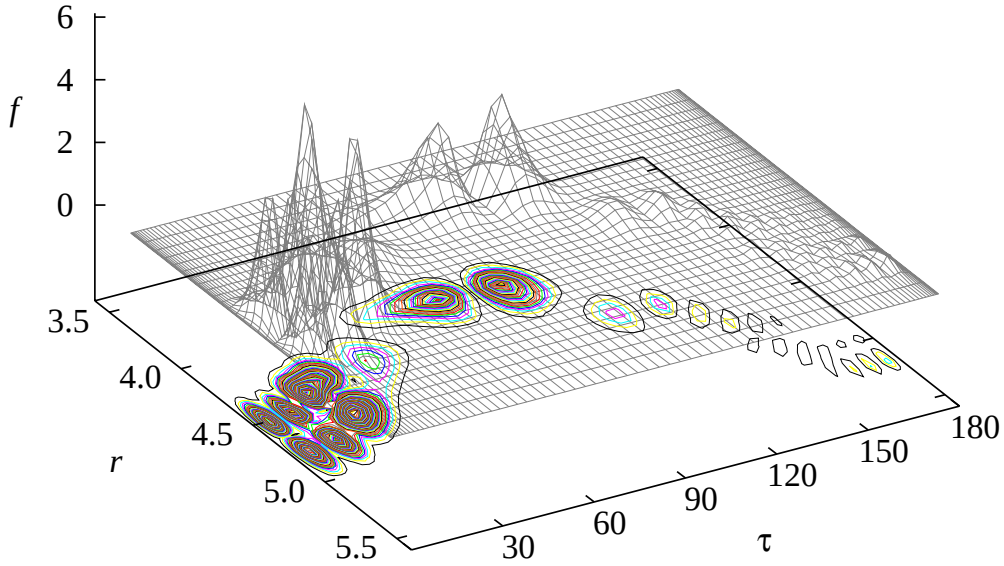


Figure 4.18: Probability density functions (See 2.5.3) for the $J = 1/2$, $\Gamma_{\text{ers}} = A$" 182th state.

Here, the $\tau$ and $r$ coordinates are given in degrees and Bohr, respectively. Figure (a) shows one-dimensional probability density functions. The blue curve is $f_-(\tau)$ (the lower electronic surface's probability density function), the red curve is $f_+(\tau)$ (the upper electronic surface's probability density function) and the black curve is $f(\tau)$ (the total probability density function). The gray surface in Figure (b) shows the two-dimensional probability density function $f(r, \tau)$. Coloured lines are the contour plot of the two-dimensional probability density function $f(r, \tau)$. Contours are plotted for 0.1 separations.

(a)

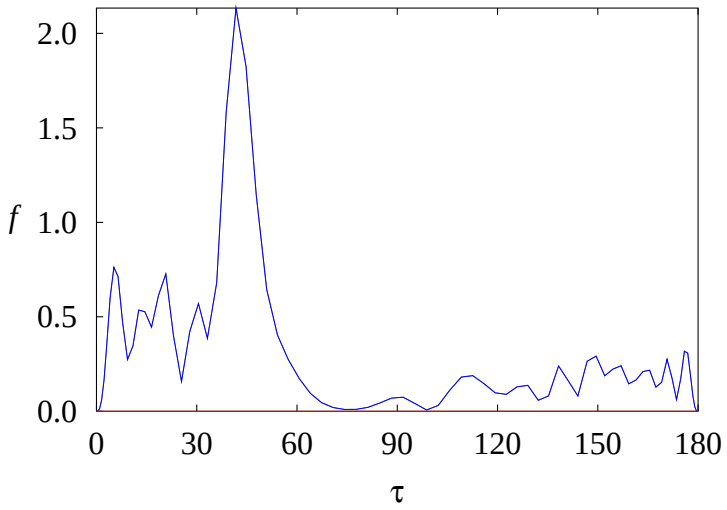


(b)

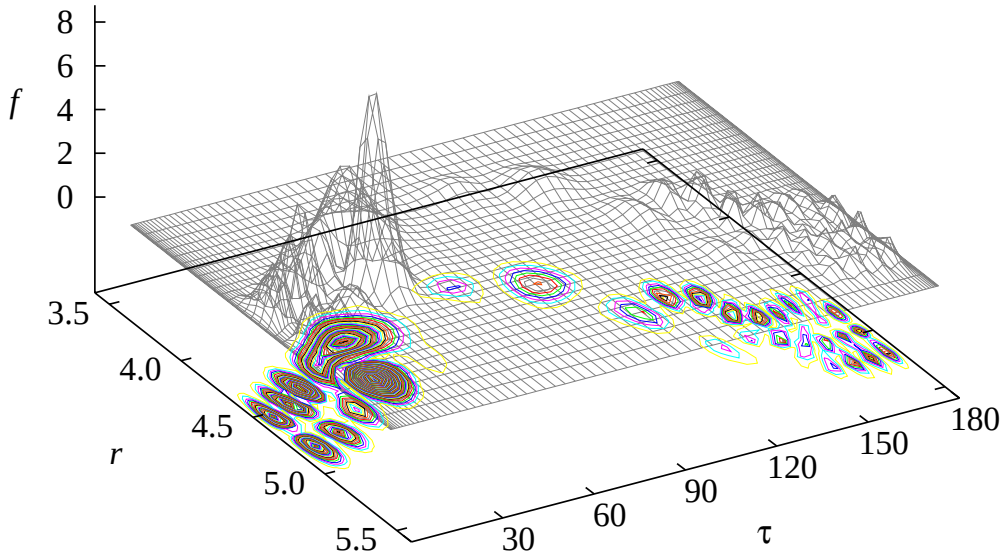


Figure 4.19: Probability density functions (See 2.5.3) for the $J = 1/2$, $\Gamma_{\text{ers}} = A$" 185th state.

Here, the $\tau$ and $r$ coordinates are given in degrees and Bohr, respectively. Figure (a) shows one-dimensional probability density functions. The blue curve is $f_-(\tau)$ (the lower electronic surface's probability density function), the red curve is $f_+(\tau)$ (the upper electronic surface's probability density function) and the black curve is $f(\tau)$ (the total probability density function). The gray surface in Figure (b) shows the two-dimensional probability density function $f(r, \tau)$. Coloured lines are the contour plot of the two-dimensional probability density function $f(r, \tau)$. Contours are plotted for 0.1 separations.

(a)

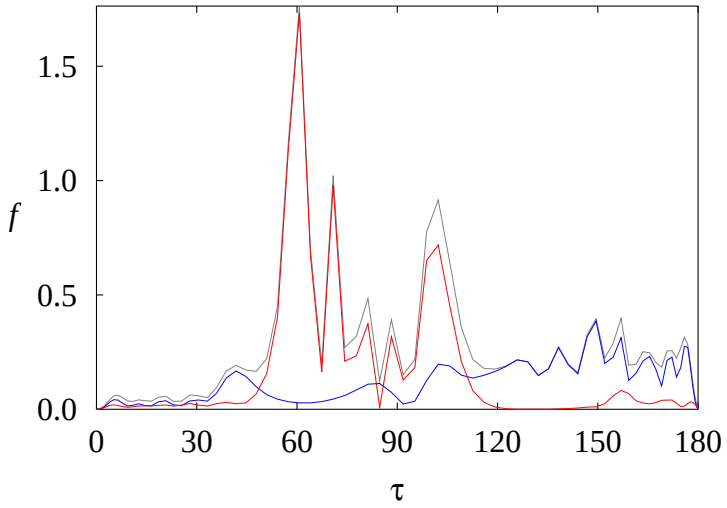


(b)

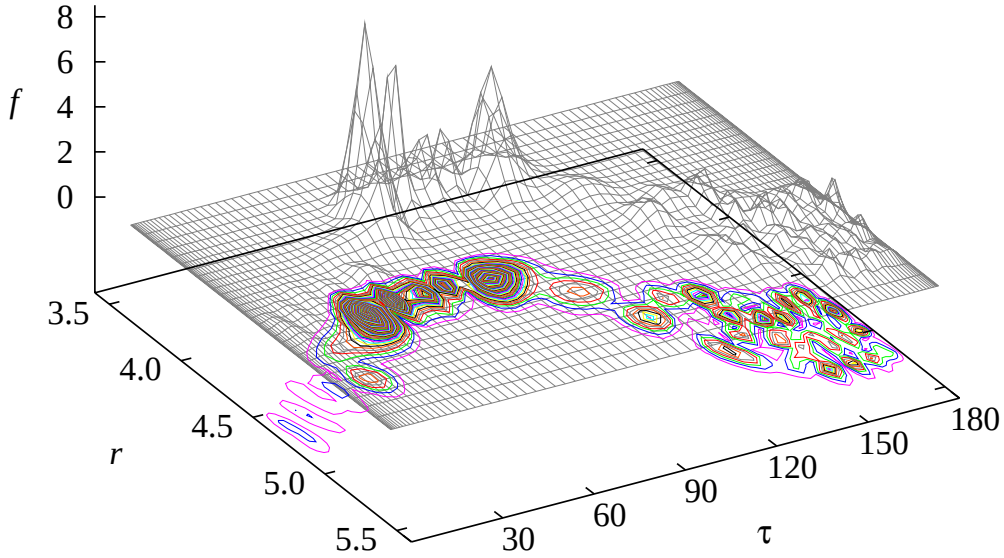


Figure 4.20: Probability density functions (See 2.5.3) for the $J = 1/2$, $\Gamma_{\text{ers}} = A$" 186th state.

Here, the $\tau$ and $r$ coordinates are given in degrees and Bohr, respectively. Figure (a) shows one-dimensional probability density functions. The blue curve is $f_-(\tau)$ (the lower electronic surface's probability density function), the red curve is $f_+(\tau)$ (the upper electronic surface's probability density function) and the black curve is $f(\tau)$ (the total probability density function). The gray surface in Figure (b) shows the two-dimensional probability density function $f(r, \tau)$. Coloured lines are the contour plot of the two-dimensional probability density function $f(r, \tau)$. Contours are plotted for 0.1 separations.

(a)

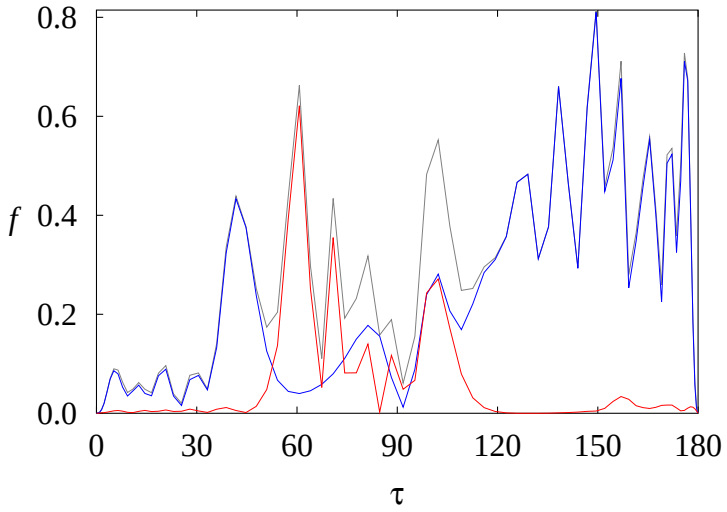


(b)

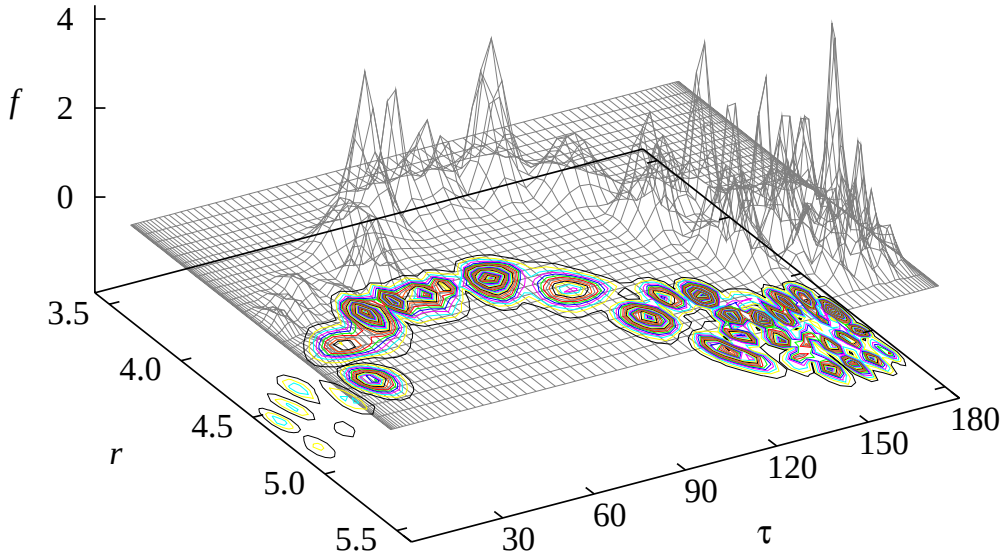


Figure 4.21: Probability density functions (See 2.5.3) for the $J = 1/2$, $\Gamma_{\text{ers}} = A$" 187th state.

Here, the $\tau$ and $r$ coordinates are given in degrees and Bohr, respectively. Figure (a) shows one-dimensional probability density functions. The blue curve is $f_-(\tau)$ (the lower electronic surface's probability density function), the red curve is $f_+(\tau)$ (the upper electronic surface's probability density function) and the black curve is $f(\tau)$ (the total probability density function). The gray surface in Figure (b) shows the two-dimensional probability density function $f(r, \tau)$. Coloured lines are the contour plot of the two-dimensional probability density function $f(r, \tau)$. Contours are plotted for 0.1 separations.

Table 4.14: Vibronic term values (in $cm^{-1}$) of MgNC.

| | | DR[a] | | Obs. Ref. [8] | | Obs.[b] | RENNER[c] | | RVIB3[d] | | PT[e] | |
|---|---|---|---|---|---|---|---|---|---|---|---|---|
| State $(\nu_1, \nu_2, \nu_3)$ | | $\nu$ | $\nu_{SO}$ | $\nu$ | $\nu_{SO}$ | $\nu$ | $\nu$ | $\nu_{SO}$ | $\nu$ | $\nu_{SO}$ | $\nu$ | $\nu_{SO}$ |
| $(0,0,0)$ | $\Pi$ | 0.00 | 34.21 | 0.00 | 36.926 | 0 | 0.0 | 34.47 | 0.0 | 34.39 | 0.0 | 34.8 |
| $(0,1,0)$ | $\mu\Sigma$ | 111.71 | | | | | 122.5 | | 111.8 | | 111.9 | |
| $(0,1,0)$ | $\kappa\Sigma$ | 203.53 | | 211.80 | | 206 | 209.2 | | 202.4 | | 203.4 | |
| $(0,2,0)$ | $\mu\Pi$ | 248.74 | 4.10 | | | 214 | 251.1 | 6.25 | 245.4 | 4.60 | 246.6 | 2.4 |
| $(0,2,0)$ | $\kappa\Pi$ | 371.33 | 5.77 | 372.60 | 8.138 | 367 | 372.4 | 6.50 | 367.9 | 5.28 | 371.7 | 2.5 |
| $(0,3,0)$ | $\mu\Sigma$ | 364.28 | | | | | | | 361.5 | | 363.6 | |
| $(0,3,0)$ | $\kappa\Sigma$ | 531.62 | | | | | | | 528.9 | | 536.5 | |
| $(0,4,0)$ | $\mu\Pi$ | 489.05 | 4.57 | | | 434 | | | 480.7 | 4.13 | 483.8 | 1.4 |
| $(0,4,0)$ | $\kappa\Pi$ | 690.13 | 5.77 | | | 678 | | | 679.1 | 10.48 | 694.4 | 1.5 |
| $(0,5,0)$ | $\mu\Sigma$ | 594.70 | | | | | | | 584.9 | | | |
| $(0,6,0)$ | $\mu\Pi$ | 717.76 | 6.12 | | | | | | 692.6 | 9.89 | | |
| | | | | | | | | | | | | |
| $(0,0,1)$ | $\Pi$ | 587.69 | 34.18 | 581.73 | 37.193 | | 583.6 | 34.36 | 584.8 | 34.43 | 585.1 | |
| $(0,1,1)$ | $\mu\Sigma$ | 703.81 | | | | | | | 702.2 | | | |
| $(0,1,1)$ | $\kappa\Sigma$ | 795.13 | | | | 794 | | | 789.8 | | | |
| $(0,2,1)$ | $\mu\Pi$ | 843.50 | 4.27 | | | 816 | | | 840.3 | 4.62 | | |

[a] Energy calculated with the program DR. [b] Observed by Fukushima *et al*, Poster presentation in HRMS2003 [47]. [c] See Appendix C. Energy calculated with the program RENNER, using part of the potential energy surface used in this work. [d] Ref. [46]. Energy calculated with the program RENNER, using part of the slightly different potential energy surface used in this work. [e] See Appendix B. Energy calculated in perturbation method, using part of the slightly different potential energy surface used in this work.

Table 4.15: Vibronic term values (in $cm^{-1}$) of bent MgNC. All energy levels with $J = 1/2, 3/2$ for $\nu_2 = 0, 1, 2$ states are listed here.

| State $(\nu_1, \nu_2, \nu_3)$ | $J$ | $\Gamma_{\rm rve}$ | No.[a] | $N^b$ | $K^b$ | $P^c_-$ | $P^c_+$ | DR[d] |
|---|---|---|---|---|---|---|---|---|
| $\kappa(0,0,0)$ | 1/2 | $A$" | 71 | 1 | 1 | 0.0 | 100.0 | 2469.19 |
| $\kappa(0,0,0)$ | 3/2 | $A$" | 135 | 1 | 1 | 0.0 | 100.0 | 2469.19 |
| $\kappa(0,0,0)$ | 1/2 | $A'$ | 71 | 0 | 0 | 0.0 | 100.0 | 2470.60 |
| $\kappa(0,0,0)$ | 3/2 | $A'$ | 135 | 2 | 2 | 0.0 | 99.8 | 2470.63 |
| $\kappa(0,0,0)$ | 1/2 | $A'$ | 72 | 1 | 1 | 0.0 | 100.0 | 2470.67 |
| $\kappa(0,0,0)$ | 3/2 | $A'$ | 136 | 1 | 1 | 0.0 | 99.9 | 2470.68 |
| $\kappa(0,0,0)$ | 3/2 | $A$" | 136 | 2 | 2 | 0.0 | 99.9 | 2471.74 |
| $\kappa(0,0,0)$ | 3/2 | $A'$ | 137 | 2 | 1 | 0.0 | 99.9 | 2472.09 |
| $\kappa(0,0,0)$ | 1/2 | $A$" | 72 | 1 | 0 | 0.0 | 100.0 | 2472.75 |
| $\kappa(0,0,0)$ | 3/2 | $A$" | 137 | 1 | 0 | 0.0 | 100.0 | 2472.75 |
| $\kappa(0,0,0)$ | 3/2 | $A$" | 138 | 2 | 1 | 0.0 | 100.0 | 2476.52 |
| $\kappa(0,0,0)$ | 3/2 | $A'$ | 138 | 2 | 0 | 0.0 | 100.0 | 2478.15 |
| | | | | | | | | |
| $\kappa(0,1,0)$ | 3/2 | $A$" | 185 | 1 | 1 | 0.0 | 99.9 | 2743.61 |
| $\kappa(0,1,0)$ | 1/2 | $A$" | 96 | 1 | 1 | 0.0 | 99.9 | 2743.74 |
| $\kappa(0,1,0)$ | 3/2 | $A'$ | 185 | 2 | 2 | 0.0 | 99.7 | 2744.46 |
| $\kappa(0,1,0)$ | 3/2 | $A'$ | 186 | 1 | 1 | 0.0 | 99.9 | 2744.81 |
| $\kappa(0,1,0)$ | 3/2 | $A$" | 186 | 2 | 2 | 0.0 | 99.9 | 2744.88 |
| $\kappa(0,1,0)$ | 1/2 | $A'$ | 96 | 1 | 1 | 0.0 | 100.0 | 2744.95 |
| $\kappa(0,1,0)$ | 3/2 | $A'$ | 187 | 2 | 1 | 0.0 | 99.9 | 2747.63 |
| $\kappa(0,1,0)$ | 1/2 | $A'$ | 97 | 0 | 0 | 0.0 | 100.0 | 2748.40 |
| $\kappa(0,1,0)$ | 1/2 | $A$" | 97 | 1 | 0 | 0.0 | 100.0 | 2750.95 |
| $\kappa(0,1,0)$ | 3/2 | $A$" | 187 | 1 | 0 | 0.0 | 100.0 | 2750.95 |
| $\kappa(0,1,0)$ | 3/2 | $A$" | 188 | 2 | 1 | 0.0 | 99.9 | 2751.22 |
| $\kappa(0,1,0)$ | 3/2 | $A'$ | 190 | 2 | 0 | 0.0 | 99.8 | 2756.48 |
| | | | | | | | | |
| $\kappa(0,2,0)$ | 3/2 | $A'$ | 238 | 2 | 2 | 0.0 | 99.7 | 3006.79 |
| $\kappa(0,2,0)$ | 3/2 | $A$" | 238 | 2 | 2 | 0.0 | 99.8 | 3006.98 |
| $\kappa(0,2,0)$ | 3/2 | $A$" | 239 | 1 | 1 | 0.0 | 99.8 | 3011.45 |
| $\kappa(0,2,0)$ | 1/2 | $A$" | 124 | 1 | 1 | 0.0 | 99.9 | 3011.69 |
| $\kappa(0,2,0)$ | 3/2 | $A'$ | 239 | 1 | 1 | 0.0 | 99.8 | 3012.47 |
| $\kappa(0,2,0)$ | 1/2 | $A'$ | 124 | 1 | 1 | 0.0 | 99.9 | 3012.73 |
| $\kappa(0,2,0)$ | 3/2 | $A'$ | 241 | 2 | 1 | 0.0 | 99.7 | 3016.47 |
| $\kappa(0,2,0)$ | 3/2 | $A$" | 242 | 2 | 1 | 0.0 | 99.8 | 3019.55 |
| $\kappa(0,2,0)$ | 1/2 | $A'$ | 127 | 0 | 0 | 0.0 | 99.9 | 3019.62 |
| $\kappa(0,2,0)$ | 3/2 | $A$" | 244 | 1 | 0 | 0.2 | 99.4 | 3022.48 |
| $\kappa(0,2,0)$ | 1/2 | $A$" | 127 | 1 | 0 | 0.0 | 99.9 | 3022.49 |
| $\kappa(0,2,0)$ | 3/2 | $A'$ | 244 | 2 | 0 | 0.0 | 99.7 | 3028.41 |

[a] The numbering of the energies found in each $P = 1/2, 3/2$, $\Gamma_{\rm ers}$ state. [b] Dominant contributed basis function's $N$ and $K$ values. [c] The over-all probability given in %. See Chapter 2.5.3. [d] Energy calculated with the program DR.

# Chapter 5

# The double Renner effect in ABB-type molecules

As an example of an ABB-type molecule, we take the electronic ground state $\widetilde{X}\ ^2A''$ and the first excited electronic state $\widetilde{A}\ ^2A'$ of $HO_2$.

## 5.1 $HO_2$

The very simple chemical reaction

$$\mathrm{H} + \mathrm{O}_2 \rightarrow \mathrm{HO} + \mathrm{O} \tag{5.1}$$

and the reverse reaction

$$\mathrm{HO} + \mathrm{O} \rightarrow \mathrm{H} + \mathrm{O}_2 \tag{5.2}$$

are very important gas phase reactions in combustion chemistry [48, 49, 50]. These reactions also play very important roles in atmospheric chemistry and interstellar chemistry [51]. The recombination reaction

$$\mathrm{H} + \mathrm{O}_2 \rightarrow \mathrm{HO}_2 \tag{5.3}$$

is thought to be an intermediate reaction of the reactions of (5.1) and (5.2). Thus $HO_2$, the hydroperoxyl radical, has been attracting huge interest from a large group of scientists.

The first prediction of the properties of this molecule was by Walsh [52] in 1952. He predicted $HO_2$ to have a ground electronic state with bent equilibrium geometry and a first excited electronic state almost as low in energy. The prediction was later confirmed by theoretical calculations [53, 54]; linear $HO_2$ has a $^2\Pi$ electronic state as ground electronic state, and this state splits into $\widetilde{X}\ ^2A''$ and $\widetilde{A}\ ^2A'$ states, with strongly bent equilibrium geometries. The $\widetilde{X}\ ^2A''$ and $\widetilde{A}\ ^2A'$ states enjoy the Renner effect.

For spectroscopy $HO_2$ is a well known light and unsymmetrical triatomic molecule. The $\widetilde{A}-\widetilde{X}$ electronic band system of $HO_2$ in the gas phase was studied in 1974, both in emission and in absorption [55, 56], and it was realized that forbidden $\Delta K_a = 0$ transitions are present; Tuckett et al. [57] suggested that these transitions result from Renner interaction. A large number of spectroscopic studies followed (See Refs. [57] - [63] and references therein). Fink and Ramsay have carried out a high-resolution recent reinvestigation of the $\widetilde{A}(0,0,0) \rightarrow \widetilde{X}(0,0,0)$ band [63]. Magnetic dipole transitions are usually too weak to be observed among electric dipole transitions. However Fink and Ramsay found that in the case of $HO_2$, the electric dipole transition moment for the electronic transition is very small and the forbidden $\Delta K_a = 0$ transitions that they observed are magnetic dipole transitions.

To confirm the analysis of Fink and Ramsay, Osmann $et\ al.$ [64] have calculated the $ab\ initio$ potential energy, transition electronic dipole and transition magnetic dipole surfaces of the $\widetilde{X}\ ^2A'' - \widetilde{A}\ ^2A'$ system and simulated the $\widetilde{A}\ ^2A' \rightarrow \widetilde{X}\ ^2A''$ emission spectrum using the program RENNER. Later, Jensen $et\ al.$ [65] calculated more points on the potential surfaces, using the same $ab\ initio$ method used in Ref. [64], to cover a wider range of bending geometries. They adjusted the shapes of the surfaces in a least squares refinement to the energies of rovibronic states involving both electronic

states. Their results provided an accurate representation of the surfaces in this energy region.

Jensen $et\ al.$ [65] have calculated the barrier to linearity of the $\widetilde{X}\ ^2A''$ state as 21358.3 cm$^{-1}$. The electronic energies of T-shaped geometries with $C_{2v}$ symmetry have recently been calculated by Lieberman [66] and the $\widetilde{X}\ ^2A''$ has a barrier to H-OO $\longleftrightarrow$ OO-H "isomerization" of 14100 cm$^{-1}$.

Both the Renner effect and the possibility of isomerization play an important role in the $\widetilde{X}\ ^2A'' - \widetilde{A}\ ^2A'$ $HO_2$ system but we have not seen any work on this system which includes these effects simultaneously. Thus we apply the program DR to $HO_2$.

## 5.2 Applying DR to $HO_2$

### 5.2.1 Global potential energy surfaces

We first tried to calculate the rovibronic energy levels using the refined potential energy surfaces in Ref. [65]. Unfortunately, however, these potential surfaces are only realistic close to their respective equilibrium geometries; at large displacements they have spurious minima ("holes") and this makes it impossible to calculate the rovibronic energies with the program DR.

Thus we have asked Prof. Buenker's group at Wuppertal to calculate $HO_2$ data with the $ab\ initio$ method they used in Ref. [64]. They employed the cc-pVTZ basis sets of Dunning [44] for hydrogen atoms. The effective core potential (ECP) [67] describing the $1s$ orbital, which is needed for taking spin-orbit effects into account, was used together with the cc-pVTZ basis set for the oxygen atom. All the $ab\ initio$ energies were calculated by the multireference single- and double-excitation (MRD-CI) configuration interaction method [68]-[74], with configuration selection and energy extrapolation using the Table-CI algorithm [75]. The final full CI energy was corrected by the formula of Davidson [76]. In these calculations, the two highest molecular orbitals were discarded

and a selection threshold of 7.2 $\times$ $10^{-8}$ Hartree was used. All the calculations were carried out in $C_{\rm s}$ symmetry.

We have fitted 709 $ab\ initio$ points (350 for the lower electronic surface $\widetilde{X}\ ^2A''$ and 359 for the upper electronic surface $\widetilde{A}\ ^2A'$) to global potential energy surfaces. We followed the idea of Bowman $et\ al.$ [77] for fitting the global potential energy surface of $HO_2$. We first prepared the $ab\ initio$ points in a grid of the $r$ and $\tau$ coordinates. We have 5 $r$-coordinate values (2.0000, 2.3244, 2.5133, 2.7968, and 3.0236 Bohr) and 13 $\tau$-coordinate values ($2.5^\circ$, $5^\circ$, $10^\circ$, $15^\circ$, $20^\circ$, $25^\circ$, $30^\circ$, $40^\circ$, $50^\circ$, $60^\circ$, $70^\circ$, $80^\circ$ and $90^\circ$). At each grid point, we have chosen 5 to 8 $R$ values among the distances 0.9000, 1.1000, 1.3000, 1.5496, 1.6441, 1.8332, 2.0785, 2.0786, 2.0787, 2.3244, 2.5000, 2.7200, 2.7500, 3.0000, 3.3000, 3.5000 and 3.8000 Bohr so that region of minimum energy is covered. We have fitted these energies as functions of the $R$-coordinate to a Morse potential function,

$$E(R)^\sigma = D^\sigma_{r,\tau}\{1-\exp[-\alpha^\sigma_{r,\tau}(R-R_{e^\sigma_{r,\tau}})]\}^2 - V^\sigma_{r,\tau}. \qquad (5.4)$$

and obtained the dissociation energy parameter $D^\sigma_{r,\tau}$, minimum energy $V^\sigma_{r,\tau}$, equilibrium geometry $R_{e^\sigma_{r,\tau}}$ and Morse parameter $\alpha^\sigma_{r,\tau}$ for both lower and upper electronic state $\sigma = \pm$. The averaged standard deviation for the lower and upper potential energy surfaces are 60.0 $cm^{-1}$, and 76.9 $cm^{-1}$, respectively. The equilibrium geometry for the lower and upper electronic surfaces are $r$ = 2.5144 Bohr, $R$ = 2.4668 Bohr, $\tau = 45.1^\circ$ and $r$ = 2.6906 Bohr, $R$ = 2.4846 Bohr, $\tau = 45.4^\circ$, respectively.

The calculated vibronic energy levels with these potential energy surfaces deviated more than hundred $cm^{-1}$ from the experimental values. To improve the surface we need much smaller grid intervals for both the $\tau$ and $r$ coordinates. The number of $ab\ initio$ points required for that is enormous, and it is not possible to calculate them at the monent.

Finally we have tried to use the potential energy surfaces in Ref. [64]. The expressions used to expand the potential energy surfaces as functions of the bond lengths

and bond angle are given in Eqs. (1)-(4) of Appendix C, and the values of the parameters are summarized in Table 5.1

### 5.2.2 Bending basis functions

We have computed the minimum energy paths from the potential energy surfaces given in the previous section. The minimum energy paths are expressed in $\sin\tau$ series,

$$V^{\sigma}(\tau) = \sum_{i} G^{i}_{V,\sigma} \sin^{i}\tau \tag{5.5}$$

$$R^{\sigma}(\tau) = \sum_{i} G^{i}_{R,\sigma} \sin^{i}\tau \tag{5.6}$$

$$r^{\sigma}(\tau) = \sum_{i} G^{i}_{r,\sigma} \sin^{i}\tau. \tag{5.7}$$

$V^{\pm}(\tau)$ are the potential energies along the minimum energy paths, $R^{\pm}(\tau)$ and $r^{\pm}(\tau)$ are $R$ and $r$ bond length changes along these paths. The parameters for equations (5.5) - (5.7) are summarized in Table 5.2. The minimum energy paths are shown in Fig. 5.1.

## 5.3 Results

### 5.3.1 Computational details

We have calculated ro-vibronic energy levels of the $\widetilde{X}\ ^2A''$ and $\widetilde{A}\ ^2A'$ $HO_2$ states by using the program DR. For the $\eta = a$ and $\eta = b$ bending basis set we employed 23 and 15 bending basis functions, respectively, calculated from the minimum energy path parameters in Table 5.2. We have 4000 integration points for the Numerov-Cooley integration, and 80 integration points for the Gauss-Laguerre integration.

For the stretching basis functions, we employed 15 and 7 functions for $R$ and $r$ coordinates, respectively. The parameters used for constructing the stretching basis functions are as follows. The equilibrium distance RE1 and RE2 are 2.5390409 and

Table 5.1: The potential surface parameters for the $\widetilde{X}\ ^2A''$ and $\widetilde{A}\ ^2A'$ states of $HO_2$ from Ref. [65].[a]

| | | | | |
|---|---|---|---|---|
| $r_{12}^{(\mathrm{ref})}$/Å | 0.95079(10)[b] | 1.34000(20) | | |
| $a_1$/Å$^{-1}$ | 2.75[c] | 2.75 | | |
| $f_{11}^{(0)}$/cm$^{-1}$ | 24640(27) | 18689(36) | | |
| $f_{13}^{(0)}$/cm$^{-1}$ | −7570(126) | | | |
| $f_{111}^{(0)}$/cm$^{-1}$ | 2544(74) | 3515(23) | | |
| $f_{113}^{(0)}$/cm$^{-1}$ | 8970(148) | −1119(44) | | |
| $f_{1111}^{(0)}$/cm$^{-1}$ | 2666(18) | 1025(12) | | |
| $f_{1133}^{(0)}$/cm$^{-1}$ | −742(43) | | | |
| | $\widetilde{X}^2A''(\sigma=-)$ | | $\widetilde{A}^2A'(\sigma=+)$ | |
| $f_0^{(1,\sigma)}$/cm$^{-1}$ | −77219(83) | | −41743(99) | |
| $f_0^{(2,\sigma)}$/cm$^{-1}$ | 131699(279) | | 56008(447) | |
| $f_0^{(3,\sigma)}$/cm$^{-1}$ | −161158(428) | | −58989(1001) | |
| $f_0^{(4,\sigma)}$/cm$^{-1}$ | 135418(304) | | 49829(1180) | |
| $f_0^{(5,\sigma)}$/cm$^{-1}$ | −58357(81) | | −20427(697) | |
| $f_0^{(6,\sigma)}$/cm$^{-1}$ | 10000 | | 3373(162) | |
| $f_1^{(1,\sigma)}$/cm$^{-1}$ | −16336(90) | 10437(94) | −4830(48) | −12356(125) |
| $f_1^{(2,\sigma)}$/cm$^{-1}$ | 27603(215) | −13922(26) | 0 | 11179(273) |
| $f_1^{(3,\sigma)}$/cm$^{-1}$ | −14367(231) | −849(58) | 6733(85) | −13050(284) |
| $f_1^{(4,\sigma)}$/cm$^{-1}$ | 684(88) | | −5482(54) | 3675(106) |
| $f_{11}^{(1,\sigma)}$/cm$^{-1}$ | 4016(90) | 4075(68) | 13137(144) | −2073(117) |
| $f_{11}^{(2,\sigma)}$/cm$^{-1}$ | −758(61) | −750(44) | −13864(227) | 9900(194) |
| $f_{11}^{(3,\sigma)}$/cm$^{-1}$ | | | 3993(117) | −6362(103) |
| $f_{13}^{(1,\sigma)}$/cm$^{-1}$ | 40283(520) | | 24902(524) | |
| $f_{13}^{(2,\sigma)}$/cm$^{-1}$ | −55426(686) | | −26344(700) | |
| $f_{13}^{(3,\sigma)}$/cm$^{-1}$ | 24156(296) | | 11011(305) | |
| $f_{111}^{(1,\sigma)}$/cm$^{-1}$ | 0 | 1155(25) | 4039(71) | −1646(63) |
| $f_{111}^{(2,\sigma)}$/cm$^{-1}$ | | | −2358(146) | 2206(53) |
| $f_{113}^{(1,\sigma)}$/cm$^{-1}$ | −12799(415) | −1929(57) | −21815(426) | −3873(146) |
| $f_{113}^{(2,\sigma)}$/cm$^{-1}$ | 5414(279) | | 13445(291) | 3348(124) |
| $f_{1111}^{(1,\sigma)}$/cm$^{-1}$ | | 648(17) | | |

[a] When two values are given for a parameter the second value is that of the parameter with the indices 1 and 3 interchanged in the subscript; this does not occur for $f_0^{()}$, $f_{13}^{()}$ or $f_{1133}^{()}$. The parameters $f_{jk\ldots}^{(0)}$ are common to both electronic states; they specify the stretching potential at linearity. A subscript 1 refers to the HO bond, whereas a subscript 3 refers to the OO bond.

[b] Quantities in parentheses are standard errors in units of the last digit given.

[c] Parameters for which no standard error is given were held fixed in the least squares fit.

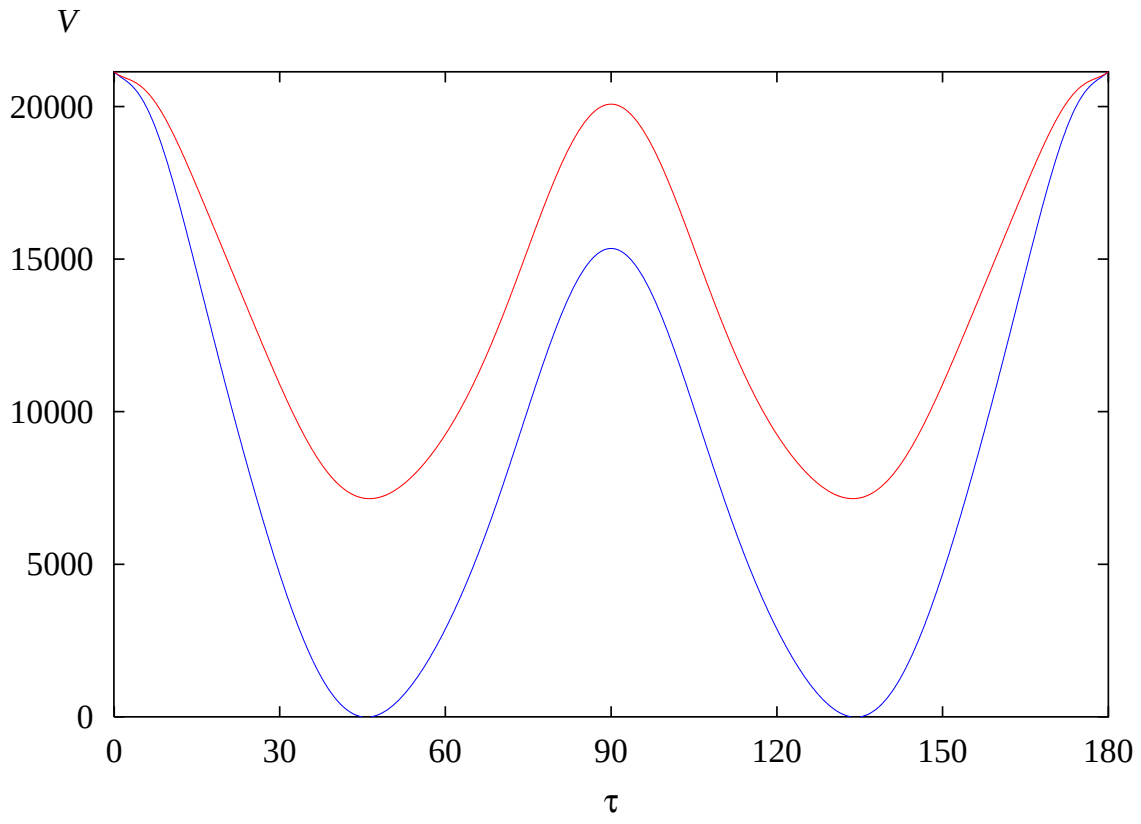


Figure 5.1: The potential energy path used to produce bending basis function for the $\widetilde{X}\ ^2A'' - \widetilde{A}\ ^2A'$ surface. See equations (5.5) - (5.7) together with the parameters in Table 5.2. $\tau$ is given in degrees and the potential $V$ is given in $\mathrm{cm}^{-1}$. The blue curve shows the lower potential energy surface and the red curve shows the upper potential energy surface.

Table 5.2: Minimum energy paths parameters in equations (5.5) - (5.7) for lower($\sigma = -$) and upper ($\sigma = +$) electronic surface

| $i$ | $G^i_{V,-}$/ Hartree | $G^i_{V,+}$/ Hartree | $G^i_{R,-}$/ Bohr | $G^i_{R,+}$/ Bohr | $G^i_{r,-}$/ Bohr | $G^i_{r,+}$/ Bohr |
|---|---|---|---|---|---|---|
| 0 | 0.096350511 | | 3.0595598 | | 2.5325190 | |
| 1 | -0.046249097 | -0.041650143 | -0.045823397 | -0.031118964 | 0.49107083 | 0.42041901 |
| 2 | 0.59401929 | 0.69481429 | 1.2350086 | 1.2479451 | -12.944801 | -10.637389 |
| 3 | -9.9529236 | -8.6415838 | -9.4737738 | -5.9379531 | 106.85489 | 86.860113 |
| 4 | 44.764315 | 37.995362 | 39.502983 | 25.059007 | -470.63994 | -379.17433 |
| 5 | -101.98301 | -87.742544 | -97.200550 | -61.707483 | 1120.7241 | 893.31598 |
| 6 | 127.90016 | 111.98051 | 136.14852 | 82.432632 | -1473.7307 | -1164.9741 |
| 7 | -83.463523 | -74.215460 | -99.198315 | -56.728167 | 1006.1328 | 789.98250 |
| 8 | 22.160796 | 19.965687 | 29.232391 | 15.887036 | -278.38945 | -217.18247 |

2.4840281 Bohr, respectively. The dissociation energy DISS1 and DISS2 are 0.175 and 15 Hartree, respectively. The harmonic frequency WE1 and WE2 are 0.004 and 0.0125 Hartree, respectively. Integration points for $R$ and $r$ coordinate are 15 and 35, respectively.

We have employed the spin-orbit interaction constant for $HO_2$, $-160.1$ cm$^{-1}$ as in Ref. [65]. The threshold limit energy constant for K-block contraction, CONTMAX, is taken to be 18000cm $^{-1}$.

### 5.3.2 Vibronic energy levels

Calculated vibronic energy levels for $\widetilde{X}\ ^2A''$ and $\widetilde{A}\ ^2A'$ $HO_2$ with $N_{K_aK_c} = 0_{00}$ are listed in Tables 5.3 - 5.9. The probability density of the lower and the upper electronic surfaces $P_-$ and $P_+$, respectively, are shown for each vibronic energy level. When an energy level is split by tunneling, the splittings are also given in the tables. When we find the vibronic energy levels from the previous theoretical studies [64, 65] with the program RENNER [9] , we listed the energy levels in the tables. Selected wavefunctions are

Table 5.3: Vibronic term values (in $cm^{-1}$) of $HO_2$. Energy levels with $N_{K_aK_c} = 0_{00}$ are listed here. When an energy level is split by tunneling, the lower component and the splitting are given.

| State | $\Gamma_{\rm rve}$ | No.[a] | $P^b_-$% | $P^b_+$/% | $\Delta^c_t$ | DR[d] | RENNER[e] | RENNER[f] |
|---|---|---|---|---|---|---|---|---|
| $\widetilde{X}(0,0,0)$, Fig. 5.2 | $A_1$ | 1 | 100.0 | 0.0 | 0.00 | 0.00 | 0.00 | 0.0 |
| $\widetilde{X}(0,0,1)$ | $A_1$ | 3 | 100.0 | 0.0 | 0.00 | 1082.59 | 1080.00 | 1097.2 |
| $\widetilde{X}(0,1,0)$ | $A_1$ | 5 | 100.0 | 0.0 | 0.00 | 1390.64 | 1381.55 | 1391.5 |
| $\widetilde{X}(0,0,2)$ | $A_1$ | 7 | 100.0 | 0.0 | 0.00 | 2144.97 | 2140.47 | 2178.9 |
| $\widetilde{X}(0,1,1)$ | $A_1$ | 9 | 100.0 | 0.0 | 0.00 | 2460.31 | 2446.37 | 2472.6 |
| $\widetilde{X}(0,2,0)$ | $A_1$ | 11 | 100.0 | 0.0 | 0.00 | 2758.34 | 2733.52 | 2747.1 |
| $\widetilde{X}(0,0,3)$ | $A_1$ | 13 | 100.0 | 0.0 | 0.00 | 3186.71 | | 3245.8 |
| $\widetilde{X}(1,0,0)$ | $A_1$ | 15 | 100.0 | 0.0 | 0.00 | 3467.28 | 3462.93 | 3435.8 |
| $\widetilde{X}(0,1,2)$ | $A_1$ | 17 | 100.0 | 0.0 | 0.00 | 3510.58 | | 3538.4 |
| $\widetilde{X}(0,2,1)$ | $A_1$ | 19 | 100.0 | 0.0 | 0.00 | 3814.41 | | 3812.1 |
| $\widetilde{X}(0,3,0)$ | $B_2$ | 21 | 100.0 | 0.0 | 0.01 | 4104.06 | | 4071.0 |
| $\widetilde{X}(0,0,4)$ | $A_1$ | 23 | 100.0 | 0.0 | 0.00 | 4207.40 | | 4298.4 |
| $\widetilde{X}(0,1,3)$ | $A_1$ | 25 | 100.0 | 0.0 | 0.00 | 4533.54 | | 4589.6 |
| $\widetilde{X}(1,0,1)$ | $A_1$ | 26 | 100.0 | 0.0 | 0.00 | 4552.74 | | 4529.2 |
| $\widetilde{X}(1,1,0)$ | $A_1$ | 29 | 100.0 | 0.0 | 0.00 | 4832.32 | 4823.77 | 4793.7 |
| $\widetilde{X}(0,2,2)$ | $A_1$ | 30 | 100.0 | 0.0 | 0.00 | 4854.35 | 4803.82 | 4862.4 |
| $\widetilde{X}(0,3,1)$ | $A_1$ | 33 | 100.0 | 0.0 | 0.00 | 5146.08 | | 5119.4 |
| $\widetilde{X}(0,0,5)$ | $A_1$ | 35 | 100.0 | 0.0 | 0.00 | 5206.67 | | 5338.0 |
| $\widetilde{X}(0,4,0)$ | $A_1$ | 37 | 100.0 | 0.0 | 0.00 | 5428.76 | | 5366.4 |
| $\widetilde{X}(0,1,4)$ | $A_1$ | 39 | 100.0 | 0.0 | 0.00 | 5544.97 | | 5630.1 |
| $\widetilde{X}(1,0,2)$ | $A_1$ | 41 | 100.0 | 0.0 | 0.00 | 5608.93 | | 5605.2 |
| $\widetilde{X}(0,2,3)$ | $B_2$ | 43 | 100.0 | 0.0 | 0.01 | 5862.49 | | 5900.6 |
| $\widetilde{X}(1,1,1)$ | $A_1$ | 45 | 100.0 | 0.0 | 0.00 | 5905.58 | | 5864.1 |
| $\widetilde{X}(0,3,2)$ | $B_2$ | 47 | 100.0 | 0.0 | 0.01 | 6163.43 | | 6155.4 |
| $\widetilde{X}(0,0,6)$ | $A_1$ | 48 | 100.0 | 0.0 | 0.00 | 6184.14 | | 6365.9 |
| $\widetilde{X}(1,2,0)$ | $B_2$ | 50 | 100.0 | 0.0 | 0.01 | 6187.87 | | 6113.2 |
| $\widetilde{X}(0,4,1)$ | $B_2$ | 53 | 100.0 | 0.0 | 0.03 | 6456.66 | | 6397.9 |
| $\widetilde{X}(0,1,5)$ | $A_1$ | 55 | 100.0 | 0.0 | 0.00 | 6532.14 | | 6641.5 |
| $\widetilde{X}(1,0,3)$ | $A_1$ | 57 | 100.0 | 0.0 | 0.00 | 6647.53 | | 6682.7 |
| $\widetilde{X}(2,0,0),+$, Fig. 5.3 | $A_1$ | 59 | 99.9 | 0.0 | 0.00 | 6732.21 | | 6648.3 |
| $\widetilde{X}(0,5,0),+$, Fig. 5.4 | $B_2$ | 60 | 99.9 | 0.0 | 0.07 | 6734.15 | | 6635.7 |
| $\widetilde{X}(0,2,4)$ | $B_2$ | 63 | 100.0 | 0.0 | 0.01 | 6859.16 | | 6904.8 |
| $\widetilde{X}(1,1,2)$ | $A_1$ | 65 | 100.0 | 0.0 | 0.00 | 6950.08 | | 6939.7 |
| $\widetilde{A}(0,0,0)$, Fig. 5.5 | $A_2$ | 67 | 0.0 | 100.0 | 0.00 | 7018.40 | 7014.57 | 7030.0 |
| $\widetilde{X}(0,0,7)$ | $A_1$ | 69 | 100.0 | 0.0 | 0.00 | 7139.97 | | 7381.7 |
| $\widetilde{X}(0,3,3)$ | $B_2$ | 71 | 100.0 | 0.0 | 0.01 | 7168.66 | | |
| $\widetilde{X}(1,2,1)$ | $B_2$ | 73 | 100.0 | 0.0 | 0.02 | 7236.30 | | 7154.5 |
| $\widetilde{X}(0,4,2)$ | $B_2$ | 75 | 100.0 | 0.0 | 0.05 | 7464.17 | | 7649.8 |
| $\widetilde{X}(0,1,6)$ | $A_1$ | 77 | 100.0 | 0.0 | 0.00 | 7497.36 | | 7653.7 |
| $\widetilde{X}(1,3,0)$ | $B_2$ | 78 | 100.0 | 0.0 | 0.08 | 7512.29 | | 7396.8 |

[a]The numbering of the energies found in each $J = 1/2$, $\Gamma_{\rm ers}$ state. [b]The over-all probability given in %. See Chapter 2.5.3 [c]Tunnel splitting energy, give in E/hc [d]Energy calculated with the program DR. [e] Ref. [64] Energy calculated with the program RENNER, using the same potential energy surface as this work. [f]Ref. [65] Energy calculated with the program RENNER, with a potential energy surface fitted to experimental data.

Table 5.4: Vibronic term values (in $cm^{-1}$) of $HO_2$. Energy levels with $N_{K_aK_c} = 0_{00}$ are listed here. When an energy level is split by tunneling, the lower component and the splitting are given.

| State | $\Gamma_{\rm rve}$ | No.[a] | $P_-^b$ % | $P_+^b$/% | $\Delta_t^c$ | DR[d] | RENNER[e] | RENNER[f] |
|---|---|---|---|---|---|---|---|---|
| $\widetilde{X}(1,0,4)$ | $A_1$ | 81 | 100.0 | 0.0 | 0.00 | 7665.45 | | 7730.9 |
| $\widetilde{X}(0,5,1)$ | $B_2$ | 83 | 100.0 | 0.0 | 0.05 | 7748.81 | | |
| $\widetilde{X}(2,0,1)$ | $A_1$ | 85 | 100.0 | 0.0 | 0.00 | 7808.08 | | 7746.8 |
| $\widetilde{X}(0,2,5)$ | $A_1$ | 87 | 100.0 | 0.0 | 0.00 | 7834.41 | | 7915.7 |
| $\widetilde{A}(0,0,1)$ | $A_2$ | 89 | 0.0 | 100.0 | 0.01 | 7916.40 | 7913.78 | 7958.3 |
| $\widetilde{X}(1,1,3)$ | $A_1$ | 91 | 100.0 | 0.0 | 0.00 | 7974.89 | | |
| $\widetilde{X}(0,6,0)$ | $B_2$ | 93 | 100.0 | 0.0 | 0.26 | 8022.24 | | 7881.2 |
| $\widetilde{X}(0,0,8)$ | $A_1$ | 95 | 100.0 | 0.0 | 0.00 | 8080.63 | | |
| $\widetilde{X}(2,1,0)$ | $B_2$ | 97 | 100.0 | 0.0 | 0.04 | 8109.51 | | 7978.5 |
| $\widetilde{X}(0,3,4)$ | $B_2$ | 99 | 100.0 | 0.0 | 0.01 | 8153.34 | | |
| $\widetilde{A}(0,1,0)$ | $A_2$ | 101 | 0.0 | 100.0 | 0.01 | 8234.73 | 8215.88 | |
| $\widetilde{X}(1,2,2)$ | $B_2$ | 103 | 100.0 | 0.0 | 0.03 | 8266.81 | | |
| $\widetilde{X}(0,1,7)$ | $A_1$ | 105 | 100.0 | 0.0 | 0.00 | 8442.20 | | |
| $\widetilde{X}(0,4,3)$ | $B_2$ | 106 | 100.0 | 0.0 | 0.06 | 8457.01 | | 8167.8 |
| $\widetilde{X}(1,3,1)$ | $B_2$ | 109 | 100.0 | 0.0 | 0.12 | 8547.07 | | |
| $\widetilde{X}(1,0,5)$ | $A_1$ | 111 | 100.0 | 0.0 | 0.00 | 8661.88 | | |
| $\widetilde{X}(0,5,2)$ | $B_2$ | 113 | 100.0 | 0.0 | 0.07 | 8748.04 | | |
| $\widetilde{X}(0,2,6)$ | $A_1$ | 115 | 99.9 | 0.0 | 0.00 | 8788.34 | | |
| $\widetilde{A}(0,0,2)$ | $A_2$ | 116 | 0.2 | 99.7 | 0.00 | 8792.02 | 8799.91 | |
| $\widetilde{X}$ | $B_2$ | 119 | 100.0 | 0.0 | 0.39 | 8827.53 | | |
| $\widetilde{X}$ | $B_2$ | 121 | 100.0 | 0.0 | 0.01 | 8864.33 | | |
| $\widetilde{X}$ | $B_2$ | 123 | 100.0 | 0.0 | 0.01 | 8978.66 | | |
| $\widetilde{X}$ | $B_2$ | 125 | 100.0 | 0.0 | 0.38 | 9027.83 | | |
| $\widetilde{X}$ | $A_1$ | 127 | 100.0 | 0.0 | 0.00 | 9077.21 | | |
| $\widetilde{X}$ | $B_2$ | 129 | 99.9 | 0.0 | 0.01 | 9118.19 | | |
| $\widetilde{A}(0,1,1)$ | $A_2$ | 130 | 0.4 | 99.6 | 0.00 | 9121.91 | | |
| $\widetilde{X}$ | $B_2$ | 133 | 100.0 | 0.0 | 0.07 | 9168.99 | | |
| $\widetilde{X}$ | $B_2$ | 135 | 100.0 | 0.0 | 0.03 | 9277.42 | | |
| $\widetilde{X}$ | $B_2$ | 136 | 100.0 | 0.0 | 0.20 | 9298.89 | | |
| $\widetilde{X}$ | $A_1$ | 139 | 100.0 | 0.0 | 0.00 | 9384.80 | | |
| $\widetilde{X}$ | $B_2$ | 141 | 99.9 | 0.0 | 0.07 | 9433.12 | | |
| $\widetilde{A}(0,2,0)$ | $A_2$ | 141 | 0.3 | 99.7 | 0.02 | 9433.86 | 9400.87 | |
| $\widetilde{X}$ | $B_2$ | 145 | 100.0 | 0.0 | 0.30 | 9470.16 | | |
| $\widetilde{X}$ | $B_2$ | 147 | 100.0 | 0.0 | 0.13 | 9563.53 | | |
| $\widetilde{X}$ | $A_1$ | 149 | 99.8 | 0.2 | 0.00 | 9636.86 | | |
| $\widetilde{A}(0,0,3)$ | $A_2$ | 150 | 0.5 | 99.5 | 0.00 | 9645.17 | | |
| $\widetilde{X}$ | $B_2$ | 153 | 100.0 | 0.0 | 0.01 | 9726.38 | | |
| $\widetilde{X}$ | $B_2$ | 154 | 100.0 | 0.0 | 0.13 | 9735.01 | | |
| $\widetilde{X}$ | $B_2$ | 157 | 100.0 | 0.0 | 0.31 | 9845.55 | | |
| $\widetilde{X}$ | $B_2$ | 158 | 100.0 | 0.0 | 0.15 | 9853.05 | | |

[a], [b], [c], [d], [e] and [f]; See footnote for Table 5.3

Table 5.5: Vibronic term values (in $cm^{-1}$) of $HO_2$. Energy levels with $N_{K_aK_c} = 0_{00}$ are listed here. When an energy level is split by tunneling, the lower component and the splitting are given.

| State | $\Gamma_{\rm rve}$ | No.[a] | $P_-^b$ % | $P_+^b$/% | $\Delta_t^c$ | DR[d] | RENNER[e] |
|---|---|---|---|---|---|---|---|
| $\widetilde{X}$ | $B_2$ | 161 | 100.0 | 0.0 | 0.01 | 9898.39 | |
| $\widetilde{X}$ | $B_2$ | 163 | 99.9 | 0.0 | 0.01 | 9961.61 | |
| $\widetilde{A}(0,1,2)$ | $A_2$ | 165 | 0.0 | 99.9 | 0.01 | 9987.33 | |
| $\widetilde{X}$ | $B_2$ | 167 | 100.0 | 0.0 | 0.49 | 10023.85 | |
| $\widetilde{X}$ | $B_2$ | 169 | 100.0 | 0.0 | 0.01 | 10066.52 | |
| $\widetilde{X}$ | $B_2$ | 171 | 100.0 | 0.0 | 1.04 | 10138.30 | |
| $\widetilde{X}$ | $B_2$ | 173 | 100.0 | 0.0 | 0.08 | 10204.93 | |
| $\widetilde{X}$ | $B_2$ | 175 | 100.0 | 0.0 | 0.04 | 10269.41 | |
| $\widetilde{X}$ | $B_2$ | 177 | 100.0 | 0.0 | 1.06 | 10300.93 | |
| $\widetilde{A}(0,2,1)$ | $A_2$ | 178 | 0.0 | 99.9 | 0.02 | 10309.89 | |
| $\widetilde{X}$ | $B_2$ | 179 | 100.0 | 0.0 | 0.00 | 10330.00 | |
| $\widetilde{X}$ | $B_2$ | 183 | 100.0 | 0.0 | 0.08 | 10394.05 | |
| $\widetilde{A}(0,0,4)$ | $A_2$ | 185 | 0.0 | 99.9 | 0.00 | 10483.17 | |
| $\widetilde{X}$ | $A_1$ | 186 | 99.8 | 0.1 | 0.00 | 10499.44 | |
| $\widetilde{X}$ | $B_2$ | 188 | 100.0 | 0.0 | 0.34 | 10509.54 | |
| $\widetilde{X}$ | $B_2$ | 191 | 100.0 | 0.0 | 0.26 | 10564.92 | |
| $\widetilde{X}$ | $B_2$ | 192 | 100.0 | 0.0 | 3.16 | 10568.97 | |
| $\widetilde{A}(1,0,0)$ | $A_2$ | 194 | 0.0 | 100.0 | 0.00 | 10591.52 | 10585.10 |
| $\widetilde{X}$ | $A_1$ | 196 | 100.0 | 0.0 | 0.00 | 10604.81 | |
| $\widetilde{A}$ | $A_2$ | 198 | 0.0 | 100.0 | 0.07 | 10618.43 | |
| $\widetilde{X}$ | $A_1$ | 201 | 100.0 | 0.0 | 0.00 | 10683.47 | |
| $\widetilde{X}$ | $B_2$ | 203 | 100.0 | 0.0 | 0.20 | 10708.46 | |
| $\widetilde{A}$ | $A_2$ | 205 | 0.0 | 99.9 | 0.01 | 10831.72 | |
| $\widetilde{X}$ | $B_2$ | 206 | 71.0 | 28.9 | 0.78 | 10833.67 | |
| $\widetilde{X}$ | $B_2$ | 209 | 100.0 | 0.0 | 0.95 | 10863.59 | |
| $\widetilde{X}$ | $B_2$ | 211 | 100.0 | 0.0 | 0.02 | 10898.57 | |
| $\widetilde{X}$ | $B_2$ | 213 | 100.0 | 0.0 | 0.11 | 10927.42 | |
| $\widetilde{X}$ | $B_2$ | 214 | 100.0 | 0.0 | 0.04 | 10939.22 | |
| $\widetilde{X}$ | $B_2$ | 217 | 100.0 | 0.0 | 0.09 | 11005.33 | |
| $\widetilde{X}$ | $B_2$ | 218 | 100.0 | 0.0 | 0.53 | 11010.85 | |
| $\widetilde{X}$ | $B_2$ | 221 | 100.0 | 0.0 | 1.13 | 11141.69 | |
| $\widetilde{A}$ | $A_2$ | 222 | 0.0 | 99.9 | 0.03 | 11165.02 | |
| $\widetilde{X}$ | $B_2$ | 225 | 99.9 | 0.0 | 0.07 | 11203.72 | |
| $\widetilde{X}$ | $B_2$ | 227 | 100.0 | 0.0 | 0.07 | 11256.00 | |
| $\widetilde{X}$ | $B_2$ | 229 | 100.0 | 0.0 | 1.37 | 11299.31 | |
| $\widetilde{X}$ | $B_2$ | 231 | 100.0 | 0.0 | 0.09 | 11342.27 | |
| $\widetilde{A}$ | $A_2$ | 232 | 0.0 | 100.0 | 0.00 | 11355.86 | |
| $\widetilde{X}$ | $B_2$ | 234 | 100.0 | 0.0 | 0.92 | 11368.11 | |
| $\widetilde{X}$ | $B_2$ | 237 | 100.0 | 0.0 | 2.81 | 11452.52 | |
| $\widetilde{A}$ | $A_2$ | 239 | 0.1 | 99.8 | 0.10 | 11483.14 | |

[a], [b], [c], [d] and [e]; See footnote for Table 5.3

Table 5.6: Vibronic term values (in $cm^{-1}$) of $HO_2$. Energy levels with $N_{K_aK_c} = 0_{00}$ are listed here. When an energy level is split by tunneling, the lower component and the splitting are given.

| | $\Gamma_{\rm rve}$ | No.[a] | $P_-^b$ | $P_+^b$ | $\Delta_t^c$ | DR[d] | | $\Gamma_{\rm rve}$ | No.[a] | $P_-^b$ | $P_+^b$ | $\Delta_t^c$ | DR[d] |
|---|---|---|---|---|---|---|---|---|---|---|---|---|---|
| $\widetilde{A}$ | $A_2$ | 240 | 0.0 | 100.0 | 0.00 | 11486.96 | $\widetilde{X}$ | $A_1$ | 321 | 100.0 | 0.0 | 0.80 | 12756.80 |
| $\widetilde{X}$ | $B_2$ | 243 | 99.7 | 0.2 | 0.15 | 11509.01 | $\widetilde{X}$ | $B_2$ | 323 | 100.0 | 0.0 | 0.01 | 12784.33 |
| $\widetilde{X}$ | $A_1$ | 244 | 100.0 | 0.0 | 0.00 | 11526.14 | $\widetilde{X}$ | $B_2$ | 324 | 99.9 | 0.0 | 0.50 | 12788.80 |
| $\widetilde{X}$ | $B_2$ | 247 | 100.0 | 0.0 | 0.20 | 11566.17 | $\widetilde{X}$ | $B_2$ | 325 | 99.9 | 0.0 | 2.66 | 12794.15 |
| $\widetilde{X}$ | $A_1$ | 248 | 100.0 | 0.0 | 0.46 | 11580.94 | $\widetilde{A}$ | $A_2$ | 329 | 0.0 | 100.0 | 0.04 | 12835.39 |
| $\widetilde{X}$ | $A_1$ | 250 | 100.0 | 0.0 | 0.00 | 11611.25 | $\widetilde{X}$ | $B_2$ | 331[e] | 100.0 | 0.0 | 11.09 | 12863.91 |
| $\widetilde{A}$ | $A_2$ | 253 | 0.0 | 100.0 | 0.01 | 11666.60 | $\widetilde{X}$ | $B_2$ | 332 | 100.0 | 0.0 | 0.04 | 12878.53 |
| $\widetilde{X}$ | $B_2$ | 254 | 99.7 | 0.2 | 0.26 | 11669.07 | $\widetilde{X}$ | $B_2$ | 333 | 99.9 | 0.0 | 2.53 | 12895.58 |
| $\widetilde{A}$ | $A_2$ | 257 | 0.0 | 100.0 | 0.03 | 11784.27 | $\widetilde{X}$ | $B_2$ | 335 | 100.0 | 0.0 | 0.55 | 12905.01 |
| $\widetilde{A}$ | $A_2$ | 258 | 0.0 | 99.9 | 0.27 | 11793.73 | $\widetilde{X}$ | $B_2$ | 339 | 99.9 | 0.0 | 1.05 | 12947.19 |
| $\widetilde{X}$ | $B_2$ | 261 | 99.7 | 0.2 | 0.09 | 11818.39 | $\widetilde{A}$ | $A_2$ | 340 | 0.1 | 99.8 | 0.09 | 12964.75 |
| $\widetilde{X}$ | $B_2$ | 262 | 99.9 | 0.0 | 0.07 | 11823.05 | $\widetilde{A}$ | $A_2$ | 343 | 0.0 | 99.9 | 0.46 | 12987.40 |
| $\widetilde{X}$ | $A_1$ | 264 | 100.0 | 0.0 | 3.66 | 11844.57 | $\widetilde{X}$ | $B_2$ | 345 | 100.0 | 0.0 | 0.24 | 13019.89 |
| $\widetilde{X}$ | $B_2$ | 267 | 100.0 | 0.0 | 1.75 | 11887.54 | $\widetilde{X}$ | $B_2$ | 347 | 100.0 | 0.0 | 0.07 | 13085.43 |
| $\widetilde{X}$ | $B_2$ | 268 | 100.0 | 0.0 | 0.05 | 11905.24 | $\widetilde{X}$ | $B_2$ | 349 | 100.0 | 0.0 | 0.21 | 13112.37 |
| $\widetilde{X}$ | $B_2$ | 271 | 100.0 | 0.0 | 0.02 | 11934.84 | $\widetilde{X}$ | $B_2$ | 350 | 100.0 | 0.0 | 3.67 | 13124.40 |
| $\widetilde{X}$ | $B_2$ | 273 | 100.0 | 0.0 | 0.70 | 11984.36 | $\widetilde{X}$ | $B_2$ | 352 | 100.0 | 0.0 | 15.94 | 13142.09 |
| $\widetilde{X}$ | $B_2$ | 274 | 100.0 | 0.0 | 0.26 | 11985.70 | $\widetilde{A}$ | $A_2$ | 354 | 0.0 | 99.9 | 3.78 | 13157.92 |
| $\widetilde{A}$ | $A_2$ | 275 | 0.2 | 99.7 | 0.03 | 12001.27 | $\widetilde{X}$ | $B_2$ | 357 | 99.9 | 0.0 | 0.10 | 13201.79 |
| $\widetilde{X}$ | $B_2$ | 277 | 99.0 | 1.0 | 0.02 | 12006.88 | $\widetilde{A}$ | $A_2$ | 358 | 0.1 | 99.8 | 0.02 | 13211.34 |
| $\widetilde{X}$ | $A_1$ | 281 | 100.0 | 0.0 | 0.21 | 12131.51 | $\widetilde{X}$ | $B_2$ | 361 | 99.9 | 0.0 | 0.16 | 13241.05 |
| $\widetilde{X}$ | $B_2$ | 283 | 100.0 | 0.0 | 0.05 | 12170.05 | $\widetilde{X}$ | $B_2$ | 362 | 100.0 | 0.0 | 2.36 | 13251.93 |
| $\widetilde{X}$ | $B_2$ | 285 | 100.0 | 0.0 | 4.21 | 12231.29 | $\widetilde{X}$ | $B_2$ | 364 | 100.0 | 0.0 | 3.39 | 13271.47 |
| $\widetilde{X}$ | $B_2$ | 286 | 100.0 | 0.0 | 0.15 | 12247.37 | $\widetilde{X}$ | $B_2$ | 367 | 100.0 | 0.0 | 0.11 | 13351.40 |
| $\widetilde{X}$ | $B_2$ | 289 | 100.0 | 0.0 | 0.82 | 12287.17 | $\widetilde{X}$ | $B_2$ | 369 | 100.0 | 0.0 | 1.78 | 13436.70 |
| $\widetilde{X}$ | $B_2$ | 290 | 100.0 | 0.0 | 1.23 | 12289.68 | $\widetilde{X}$ | $B_2$ | 370 | 99.9 | 0.0 | 1.30 | 13448.82 |
| $\widetilde{A}$ | $A_2$ | 293 | 0.0 | 99.9 | 0.10 | 12328.51 | $\widetilde{X}$ | $B_2$ | 372 | 100.0 | 0.0 | 1.95 | 13466.84 |
| $\widetilde{A}$ | $A_2$ | 295 | 0.0 | 100.0 | 0.01 | 12360.17 | $\widetilde{A}$ | $A_2$ | 374 | 0.0 | 99.8 | 0.24 | 13485.79 |
| $\widetilde{A}$ | $A_2$ | 296 | 0.0 | 100.0 | 0.00 | 12363.81 | $\widetilde{A}$ | $A_2$ | 375 | 0.0 | 99.9 | 0.02 | 13490.26 |
| $\widetilde{X}$ | $B_2$ | 299 | 100.0 | 0.0 | 0.44 | 12419.69 | $\widetilde{A}$ | $A_2$ | 379 | 0.0 | 99.9 | 0.08 | 13536.25 |
| $\widetilde{X}$ | $A_1$ | 301 | 100.0 | 0.0 | 0.79 | 12450.36 | $\widetilde{X}$ | $B_2$ | 380 | 99.8 | 0.0 | 0.07 | 13552.51 |
| $\widetilde{X}$ | $B_2$ | 302 | 100.0 | 0.0 | 0.06 | 12473.35 | $\widetilde{X}$ | $A_1$ | 382 | 99.9 | 0.0 | 0.18 | 13575.22 |
| $\widetilde{X}$ | $A_1$ | 303 | 100.0 | 0.0 | 0.00 | 12477.00 | $\widetilde{X}$ | $B_2$ | 384 | 99.9 | 0.0 | 1.20 | 13582.31 |
| $\widetilde{A}$ | $A_2$ | 307 | 0.0 | 99.9 | 0.01 | 12551.89 | $\widetilde{X}$ | $B_2$ | 387 | 100.0 | 0.0 | 5.06 | 13643.55 |
| $\widetilde{X}$ | $B_2$ | 308 | 100.0 | 0.0 | 0.10 | 12564.57 | $\widetilde{A}$ | $A_2$ | 388 | 0.0 | 100.0 | 0.01 | 13670.96 |
| $\widetilde{X}$ | $B_2$ | 310 | 100.0 | 0.0 | 0.09 | 12586.00 | $\widetilde{X}$ | $B_2$ | 391 | 100.0 | 0.0 | 0.01 | 13720.77 |
| $\widetilde{X}$ | $B_2$ | 313 | 100.0 | 0.0 | 0.34 | 12620.17 | $\widetilde{X}$ | $B_2$ | 393 | 99.9 | 0.0 | 0.53 | 13749.14 |
| $\widetilde{X}$ | $B_2$ | 314 | 100.0 | 0.0 | 0.01 | 12634.71 | $\widetilde{A}$ | $A_2$ | 394 | 0.0 | 99.9 | 0.03 | 13755.38 |
| $\widetilde{A}$ | $A_2$ | 316 | 0.0 | 99.9 | 0.25 | 12648.51 | $\widetilde{X}$ | $B_2$ | 395[f] | 100.0 | 0.0 | 19.16 | 13765.20 |
| $\widetilde{A}$ | $A_2$ | 318 | 0.0 | 100.0 | 0.07 | 12671.15 | $\widetilde{X}$ | $B_2$ | 399 | 100.0 | 0.0 | 0.03 | 13811.69 |

[a], [b], [c] and [d]; See footnote for Table 5.3 [e]; Probability density function is shown in Fig. 5.6. [f]; Probability density function is shown in Fig. 5.7.

Table 5.7: Vibronic term values (in $cm^{-1}$) of $HO_2$. Energy levels with $N_{K_aK_c} = 0_{00}$ are listed here. When an energy level is split by tunneling, the lower component and the splitting are given.

| | $\Gamma_{\rm rve}$ | No.[a] | $P_-^b$ | $P_+^b$ | $\Delta_t^c$ | DR[d] | | $\Gamma_{\rm rve}$ | No.[a] | $P_-^b$ | $P_+^b$ | $\Delta_t^c$ | DR[d] |
|---|---|---|---|---|---|---|---|---|---|---|---|---|---|
| $\widetilde{A}$ | $A_2$ | 400 | 0.2 | 99.6 | 0.35 | 13819.68 | $\widetilde{X}$ | $B_2$ | 479 | 100.0 | 0.0 | 0.05 | 14780.41 |
| $\widetilde{X}$ | $B_2$ | 402 | 99.7 | 0.2 | 5.02 | 13841.24 | $\widetilde{A}$ | $A_2$ | 483 | 0.0 | 99.9 | 0.08 | 14831.47 |
| $\widetilde{A}$ | $A_2$ | 404 | 0.1 | 99.8 | 0.43 | 13858.11 | $\widetilde{X}$ | $B_2$ | 485 | 99.8 | 0.1 | 3.24 | 14863.89 |
| $\widetilde{X}$ | $B_2$ | 406 | 99.7 | 0.2 | 3.69 | 13869.20 | $\widetilde{A}$ | $B_1$ | 485 | 5.5 | 94.5 | 0.03 | 14868.27 |
| $\widetilde{X}$ | $B_2$ | 408 | 100.0 | 0.0 | 10.66 | 13884.80 | $\widetilde{X}$ | $B_2$ | 487 | 99.9 | 0.0 | 5.16 | 14875.90 |
| $\widetilde{X}$ | $B_2$ | 409 | 100.0 | 0.0 | 0.02 | 13892.64 | $\widetilde{X}$ | $B_2$ | 489 | 99.9 | 0.0 | 5.42 | 14887.94 |
| $\widetilde{X}$ | $B_2$ | 411 | 99.9 | 0.0 | 3.11 | 13912.85 | $\widetilde{X}$ | $B_2$ | 491 | 100.0 | 0.0 | 7.96 | 14898.40 |
| $\widetilde{A}$ | $A_2$ | 415 | 0.0 | 100.0 | 0.03 | 13974.14 | $\widetilde{A}$ | $A_2$ | 494 | 0.0 | 100.0 | 0.02 | 14921.28 |
| $\widetilde{A}$ | $A_2$ | 417 | 0.0 | 99.9 | 0.13 | 13995.07 | $\widetilde{A}$ | $A_2$ | 497 | 0.0 | 99.9 | 0.07 | 14961.11 |
| $\widetilde{X}$ | $B_2$ | 418 | 100.0 | 0.0 | 0.11 | 14013.54 | $\widetilde{X}$ | $B_2$ | 498 | 99.9 | 0.0 | 0.09 | 14979.53 |
| $\widetilde{X}$ | $B_2$ | 420 | 99.9 | 0.0 | 0.27 | 14037.47 | $\widetilde{A}$ | $A_2$ | 500 | 0.0 | 99.8 | 1.00 | 14999.86 |
| $\widetilde{A}$ | $A_2$ | 422 | 0.1 | 99.8 | 0.01 | 14048.07 | $\widetilde{X}$ | $B_2$ | 503 | 99.9 | 0.0 | 0.43 | 15028.40 |
| $\widetilde{X}$ | $B_2$ | 425 | 100.0 | 0.0 | 0.25 | 14083.60 | $\widetilde{X}$ | $B_2$ | 505 | 99.9 | 0.0 | 0.79 | 15053.11 |
| $\widetilde{X}$ | $B_2$ | 427 | 100.0 | 0.0 | 2.45 | 14112.24 | $\widetilde{X}$ | $B_2$ | 506 | 99.3 | 0.6 | 17.82 | 15066.88 |
| $\widetilde{X}$ | $B_2$ | 428 | 100.0 | 0.0 | 18.74 | 14114.63 | $\widetilde{A}$ | $A_2$ | 508 | 1.0 | 98.8 | 15.61 | 15083.72 |
| $\widetilde{A}$ | $A_2$ | 430 | 26.9 | 73.0 | 0.18 | 14148.56 | $\widetilde{X}$ | $A_1$ | 509 | 94.5 | 5.4 | 4.25 | 15093.47 |
| $\widetilde{A}$ | $B_1$ | 431 | 9.5 | 90.2 | 7.75 | 14149.97 | $\widetilde{X}$ | $B_2$ | 511 | 100.0 | 0.0 | 0.10 | 15111.81 |
| $\widetilde{X}$ | $B_2$ | 433 | 100.0 | 0.0 | 0.09 | 14168.57 | $\widetilde{X}$ | $A_1$ | 514 | 99.9 | 0.0 | 8.47 | 15126.23 |
| $\widetilde{X}$ | $A_1$ | 436 | 99.9 | 0.1 | 3.90 | 14189.96 | $\widetilde{A}$ | $A_2$ | 517 | 0.8 | 99.1 | 0.27 | 15157.57 |
| $\widetilde{A}$ | $A_2$ | 438 | 0.1 | 99.8 | 1.60 | 14212.00 | $\widetilde{A}$ | $A_2$ | 518 | 1.4 | 98.5 | 0.21 | 15172.18 |
| $\widetilde{X}$ | $B_2$ | 439 | 99.9 | 0.0 | 1.37 | 14220.27 | $\widetilde{X}$ | $B_2$ | 519 | 98.7 | 1.2 | 3.93 | 15175.80 |
| $\widetilde{X}$ | $B_2$ | 441 | 100.0 | 0.0 | 0.47 | 14227.90 | $\widetilde{X}$ | $B_2$ | 521 | 97.0 | 2.9 | 1.62 | 15182.89 |
| $\widetilde{X}$ | $B_2$ | 445 | 100.0 | 0.0 | 5.96 | 14276.54 | $\widetilde{X}$ | $A_1$ | 523 | 99.9 | 0.0 | 1.36 | 15201.85 |
| $\widetilde{A}$ | $A_2$ | 447 | 0.0 | 99.9 | 0.27 | 14311.48 | $\widetilde{A}$ | $A_2$ | 526 | 0.2 | 99.7 | 0.11 | 15216.92 |
| $\widetilde{X}$ | $B_2$ | 449 | 99.9 | 0.0 | 8.88 | 14337.87 | $\widetilde{X}$ | $B_2$ | 529 | 99.5 | 0.5 | 0.19 | 15239.65 |
| $\widetilde{X}$ | $B_2$ | 450 | 99.9 | 0.0 | 0.24 | 14347.38 | $\widetilde{X}$ | $B_2$ | 531 | 100.0 | 0.0 | 3.59 | 15278.39 |
| $\widetilde{A}$ | $A_2$ | 453 | 0.0 | 99.9 | 0.09 | 14381.14 | $\widetilde{A}$ | $B_1$ | 531 | 0.0 | 100.0 | 0.00 | 15281.70 |
| $\widetilde{X}$ | $B_2$ | 455 | 100.0 | 0.0 | 3.86 | 14423.00 | $\widetilde{X}$ | $B_2$ | 533 | 100.0 | 0.0 | 0.21 | 15294.37 |
| $\widetilde{X}$ | $B_2$ | 457 | 100.0 | 0.0 | 2.22 | 14464.64 | $\widetilde{A}$ | $A_2$ | 537 | 0.0 | 99.8 | 1.02 | 15369.94 |
| $\widetilde{X}$ | $B_2$ | 458 | 100.0 | 0.0 | 13.87 | 14468.05 | $\widetilde{X}$ | $B_2$ | 539 | 99.9 | 0.0 | 2.70 | 15394.84 |
| $\widetilde{X}$ | $B_2$ | 460 | 100.0 | 0.0 | 1.44 | 14494.42 | $\widetilde{X}$ | $B_2$ | 540 | 99.9 | 0.0 | 3.52 | 15405.27 |
| $\widetilde{X}$ | $A_1$ | 463 | 100.0 | 0.0 | 0.28 | 14541.56 | $\widetilde{X}$ | $B_2$ | 541 | 99.9 | 0.1 | 11.37 | 15412.40 |
| $\widetilde{X}$ | $B_2$ | 464 | 99.9 | 0.0 | 2.66 | 14558.44 | $\widetilde{X}$ | $B_2$ | 545 | 99.7 | 0.2 | 1.50 | 15459.51 |
| $\widetilde{A}$ | $A_2$ | 467 | 0.0 | 99.9 | 0.04 | 14602.71 | $\widetilde{A}$ | $A_2$ | 546 | 0.5 | 99.3 | 0.71 | 15477.52 |
| $\widetilde{A}$ | $A_2$ | 469 | 0.2 | 99.6 | 0.59 | 14652.44 | $\widetilde{X}$ | $B_2$ | 549 | 100.0 | 0.0 | 0.33 | 15510.72 |
| $\widetilde{X}$ | $B_2$ | 470 | 99.7 | 0.3 | 1.52 | 14661.72 | $\widetilde{X}$ | $A_1$ | 550 | 98.8 | 1.1 | 10.30 | 15515.47 |
| $\widetilde{X}$ | $B_2$ | 471 | 99.6 | 0.4 | 7.44 | 14663.12 | $\widetilde{X}$ | $B_2$ | 550 | 99.5 | 0.5 | 5.86 | 15521.06 |
| $\widetilde{A}$ | $A_2$ | 475 | 0.0 | 99.9 | 0.42 | 14716.43 | $\widetilde{X}$ | $B_2$ | 552[e] | 99.9 | 0.0 | 61.29 | 15532.62 |
| $\widetilde{X}$ | $B_2$ | 477 | 100.0 | 0.0 | 9.37 | 14761.68 | $\widetilde{A}$ | $A_2$ | 553 | 35.9 | 63.9 | 1.79 | 15534.76 |
| $\widetilde{X}$ | $B_2$ | 478 | 99.9 | 0.0 | 4.8 | 14771.20 | $\widetilde{A}$ | $A_2$ | 558 | 0.0 | 99.8 | 0.46 | 15558.58 |

[a], [b], [c] and [d]; See footnote for Table 5.3 [e]; Probability density function is shown in Fig. 5.8. The probability density function of the tunneling pair state, 560th $\widetilde{X}$ $A_1$, is shown in Fig. 5.9.

Table 5.8: Vibronic term values (in $cm^{-1}$) of $HO_2$. Energy levels with $N_{K_aK_c} = 0_{00}$ are listed here. When an energy level is split by tunneling, the lower component and the splitting are given.

| | $\Gamma_{rve}$ | No.[a] | $P_-^b$ | $P_+^b$ | $\Delta_t^c$ | DR[d] | | $\Gamma_{rve}$ | No.[a] | $P_-^b$ | $P_+^b$ | $\Delta_t^c$ | DR[d] |
|---|---|---|---|---|---|---|---|---|---|---|---|---|---|
| $\widetilde{X}$ | $B_2$ | 560 | 99.9 | 0.0 | 0.72 | 15623.47 | $\widetilde{A}$ | $A_2$ | 632 | 0.0 | 99.9 | 0.63 | 16334.84 |
| $\widetilde{X}$ | $B_2$ | 563 | 99.9 | 0.0 | 0.38 | 15655.83 | $\widetilde{X}$ | $B_2$ | 635 | 99.7 | 0.3 | 3.32 | 16376.10 |
| $\widetilde{X}$ | $B_2$ | 564 | 100.0 | 0.0 | 1.07 | 15668.33 | $\widetilde{X}$ | $B_2$ | 636 | 99.7 | 0.2 | 4.92 | 16386.05 |
| $\widetilde{A}$ | $A_2$ | 567 | 0.2 | 99.7 | 0.14 | 15698.64 | $\widetilde{A}$ | $A_2$ | 637 | 1.1 | 98.8 | 0.52 | 16401.97 |
| $\widetilde{X}$ | $B_2$ | 568 | 99.5 | 0.5 | 0.02 | 15706.46 | $\widetilde{A}$ | $A_2$ | 641 | 0.2 | 99.7 | 3.31 | 16425.84 |
| $\widetilde{A}$ | $A_2$ | 571 | 0.0 | 100.0 | 0.06 | 15740.73 | $\widetilde{A}$ | $A_2$ | 642 | 1.0 | 98.9 | 1.45 | 16445.77 |
| $\widetilde{X}$ | $B_2$ | 572 | 99.9 | 0.0 | 2.62 | 15755.61 | $\widetilde{A}$ | $B_1$ | 642 | 89.1 | 10.4 | 13.70 | 16446.75 |
| $\widetilde{X}$ | $B_2$ | 574 | 100.0 | 0.0 | 0.10 | 15760.94 | $\widetilde{X}$ | $B_2$ | 646 | 99.9 | 0.0 | 2.35 | 16473.41 |
| $\widetilde{X}$ | $B_2$ | 575 | 100.0 | 0.0 | 7.61 | 15772.24 | $\widetilde{X}$ | $B_2$ | 648 | 99.9 | 0.0 | 2.70 | 16492.66 |
| $\widetilde{X}$ | $B_2$ | 576 | 99.9 | 0.0 | 2.44 | 15779.44 | $\widetilde{A}$ | $A_2$ | 650 | 0.1 | 99.8 | 0.02 | 16499.48 |
| $\widetilde{X}$ | $B_2$ | 581 | 99.3 | 0.7 | 3.82 | 15839.30 | $\widetilde{X}$ | $B_2$ | 653 | 99.9 | 0.0 | | 16527.58 |
| $\widetilde{A}$ | $A_2$ | 582[e] | 44.7 | 55.0 | 0.56 | 15841.87 | $\widetilde{X}$ | $B_2$ | 654 | 100.0 | 0.0 | 1.08 | 16546.92 |
| $\widetilde{X}$ | $B_2$ | 585 | 99.3 | 0.6 | 13.91 | 15873.01 | $\widetilde{X}$ | $A_1$ | 655 | 100.0 | 0.0 | | 16564.75 |
| $\widetilde{X}$ | $B_2$ | 586 | 100.0 | 0.0 | | 15900.39 | $\widetilde{X}$ | $B_2$ | 656 | 100.0 | 0.0 | | 16578.36 |
| $\widetilde{X}$ | $B_2$ | 587 | 99.8 | 0.1 | 1.02 | 15917.85 | $\widetilde{A}$ | $A_2$ | 658 | 0.1 | 99.8 | 0.05 | 16591.32 |
| $\widetilde{A}$ | $A_2$ | 589 | 1.6 | 98.4 | 0.02 | 15927.83 | $\widetilde{X}$ | $A_1$ | 657 | 98.7 | 1.3 | | 16592.13 |
| $\widetilde{X}$ | $B_2$ | 590 | 93.0 | 6.9 | 0.06 | 15933.66 | $\widetilde{X}$ | $B_2$ | 660 | 100.0 | 0.0 | 1.35 | 16615.71 |
| $\widetilde{A}$ | $A_2$ | 592 | 0.1 | 99.6 | 1.32 | 15946.34 | $\widetilde{X}$ | $B_2$ | 662 | 99.9 | 0.0 | 21.49 | 16624.84 |
| $\widetilde{X}$ | $B_2$ | 596 | 99.8 | 0.1 | 0.57 | 15974.29 | $\widetilde{X}$ | $B_2$ | 665 | 83.5 | 16.3 | 34.16 | 16675.84 |
| $\widetilde{X}$ | $A_1$ | 596 | 99.8 | 0.1 | 0.13 | 15974.95 | $\widetilde{A}$ | $A_2$ | 665 | 6.3 | 91.9 | 1.19 | 16675.91 |
| $\widetilde{X}$ | $B_2$ | 598 | 99.9 | 0.0 | 0.29 | 15998.41 | $\widetilde{X}$ | $A_1$ | 666 | 100.0 | 0.0 | 3.41 | 16692.04 |
| $\widetilde{X}$ | $A_1$ | 601[f] | 100.0 | 0.0 | | 16009.16 | $\widetilde{X}$ | $B_2$ | 671 | 99.7 | 0.2 | 4.95 | 16744.38 |
| $\widetilde{X}$ | $B_2$ | 603 | 99.9 | 0.0 | 10.81 | 16048.80 | $\widetilde{A}$ | $A_2$ | 673 | 0.2 | 99.6 | 0.54 | 16780.63 |
| $\widetilde{A}$ | $A_2$ | 604 | 0.0 | 99.9 | 0.28 | 16063.20 | $\widetilde{A}$ | $A_2$ | 674 | 1.1 | 98.8 | 0.29 | 16798.48 |
| $\widetilde{X}$ | $B_2$ | 605 | 99.9 | 0.0 | 1.20 | 16078.52 | $\widetilde{X}$ | $B_2$ | 675 | 93.0 | 7.0 | 3.09 | 16804.38 |
| $\widetilde{X}$ | $B_2$ | 607 | 99.9 | 0.0 | 1.76 | 16082.50 | $\widetilde{A}$ | $A_2$ | 677 | 8.9 | 90.8 | 1.65 | 16809.67 |
| $\widetilde{A}$ | $A_2$ | 609 | 5.9 | 94.0 | 0.00 | 16101.88 | $\widetilde{X}$ | $B_2$ | 680 | 99.9 | 0.0 | 13.15 | 16832.20 |
| $\widetilde{X}$ | $B_2$ | 612 | 100.0 | 0.0 | | 16114.83 | $\widetilde{X}$ | $B_2$ | 682 | 99.9 | 0.0 | 18.11 | 16844.55 |
| $\widetilde{X}$ | $A_1$ | 613 | 100.0 | 0.0 | | 16123.01 | $\widetilde{X}$ | $A_1$ | 685 | 99.9 | 0.0 | 0.07 | 16909.44 |
| $\widetilde{X}$ | $B_2$ | 614 | 99.9 | 0.0 | | 16141.15 | $\widetilde{X}$ | $B_2$ | 686 | 99.9 | 0.0 | 0.26 | 16922.99 |
| $\widetilde{A}$ | $A_2$ | 616 | 0.0 | 99.8 | 0.20 | 16154.47 | $\widetilde{A}$ | $A_2$ | 688 | 0.0 | 99.9 | 0.28 | 16933.04 |
| $\widetilde{X}$ | $B_2$ | 618 | 100.0 | 0.0 | | 16184.53 | $\widetilde{X}$ | $B_2$ | 689 | 99.9 | 0.0 | 1.07 | 16943.33 |
| $\widetilde{X}$ | $A_1$ | 618 | 99.9 | 0.0 | 16.09 | 16189.53 | $\widetilde{X}$ | $B_2$ | 692 | 99.9 | 0.0 | 0.72 | 16953.50 |
| $\widetilde{X}$ | $A_1$ | 619 | 99.9 | 0.0 | | 16197.14 | $\widetilde{A}$ | $A_2$ | 693[g] | 1.1 | 98.7 | 10.92 | 16964.59 |
| $\widetilde{X}$ | $A_1$ | 621 | 99.9 | 0.0 | 0.46 | 16214.35 | $\widetilde{X}$ | $A_1$ | 696 | 99.9 | 0.0 | | 16985.22 |
| $\widetilde{X}$ | $A_1$ | 623 | 99.7 | 0.2 | | 16236.10 | $\widetilde{X}$ | $B_2$ | 696 | 98.7 | 1.3 | | 16991.14 |
| $\widetilde{X}$ | $B_2$ | 623 | 100.0 | 0.0 | 0.91 | 16239.97 | $\widetilde{X}$ | $A_1$ | 698 | 99.9 | 0.0 | 4.85 | 17019.79 |
| $\widetilde{A}$ | $A_2$ | 625 | 0.4 | 99.4 | 1.31 | 16251.00 | $\widetilde{X}$ | $A_1$ | 700 | 99.8 | 0.1 | 4.96 | 17027.71 |
| $\widetilde{X}$ | $B_2$ | 629 | 99.6 | 0.3 | 5.09 | 16276.05 | $\widetilde{A}$ | $A_2$ | 701 | 0.2 | 99.7 | 0.11 | 17037.60 |
| $\widetilde{X}$ | $B_2$ | 630 | 99.7 | 0.2 | 18.54 | 16299.35 | $\widetilde{X}$ | $B_2$ | 704 | 99.9 | 0.0 | | 17055.26 |

[a], [b], [c] and [d]; See footnote for Table 5.3 [e]; Probability density function is shown in Fig. 5.10. [f]; Probability density function is shown in Fig. 5.11. [g]; Probability density function is shown in Fig. 5.12.

(a)

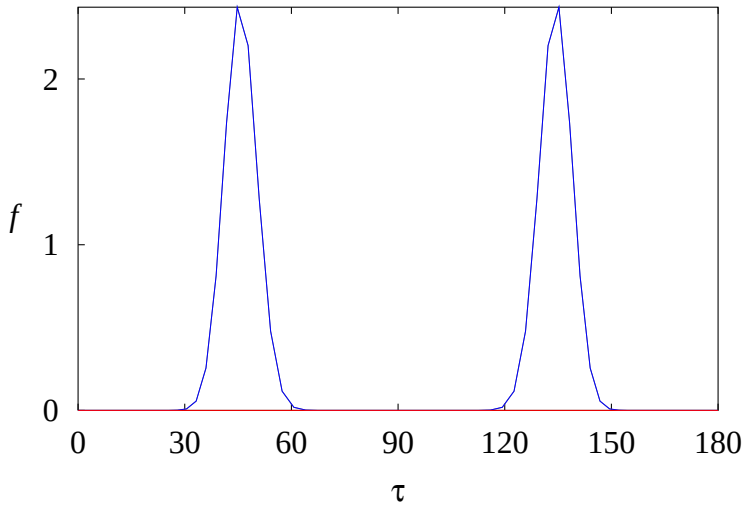


(b)

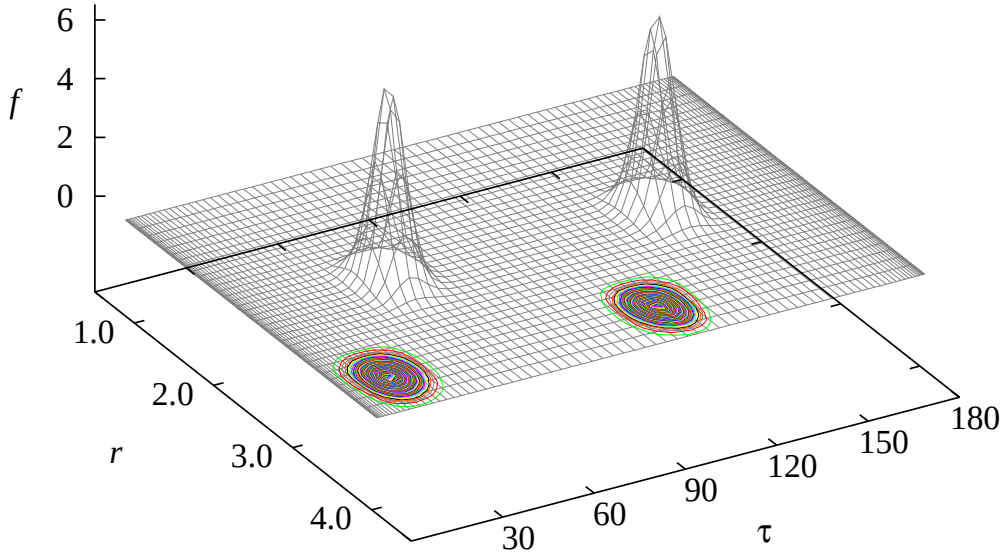


Figure 5.2: Probability density functions (See 2.5.3) for the $\widetilde{X}^2$ $HO_2$ $(0,0,0)$ state.

Here, the $\tau$ and $r$ coordinates are given in degrees and Bohr, respectively. Figure (a) shows one-dimensional probability density functions. The blue curve is $f_-(\tau)$ (the lower electronic surface's probability density function), the red curve is $f_+(\tau)$ (the upper electronic surface's probability density function) and the black curve is $f(\tau)$ (the total probability density function). The gray surface in Figure (b) shows the two-dimensional probability density function $f(r,\tau)$. Coloured lines are the contour plot of the two-dimensional probability density function $f(r,\tau)$. Contours are plotted for 0.1 separations.

(a)

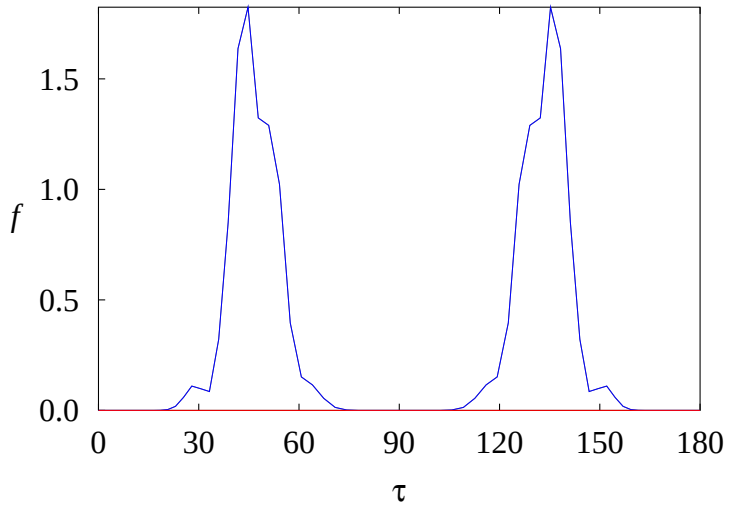


(b)

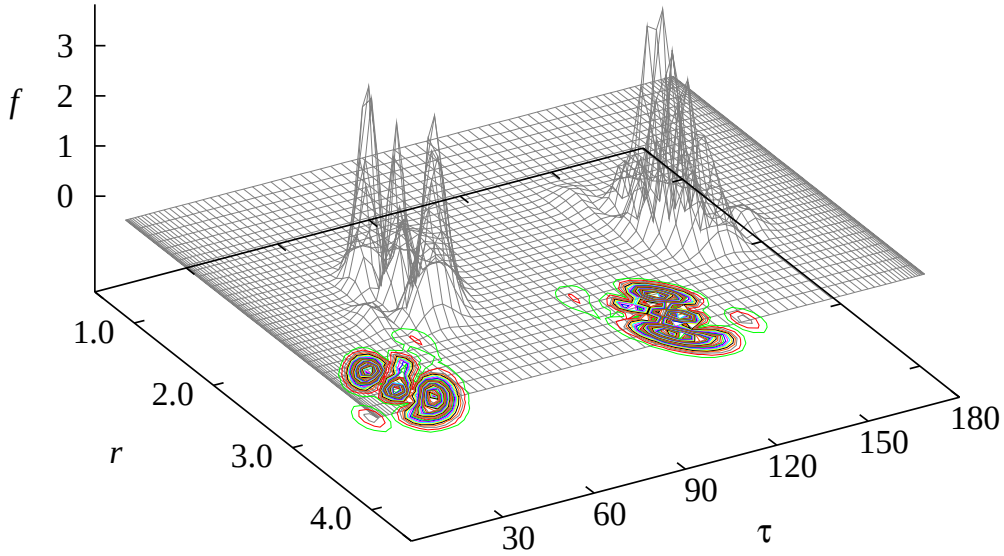


Figure 5.3: Probability density functions (See 2.5.3) for the Fermi-resonance $\widetilde{X}^2$ $HO_2$ $(2,0,0)$ state.

Here, the $\tau$ and $r$ coordinates are given in degrees and Bohr, respectively. Figure (a) shows one-dimensional probability density functions. The blue curve is $f_-(\tau)$ (the lower electronic surface's probability density function), the red curve is $f_+(\tau)$ (the upper electronic surface's probability density function) and the black curve is $f(\tau)$ (the total probability density function). The gray surface in Figure (b) shows the two-dimensional probability density function $f(r,\tau)$. Coloured lines are the contour plot of the two-dimensional probability density function $f(r,\tau)$. Contours are plotted for 0.1 separations.

(a)

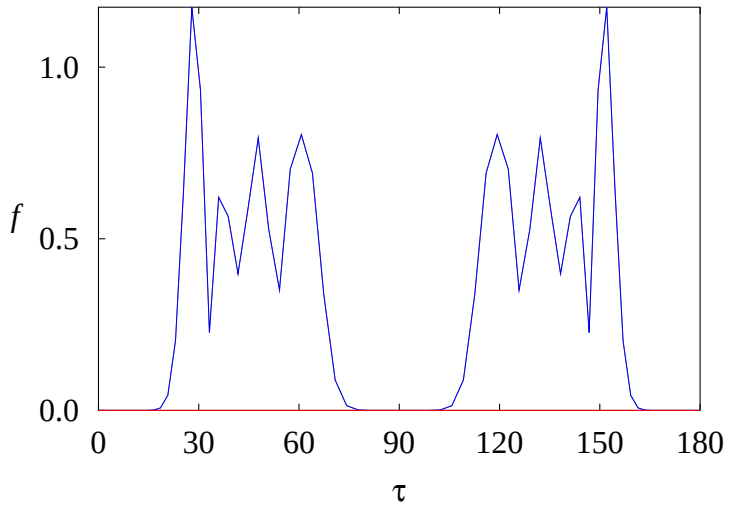


(b)

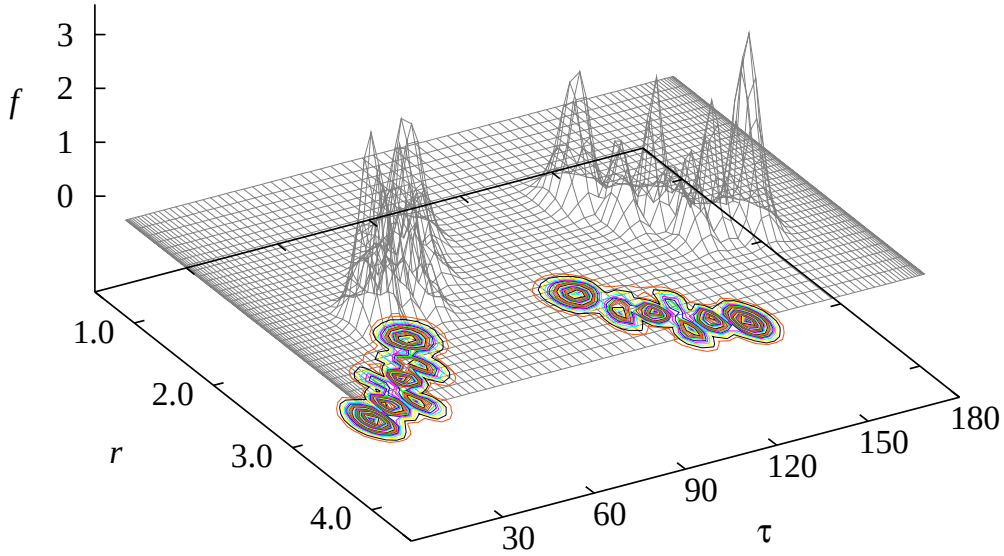


Figure 5.4: Probability density functions (See 2.5.3) for the Fermi-resonance $\widetilde{X}^2$ $HO_2$ $(0, 5, 0)$ state.

Here, the $\tau$ and $r$ coordinates are given in degrees and Bohr, respectively. Figure (a) shows one-dimensional probability density functions. The blue curve is $f_-(\tau)$ (the lower electronic surface's probability density function), the red curve is $f_+(\tau)$ (the upper electronic surface's probability density function) and the black curve is $f(\tau)$ (the total probability density function). The gray surface in Figure (b) shows the two-dimensional probability density function $f(r, \tau)$. Coloured lines are the contour plot of the two-dimensional probability density function $f(r, \tau)$. Contours are plotted for 0.1 separations.

(a)

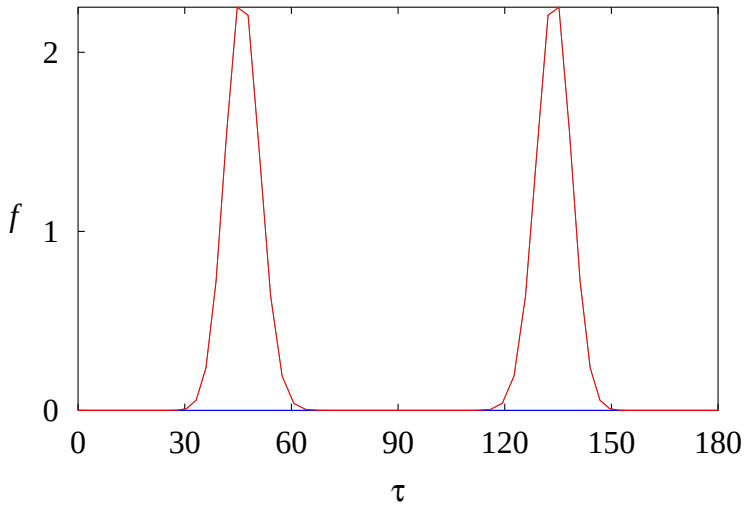


(b)

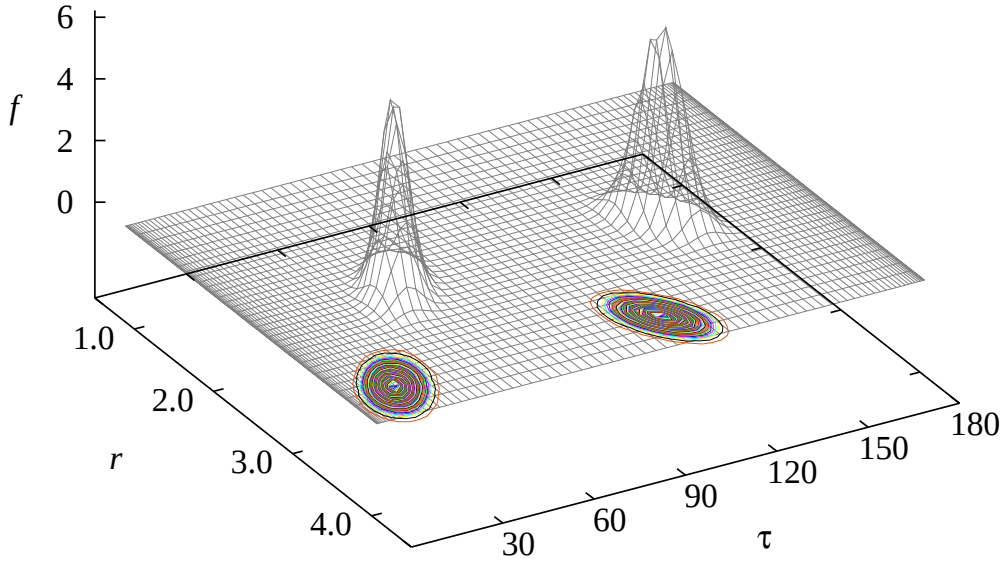


Figure 5.5: Probability density functions (See 2.5.3) for the $\widetilde{A}^2$ $HO_2$ $(0,0,0)$ state.

Here, the $\tau$ and $r$ coordinates are given in degrees and Bohr, respectively. Figure (a) shows one-dimensional probability density functions. The blue curve is $f_-(\tau)$ (the lower electronic surface's probability density function), the red curve is $f_+(\tau)$ (the upper electronic surface's probability density function) and the black curve is $f(\tau)$ (the total probability density function). The gray surface in Figure (b) shows the two-dimensional probability density function $f(r,\tau)$. Coloured lines are the contour plot of the two-dimensional probability density function $f(r,\tau)$. Contours are plotted for 0.1 separations.

Table 5.9: Vibronic term values (in $cm^{-1}$) of $HO_2$. Energy levels with $N_{K_aK_c} = 0_{00}$ are listed here. When an energy level is split by tunneling, the lower component and the splitting are given.

| | $\Gamma_{rve}$ | No.[a] | $P_-^b$ | $P_+^b$ | $\Delta_t^c$ | DR[d] | | $\Gamma_{rve}$ | No.[a] | $P_-^b$ | $P_+^b$ | $\Delta_t^c$ | DR[d] |
|---|---|---|---|---|---|---|---|---|---|---|---|---|---|
| $\widetilde{X}$ | $A_1$ | 706 | 99.8 | 0.0 | | 17084.31 | $\widetilde{X}$ | $B_2$ | 727 | 99.2 | 0.6 | 4.00 | 17271.60 |
| $\widetilde{X}$ | $B_2$ | 706 | 99.8 | 0.0 | 0.37 | 17096.43 | $\widetilde{A}$ | $A_2$ | 728 | 2.5 | 97.4 | 0.38 | 17278.96 |
| $\widetilde{A}$ | $A_2$ | 707 | 0.6 | 99.3 | 1.78 | 17103.00 | $\widetilde{A}$ | $A_2$ | 730 | 11.5 | 88.2 | 4.95 | 17295.55 |
| $\widetilde{A}$ | $A_2$ | 710 | 4.1 | 95.6 | 0.50 | 17124.93 | $\widetilde{X}$ | $B_2$ | 730 | 84.2 | 15.6 | 1.03 | 17295.63 |
| $\widetilde{X}$ | $B_2$ | 712 | 72.4 | 27.3 | 0.73 | 17129.85 | $\widetilde{X}$ | $B_2$ | 734 | 80.0 | 19.7 | 25.49 | 17301.40 |
| $\widetilde{X}$ | $A_1$ | 714 | 99.3 | 0.6 | 0.80 | 17150.21 | $\widetilde{X}$ | $A_1$ | 734 | 77.4 | 22.3 | | 17306.21 |
| $\widetilde{X}$ | $B_2$ | 716 | 99.9 | 0.0 | | 17160.96 | $\widetilde{X}$ | $B_2$ | 737 | 99.6 | 0.3 | | 17327.95 |
| $\widetilde{X}$ | $B_2$ | 717 | 99.9 | 0.0 | 12.78 | 17165.94 | $\widetilde{X}$ | $A_1$ | 739 | 87.1 | 12.6 | | 17338.06 |
| $\widetilde{A}$ | $A_2$ | 719 | 0.0 | 99.9 | 0.15 | 17185.19 | $\widetilde{A}$ | $A_2$ | 739 | 0.0 | 99.8 | 0.12 | 17338.45 |
| $\widetilde{X}$ | $A_1$ | 721 | 99.7 | 0.2 | 14.05 | 17193.96 | $\widetilde{A}$ | $A_2$ | 740 | 0.1 | 99.7 | | 17339.79 |
| $\widetilde{A}$ | $A_2$ | 723 | 0.0 | 99.9 | 0.07 | 17216.31 | $\widetilde{A}$ | $B_1$ | 740[e] | 20.8 | 78.8 | | 17339.89 |
| $\widetilde{X}$ | $B_2$ | 726 | 99.8 | 0.1 | 21.30 | 17240.31 | $\widetilde{A}$ | $A_2$ | 744 | 0.5 | 99.4 | 0.79 | 17362.81 |

[a], [b], [c] and [d]; See footnote for Table 5.3 [e]; Probability density function is shown in Fig. 5.13.

shown in Figs. 5.2 - 5.13. The over-all probability ($P_-$ and $P_+$) and the probability density functions are calculated from the coefficient matrix elements $\mathbf{C}_{\mathbf{i,g}}^{\mathbf{J,M_J,S,\Gamma}_{rve}}$ (See (2.206)) bigger than 0.05. Some rovibronic energy levels with $J = 1/2, 3/2$ are summarized together with some experimental results in Table 5.10.

The wavefunction of the $\widetilde{X}(0,0,0)$ state is shown in Fig. 5.2. The zero point vibrational energy is calculated as 3063 $cm^{-1}$. As shown in Table 5.3, the total probability of the lower electronic surface $P_-$ is $100\%$, so that the total probability of the upper electronic surface $P_+$ is $0\%$. The $\widetilde{X}(0,0,0)$ state originates in the lower electronic surface (the $\widetilde{X}\ ^2A''$ state). At 6732 and 6734 $cm^{-1}$ we see Fermi-resonance states originating in the lower electronic surface. These states are shown in Figs. 5.3 and 5.4. We calculate a very small tunneling splitting (0.07 $cm^{-1}$) for the $\widetilde{X}(0,5,0)$ state (Fig. 5.4). The zero point vibrational state of the upper electronic surface, $\widetilde{A}(0,0,0)$, is at 7018 $cm^{-1}$ (See Fig. 5.5).

As described in the previous section, we have used the same potential energy surface as the previous study by Osmann $et\ al.$ [64]. As shown in Tables 5.3 - 5.5, the agreement between the calculated energy levels is very good (1 to 7 $cm^{-1}$) in case of

Table 5.10: Calculated rovibronic state with the program DR for the $\widetilde{X}\ ^2A''$ and $\widetilde{A}\ ^2A'$ states of $HO_2$ (in $cm^{-1}$) in comparision with experiments.

| | $J$ | $N$ | $K_a$ | $K_c$ | DR[a] | Obs[a] | | $J$ | $N$ | $K_a$ | $K_c$ | DR[a] | Obs[a] |
|---|---|---|---|---|---|---|---|---|---|---|---|---|---|
| $\widetilde{X}(0,0,0)^b$ | 1/2 | 0 | 0 | 0 | 0 | 0 | $\widetilde{X}(0,0,1)^d$ | 1/2 | 0 | 0 | 0 | 1082.59 | 1097.011 |
| | 1/2 | 1 | 0 | 1 | 2.13 | 2.182 | | 1/2 | 1 | 0 | 1 | 2.11 | 2.1494 |
| | 1/2 | 1 | 1 | 1 | 22.09 | 22.2504 | | 1/2 | 1 | 1 | 1 | 22.07 | 22.1896 |
| | 1/2 | 1 | 1 | 0 | 22.15 | 22.3241 | | 1/2 | 1 | 1 | 0 | 22.13 | 22.2647 |
| | 3/2 | 1 | 0 | 1 | 2.13 | 2.1672 | | 3/2 | 1 | 0 | 1 | 2.11 | 2.134 |
| | 3/2 | 1 | 1 | 0 | 20.73 | 20.9178 | | 3/2 | 1 | 1 | 0 | 20.65 | 20.8144 |
| | 3/2 | 1 | 1 | 1 | 20.68 | 20.8628 | | 3/2 | 1 | 1 | 1 | 20.59 | 20.7588 |
| | 3/2 | 2 | 0 | 2 | 6.39 | 6.5312 | | 3/2 | 2 | 0 | 2 | 6.32 | 6.4328 |
| | 3/2 | 2 | 1 | 1 | 26.14 | 26.4128 | | 3/2 | 2 | 1 | 1 | 26.06 | 26.2833 |
| | 3/2 | 2 | 1 | 2 | 25.97 | 26.21 | | 3/2 | 2 | 1 | 2 | 25.89 | 26.0771 |
| | 3/2 | 2 | 2 | 0 | 84.56 | 85.1161 | | 3/2 | 2 | 2 | 0 | 84.42 | 84.739 |
| | 3/2 | 2 | 2 | 1 | 84.56 | 85.1159 | | 3/2 | 2 | 2 | 1 | 84.42 | 84.7389 |
| $\widetilde{X}(1,0,0)^c$ | 1/2 | 0 | 0 | 0 | 3467.28 | 3436.006 | $\widetilde{A}(0,0,0)^e$ | 1/2 | 0 | 0 | 0 | 7018.4 | 7029.003 |
| | 1/2 | 1 | 0 | 1 | 2.14 | 2.1896 | | 1/2 | 1 | 0 | 1 | 1.93 | 2.0098 |
| | 1/2 | 1 | 1 | 1 | 21.28 | 21.5024 | | 1/2 | 1 | 1 | 1 | 20.02 | 20.5161 |
| | 1/2 | 1 | 1 | 0 | 21.34 | 21.5804 | | 1/2 | 1 | 1 | 0 | 20.07 | 20.5634 |
| | 3/2 | 1 | 0 | 1 | 2.14 | 2.1724 | | 3/2 | 1 | 0 | 1 | 1.93 | 1.9864 |
| | 3/2 | 1 | 1 | 0 | 19.99 | 20.2993 | | 3/2 | 1 | 1 | 0 | 21.36 | 21.7694 |
| | 3/2 | 1 | 1 | 1 | 19.94 | 20.2429 | | 3/2 | 1 | 1 | 1 | 21.32 | 21.7288 |
| | 3/2 | 2 | 0 | 2 | 6.4 | 6.5513 | | 3/2 | 2 | 0 | 2 | 5.79 | 6.0061 |
| | 3/2 | 2 | 1 | 1 | 25.34 | 25.7068 | | 3/2 | 2 | 1 | 1 | 24.75 | 25.298 |
| | 3/2 | 2 | 1 | 2 | 25.17 | 25.4942 | | 3/2 | 2 | 1 | 2 | 24.62 | 25.1623 |
| | 3/2 | 2 | 2 | 0 | 81.36 | 82.3433 | | 3/2 | 2 | 2 | 0 | 80.27 | 81.9908 |
| | 3/2 | 2 | 2 | 1 | 81.36 | 82.3431 | | 3/2 | 2 | 2 | 1 | 80.27 | 81.9907 |
| $\widetilde{X}(0,1,0)^d$ | 1/2 | 0 | 0 | 0 | 1390.64 | 1391.01 | $\widetilde{A}(0,0,1)^f$ | 1/2 | 0 | 0 | 0 | 7916.4 | 7958.012 |
| | 1/2 | 1 | 0 | 1 | 2.12 | 2.1759 | | 1/2 | 1 | 0 | 1 | 1.91 | 1.9885 |
| | 1/2 | 1 | 1 | 1 | 22.76 | 22.9007 | | 1/2 | 1 | 1 | 1 | 19.97 | 20.6179 |
| | 1/2 | 1 | 1 | 0 | 22.83 | 22.9813 | | 1/2 | 1 | 1 | 0 | 20.02 | 20.5995 |
| | 3/2 | 1 | 0 | 1 | 2.12 | 2.1576 | | 3/2 | 1 | 0 | 1 | 1.91 | 1.9576 |
| | 3/2 | 1 | 1 | 0 | 21.3 | 21.4681 | | 3/2 | 1 | 1 | 0 | 21.36 | 21.7996 |
| | 3/2 | 1 | 1 | 1 | 21.25 | 21.4098 | | 3/2 | 1 | 1 | 1 | 21.32 | 21.7599 |
| | 3/2 | 2 | 0 | 2 | 6.37 | 6.5093 | | 3/2 | 2 | 0 | 2 | 5.71 | 5.9349 |
| | 3/2 | 2 | 1 | 1 | 26.79 | 27.0434 | | 3/2 | 2 | 1 | 1 | 24.71 | 25.2918 |
| | 3/2 | 2 | 1 | 2 | 26.61 | 26.8238 | | 3/2 | 2 | 1 | 2 | 24.58 | 25.1505 |
| | 3/2 | 2 | 2 | 0 | 87.13 | 87.6772 | | 3/2 | 2 | 2 | 0 | 80.2 | 82.2372 |
| | 3/2 | 2 | 2 | 1 | 87.13 | 87.677 | | 3/2 | 2 | 2 | 1 | 80.2 | 82.2371 |

[a] For each excited vibronic state, the energy of the $(J; N_{K_a K_c}) = (1/2; 0_{00})$ level is measured relative to the $(1/2; 0_{00})$ level of the $\widetilde{X}(0,0,0)$ state. All other term values are measured relative to the $(1/2; 0_{00})$ level of the vibronic state in question. [b], [c], [d], [e] and [f] Observed values are generated from Table.2 of [65]. [b] Effective parameter values used for calculating term values are from [62]. [c] Effective parameter values used for calculating term values are from [59]. [d] Effective parameter values used for calculating term values are from [60]. [e] Effective parameter values used for calculating term values are from [63]. [f] Effective parameter values used for calculating term values are from [78].

zero bending quanta states. Those states with more than 1 bending quantum differ by 9 to 50 cm$^{-1}$ from the previous study. Except for the $\widetilde{A}(0,0,2)$ state, we have obtained higher energies than with RENNER. In Tables 5.3 - 5.4, we have compared our result with the previous study by Jensen $et\ al.$ [65]. The fundamental vibrational states differ up to 32 cm$^{-1}$, and other states do not agree so well. The $\nu_1$ and $\nu_2$ states are calculated at higher energies than in the previous study, and $\nu_3$ bands are calculated at lower energies.

The potential energy surface by Osmann $et\ al.$ [64] are fitted by constraining $f_0^{(6,-)}$ = 10000 cm$^{-1}$ in order to ensure that the bending potential energy of the $\widetilde{X}$ state increases monotonically with increasing bending coordinate $\bar{\rho}$. Their studies does not cover large bending amplitude, but with the program DR we include all the bending amplitudes. The discrepancy between the calculated energy with the program DR and the previous study [64] can be explained by this, but it can also suggest that we should use larger basis set in order to have high accuracy, although we used the biggest basis sets allowed by our computer resources in the calculation with the program DR.

The comparision with experiment is shown in Table 5.10. The rotational states differ less than 1 cm$^{-1}$ from the experimental values, except $\widetilde{A}(0,0,1)\ J = 3/2\ N_{K_aK_c} = 2_{20}$ and $N_{K_aK_c} = 2_{21}$ state.

As the energies increases, we start to see larger tunneling splittings. Vibronic states with energies under 10000 cm$^{-1}$, the state with the biggest tunneling splitting in the $J = 1/2$ state is the 119th $\Gamma_{\rm rve} = B_2$ state with 100% contribution from the lower electronic state ($P_- = 100\%$). This state has a 0.39 cm$^{-1}$ tunneling splitting. In the energy range 10000 to 11000 cm$^{-1}$, we have a state with a 3.16 cm$^{-1}$ tunneling splitting (the 192nd $\Gamma_{\rm rve} = B_2$ state, $P_- = 100\%$). In this energy range, the states originating solely in the upper electronic state at most have 0.07 cm$^{-1}$ tunneling splitting. The 206th $\Gamma_{\rm rve} = B_2$ state has mixed origin ($P_- = 71\%$ and $P_+ = 29\%$). This state have 0.78cm$^{-1}$ tunneling splitting. We can see that the contribution from the upper elctronic

state can make the tunneling splitting bigger.

In the energy range 11000 to 12000 cm$^{-1}$ we have a state with a 3.66 cm$^{-1}$ tunneling splitting, it originates in the lower electronic state (the 264th $\Gamma_{\rm rve} = A_1$ state, $P_- = 100\%$). The 258th $\Gamma_{\rm rve} = A_2$ state, $P_+ = 100\%$ had the biggest tunneling splitting, 0.27 cm$^{-1}$, among the states which originate solely in the upper electronic state.

In the energy range 12000 to 13000 cm$^{-1}$, the state with the biggest tunneling splitting is the 331st $\Gamma_{\rm rve} = B_2$ state with $P_- = 100\%$. The tunneling splitting of this state is 11.09 cm$^{-1}$ and the probability density function is shown in Fig. 5.6. The states originate solely in the upper electronic surface and have at most 0.46 cm$^{-1}$ tunneling splitting (the 343rd $\Gamma_{\rm rve} = A_2$ state, $P_+ = 100\%$).

In the energy range 13000 to 14000 cm$^{-1}$, the states originating in the upper electronic surface have at most 3.78 cm$^{-1}$ tunneling splitting (the 354th $\Gamma_{\rm rve} = A_2$ state, $P_+ = 100\%$). In contrast, the states originating in lower electronic surface have at most 19.16 cm$^{-1}$ tunneling splitting. This is the 395th $\Gamma_{\rm rve} = B_2$ state and the probability density function is shown in Fig. 5.7.

In the energy range 14000 to 15000 cm$^{-1}$, more than half of the states have tunneling splittings bigger than 1 cm$^{-1}$. At 15532 cm$^{-1}$, we have the 552nd $\Gamma_{\rm rve} = B_2$ state with $P_- = 100\%$, with the tunneling splitting as 61.29 cm$^{-1}$. The probability density function is shown in Fig. 5.8 and the probability density function of the tunneling pair is shown in Fig. 5.9.

At 15842 cm$^{-1}$, we have a well-mixed state with contributions from the lower and upper electronic surface. It is the 582nd $\Gamma_{\rm rve} = A_2$ state and the contribution from the lower electronic surface $P_-$ is $45\%$ and the contribution from the upper electronic surface $P_+$ is $55\%$ (Fig. 5.10).

At 15900 cm$^{-1}$, we have the 586th $\Gamma_{\rm rve} = B_2$ state with $P_- = 100\%$, which could not be assigned to a tunneling pair. Above this state, more vibronic states start to have larger tunneling splittings, and some states are delocalized and cannot be assigned

(a)

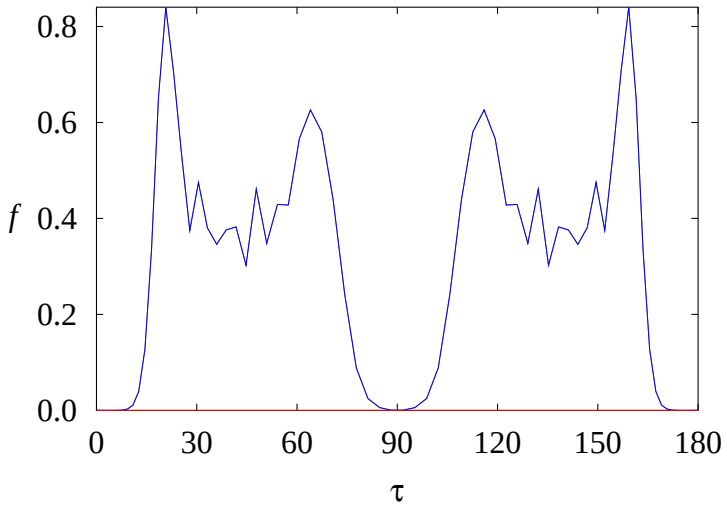


(b)

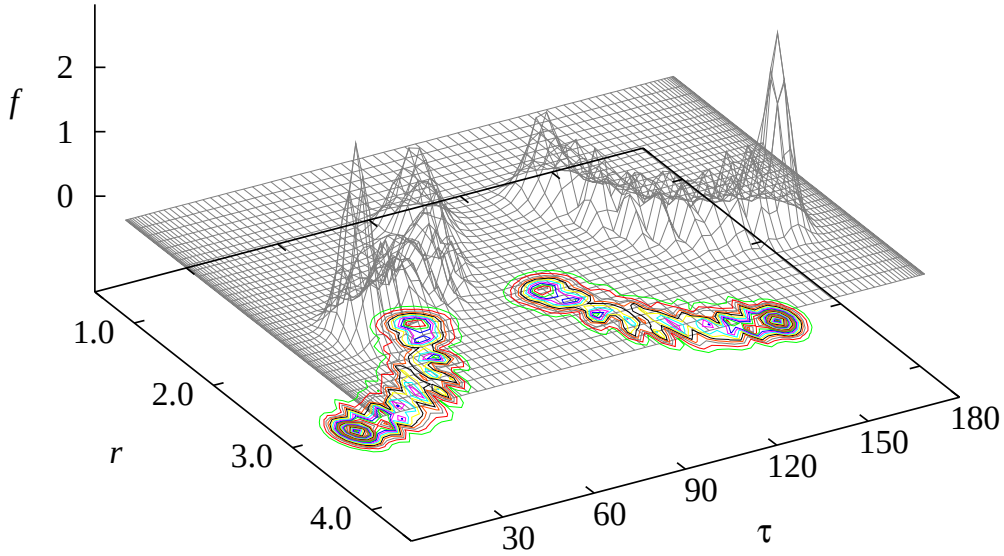


Figure 5.6: Probability density functions (See 2.5.3) for the $\widetilde{X}^2$ $HO_2$ $J = 1/2$, $\Gamma_{\text{ers}} = B_2$ 331st state.

Here, the $\tau$ and $r$ coordinates are given in degrees and Bohr, respectively. Figure (a) shows one-dimensional probability density functions. The blue curve is $f_-(\tau)$ (the lower electronic surface's probability density function), the red curve is $f_+(\tau)$ (the upper electronic surface's probability density function) and the black curve is $f(\tau)$ (the total probability density function). The gray surface in Figure (b) shows the two-dimensional probability density function $f(r, \tau)$. Coloured lines are the contour plot of the two-dimensional probability density function $f(r, \tau)$. Contours are plotted for 0.1 separations.

(a)

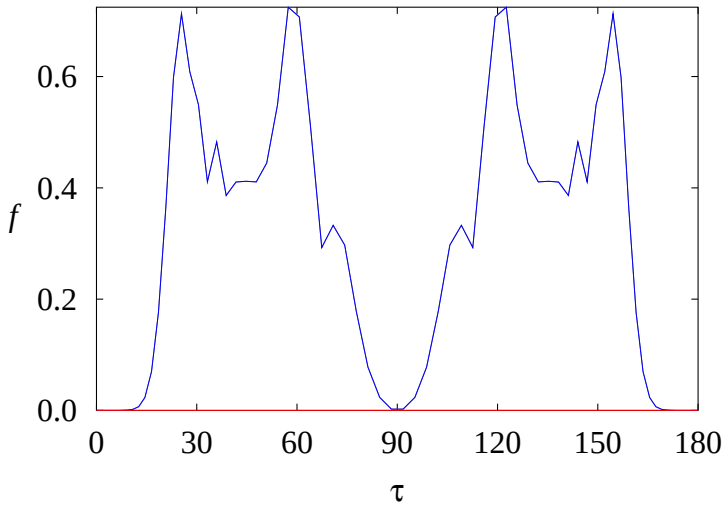


(b)

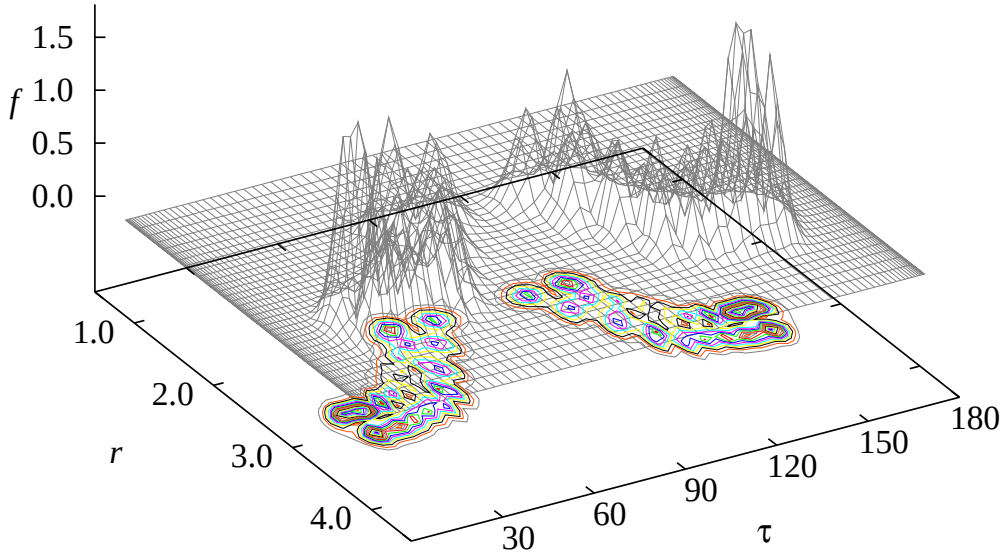


Figure 5.7: Probability density functions (See 2.5.3) for the $\widetilde{X}^2$ $HO_2$ $J = 1/2$, $\Gamma_{ers} = B_2$ 395th state.

Here, the $\tau$ and $r$ coordinates are given in degrees and Bohr, respectively. Figure (a) shows one-dimensional probability density functions. The blue curve is $f_-(\tau)$ (the lower electronic surface's probability density function), the red curve is $f_+(\tau)$ (the upper electronic surface's probability density function) and the black curve is $f(\tau)$ (the total probability density function). The gray surface in Figure (b) shows the two-dimensional probability density function $f(r, \tau)$. Coloured lines are the contour plot of the two-dimensional probability density function $f(r, \tau)$. Contours are plotted for 0.1 separations.

(a)

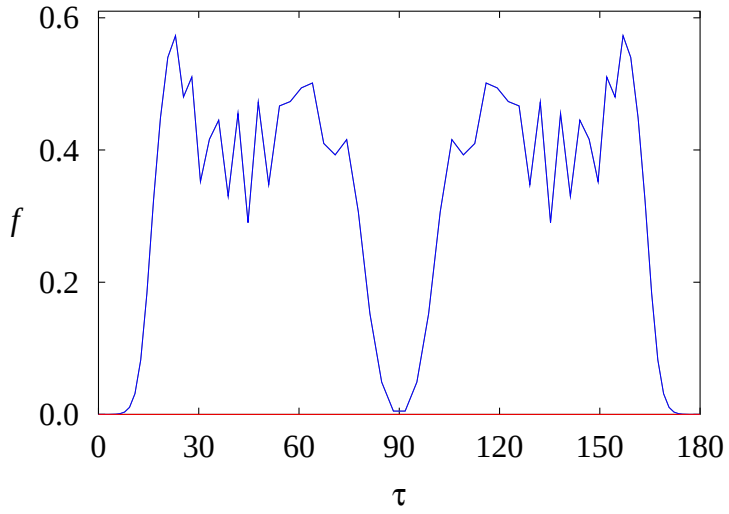


(b)

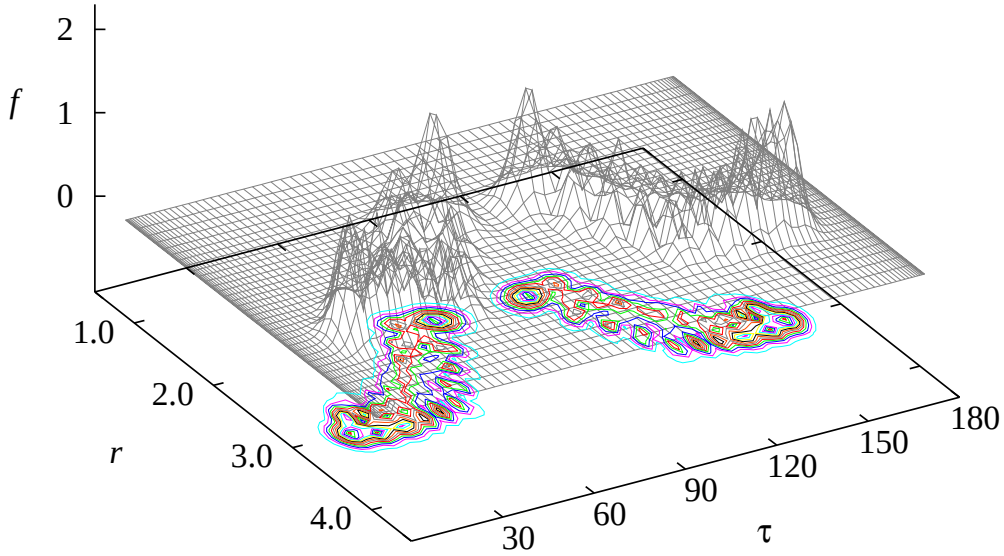


Figure 5.8: Probability density functions (See 2.5.3) for the $\widetilde{X}^2$ $HO_2$ $J = 1/2$, $\Gamma_{\text{ers}} = B_2$ 552nd state.

Here, the $\tau$ and $r$ coordinates are given in degrees and Bohr, respectively. Figure (a) shows one-dimensional probability density functions. The blue curve is $f_-(\tau)$ (the lower electronic surface's probability density function), the red curve is $f_+(\tau)$ (the upper electronic surface's probability density function) and the black curve is $f(\tau)$ (the total probability density function). The gray surface in Figure (b) shows the two-dimensional probability density function $f(r, \tau)$. Coloured lines are the contour plot of the two-dimensional probability density function $f(r, \tau)$. Contours are plotted for 0.1 separations.

(a)

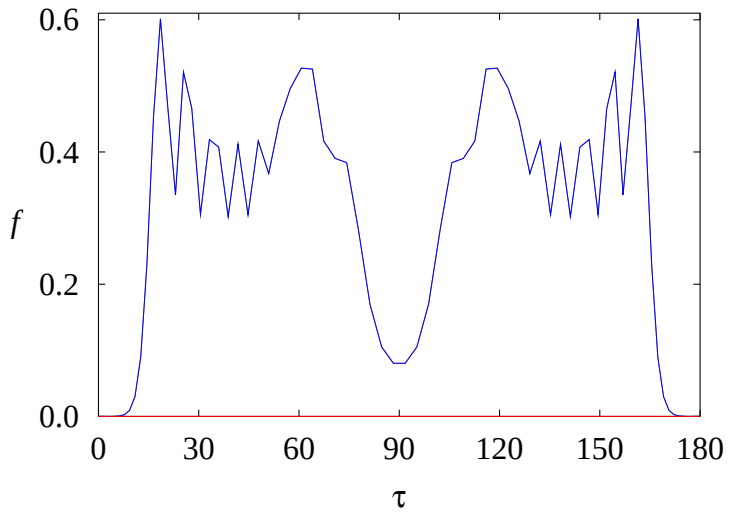


(b)

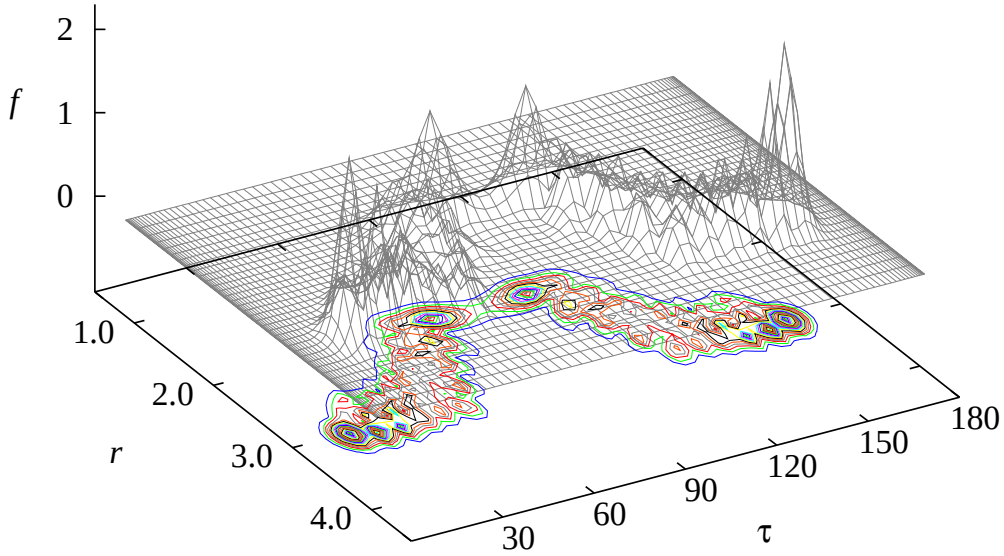


Figure 5.9: Probability density functions (See 2.5.3) for the $\widetilde{X}^2$ $HO_2$ $J = 1/2$, $\Gamma_{\text{ers}} = A_1$ 560th state.

Here, the $\tau$ and $r$ coordinates are given in degrees and Bohr, respectively. Figure (a) shows one-dimensional probability density functions. The blue curve is $f_-(\tau)$ (the lower electronic surface's probability density function), the red curve is $f_+(\tau)$ (the upper electronic surface's probability density function) and the black curve is $f(\tau)$ (the total probability density function). The gray surface in Figure (b) shows the two-dimensional probability density function $f(r, \tau)$. Coloured lines are the contour plot of the two-dimensional probability density function $f(r, \tau)$. Contours are plotted for 0.1 separations.

(a)

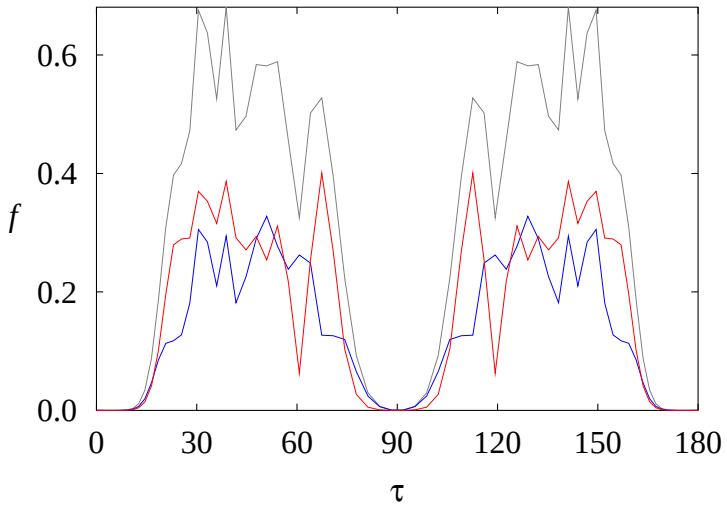


(b)

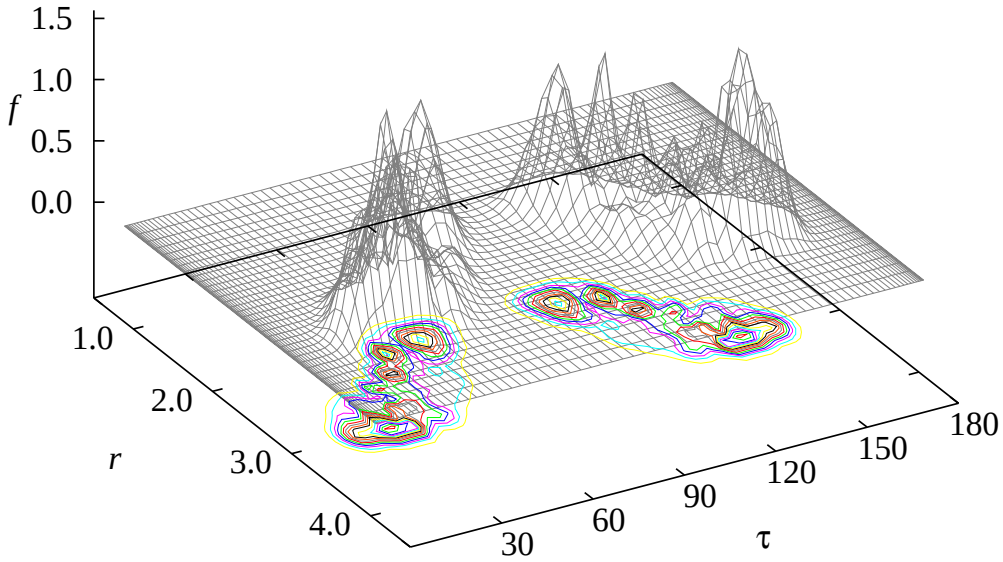


Figure 5.10: Probability density functions (See 2.5.3) for the $\widetilde{A}^2$ $HO_2$ $J = 1/2$, $\Gamma_{\text{ers}} = A_2$ 582nd state.

Here, the $\tau$ and $r$ coordinates are given in degrees and Bohr, respectively. Figure (a) shows one-dimensional probability density functions. The blue curve is $f_-(\tau)$ (the lower electronic surface's probability density function), the red curve is $f_+(\tau)$ (the upper electronic surface's probability density function) and the black curve is $f(\tau)$ (the total probability density function). The gray surface in Figure (b) shows the two-dimensional probability density function $f(r, \tau)$. Coloured lines are the contour plot of the two-dimensional probability density function $f(r, \tau)$. Contours are plotted for 0.1 separations.

(a)

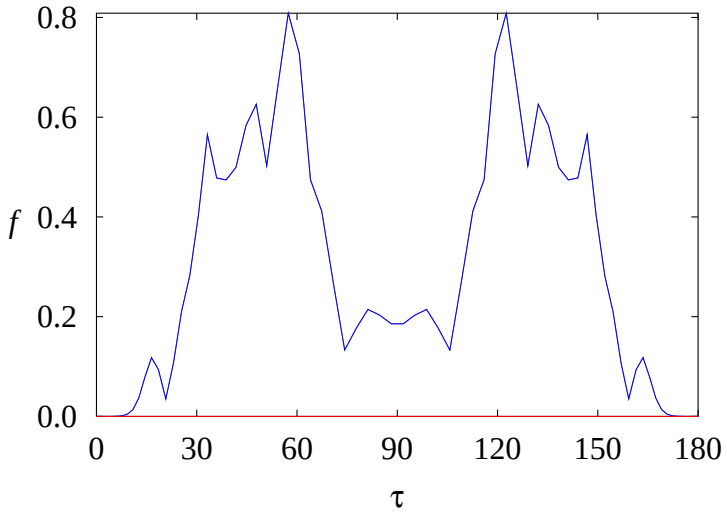


(b)

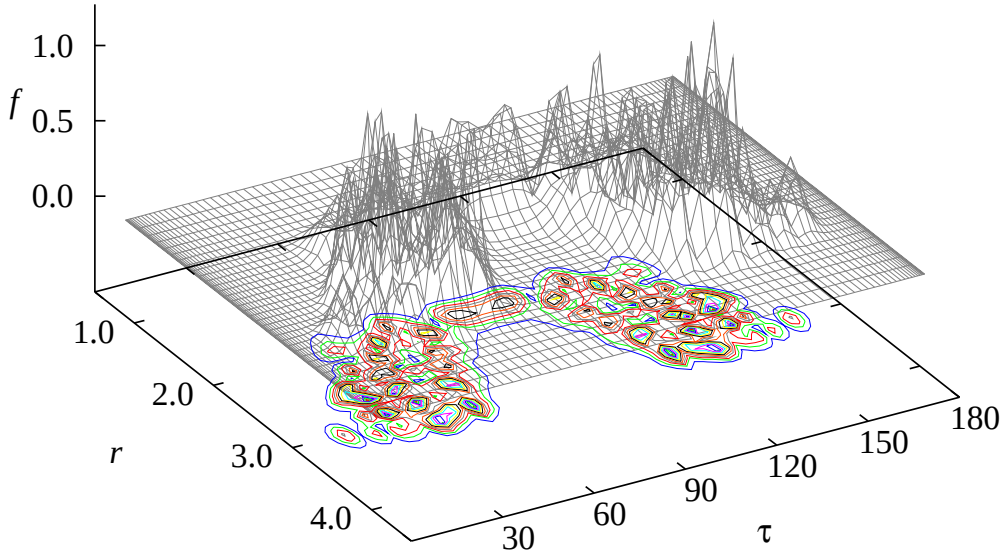


Figure 5.11: Probability density functions (See 2.5.3) for the $\widetilde{X}^2$ $HO_2$ $J = 1/2$, $\Gamma_{\text{ers}} = A_1$ 601st state.

Here, the $\tau$ and $r$ coordinates are given in degrees and Bohr, respectively. Figure (a) shows one-dimensional probability density functions. The blue curve is $f_-(\tau)$ (the lower electronic surface's probability density function), the red curve is $f_+(\tau)$ (the upper electronic surface's probability density function) and the black curve is $f(\tau)$ (the total probability density function). The gray surface in Figure (b) shows the two-dimensional probability density function $f(r, \tau)$. Coloured lines are the contour plot of the two-dimensional probability density function $f(r, \tau)$. Contours are plotted for 0.1 separations.

(a)

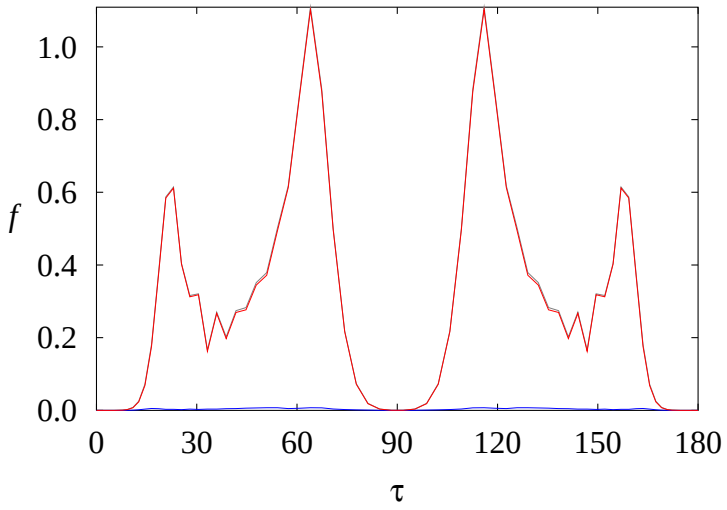


(b)

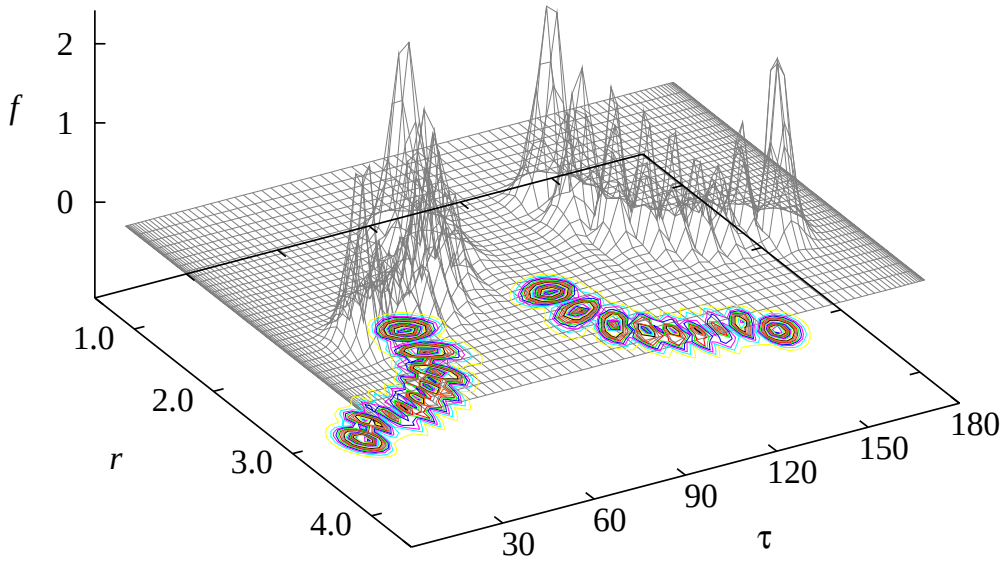


Figure 5.12: Probability density functions (See 2.5.3) for the $\widetilde{A}^2$ $HO_2$ $J = 1/2$, $\Gamma_{\text{ers}} = A_2$ 693rd state.

Here, the $\tau$ and $r$ coordinates are given in degrees and Bohr, respectively. Figure (a) shows one-dimensional probability density functions. The blue curve is $f_-(\tau)$ (the lower electronic surface's probability density function), the red curve is $f_+(\tau)$ (the upper electronic surface's probability density function) and the black curve is $f(\tau)$ (the total probability density function). The gray surface in Figure (b) shows the two-dimensional probability density function $f(r, \tau)$. Coloured lines are the contour plot of the two-dimensional probability density function $f(r, \tau)$. Contours are plotted for 0.1 separations.

(a)

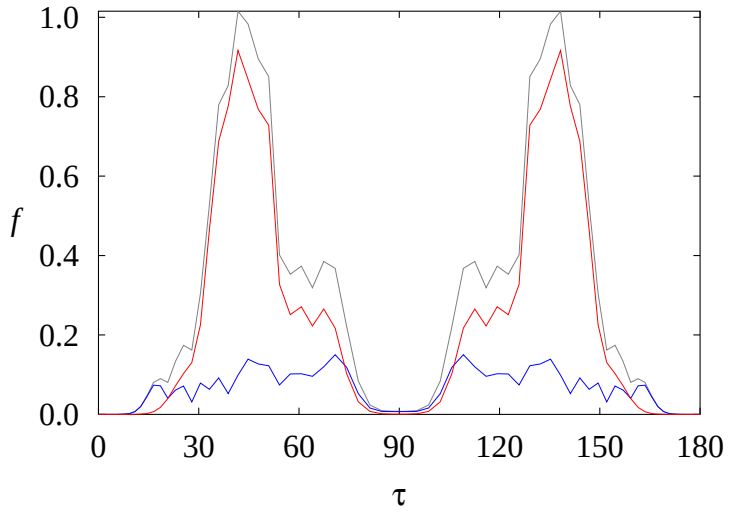


(b)

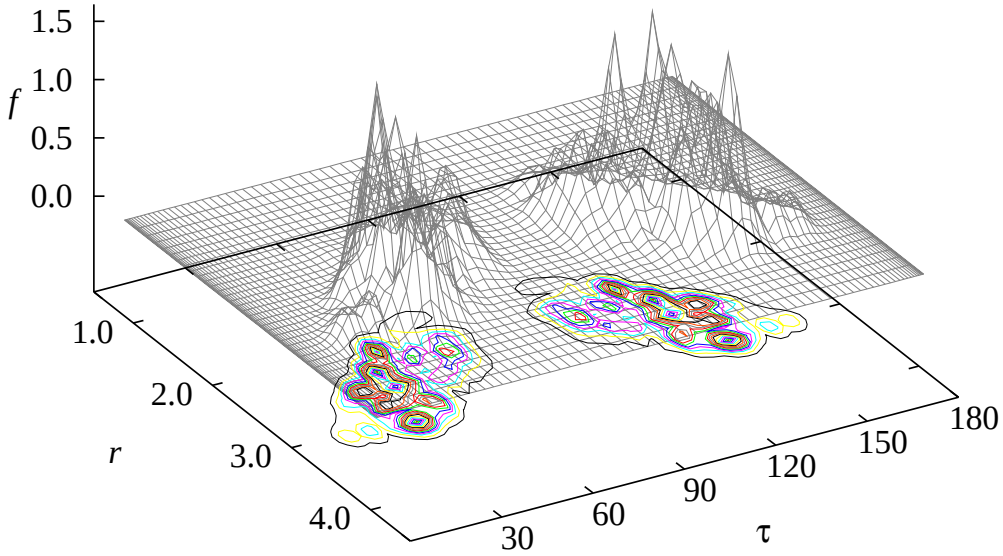


Figure 5.13: Probability density functions (See 2.5.3) for the $\widetilde{X}^2$ $HO_2$ $J = 1/2$, $\Gamma_{\text{ers}} = B_1$ 740th state.

Here, the $\tau$ and $r$ coordinates are given in degrees and Bohr, respectively. Figure (a) shows one-dimensional probability density functions. The blue curve is $f_-(\tau)$ (the lower electronic surface's probability density function), the red curve is $f_+(\tau)$ (the upper electronic surface's probability density function) and the black curve is $f(\tau)$ (the total probability density function). The gray surface in Figure (b) shows the two-dimensional probability density function $f(r, \tau)$. Coloured lines are the contour plot of the two-dimensional probability density function $f(r, \tau)$. Contours are plotted for 0.1 separations.

as tunneling pair states. As an example of this kind, we show the probability density function of the 601st $\Gamma_{\rm rve} = A_1$ state with $P_- = 100\%$ in Fig. 5.11. This state is solely originates in the lower electronic state. We have tried to find the delocalized states which originate in the upper electonic state. Unfortunately, in the energy range we could calculate with our computer resources, we did not find any states as well-delocalized state, as much as delocalized as in Fig. 5.11. We have 693rd $\Gamma_{\rm rve} = A_2$ state with $P_- = 1\%$ and $P_+ = 99\%$, as shown in Fig. 5.12. This state has the biggest tunneling splittings among the states which originate in the upper electronic surface (10.92 cm$^{-1}$). Also we have a some what delocalized state the 740th $\Gamma_{\rm rve} = B_1$ state with $P_- = 21\%$ and $P_+ = 79\%$, shown in Fig. 5.13.

# Chapter 6

# Conclusion

In previous theoretical descriptions of the Renner effect, starting with Renner's 1934 paper [1], only one linear geometry with a double degenerate electronic energy is considered. In this thesis, a hitherto unstudied phenomenon, the double Renner effect is described; we consider two linear geometries of a triatomic molecule with the Renner effect simultaneously. The rotation-vibration Hamiltonian of the double Renner effect for a triatomic molecule has been constructed in terms of Jacobi coordinates. A program to calculate rotation-vibration energies of a triatomic molecule with the double Renner effect has been constructed. The program, DR, can treat both ABC- and ABB-type of molecules; isomerization of a molecule (ABC to BCA or ABB to BBA) can be studied together with the Renner effect, the spin-orbit interaction and all the rotational and vibrational motion within a triatomic molecule.

The Numerov-Cooley numerical integration method has been used to construct the bending basis functions, and Morse-like stretching functions were used to construct the $r$- and $R$- stretching basis functions. Rotational-spin basis functions were constructed from rigid rotor functions.

The resulting Hamiltonian matrix mainly consists of nine components. In order to have a smaller matrix size for the diagonalization, the Hamiltonian matrix was diago-

nalized in two steps. The first step is the $K$-block diagonalization. In this step, six of the resulting Hamiltonian matrix components, **HAMILV**, **HBL1**, **HBL2**, **HAMILBA** and **HAMILBB**, were combined and diagonalized. The next step is the $J$-block diagonalization. Three of the resulting Hamiltonian matrix components, **HAMILNK**, **HAMILDK** and **HAMILSO** were combined together with the diagonalized $K$-block matrices and diagonalized.

All the theory behind the double Renner effect rovibronic energy calculations is described in Chapter 2. The methods to understand the nature of each rovibronic energy level are also shown in Chapter 2. For example, in order to understand the nature of the double Renner effect, we used the probability density function to analyze the eigenfunctions. The description of the program DR was summarized in Chapter 3.

As examples of ABC- and ABB-type molecules, the program was applied to $\widetilde{A}\ ^2\Pi$ MgNC/MgCN states and to $HO_2$ in the $\widetilde{X}\ ^2A''$ and $\widetilde{A}\ ^2A'$ states. In Chapter 4, the application to ABC-type molecules was shown and the application to ABB-type molecules was shown in Chapter 5.

In both cases, calculated fundamental vibration energies with the program DR agreed well with the previous studies. In case of $\widetilde{A}\ ^2\Pi$ MgNC/MgCN, a "triangle" local minimum was found in both Renner-component electronic surfaces (the lower $1^2A"$ electronic state and the upper $2^2A'$ electronic state). The $2^2A'$ state has a much bigger "lake" in the potential energy surface around $\tau = 90^\circ$ than the $1^2A"$ state. The calculation with the program DR found several rovibronic energies originating in the bent $2^2A'$ state, but not in the $1^2A"$ state. The minimum around $\tau = 90^\circ$ in the $1^2A"$ electronic surface was too shallow and too small, and it could not produce well bent $1^2A"$ MgNC vibrational states.

Many delocalized states were observed in the $\widetilde{A}\ ^2\Pi$ MgNC/MgCN system and $HO_2$ ($\widetilde{X}\ ^2A''$ and $\widetilde{A}\ ^2A'$) systems. The probability density functions showed that some delocalized states were composed of both of the lower and the upper electronic states,

and some belonged to only one of the electronic surfaces. Each delocalized state was different from the others, showing the nature of the Renner effect; it is chaotic and beautiful! In the calculation of the $\widetilde{X}\ ^2A''$ $HO_2$ and $\widetilde{A}\ ^2A'$ $HO_2$ electronic states, the tunneling splitting energies were affected by the Renner effect. This is the first theoretical calculation to prove the importance of treating the Renner effect together with the isomerization (in other words, the double Renner effect) in the $HO_2$ $\widetilde{X}\ ^2A''$ and $\widetilde{A}\ ^2A'$ electronic states.

The accuracies of the bent $2^2A'$ MgNC rovibronic states found in the calculation with the program DR depend on the accuracy of the $ab\ initio$ potential energy surfaces and the size of the basis set we employed for the calculation with DR. The largest basis set allowed by the restrictions of the computational resources is used in the calculation with the program DR. The $ab\ initio$ program took three days to calculate just one $ab\ initio$ point. Extensive $ab\ initio$ calculations, which represent the potential energy very well around $\widetilde{A}\ ^2\Pi$ MgNC equilibrium geometry were carried out, but this does not prove that it will reproduce bent MgNC as well as it does its linear geometry. Unfortunately the methods used for constructing the potential energy surfaces from the $ab\ initio$ points were not the ideal ones. The fitting to an analytical surface which covers the complete $\tau$ coordinate region ($\tau = 0^\circ$ to $180^\circ$), was very difficult. We could not find suitable analytical global potential energy functions. Thus interpolated numerical global potential energy functions were used. Interpolated numerical functions tend to have less smoothness in reproducing potential energy surfaces than analytical functions.

In case of $\widetilde{X}\ ^2A''$ $HO_2$ and $\widetilde{A}\ ^2A'$ $HO_2$, we have used an analytical potential energy surface. However, the potential energy surface did not result from fitting $ab\ initio$ points with full $\tau$ region. Fitting all the $ab\ inito$ points we have in the MgNC/MgCN system or in the $HO_2$ system to an analytical expression together with more $ab\ initio$ points will help us having more ”real” potential energy surfaces.

At this point, we did everything we could to apply the program DR for these two

molecules, but in future, I believe with the progress of computational methods, we will have much more accurate global potential energy surfaces, and be able to extend the calculations. In collaboration with the Institute of Applied Mathematics, University of Wuppertal, new diagonalization methods for the program DR are being developed and part of the program are planned to be parallelized. This will allow the program to perform much bigger calculations with much bigger basis sets, and the results will be much more accurate. The program DR can be used to study new phenomena with the two degenerate surfaces including isomerization, and I believe this will open a new area in computational molecular spectroscopy.

# List of Figures


2.1 The Jacobi coordinate system. A, B and C represents the atoms in this coordinate system. $R$ and $r$ are the bond lengths. $\tau$ is the Jacobi angle. 10

2.2 The ABB molecule with molecular fixed coordinate system. Nuclei 1 and 2 correspond to nucleus B of the ABB molecule, and nucleus 3 corresponds to the nucleus A. The $a$ axes points from nucleus 1 to nucleus 2. The $b$ axes points from nucleus 1 and 2 to nucleus 3. The $c$ axis points out of the plane of paper, so that it makes a right handed coordinate system. . . . . 56

3.1 A symmetry matrix element $(i, j)$ are saved in n th vector element. . . . 65

3.2 A schematic drawing for the program DR with $K$-block Hamiltonian matrix construction and $K$-block diagonalization. $\mathbf{BASS1}$, $\mathbf{BASS2}$ and $\mathbf{BASSB}$ contain the stretching basis function for $R$ and $r$ coordinate and the bending basis function respectively. $\mathbf{HBL1}$, $\mathbf{HBL2}$, $\mathbf{R1M2}$, $\mathbf{R2M2}$, $\mathbf{HAMILB}$, $\mathbf{HAMILBA}$, $\mathbf{HAMILBB}$, $\mathbf{HAMILSO}$ and $\mathbf{HAMILV}$ are the Hamiltonian matrix elements. See details in the text. . . . . 66

3.3 A schematic diagram showing how the program DR constructs the $J$-block Hamiltonian matrix from the contracted $K$-block Hamiltonian matrix. $\mathbf{HAMILDIAG}$, $\mathbf{HAMILDK}$ and $\mathbf{HAMILDN}$ have the shorthand notations $\mathbf{DIAG}$, $\mathbf{DK}$ and $\mathbf{DN}$, respectively. See details in the text. . . 70

3.4 A schematic representation of the program DR with $J$-block Hamiltonian matrix construction and $J$-block diagonalization. $\mathbf{HAMILDIAG}$, $\mathbf{HAMILDK}$ and $\mathbf{HAMILDN}$ are the Hamiltonian matrix elements. See details in the text. . . . . 71

4.1 The minimum energy path of $\widetilde{A}^2\Pi$ MgNC/MgCN produced from the potential energy function expanded in Eq. (4.3) together with the parameters in Tables 4.1 - 4.5. $\tau$ is given in degrees and the potential $V$ is given in cm$^{-1}$. The blue curve shows the lower potential energy surface and the red curve shows the upper potential energy surface. . . . . 84

4.2 The potential energy path used to produce bending basis functions for the $\widetilde{A}^2\Pi$ MgNC/MgCN. The expressions for the functions are given in Eq. (4.4) and the parameter values are given in Table 4.6. $\tau$ is given in degrees and the potential $V$ is given in cm$^{-1}$. The blue curve shows the lower potential energy surface and the red curve shows the upper potential energy surface. . . . . 85

4.3 Probability density functions (See 2.5.3) for the $\widetilde{A}^2\Pi$ MgCN $(0,0,0)$ state. 95

4.4 Probability density functions (See 2.5.3) for the $\widetilde{A}^2\Pi$MgNC $(0,0,0)$ state. 96

4.5 Probability density functions (See 2.5.3) for the bent $2^2A'$MgNC $(0,0,0)$ state. . . . . 97

4.6 Probability density functions (See 2.5.3) for the bent $2^2A'$MgNC $(0,1,0)$ state. . . . . 98

4.7 Probability density functions (See 2.5.3) for the $J = 1/2$, $\Gamma_{\rm ers} = A$" 104th state. . . . . 99

4.8 Probability density functions (See 2.5.3) for the $J = 1/2$, $\Gamma_{\rm ers} = A'$ 104th state. . . . . 100

4.9 Probability density functions (See 2.5.3) for the bent $2^2A'$MgNC $(0,2,0)$ state. . . . . 101

4.10 Probability density functions (See 2.5.3) for the bent $2^2A'$MgNC $(0,3,0)$ state. . . . . 102
4.11 Probability density functions (See 2.5.3) for the $J = 1/2$, $\Gamma_{\rm ers} = A$" 158th state. . . . . 103
4.12 Probability density functions (See 2.5.3) for the $J = 1/2$, $\Gamma_{\rm ers} = A$" 161st state. . . . . 107
4.13 Probability density functions (See 2.5.3) for the $J = 1/2$, $\Gamma_{\rm ers} = A$" 162nd state. . . . . 108
4.14 Probability density functions (See 2.5.3) for the $J = 1/2$, $\Gamma_{\rm ers} = A$" 168th state. . . . . 109
4.15 Probability density functions (See 2.5.3) for the $J = 1/2$, $\Gamma_{\rm ers} = A$" 171th state. . . . . 110
4.16 Probability density functions (See 2.5.3) for the $J = 1/2$, $\Gamma_{\rm ers} = A$" 178th state. . . . . 111
4.17 Probability density functions (See 2.5.3) for the $J = 1/2$, $\Gamma_{\rm ers} = A$" 180th state. . . . . 112
4.18 Probability density functions (See 2.5.3) for the $J = 1/2$, $\Gamma_{\rm ers} = A$" 182th state. . . . . 113
4.19 Probability density functions (See 2.5.3) for the $J = 1/2$, $\Gamma_{\rm ers} = A$" 185th state. . . . . 114
4.20 Probability density functions (See 2.5.3) for the $J = 1/2$, $\Gamma_{\rm ers} = A$" 186th state. . . . . 115
4.21 Probability density functions (See 2.5.3) for the $J = 1/2$, $\Gamma_{\rm ers} = A$" 187th state. . . . . 116

5.1 The potential energy path used to produce bending basis function for the $\widetilde{X}\ ^2A'' - \widetilde{A}\ ^2A'$ surface. See equations (5.5) - (5.7) together with the parameters in Table 5.2. $\tau$ is given in degrees and the potential $V$ is given in cm$^{-1}$. The blue curve shows the lower potential energy surface and the red curve shows the upper potential energy surface. . . . . 125
5.2 Probability density functions (See 2.5.3) for the $\widetilde{X}^2$ $HO_2$ $(0,0,0)$ state. . 133
5.3 Probability density functions (See 2.5.3) for the Fermi-resonance $\widetilde{X}^2$ $HO_2$ $(2,0,0)$ state. . . . . 134
5.4 Probability density functions (See 2.5.3) for the Fermi-resonance $\widetilde{X}^2$ $HO_2$ $(0,5,0)$ state. . . . . 135
5.5 Probability density functions (See 2.5.3) for the $\widetilde{A}^2$ $HO_2$ $(0,0,0)$ state. . . 136
5.6 Probability density functions (See 2.5.3) for the $\widetilde{X}^2$ $HO_2$ $J = 1/2$, $\Gamma_{\rm ers} = B_2$ 331st state. . . . . 141
5.7 Probability density functions (See 2.5.3) for the $\widetilde{X}^2$ $HO_2$ $J = 1/2$, $\Gamma_{\rm ers} = B_2$ 395th state. . . . . 142
5.8 Probability density functions (See 2.5.3) for the $\widetilde{X}^2$ $HO_2$ $J = 1/2$, $\Gamma_{\rm ers} = B_2$ 552nd state. . . . . 143
5.9 Probability density functions (See 2.5.3) for the $\widetilde{X}^2$ $HO_2$ $J = 1/2$, $\Gamma_{\rm ers} = A_1$ 560th state. . . . . 144
5.10 Probability density functions (See 2.5.3) for the $\widetilde{A}^2$ $HO_2$ $J = 1/2$, $\Gamma_{\rm ers} = A_2$ 582nd state. . . . . 145
5.11 Probability density functions (See 2.5.3) for the $\widetilde{X}^2$ $HO_2$ $J = 1/2$, $\Gamma_{\rm ers} = A_1$ 601st state. . . . . 146
5.12 Probability density functions (See 2.5.3) for the $\widetilde{A}^2$ $HO_2$ $J = 1/2$, $\Gamma_{\rm ers} = A_2$ 693rd state. . . . . 147
5.13 Probability density functions (See 2.5.3) for the $\widetilde{X}^2$ $HO_2$ $J = 1/2$, $\Gamma_{\rm ers} = B_1$ 740th state. . . . . 148

# List of Tables


2.1 The character table of the MS group $C_{\rm s}(\rm M)$. . . . . 33

2.2 The symmetry $\Gamma_{\rm rs}$ of the rotation-spin basis function in the MS group $C_{\rm s}(\rm M)$. . . . . 33

2.3 The relation of the $K$, $N$ quantum numbers and $\eta$ states to the symmetry $\Gamma_{\rm ers}$ of the electronic-rotation-spin basis function and the symmetry $\Gamma_{\rm rve}$ of the total basis function in the MS group $C_{\rm s}(\rm M)$. . . . . 34

2.4 The character table of the MS group $C_{2\rm v}(\rm M)$. Atom B corresponds to atom 1 and 2. . . . . 35

2.5 The symmetry $\Gamma_{\rm rs}$ of the rotation-spin basis function in the MS group $C_{2\rm v}(\rm M)$. . . . . 35

2.6 The relation of the $K$, $N$ quantum numbers and $\eta$ states to the symmetry $\Gamma_{\rm ers}$ of the electronic-rotation-spin basis function in the MS group $C_{2\rm v}(\rm M)$. 36

2.7 The relation of the $K$, $N$ quantum numbers and $\eta$ states to the symmetry $\Gamma_{\rm rve}$ in the total basis function of the MS group $C_{2\rm v}(\rm M)$. . . . . 36

2.8 The identification of the symmetry elements of MS group $C_{2\rm v}(\rm M)$. . . . . 57

2.9 Representation of the $C_{2\rm v}(\rm M)$ group for a molecule ABB generated by the basis functions $|N, K_a, M\rangle$ and $|N, K_c, M\rangle$ . . . . . 58

2.10 Symmetry species of rotational functions of a molecule ABB. . . . . 58

2.11 Symmetry species of $\Gamma_{\rm rve}$ of a molecule ABB, with $\Gamma_e$ and $\Gamma_{\rm vib}$. . . . . 58

4.1 Potential energy parameters for equation (4.3), with $\tau = 60°$. . . . . 78
4.2 Potential energy parameters for equation (4.3), with $\tau = 80°$. . . . . 79
4.3 Potential energy parameters for equation (4.3), with $\tau = 90°$. . . . . 80
4.4 Potential energy parameters for equation (4.3), with $\tau = 100°$. . . . . 81
4.5 Potential energy parameters for equation (4.3), with $\tau = 120°$. . . . . 82
4.6 Minimum energy paths parameters in equation (4.6) for lower($\sigma = -$) and upper ($\sigma = +$) electronic surface . . . . . 86
4.7 Vibronic term values (in cm$^{-1}$) of MgNC. Energy levels with $P = J = 1/2, 3/2$ are listed here. When an energy have $e$ and $f$ pairs, the lower component and the splitting are given. . . . . 88
4.8 Vibronic term values (in cm$^{-1}$) of MgNC. Energy levels with $P = J = 1/2, 3/2$ are listed here. When an energy have $e$ and $f$ pairs, the lower component and the splitting are given. . . . . 89
4.9 Vibronic term values (in cm$^{-1}$) of MgNC. Energy levels with $P = J = 1/2, 3/2$ are listed here. When an energy have $e$ and $f$ pairs, the lower component and the splitting are given. . . . . 90
4.10 Vibronic term values (in cm$^{-1}$) of MgNC. Energy levels with $P = J = 1/2, 3/2$ are listed here. When an energy have $e$ and $f$ pairs, the lower component and the splitting are given. . . . . 91
4.11 Vibronic term values (in cm$^{-1}$) of MgNC. Energy levels with $P = J = 1/2, 3/2$ are listed here. When an energy have $e$ and $f$ pairs, the lower component and the splitting are given. . . . . 92
4.12 Vibronic term values (in cm$^{-1}$) of MgNC. Energy levels with $P = J = 1/2, 3/2$ are listed here. When an energy have $e$ and $f$ pairs, the lower component and the splitting are given. . . . . 93

4.13 Vibronic term values (in cm$^{-1}$) of MgNC. Energy levels with $P = J = 1/2, 3/2$ are listed here. When an energy have $e$ and $f$ pairs, the lower component and the splitting are given. . . . . 94
4.14 Vibronic term values (in cm$^{-1}$) of MgNC. . . . . 117
4.15 Vibronic term values (in cm$^{-1}$) of bent MgNC. All energy levels with $J = 1/2, 3/2$ for $\nu_2 = 0, 1, 2$ states are listed here. . . . . 118

5.1 The potential surface parameters for the $\widetilde{X}\ ^2A''$ and $\widetilde{A}\ ^2A'$ states of $HO_2$ from Ref. [65].$^a$ . . . . . 124
5.2 Minimum energy paths parameters in equations (5.5) - (5.7) for lower($\sigma = -$) and upper ($\sigma = +$) electronic surface . . . . . 126
5.3 Vibronic term values (in cm$^{-1}$) of $HO_2$. Energy levels with $N_{K_aK_c} = 0_{00}$ are listed here. When an energy level is split by tunneling, the lower component and the splitting are given. . . . . 127
5.4 Vibronic term values (in cm$^{-1}$) of $HO_2$. Energy levels with $N_{K_aK_c} = 0_{00}$ are listed here. When an energy level is split by tunneling, the lower component and the splitting are given. . . . . 128
5.5 Vibronic term values (in cm$^{-1}$) of $HO_2$. Energy levels with $N_{K_aK_c} = 0_{00}$ are listed here. When an energy level is split by tunneling, the lower component and the splitting are given. . . . . 129
5.6 Vibronic term values (in cm$^{-1}$) of $HO_2$. Energy levels with $N_{K_aK_c} = 0_{00}$ are listed here. When an energy level is split by tunneling, the lower component and the splitting are given. . . . . 130
5.7 Vibronic term values (in cm$^{-1}$) of $HO_2$. Energy levels with $N_{K_aK_c} = 0_{00}$ are listed here. When an energy level is split by tunneling, the lower component and the splitting are given. . . . . 131

5.8 Vibronic term values (in $cm^{-1}$) of $HO_2$. Energy levels with $N_{K_aK_c} = 0_{00}$ are listed here. When an energy level is split by tunneling, the lower component and the splitting are given. . . . . 132
5.9 Vibronic term values (in $cm^{-1}$) of $HO_2$. Energy levels with $N_{K_aK_c} = 0_{00}$ are listed here. When an energy level is split by tunneling, the lower component and the splitting are given. . . . . 137
5.10 Calculated rovibronic state with the program DR for the $\widetilde{X}\ ^2A''$ and $\widetilde{A}\ ^2A'$ states of $HO_2$ (in $cm^{-1}$) in comparision with experiments. . . . . 138

# Bibliography


[1] R. Renner, *Z. Phys.*, **92**, 172 (1934).

[2] K. Dressler and D. A. Ramsay, *J. Chem. Phys.*, **27**, 971 (1957).

[3] K. Dressler and D. A. Ramsay, *Phil. Trans. Roy. Soc. (London)*, **A251**, 69 (1959).

[4] J. A. Pople and H. C. Longuet-Higgins, *J. Chem. Phys.*, **27**, 971 (1957).

[5] H. C. Longuet-Higgins, *Adv. Spectrosc.*, **2**, 429 (1961).

[6] R. N. Dixon, *Phil. Trans. Roy. Soc. (London)*, **A252**, 165 (1960).

[7] P. Jensen, *J. Mol. Spectrosc.*, **128**, 478 (1988).

[8] R. R. Wright and T. A. Miller, *J. Mol. Spectrosc.*, **194**, 219 (1999).

[9] P. Jensen, G. Osmann, and P.R. Bunker, "Computational Molecular Spectroscopy" (P. Jensen and P. R. Bunker, Eds.), Wiley, Chichester, 2000.

[10] E. B. Wilson, J. C. Decius, and P. C. Cross, "Molecular Vibrations", McGraw-Hill, New York, 1955, Section 5.

[11] B. Podolsky, *Phys. Rev.*, **32**, 812 (1928).

[12] P. R. Bunker and P. Jensen, "Molecular Symmetry and Spectroscopy", 2nd Edition, NRC Research Press, Ottawa, Canada, 1998.

[13] R. N. Zare, "Angular Momentum", Wiley, New York, 1988.

[14] T. Barrow, R. N. Dixon, and G. Duxbury, *Mol. Phys.,* **27**, 1217 (1974).

[15] P. Jensen, *Comput. Phys. Rep.*, **1**, 1 (1983).

[16] J. Tennyson and B. T. Sutcliffe, *J. Chem. Phys.,* **77**, 4061 (1982).

[17] K.-E. J. Hallin and A.J.Merer, *J. Mol. Spectrosc.,* **65**, 163 (1977).

[18] Linear Algebra PACKage. See *http://www.netlib.org/lapack/*

[19] J. T. Hougen, *J. Chem. Phys.,* **36**, 519 (1962).

[20] J. M. Brown, J. T. Hougen, K.-P. Huber, J. W. C. Johns, I. Kopp, H. Lefebvre-Brion, A. J. Merer, D. A. Ramsay, J. Rostas, and R. N. Zare, *J. Mol. Spectrosc.,* **55**, 500 (1975).

[21] M. Guélin, J. Cernicharo, C. Kahane, and J. Gomez-Gonzales, *Astron. Astrophys,* **157**, L17 (1986).

[22] C. W. Bauschlicher, S. R. Langhoff, and H. Partridge, *Chem. Phys. Lett.,* **115**, 124 (1985).

[23] K. Kawaguchi, E. Kagi, T. Hirano, S. Takano, and S. Saito, *Astrophys. J.* **406**, L39 (1993).

[24] K. Ishii, T. Hirano, U. Nagashima, B. Weis, and K. Yamashita, *Astrophys. J.* **410**, L43 (1993).

[25] K. Ishii, T. Hirano, U. Nagashima, B. Weis, and K. Yamashita, *J. Mol. Struct. (THEOCHEM)* **305**, 117 (1994).

[26] C. Barrientos and A. Largo, *J. Mol. Struct. (THEOCHEM)* **336**, 29 (1995).

[27] S. Petrie, *J. Chem. Soc., Faraday Trans.* **92**, 1135 (1996).

[28] M. Guélin, M. Forestini, P. Valiron, L. M. Ziurys, M. A. Anderson, J. Cernicharo, and C. Kahane, *Astron. Astrophys,* **297**, 183 (1995).

[29] D. Woon, *Astrophys. J.* **456**, 602 (1996).

[30] M. Kieninger, K. Irving, F. Rivas-Silva, A. Palma, and O. N. Ventura, *J. Mol. Struct. (THEOCHEM)* **422**, 133 (1998).

[31] M. A. Anderson and L. M. Ziurys, *Chem. Phys. Lett.,* **231**, 164 (1994).

[32] E. Kagi, K. Kawaguchi, S. Takano, and T. Hirano, *J. Chem. Phys.,* **104**, 1263 (1996).

[33] E. Kagi and K. Kawaguchi, *J. Mol. Spectrosc.,* **199**, 309 (2000).

[34] L. M. Ziurys, A. J. Apponi, M. Guèlin, and J. Cernicharo, *Astrophys. J.* **445**, L47 (1995).

[35] M. A. Anderson, T. C. Steimle, and L. M. Ziurys, *Astrophys. J.* **429**, L41 (1994).

[36] P. J. Gardner, S. R. Preston, R. Siertsema, and D. Steele, *J. Comp. Chem.* **14**, 1523 (1993).

[37] O. Bludský, V. Špirko, T. E. Odaka, T. Hirano, and P. Jensen *J. Mol. Spectrosc.,* acceptted for publication

[38] M. Fukushima and T. Ishiwata, *J. Mol. Spectrosc.,* **216**, 159 (2002).

[39] T. C. Steimle and R. R. Bousquet, *J. Chem. Phys.,* **115**, 5203 (2001).

[40] H. J. Werner and P. J. Knowles, *J. Chem. Phys.,* **89**, 5803 (1988).

[41] P. J. Knowles and H. J. Werner, *Chem. Phys. Lett.,* **145**, 514 (1988).

[42] P. J. Knowles and H. J. Werner, *Theor. Chim. Acta* **84**, 95 (1992).

[43] S. R. Langhoff and E. R. Davidson, *Int. J. Quantum Chem.* **8**, 61 (1974).

[44] T. H. Dunning, Jr., *J. Chem. Phys.,* **90**, 1007 (1989).

[45] R. A. Kendall, T. H. Dunning, Jr., and R. J. Harrison, *J. Chem. Phys.,* **96**, 6796 (1992).

[46] T. Taketsugu and S. Carter , *Chem. Phys. Lett.,* **340**, 385 (2001).

[47] M. Fukushima and T. Ishiwata, The Eighteenth Colloquium on High Resolution Molecular Spectroscopy, France, Dijon (HRMS2003) F19

[48] L.B. Harding, J. Troe and V.G.Ushakov, *Phys. Chem. Chem. Phys.,* **2**, 631 (2000).

[49] L.B. Harding, A.I.Maergoiz, J. Troe and V.G.Ushakov, *J. Chem. Phys.*, **113**, 11019 (2000)

[50] J. Troe and V.G.Ushakov, *J. Chem. Phys.,* **115**, 3621 (2001).

[51] S. Viti, E. Roueff, T. W. Hartquist, G. Pineau des Foriêts, and D. A. Williams, *Astron. Astrophys,* **370**, 557 (2001).

[52] A. D. Walsh, *J. Chem. Soc.* 2288 (1953)

[53] J. L. Gole and D. F. Hayes, *J. Chem. Phys.,* **57**, 360 (1972).

[54] R. J. Buenker and S. D. Peyerimhoff, *Chem. Phys.,* **28**, 299 (1978).

[55] H. E. Hunziker and H. R. Wendt, *J. Chem. Phys.,* **60**, 4622 (1974).

[56] K. H. Becker, E. H. Fink, A. Leiss and U. Schurath, *J. Chem. Phys.,* **60**, 4623 (1974).

[57] R. P. Tuckett, P. A. Freedman and W. J. Jones, *Mol. Phys.* **37**, 379 (1979).

[58] S. Saito and C. Matsumura, *J. Mol. Spectrosc.* **80**, 34 (1980).

[59] C. Yamada, Y. Endo, and E. Hirota, *J. Chem. Phys.* **78**, 4379 (1983).

[60] J. B. Burkholder, P. D. Hammer, C. J. Howard, J. P. Towle, and J. M. Brown, *J. Mol. Spectrosc.* **151**, 493 (1992).

[61] K. V. Chance, K. Park, K. M. Evenson, L. R. Zink, and F. Stroh, *J. Mol. Spectrosc.* **172**, 407 (1995).

[62] K. V. Chance, K. Park, K. M. Evenson, L. R. Zink, F. Stroh, E. H. Fink, and D. A. Ramsay, *J. Mol. Spectrosc.* **183**, 418 (1997).

[63] E. H. Fink and D. A. Ramsay, *J. Mol. Spectrosc.,* **185**, 304 (1997).

[64] G. Osmann, P. R. Bunker, P. Jensen, R. J. Buenker, J.-P. Gu, and G. Hirsch, *J. Mol. Spectrosc.,* **197**, 262 (1999).

[65] P. Jensen, R. J. Buenker, J.-P. Gu, G. Osmann and P. R. Bunker, *Can. J. Phys,* **79**, 641 (2001).

[66] P. Lieberman, private communication.

[67] L. F. Pacios and P. A. Christiansen, *J. Chem. Phys.,* **82**, 2664 (1985).

[68] R. J. Buenker and S. D. Peyerimhoff, *Theor. Chim. Acta* **35**, 33 (1974).

[69] R. J. Buenker and S. D. Peyerimhoff, *Theor. Chim. Acta* **39**, 217 (1975).

[70] R. J. Buenker, S. D. Peyerimhoff and W. Butscher, *Mol. Phys.,* **35**, 771 (1978).

[71] R. J. Buenker, *Int. J. Quantum Chem.* **29**, 435 (1986).

[72] R. J. Buenker, in *Proceedings of the Workshop on Quantum Chemistry and Molecular Physics*, Wollongong, Australia, ed. P. Burton (University Press, Wollongong, 1980)

[73] R. J. Buenker, in: *Studies in Physical and Theoretical Chemistry*, Vol. 21. Current Aspects of Quantum Chemistry, ed. R. Carbo (Elsevier, Amsterdam, 1981) p.17

[74] S. Krebs and R. J. Buenker, *J. Chem. Phys.,* **103**, 5613 (1995).

[75] R. J. Buenker and R. A. Phillips, *J. Mol. Struct. THEOCHEM* **123**, 291 (1985).

[76] E. R. Davidson, *The World of Quantum Chemistry*, ed. by R. Daudel and B. Pullman (Reidel, 1974), p.17

[77] J. M. Bowman, B. Gazdy, J. A. Bentley, T. J. Lee and C. E. Dateo, *J. Chem. Phys.*, **99**, 308 (1993).

[78] E. H. Fink and D. A. Ramsay, private communication.

# Appendix A

# A Theoretical Study of MgNC and MgCN in the $\widetilde{X}\ ^2\Sigma$ Electronic State

T. Hirano, K. Ishii, T. E. Odaka and P. Jensen

Published in

*Journal of Molecular Spectroscopy* **211**, 147-161 in 2002.

http://www.sciencedirect.com/science/journal/00222852

# Appendix B

# *Ab initio* molecular orbital prediction of the Renner-Teller effect for the first excited state $^2\Pi$ of MgNC: Reinterpretation of the laser-induced fluorescence spectrum based on the predicted spectroscopic constants

T. E. Odaka, T. Taketsugu, T. Hirano and U. Nagashima

Published in

*Journal of Chemical Physics*, **115**, 1349-1354 in 2001.

http://jcp.aip.org/jcp/top.jsp

# Appendix C

# An *ab initio* study of the $\widetilde{A}\ ^2\Pi$ State and the $\widetilde{A}\ ^2\Pi \leftarrow \widetilde{X}\ ^2\Sigma$ Electronic Transition of MgNC

T. E. Odaka, T. Hirano and P. Jensen

Published in

*Journal of Molecular Spectroscopy*, **211**, 147-161 in 2002.

http://www.sciencedirect.com/science/journal/00222852

# Appendix D

# The Renner effect in triatomic molecule with appication to $CH_2^+$, MgNC and $NH_2$

P. Jensen, T. E. Odaka, W. P. Kraemer, T. Hirano, P. R. Bunker

Published in

*Spectrochimica Acta Part A*, **58**, 763-794 in 2002.

http://www.sciencedirect.com/science/journal/13861425

# Appendix E

# A Theoretical Study of $\widetilde{A}\ ^2\Pi$ MgCN

T. E. Odaka, T. Hirano and P. Jensen

Published in

*Journal of Molecular Spectroscopy*, **216**, 379-396 in 2002.

http://www.sciencedirect.com/science/journal/00222852